Modelling, Estimation and Control of a Twin-Helicopter Slung Load Transportation System

Yashren Reddi
BScEng, MScEng (KwaZulu Natal)

Thesis Presented for the Degree of
Doctor of Philosophy
In the Department of Electrical Engineering
University of Cape Town
September 2018

Declaration

I, Yashren Reddi, hereby declare that the work on which this thesis is based is my original work (except where acknowledgements indicate otherwise) and that neither the whole work nor any part of it has been, is being, or is to be submitted for another degree in this or any other university. I authorise the University to reproduce for the purpose of research either the whole or any portion of the contents in any manner whatsoever.

Signed by candidate

Author

26 · 09 · 2018

Date

Abstract

The development of a control system to transport and assemble cargo using two helicopters is presented in this thesis. It is more economical to use multiple lower cost helicopters in a coordinated manner to carry cargo than to use a single high performance helicopter for the transportation task. The reason for the generally higher cost of hiring high performance helicopters, is because they are not required often, and so, remain idle for most of their lifetime. Thus, using less specialised, lower performing helicopters to share the load is cheaper. Beyond just sharing the load of the cargo, the objective in this investigation is to control the attitude such that precise placement of the cargo can be made. This objective cannot be achieved using a single helicopter, unless a sophisticated tethering mechanism is developed. The installation of wind-turbine blades, powerline towers and radio masts in remote locations, are examples of where the application of this technology may be useful.

The investigation of this thesis is around modelling, estimation and control of the twin-helicopter slung load transportation system. The title reflects the investigation that was required to be done to determine whether a scheme could be realisable. To test the concept, an experimental platform was developed. A small, light-weight and high performance avionics system was designed and interfaced to the helicopters. The experimentation was done indoors, and hence, the flying volume was limited. For the purpose of feedback and analysis, a motion capture system was developed to track the position and attitude of the helicopters. A high-fidelity mathematical model of a small-scale helicopter was developed. Estimation algorithms were then developed to optimally fuse the data from the instrumentation designed. The data was then used in a system identification exercise to find the parameters that capture the dynamics of the helicopter. The full constrained model of the twin-helicopter slung load dynamics was then developed. The high-fidelity multivariable, interacting system was then linearised to generate a set of uncertain plants. Unexpected resonant modes were investigated using modal analysis to understand their source. Robust controllers were designed using Quantitative Feedback Theory (QFT) for the individual helicopter attitude and altitude loops. A solution was found for the twin-helicopter load transportation system by decoupling the plant with a static pre-compensator and then designing a decentralised QFT controller for the 6×6 plant. The effort of this thesis is towards the (practical) realisation of a twin-helicopter aerial crane capable of attitude control; the architecture for the industrialisation of the twin-helicopter load transportation system is proposed.

Acknowledgements

I would like to firstly thank my mother for her unwavering support, encouragement and for never having a thread of doubt in me. Her work ethic has been the kernel of my existence. To my father and sister, thank you for setting me at ease when there seemed to be “no solution”.

I would like to thank all the staff and my colleagues at the University of KwaZulu Natal, where this work began, for the countless interactions that led to the completion of this work. In particular, I would like to acknowledge Trevor Lorimer for the number of late evening discussions regarding the modelling and flying of helicopters. Our discussions were essential to my understanding of flight dynamics. In addition to that, I need to express my gratitude for the general mechanical engineering insight that you have given me through the years, of which cannot be learned from any book. I would also like to thank the administrative staff of the University of KwaZulu Natal for allowing me to continue my work at the University of Cape Town.

Moving to Cape Town to continue research was not easy. But the staff and my colleagues at the University of Cape Town helped me settle into the new environment. I would like to thank Arnold Pretorius for our numerous discussions on control design; it is very rare to find people with such sincere curiosity and determination for understanding control systems theory.

None of the research would be possible without the financial support from the National Research Foundation (NRF), so I thank the NRF who supported me while I was a full-time student.

Lastly, I would like to thank my supervisor Professor Edward Boje, and the “father” of control systems at my alma mater, Professor Eduard Eitelberg. Thank you both for the guidance and inspiration you have provided. To Professor Boje, thank you for all your far reaching intellectual remarks that I only seem to make sense of weeks later. Your standard for excellence keeps me pushing my own boundaries. I would like to thank Professor Eitelberg for bringing my attention to the twin-helicopter slung load transportation problem, and our initial discussion that convinced me to take it on. The education you both have given me in the form of Quantitative Feedback Theory (QFT), has instilled Isaac Horowitz’ principle of “Scientific work done honestly…”, not only in my scientific endeavours, but also in my life philosophies.

Contents

Nomenclature

Rotor Variables

β	Blade flapping angle (rad)
Ω	Blade rotation rate (rad/s)
Ψ	Angle that a rotor blade makes with respect to the rear of the helicopter looking from above (rad)
ρ	Air density ($\mathrm{kg/m^3}$)
θ_{mr}	Blade pitch angle of the main rotor (rad)
θ_{tr}	Blade pitch angle of the tail rotor (rad)
$\vec{\boldsymbol{v}}_{bi}$	Velocity of helicopter with respect to rotor induced velocity (m/s)
b	Number of blades
C_d^l	Coefficient of drag of the surface of the load
C_{dtr}	Coefficient of drag of the tail rotor blade
C_{lmr}	Coefficient of lift of the main rotor blade
C_{lst}	Coefficient of lift of the stabiliser blade
C_{ltr}	Coefficient of lift of the tail rotor blade
c_{mr}	Chord length of main rotor blade (m)
c_{st}	Chord length of stabiliser blade (m)
e_{mr}	Displacement between rotor center and virtual hinge (main rotor blade) (m)
I_{bmr}	Main rotor blade inertia about flapping axis ($\mathrm{kg\,m^2}$)
I_{bst}	Stabilise rotor blade inertia about flapping axis (virtual hinge) ($\mathrm{kg\,m^2}$)
K_{smr}	Hinge spring constant ($\mathrm{N\,m/rad}$)
M_b	Main rotor blade mass (kg)

R_i	Displacement from rotor center to start of stabiliser blade (m)
R_{mr}	Main rotor length (m)
R_{st}	Displacement from rotor center to end of stabiliser blade (m)
v_i	Induced velocity (m/s)

Helicopter Flapping Variables

$\dot{a}_{con,mr}$	Coning angular rate of main rotor (rad/s)
$\dot{a}_{lon,mr}$	Longitudinal flapping angular rate of main rotor(rad/s)
$\dot{a}_{lon,st}$	Longitudinal flapping angular rate of stabiliser bar (rad/s)
$\dot{b}_{lat,mr}$	Lateral flapping angular rate of main rotor(rad/s)
$\dot{b}_{lat,st}$	Lateral flapping angular rate of stabiliser bar (rad/s)
$a_{con,mr}$	Main rotor coning angle (rad)
$a_{lon,mr}$	Longitudinal flapping angle of main rotor (rad)
$a_{lon,st}$	Longitudinal flapping angle of stabiliser bar(rad)
$b_{lat,mr}$	Lateral flapping angle of main rotor (rad)
$b_{lat,st}$	Lateral flapping angle of stabiliser bar(rad)

Helicopter Kinematics Variables

$\boldsymbol{I}_{h,i}$	Mass moment of inertia of helicopter i ($\mathrm{kg\,m^2}$)
$\boldsymbol{R}(\vec{\boldsymbol{q}})$	Rotation matrix as a function of the quaternion
$\vec{\boldsymbol{\Delta}}_{servo}$	Change in servo angle from nominal with elements representing left, right, rear and rudder servo input respectively (rad)
$\vec{\boldsymbol{\omega}}_h^{b,i}$	Angular rate of helicopter i measured in the body frame (rad/s)
$\vec{\boldsymbol{F}}_{h,c}^{b,i}$	Force in the body frame of helicopter i due to the cable - load attachment (N)
$\vec{\boldsymbol{F}}_{h,g}^{b,i}$	Force in the body frame of helicopter i due to gravity (N)
$\vec{\boldsymbol{F}}_{h,h}^{b,i}$	Force in the body frame of helicopter i due to the main and tail rotor (N)
$\vec{\boldsymbol{q}}_h^{i}$	Quaternion representing the rotation from inertial to body frame for helicopter i
$\vec{\boldsymbol{r}}_h^{b}$	Position of cable attachment on the helicopter with respect to center of mass of the helicopter (m)

$\vec{\boldsymbol{T}}'$	Blade pitch vector with elements representing the pitch for collective, lateral, longitudinal and rudder inputs (rad)
$\vec{\boldsymbol{T}}$	Pilot input with elements representing collective, lateral, longitudinal and yaw inputs (µs)
$\vec{\boldsymbol{T}}_{h,c}^{b,i}$	Torque in the body frame of helicopter i due to the cable - load attachment (N m)
$\vec{\boldsymbol{T}}_{h,h}^{b,i}$	Torque in the body frame of helicopter i due to the main and tail rotor (N m)
$\vec{\boldsymbol{v}}_{h}^{b,i}$	Velocity of helicopter i in the body frame (m/s)
$\vec{\boldsymbol{v}}_{h}^{e,i}$	Velocity of helicopter i in the inertial frame (m/s)
$\vec{\boldsymbol{v}}_{i}^{e}$	Velocity of helicopter i in the inertial frame; superscript e used to denote earth (m/s)
$\vec{\boldsymbol{x}}_{h}^{e,i}$	Position of helicopter i in the inertial frame (m)
$\vec{\boldsymbol{x}}_{i}^{e}$	Position of helicopter i in the inertial frame (m)
ζ_s	Second-order dynamics damping factor of servo
$k_m p$	Rotor plant DC gain (rad/s/µs)
K_s	Servo DC gain for second-order dynamics model (rad/µs)
$M_{h,i}$	Mass of helicopter i (kg)
R_{slim}	Servo rate-limit (rad/s)
T_{md}	Rotor plant dead-time (s)
T_{sd}	Servo dead-time (s)
ω_{mn}	First-order natural frequency of rotor plant (rad/s)
ω_{sn}	Second-order natural frequency of servo (rad/s)
ϕ^e	Pitch angle in inertial frame using yaw, pitch, roll rotation sequence (rad)
ψ^e	Yaw angle in inertial frame using yaw, pitch, roll rotation sequence (rad)
θ^e	Roll angle in inertial frame using yaw, pitch, roll rotation sequence (rad)
$\vec{\boldsymbol{\Sigma}}^{i}$	Euler angles of helicopter i (yaw, pitch, roll sequence) (rad)
K_{col}	Pitch mixer gain (rad/µs)
K_{lat}	Lateral mixer gain(rad/µs)
K_{lon}	Longitudinal mixer gain(rad/µs)

K_{rud}	Rudder mixer gain(rad/µs)

Load Kinematics Variables

$\boldsymbol{I}_l$	Mass moment of inertia of load ($\mathrm{kg\,m^2}$)
$\vec{\boldsymbol{\omega}}_l^b$	Angular rate of load measured in the body frame (rad/s)
$\vec{\boldsymbol{F}}_{l,ci}^b$	Force in the body frame of the load due to the cable attachment between helicopter i and load (N)
$\vec{\boldsymbol{F}}_{l,g}^b$	Force of gravity in the body frame of load (N)
$\vec{\boldsymbol{q}}_l$	Quaternion representing the rotation from inertial to body frame of the load
$\vec{\boldsymbol{r}}_l^b$	Position of cable attachment on the load with respect to center of mass of the load (m)
$\vec{\boldsymbol{T}}_{l,ci}^b$	Torque in the body frame of the load due to helicopter i cable - load attachment (N m)
$\vec{\boldsymbol{v}}_l^b$	Velocity of the load in the body frame (m/s)
$\vec{\boldsymbol{x}}_l^e$	Position of the load in the inertial frame (m)
M_l	Mass of load (kg)
$\vec{\boldsymbol{\Sigma}}_l$	Load Euler angles (yaw, pitch, roll sequence) (rad)

Abbreviations

ACAH	Attitude Command and Attitude Hold
CAD	Computer Aided Design
DCM	Direction Cosine Matrix
DOF	Degrees of Freedom
EKF	Extended Kalman Filter
ESC	Electronic Speed Controller
FCB	Flight Controller Board
GPS	Global Positioning System
IMU	Inertial Measurement Unit
LED	Light Emitting Diode
LTI	Linear Time-Invariant
MIMO	Multi-Input Multi-Output
MLAS	Multi-Lift Augmentation System
PID	Proportional, Integral and Derivative
PWM	Pulse Width Modulation
QFT	Quantitative Feedback Theory
RC	Radio Control
SAS	Stability Augmentation System
TCC	Twin-lift Communication and Control
TCS	Twin-lift Control System
TLS	Twin-lift Load Sensor
UAV	Unmanned Aerial Vehicle
VTOL	Vertical Take Off and Landing

Chapter 1

Introduction

1.1 Motivation

The operating cost of using purpose-built, heavy-load carrying helicopters to transport cargo can be much more expensive, than using multiple lower cost helicopters in a coordinated manner (Mittal, Manoj and Prasad, JVR and Schrage, Daniel P 1991). An example of a purpose-built, heavy-load carrying helicopter is the Erickson Aircrane shown in Fig. 1.1.1. In remote areas, where heavy cargo needs to be transported and fitted, the only option may be through the air, if the terrain does not permit (mountains or offshore) abnormal land transportation . The transportation, placement and fitting of powerline towers, wind-turbine blades and radio masts are the applications of interest in this thesis. According to Bisgaard et al. (2009), the use of slung-loads have also found application in mine detection and demining.

Although the industrialisation of a coordinated multi-lift scheme may contribute economically and technologically, the problem is also an enticing academic challenge. The problem was first described to the author as an "...interesting control problem" by Professor Eitelberg, who was then, at the University of KwaZulu Natal. Professor Eitelberg explained that it was in the late 1980s, during a visit to Germany where he came across a newspaper article showing the crash of two helicopters which attempted to share a load - it is believed that there was no automation except for the independent pilots' biological feedback. It was then that he identified the multivariable load sharing problem. Designing a robust controller for a single helicopter in itself is a difficult problem due to the cross-coupling in the rotor dynamics and model uncertainty. The twin-helicopter lift problem adds further interaction from the tethering of the two helicopters to the cargo that needs transportation. In this study, the problem is even more challenging because the requirement is to not only control the position of the load but the attitude as well. The focus of this thesis is on the development of a practical control system for implementation. Hence, a lot of attention has been placed on capturing the uncertainty in modelling for a *realistic* representation of the physical system, estimating the optimal state variables given *realistic* noises, and designing and implementing a *realistic* control algorithm to satisfy stability and performance specifications across the uncertainty.

Figure 1.1.1: Erickson Aircrane placing a powerline tower (Incorporated 2013)

1.2 Literature Review

A comprehensive study of slung-load modelling for multiple attachment points is given in Cicolani & Kanning (1992). The principle of virtual work is the framework in which these constrained problems are solved. Cicolani & Kanning (1992) also investigates multi-lift modelling and the use of inelastic suspensions.

The earliest work on slung-load transportation using a twin-lift configuration was by Menon, PKA and Prasad, JVR and Schrage, DP (1991), (Mittal et al. 1991). Their focus was on the design of nonlinear controllers for the twin-lift configuration with a separation bar, although, this was done for the lateral/vertical plane only. Input-output feedback linearisation was used to present a linear plant to a set of PID controllers to meet the control objectives. Plant uncertainty was assumed to be to changes in the cargo mass only. This was addressed by means of estimating the cargo mass and updating the model.

There are two notable publications on multiple helicopter slung-load transportation systems with 6 degrees-of-freedom (DOF) models. The first is by Bernard & Kondak (2009), who proposed a control scheme for multi-lift systems. Their work has focused on a generic multi-lift control system which allows for the addition of helicopters into the system. The cargo is assumed to be a point-mass (single point of tether attachment), thus no modelling or analysis of the cargo attitude was done.

The second related publication is by Bisgaard, Morten and Bendtsen, Jan Dimon and Cour-Harbo, Anders La (2009), who focused on modelling and design for a *single helicopter* slung-load system; although, models for the multi-lift configuration are also produced. The model by Bernard & Kondak (2009) is crude compared to the more comprehensive model by Bisgaard et al. (2009). Although Bisgaard et al. (2009) model the attitude of the cargo as a function of the attachment points, there is no concern with the control of the cargo attitude.

More recently, work on coordinated transport of a load using a team of autonomous rotorcraft by Li et al. (2014) was published. As described in the paper, helicopter control was not the focus of the work but rather computing the force required at each helicopter attachment point to achieve transport requirement. The simplified point mass helicopter model does not capture the effect of the cable tension on the helicopter attitude (it is assumed that commanded attitude will be reached despite the torque on the helicopter due to the cable tension and attachment point). In Section 5.2.3, a *tension tracking* approach was attempted, similar to Li et al. (2014), albeit to a much higher fidelity helicopter model. It was found that the limited bandwidth of the helicopter was not sufficient to stabilise the twin-lift configuration when using a more representative model of full-scale helicopters.

In all of the work stated above, no attention was given to uncertainty in the plant and robust controller design. At the time of writing, and to the best of the author's knowledge, there are no published work on general attitude control of cargo using multiple helicopters.

The application of Quantitative Feedback Theory (QFT) was made to a bench-top helicopter by Mansor et al. (2010). Although a 3DOF model (attitude only) was investigated, the control design was limited to only pitch control of the model and no attention to cross-coupling in attitude was given. The QFT methodology was shown to be superior to a PI controller. In comparison, work of this thesis is focused on the eventual realisation of the twin-helicopter slung load transportation system for full-scale commercial helicopters, thus, robust control of full 6DOF plants with representative rotor dynamics are essential. The "bench-top" helicopter used in Mansor et al. (2010) does not exhibit any of the salient features present in full-scale helicopters, particularly in the rotor dynamics. An application that uses MIMO QFT for the pitch rate and heave rate loop for longitudinal flight is done in Hess & Gorder (1993). The successful design and implementation of a MIMO controller to a helicopter using H_∞ control was done in (Smerlas et al. 1998), (La Civita et al. 2002). Walker et al. (2001) gives a technical report on the practical aspects of implementing H_∞ controllers on helicopters.

Although the application of MIMO QFT to complex helicopter-based plants are rare, practical application of non-diagonal MIMO QFT to spacecraft control was done in (Garcia-Sanz et al. 2008) and the application to wind turbine control in (Houpis & Garcia-Sanz 2012).

1.3 Outline and Contributions

In recent years, there has been a large amount of research into using Unmanned Aerial Vehicles (UAV) as platforms for testing new ideas for civilian and military applications. The pervasive use of multirotor UAVs in sport/movie filming, search-and-rescue, military surveillance and border monitoring is attributed to the early research done into multirotor UAV design (Gupte et al. 2012). The University of Pennsylvania (UPENN), the Swiss Federal Institute of Technology (ETH) Zürich and Massachusetts Institute of Technology (MIT) have been at the forefront of research into UAV applications, this has been largely due to the reduction in size and cost of the essential components required for an autonomous flying vehicle. MIT's Aerospace Controls Lab (ACL) (How et al. 2008), ETH's Flying Machine Area (FMA) (Lupashin et al. 2014) and UPENN's General Robotics, Automation, Sensing and Perception (GRASP) (Michael et al. 2010) are among the most prominent laboratories in the world that have been developed for UAV research.

In the current research, small-scale helicopters are used as the platform to test the twin-lift concept. The supporting instrumentation for this investigation had to be developed because of a lack of heritage at the University of Cape Town in UAV research. The intention was to create sustainable simulation models, avionics hardware and software, and a motion capture system that can be used at the University by researchers interested in UAV development. These three major development topics are depicted in the workflow stream shown in Fig. 1.3.1. The development of the simulation model, avionics and motion capture system were approached as concurrent work *threads*. The convergence of these threads occurred at the integration level where system identification and model verification was done. The simulation model development involved constructing a single helicopter mathematical model with sufficient fidelity, incorporating the cargo and cable dynamics and lastly, adding on the second helicopter to build up the complete twin-helicopter slung-load system. In order to capture signals for system identification and performing autopilot tasks, an avionics unit consisting of the relevant hardware and software was developed. The radio multiplexer is an ancillary hardware unit that was developed that allows easy switching between manual and autopilot mode. The last thread was the design of a motion capture system capable of tracking position and orientation of the helicopters in the flying volume. Part of this stream was the optimal sensor fusion of the on-board sensor data with visual information. These three threads converge when flight tests began in the flight room (Reddi & Boje 2014). The successful validation of the mathematical model and refinement of the uncertain parameters was followed by a robust control design for the attitude of the helicopters. The last phase was the development of the robust controller design for the coordinated transport and attitude control of the cargo.

This work contributes to the knowledge in the field, as follows:

- The development of a low-cost, high-performance indoor position and attitude tracking (motion capture) system. No specialised hardware is required and the software was developed from existing open-source software such as OpenCV, for the Linux operating system. The design has been made open-source and can be found on a git repository

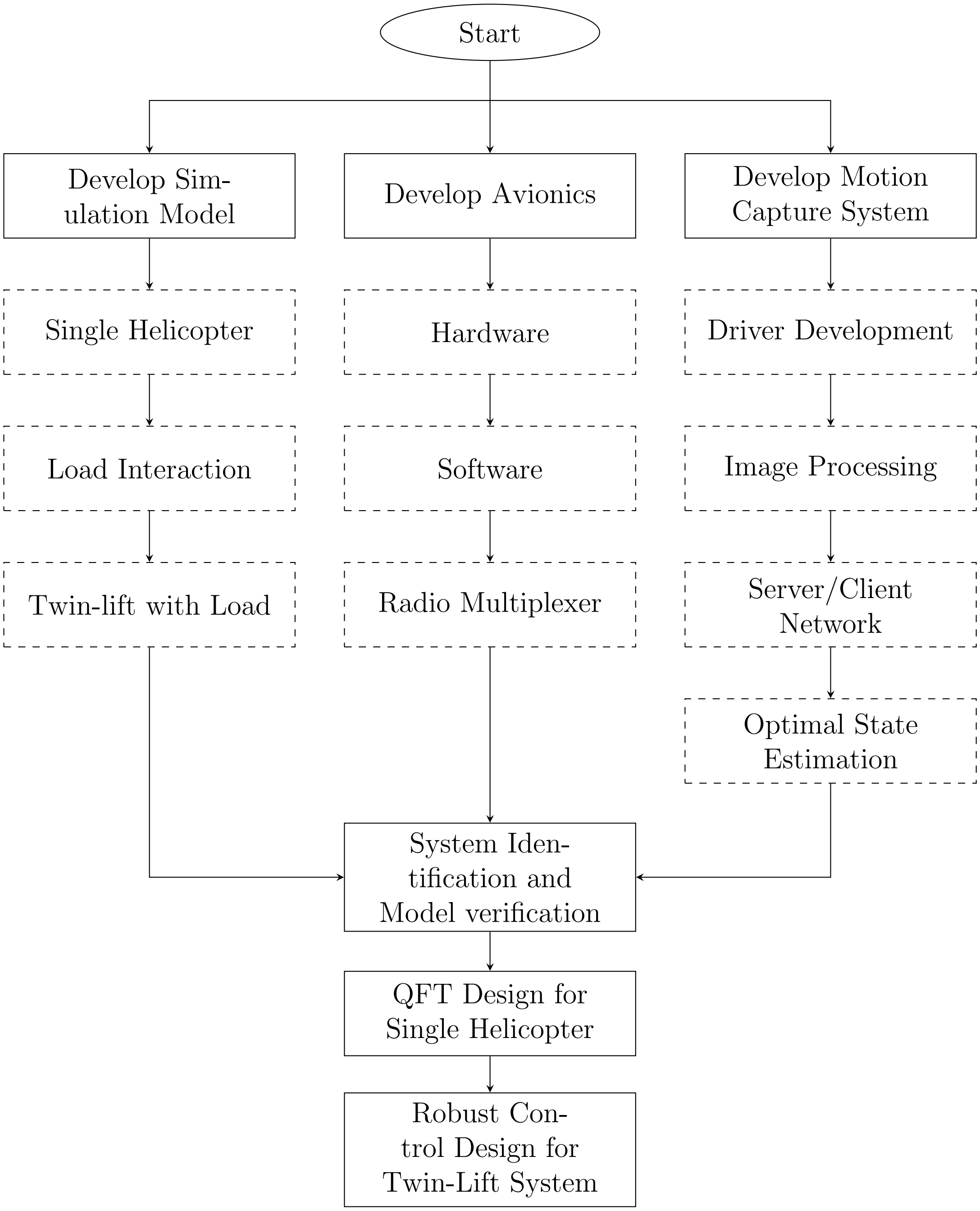

Figure 1.3.1: An outline of the research process taken

(see below), so that other academic institutions can setup their own flight room for UAV research.

- A very high-fidelity model of a small-scale helicopter was developed. Further, the modelling of the constrained multibody system is presented in a decoupled, physically realistic form. It is shown through experimental flight tests that the helicopter model captures resonant modes that are not found in the literature. The set of linearised plants extracted from the nonlinear model, captures the uncertainty of the plant in hover operation. The uncertain multivariable (6×6) plant can be used as a benchmark problem for further research in robust multivariable control and load sharing control.

- Development of a low-cost, high-performance avionics unit used for system identification and autopilot control (Reddi & Boje 2014). The avionics hardware was designed to serve any aerial application. The hardware and software design is available through a git repository (see below) for other academic institutions interested in UAV research. The avionics unit integrates with the motion capture system to form a product that outputs high bandwidth position and attitude information.
- Development of robust QFT controllers for a single helicopter with plant uncertainty. Attention is given to the affect of uncertainty on the stability and digital implementation.
- Proving that a realisable solution of a novel aerial crane concept exists. A MIMO QFT robust solution for controlling the attitude and translation of the load using the Twin-helicopter load lift scheme is presented for carrying long slender loads such as wind turbine blades. This includes the design and analysis around uncertain resonant modes and cross-coupling that exists in the plant. By designing in the frequency domain, the effect of uncertainty on the stability and performance is presented.

The repository that contains the hardware and software development may be found at `https://github.com/rddyas002/Twin-Helicopter-Slung-Load-Transportation-System`.

Synopsis of Chapters to follow:

The development of the instrumentation required for the practical aspects of modelling, estimation and control design is presented in Chapter 2.

Chapter 3 presents the mathematical model derivation as well as the analysis of the individual helicopter and the twin-helicopter lift interacting model. System identification used for estimating the parameters that were difficult to measure is also presented. The helicopter kinematic state variables are displayed against real flight data to show the accuracy of the high-fidelity model developed. Resonant modes were analysed using Modal analysis and an explanation presented.

The derivation of the state-estimation equations is presented in Chapter 4, together with the performance results. The methodology around the image processing required to extract the fiducial markers, dealing with occlusions and resolving multiple markers of the same color is also presented.

Chapter 5 contains a section on Independent Helicopter Control and Coordinated Helicopter Control. The former contains the design and analysis of a robust position controller for an uncertain single helicopter. The idea behind this section was to have a fallback controller in case the more complicated controller fails. The Coordinated Helicopter Control chapter presents the design and analysis of the control system to control both the position and attitude of the load. Due to the difficulty of the problem, simplified problems were investigated to gain insight in solving the real problem. The design and analysis of a decoupler for performance and stability of an uncertain multivariable plant is presented. The results of the work is presented as a simulation of the nonlinear system tracking both attitude and translation trajectories.

The conclusion of this investigation is done in Chapter 6.

Chapter 2

Experimental Platform

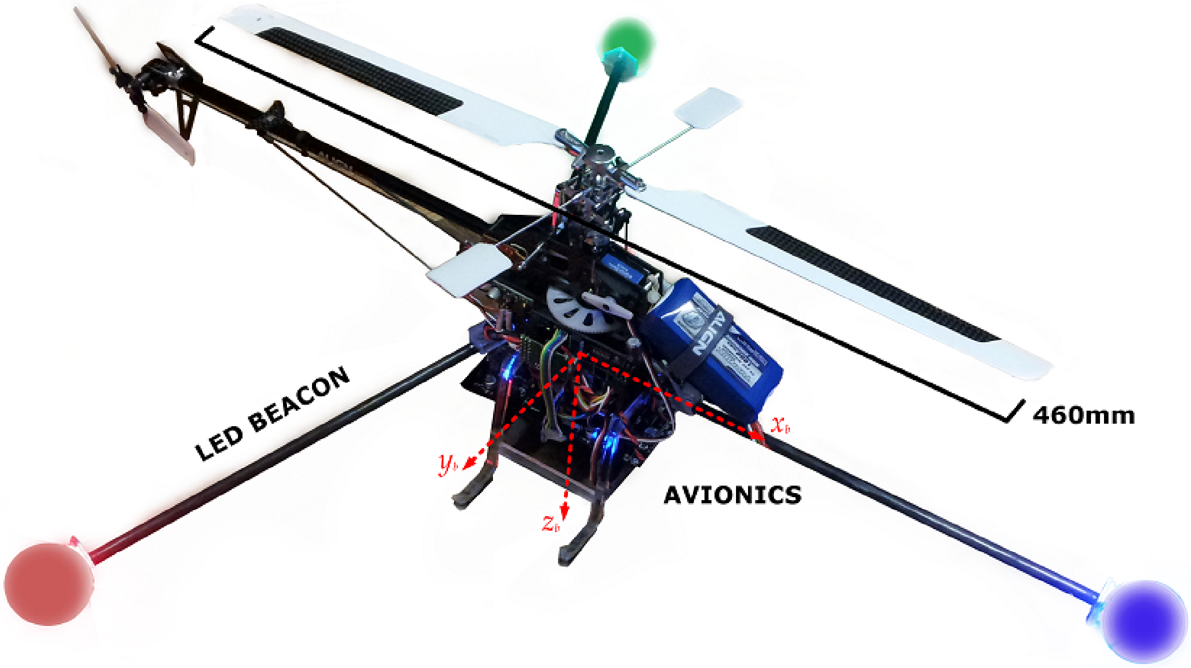

This chapter presents the development of an experimental platform used for model verification and flight control system testing. The platform consists of the twin-helicopter lift system, helicopter avionics, a motion capture system and a ground station. Modifications of the standard helicopter for autonomous control is presented. A description of the design and usage of the motion capture system is given. The combination of the on-board avionics and the motion capture equipment is used to determine the kinematic state variables of the helicopter. The on-board avionics measure high-bandwidth helicopter body parameters, such as angular rates and accelerations. The low-bandwidth position and attitude information is computed by an external motion capture system designed specifically for the experiment. Lastly, a description of the software classes that were developed and their interaction is explained.

2.1 Flight Room

The flight room floor area was limited to 4 m by 4 meter. The height limit was 3 m. A rendering of the flight floor area relative to the helicopter size is shown in Fig. 2.1.1 to give an idea of the flying volume limitation (always less than four blade diameters from the wall). Figure 2.1.1 also shows the four white square markers used for calibration of the extrinsic parameters of the individual cameras. The cameras are placed on each upper corner of the flight room. Given the agility of the helicopters, and the limited flight volume, it is critical

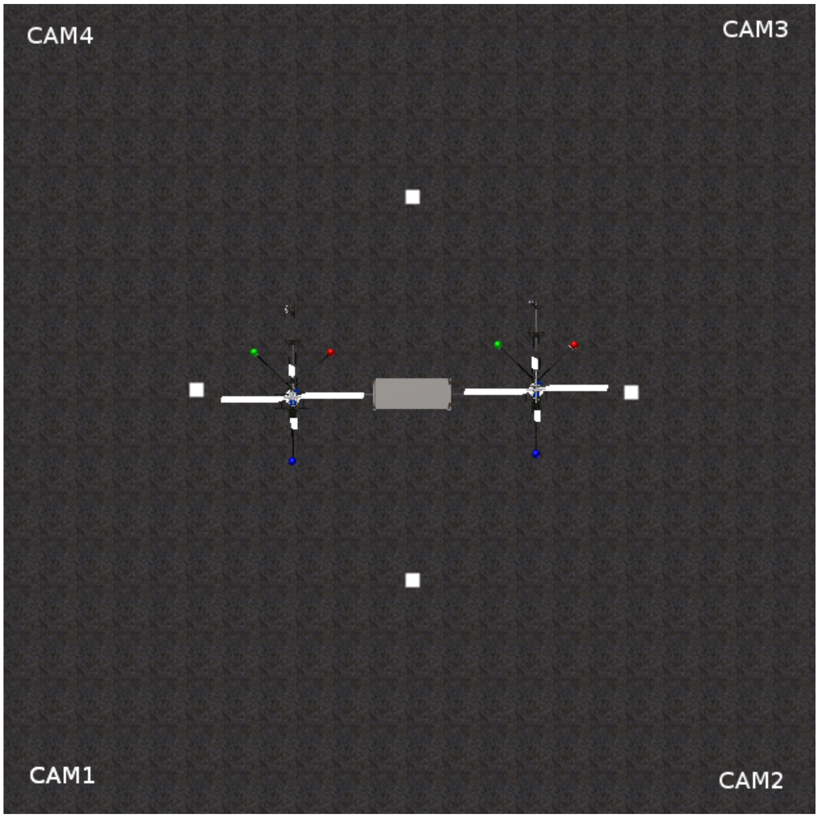

Figure 2.1.1: Rendering of flying floor area relative to the size of the helicopter

that the instrumentation provide fast and accurate information to the controller to prevent collision with the boundary walls.

2.2 Helicopter

2.2.1 Standard Helicopter

The helicopter used is an off-the-shelf Align T-Rex 250SE helicopter designed for radio control hobbyists, shown in Fig. 2.2.1. From the physical specifications shown in Table 2.2.1, it can be seen that the size of the helicopter used in this investigation is much smaller than those used in other slung-load transportation research (Bernard & Kondak 2009), (Bisgaard et al. 2009). The smaller mass and inertia in comparison with other investigations makes for a much higher bandwidth plant. A further challenge is incorporating the required electronics into the helicopter with tight payload mass and space constraints.

Figure 2.2.1: T-Rex 250SE helicopter from Align (Smart 2013)

Table 2.2.1: T-Rex 250SE specifications

Parameter	Value
Length	430 mm
Height	163 mm
Main rotor diameter	460 mm
Tail rotor diameter	108 mm
Flying weight	340 g
Hover main rotor speed	3500 rpm
Tail rotor speed	15 000 rpm

The helicopter has a Bell-Hiller mixing rotor system. The Bell-Hiller system consist of the main rotor blades to provide primary lift and thrust vectoring, and a stabiliser bar with aerofoils that provide mechanical feedback. The mechanical feedback assists in attitude stability and disturbance rejection, without which, it would be extremely difficult for the helicopter to be flown. The Bell-Hiller system also has a pre-filtering effect on the pilot's input, slowing down the inputs to the actual blade angle. According to Mettler et al. (1999), small-scale helicopters with the Bell-Hiller rotor system retain the salient dynamics of the large-scale counterpart. This suggests that the research done on the experimental platform may be transferable to full-scale helicopters for the slung-load transportation system.

The standard drive-system power unit consist of a "3400 KV" (which is the motor speed constant with unit rpm/V) brushless motor powered by a 15 A amp electronic speed controller. The gear reduction from the motor to the main rotor produces a nominal speed of 3500 rpm to the main blades. The main rotor shaft is then geared up through a belt-driven pulley to spin the tail rotor at 15 000 rpm. The standard helicopter was designed for 3D flight capability (high agility manoeuvring such as inverted flight), hence it is in no way limited in actuation, in comparison with typical large-scale helicopters.

2.2.2 Chassis modifications

In order to interface the standard T-Rex helicopter with the instrumentation that is required for the flight control system, modifications of the chassis had to be made. The motion capture system require LED beacons (fiducial points) to be mounted in a triangular fashion around the helicopter. Carbon fibre rods were used to place the beacons sufficiently far from the main rotor wake. The mass of the beacon and the carbon fibre rod is sufficiently small that the rotational dynamics of the original system is essentially preserved. The bending modes expected are in a frequency range much higher than the system bandwidth.

A landing gear was designed to incorporate the LED beacons and an avionics compartment, and to be compatible with the existing chassis. In order to prevent saturation of the inertial sensors, mechanical damping had to be accommodated within the landing gear. The avionics board is suspended within the landing gear using a damping rubber material - chosen experimentally to provide maximum vibration damping at the affected frequency. The actual helicopter used in the experiment with the LED beacons and avionics mounted is shown in Fig. 2.2.2. A detailed rendering of the landing gear is shown in Fig. 2.2.3. The flying weight of the instrumented helicopter with the new landing gear is 560 g. Static thrust tests showed that the instrumented helicopter would have enough thrust to demonstrate the aims of this project.

A cable release mechanism was designed to quickly release the cable attachment to the helicopter chassis in the event it becomes to difficult to control the load. The release mechanism integrated into the landing gear is shown in Fig. 2.2.4b.

2.2.3 Avionics

The avionics hardware (referred to as the Flight Controller Board (FCB) from now) was designed with an intention to be a general computational platform that could be used for any aerial application. The FCB was designed to interface with standard radio transmitters

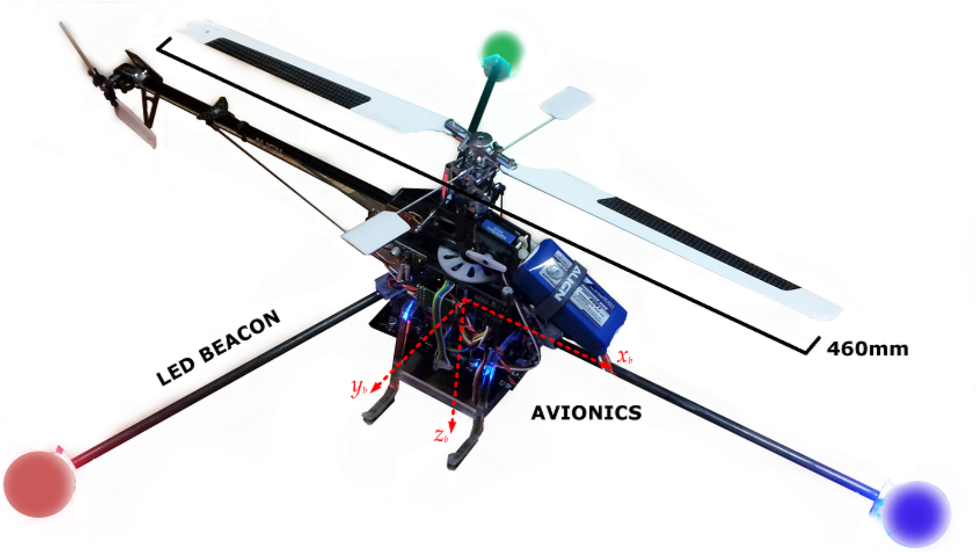

Figure 2.2.2: T-Rex 250 with modified chassis

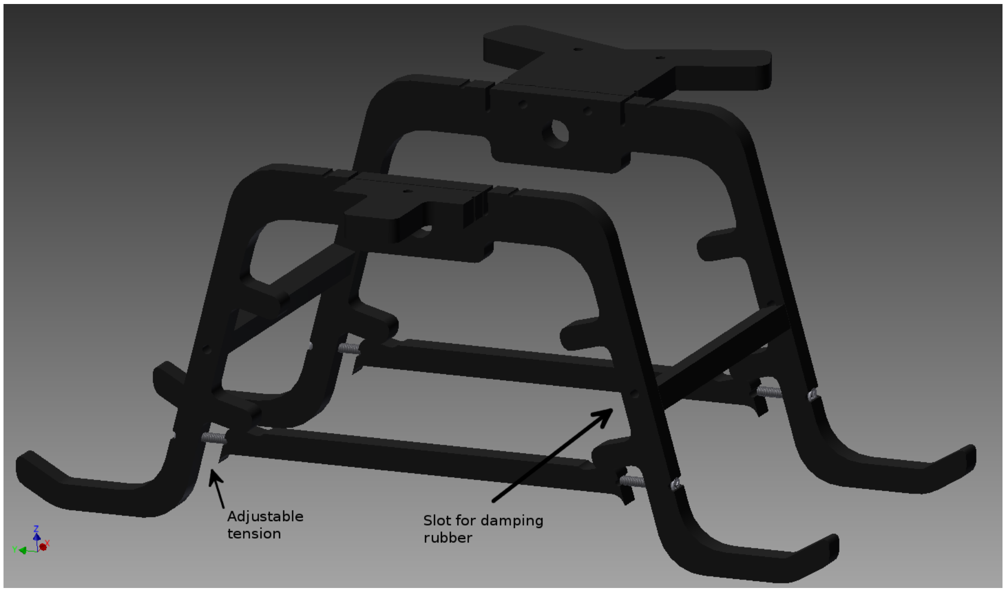

Figure 2.2.3: 3D CAD rendering of the landing gear

and receivers for manual control. In manually piloted helicopters, pulse-width modulated (PWM) input to the servos and the electronic speed controller (ESC) are generated in the radio receiver. A PWM multiplexer board was designed so that PWM signals from the radio receiver are multiplexed with PWM signals from the flight control system. This allows for the user to switch easily between autonomous and manual flight modes. The PWM multiplexer board is shown in Fig. 2.2.5. The control signals from the flight controller board are transmitted on the I2C bus. A time-out feature on the PWM multiplexer board will automatically override to manual mode if the FCB does not transmit a valid packet for more than 50 ms.

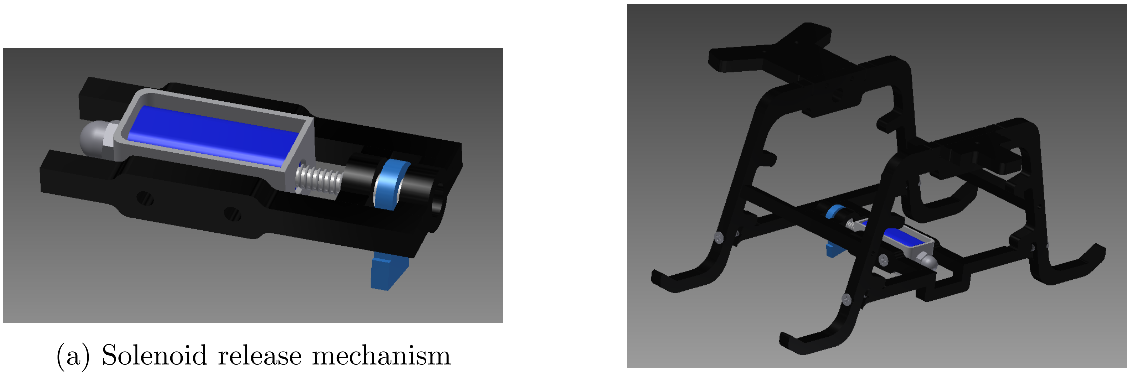

(a) Solenoid release mechanism

(b) Release mechanism integrated into chassis

Figure 2.2.4: Cable release mechanism

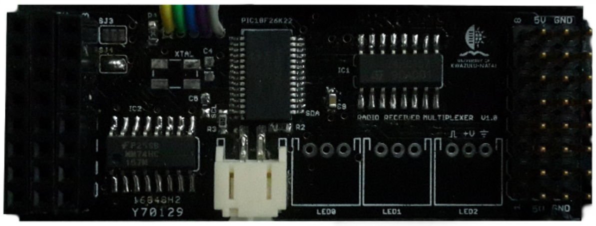

Figure 2.2.5: PWM multiplexer board

The FCB was designed to contain all general sensors required for aerial applications. Figure 2.2.6 shows the key features available on the board. It can be seen from Fig 2.2.7 that even the bottom side was populated with components to minimise the PCB size. A microcontroller from Microchip® was chosen as the processing unit responsible for communicating with all the on-board modules and executing the control system algorithms. The PIC32MX795F512L microcontroller has a 32-bit 80 MHz processor with 105 DMIPS, 512 kB flash and 128 kB RAM. The chip has 8 DMA (direct memory access) channels which are used for all sensor data transfer; this frees the CPU to do arithmetic and logic operations only. A MIPS technology processor was chosen over an ARM processor due to the better processing power per energy resource available with MIPS processors (MIPS Technologies Inc. 2010), for the weight and size constraints.

Two 3 A switch-mode regulators step down the voltage supplied by the helicopter's Lithium-Polymer (LiPo) battery. The switch-mode outputs are further regulated by low-noise linear regulators to supply power to the electronics. An external output is made available for supplying power to other accessories such as servos and receivers. The reason two high capacity switch mode regulators are present is to isolate logic and inductive loads.

The inertial sensors on-board consist of a 3-axis gyroscope, 3-axis accelerometer and a 3-axis magnetometer. All sensors communicate with the processor over the I2C bus. A GPS sensor

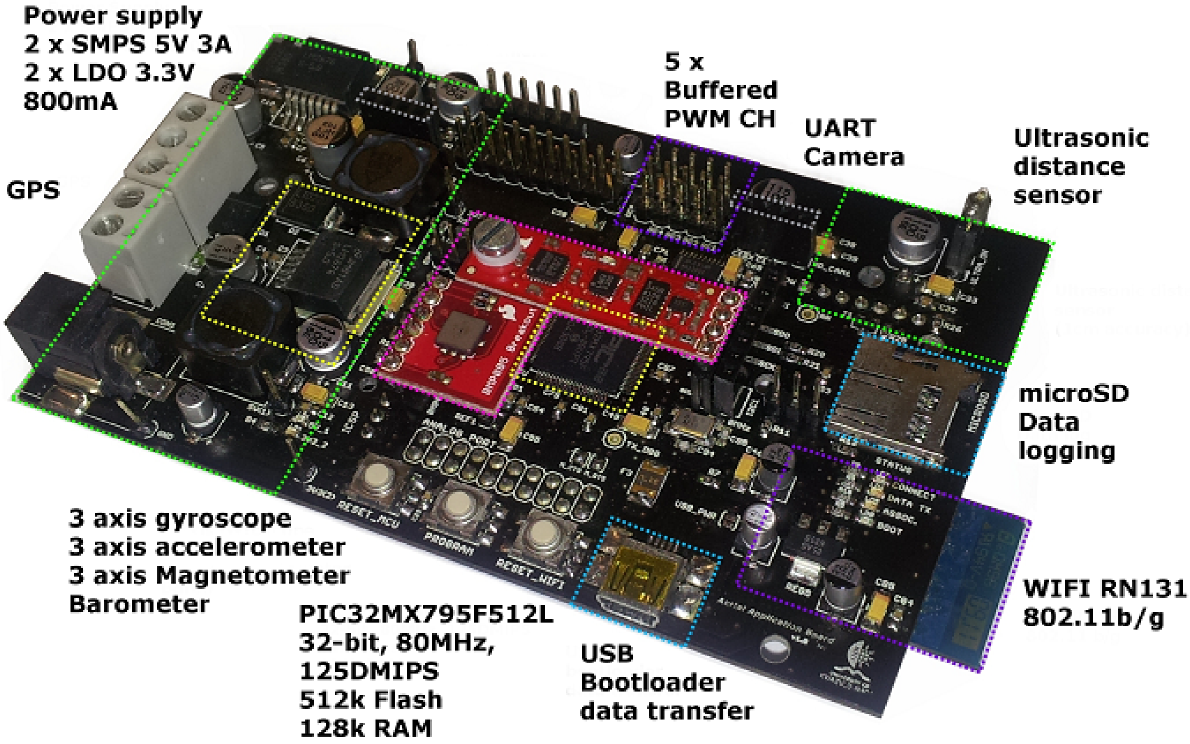

Figure 2.2.6: Flight controller board highlighting key features

can be accommodated in order to provide position information in outdoor applications. The pressure and ultrasonic sensors are intended for altitude information. The barometer has a typical resolution of 8 cm and the ultrasonic sensor has a resolution of 1 cm for heights less than 7 m above the ground.

A WiFi module is used as the primary communication link between the flight controller board and the ground station. Telemetry as well as reference commands are transmitted over the WiFi channel. High rate telemetry is logged on a microSD card on the FCB. USB 2.0 capability is provided for flashing firmware, and as an alternative debugging channel. The FCB was designed to accommodate standard 2.4 GHz Digital Spectrum Modulation (DSM) radio transmitters and receivers. The standard radio is used as a fail-safe in case the primary communication channel fails. This secondary communication channel is robust to packet-loss and jitter in timing compared with the WiFi link. A summary of the features of the flight controller board is shown in Table 2.2.2.

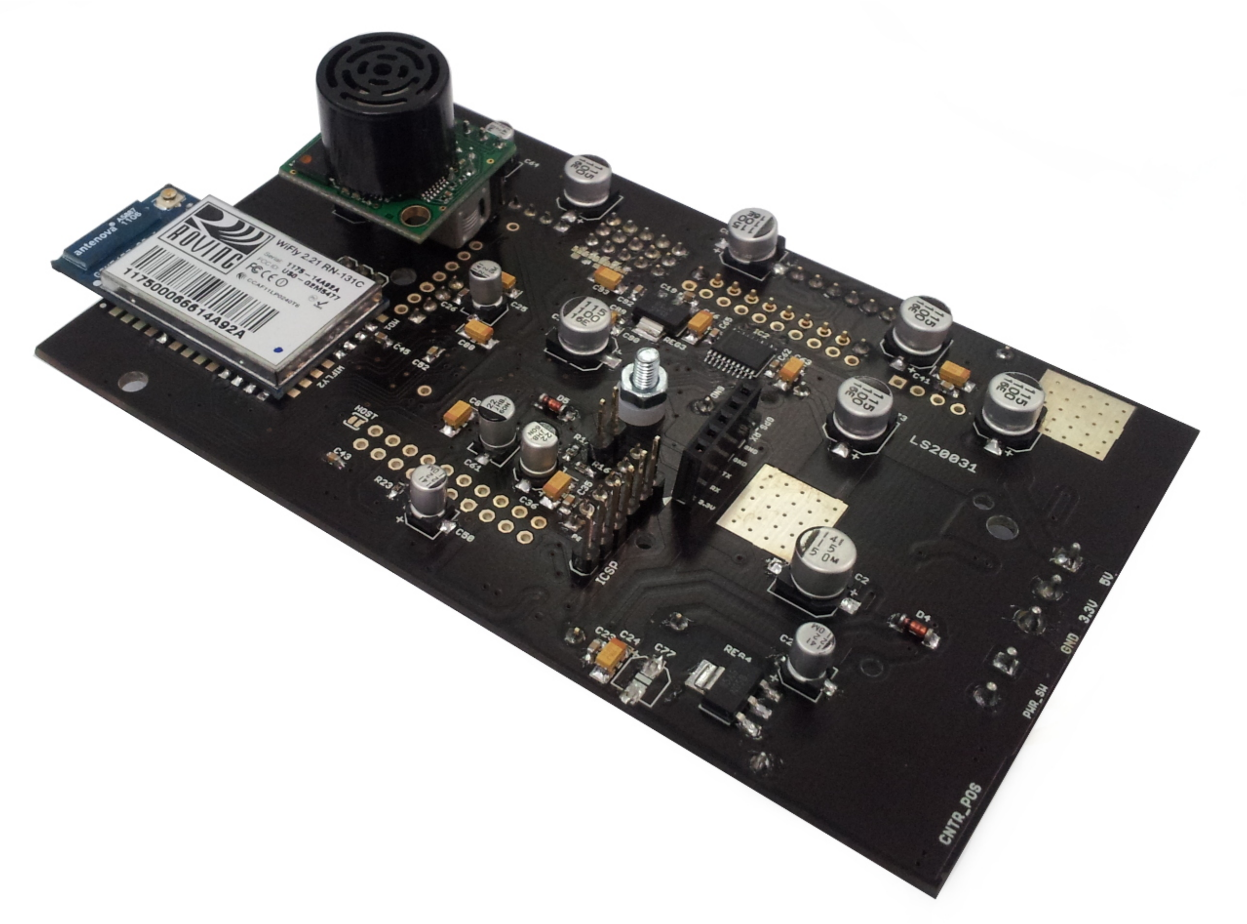

Figure 2.2.7: Bottom side of flight controller board

Feature	Description
Power	Input range: 7 V-40 V 2 × 3 A 5 V SMPS–logic and servo power 2 × 800 mA 3.3 V LDO; 5 V and 3.3 V output
Processing	PIC32MX795F512L 80 MHz 32-bit processor with 105 DMIPS 512 kB Flash, 128 kB RAM 8 DMA channels
Motion/Location sensors	3 axis gyroscope - ITG3200; 2000°/s, 16-bit ADC, noise 0.38 °/s-rms 3 axis accelerometer - ADXL345 - noise x,y = 0.75 LSB rms, z = 0.75 LSB rms 3 axis magnetometer - HMC5883L GPS Module LS20031
Altitude sensors	Barometer BMP085 Ultrasonic distance sensor; 1 cm accuracy; Range of 7 m
Communication and data logging	WiFi RN131 802.11b/g module;range of 100 m open-air USB 2.0 communication link for data streaming and firmware upgrade microSD card for logging data; up to 32 GB
General	All unused I/O pins and ADC channels broken-out for extensibility; Two UART ports provided–intended for UART interfaced cameras; 5 × buffered PWM channels

Table 2.2.2: Summary of the key features on the flight controller board

2.3 Motion Capture System

The control of the position of helicopters require position sensors for feedback control (Reddi & Boje 2014). In outdoor applications the use of GPS (and differential GPS) as absolute position sensors can provide reasonable accuracies depending on the application. Since the experiment was designed for indoor use, GPS cannot be used for position information. A system that seemed most promising was the use of vision systems, such as those used at ETH (ETH Zürich 2013) and the University of Pennsylvania (Vicon 2013). Both institutions use the Vicon motion capture system for obtaining position information of their quadrotors in the flying volume. The state of the art Vicon motion capture system (at the time of writing) can cost as much as US$500000 (Muir 2013). The MX40 system has the following key specifications (Vicon 2004):

- A minimum of 12 cameras
- Data transfer limit of 166 frames per second at 4 megapixels
- A latency of 2.5 ms
- Has a resolution of 1 mm
- Works in the infrared band

An assessment of the specifications proved that the Vicon motion capture system would be over-specified for the requirement of this project. It was decided that an in-house motion capture system will be developed for tracking aerial platforms within the flying volume, based on the concept of the Vicon system.

The most important piece of hardware for a motion capture system is the imaging device. For the relatively small room size that was available for the experimental work, the camera frame rate was a more useful performance metric over resolution. After an investigation of the cameras on the market, the PlayStation® Eye camera was chosen as the imaging device. For a cost of less than US$20, the PlayStation® Eye camera is capable of 125 frames per second at a resolution of 320 × 240. This is by far, superior to most of the webcams on the market having prices even double that of the PlayStation® Eye camera. For simplicity, the fiducial points were chosen to be active LEDs in the visible spectrum. The tracked platform consists of a red, green and blue beacon. High power LEDs were chosen to simplify the segmentation phase in the image processing. Ping-pong balls were chosen to diffuse the bright LEDs so that a spherical illumination is achieved. A rendering of the helicopter with the tracking beacon is shown in Fig. 2.3.2. Performing segmentation based on colour reduces the computation complexity required to determine the pose of the helicopters - compared with solving for the 3D pattern.

The high-level overview of the motion capture system is shown in Fig. 2.3.1. It was found that four cameras, one in each upper corner of the flying volume, cover the flying space fairly well under typical occlusions that may occur for the experiment. The USB interface was found to be the bottleneck that prevented the use of one PC to perform the image

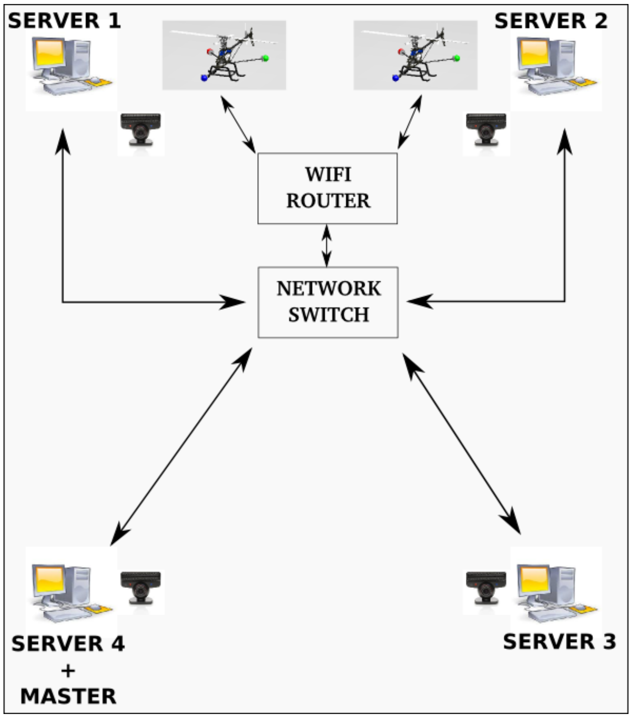

Figure 2.3.1: High-level architecture of motion capture system

processing for all cameras. Hence each camera is connected to a PC which performs basic image processing operations. The need for high-specification computers were not required, so old unused PC's were incorporated into the system. Conceptually, each computer and camera form an independent vision unit and exist as a server on the network. The master computer serve two purposes: acts as a vision unit; and runs the base station software which requests blob data of the scene from each vision unit and estimates the pose of the helicopters. The computers communicate with each other over a controlled local network using the TCP/IP protocol. Isolating the network minimises the latency and jitter over the communication channel . The helicopters are connected to the same network over WiFi using the UDP protocol as worst-case latencies are more severe over the wireless channel. The pose estimation performed by the master computer uses data from the helicopters and the motion capture system to optimally estimate the kinematics of the helicopters. A real-time pre-emptive Linux kernel is used on the server units to minimise latencies from the operating system. The performance specifications achieved with the motion capture system designed are:

- Latency of 16 ms from scene to client (includes capture, blob detection, transmission)
- Maximum sampling of 62.5 Hz (driver limitation)
- Resolution of 5 mm in the flying volume (measured at the center of the room)

The motion capture performance achieved are much more than what is required for good position control of typical RC sized helicopters. The cost to setup a motion capture system described above is incomparable to the cost that is required for an off-the-shelf motion

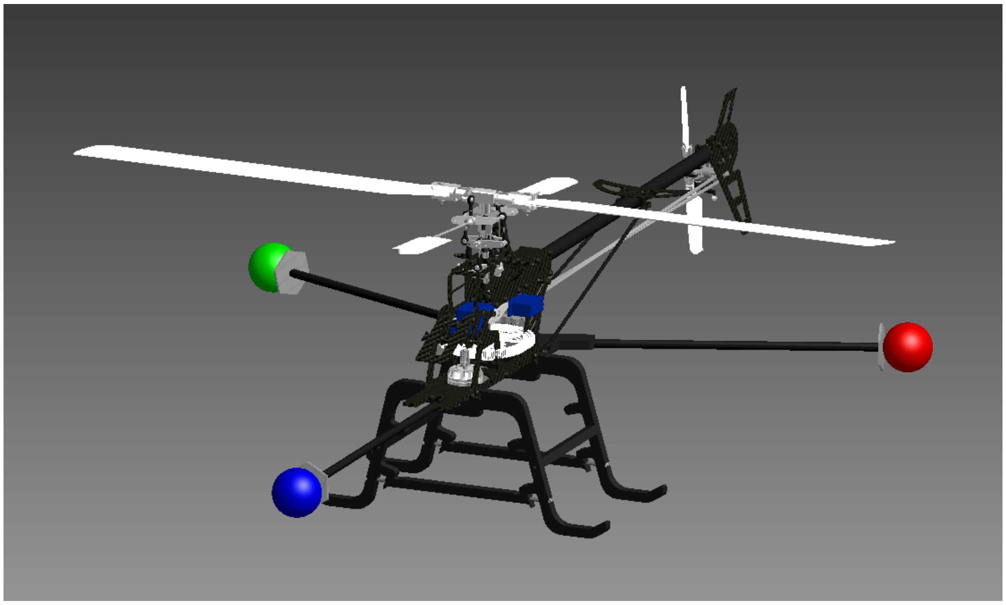

Figure 2.3.2: Rendering of T-Rex 250SE with custom landing gear and tracking beacon

capture system. The software for the vision server units and the base station is made open-source on a Github repository (`https://github.com/rddyas002/Twin-Helicopter-Slung-Load-Transportation-System/tree/master/Software/Base%20Station`) so that other researchers may make use of the project. All that is required to set-up the motion capture system are four webcams, four old unused computers and the motion capture software. Current development is taking place to migrate the vision unit technology to a Raspberry Pi computer. This will add a further reduction in cost and make the vision unit portable and mobile. The further addition of WiFi to vision units will allow for the vision system to be easily deployed to new locations. More detail on the image processing and estimation is given in Chapter 4. A plot of the trajectory of the helicopter as it was moved within the flight volume is shown in Fig. 2.3.3.

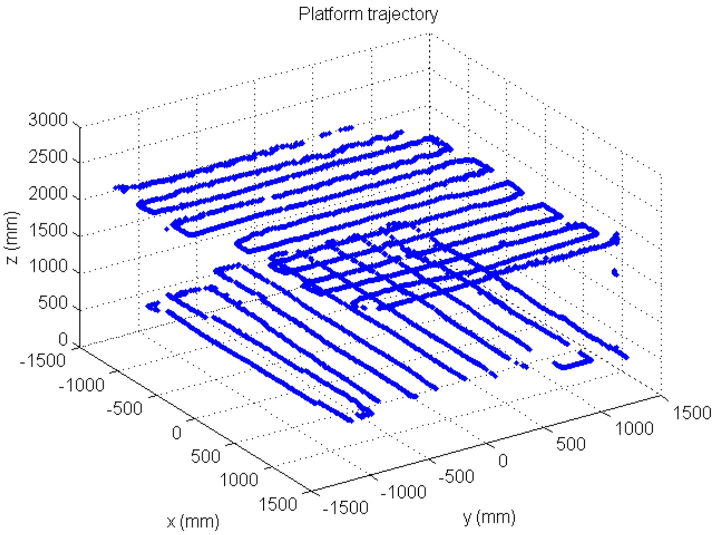

Figure 2.3.3: 3D plot of tracking data from experiment used to find bounds of flying volume

2.4 Command and Control

The base station is the hub of information transfer between the helicopters and the vision units. The purpose of this section is to give the reader an understanding of the system integration required for the hardware modules that make up the experimental test-bed. A software (abstracted) perspective of the modules, makes it easier to understand the flow of the interactive system. Some of the tasks that need to be performed by the base station for the experimental missions are:

- Act as a client to each vision unit to request blob data
- Receive the inertial sensor data from each individual helicopter
- Perform optimal state-estimation of the helicopter kinematic state variables using blob data and inertial measurements
- Receive and log other vital information such as voltages, motor speed, temperatures, etc.
- Compute and transmit high-level control signals for trajectory following and load-sharing

A description of the main classes that represent actual hardware elements and physical tasks follow.

Software Description

UAV Control Class The UAV control class is at the highest level of the class hierarchy. It is responsible for configuring the application with helicopter specific data. An example of a configuration script for a single helicopter setup is shown in Listing 2.4.1. The underlying system was designed to be generic so that other UAV-like projects can seamlessly be interfaced to the motion capture state-estimation system. UAVControl class instantiates the subclasses and is responsible for synchronisation between classes and the vision system. The standard Network Time Protocol (NTP) took too long to synchronise the computers so a custom protocol was developed for short time-span synchronisation.

Listing 2.4.1: Example of a Configuration File

```
ID=1                          % HELICOPTER IDENTIFICATION
IP_ADDRESS=192.168.1.1        % HELICOPTER IP ADDRESS
IP_PORT=2002                  % HELICOPTER IP PORT
PC_PORT=2001                  % PC PORT HELICOPTER COMMUNICATES THROUGH
MULTICAST_PORT=12345          % PORT PROCESSED DATA IS ROUTED THROUGH
INITIAL_POSE=0,0,70,0,1,0,0
RED_BLOB=-150,260,0           % POSITION OF BLOB W.R.T. HELICOPTER ...
GREEN_BLOB=-145,-260,0        % FRAME ORIGIN IN MILLIMETERS
BLUE_BLOB=310,0,0
GYRORAW2DEGREES=14.375,14.375,14.375
ACCELRAW2G=272,258,225
```

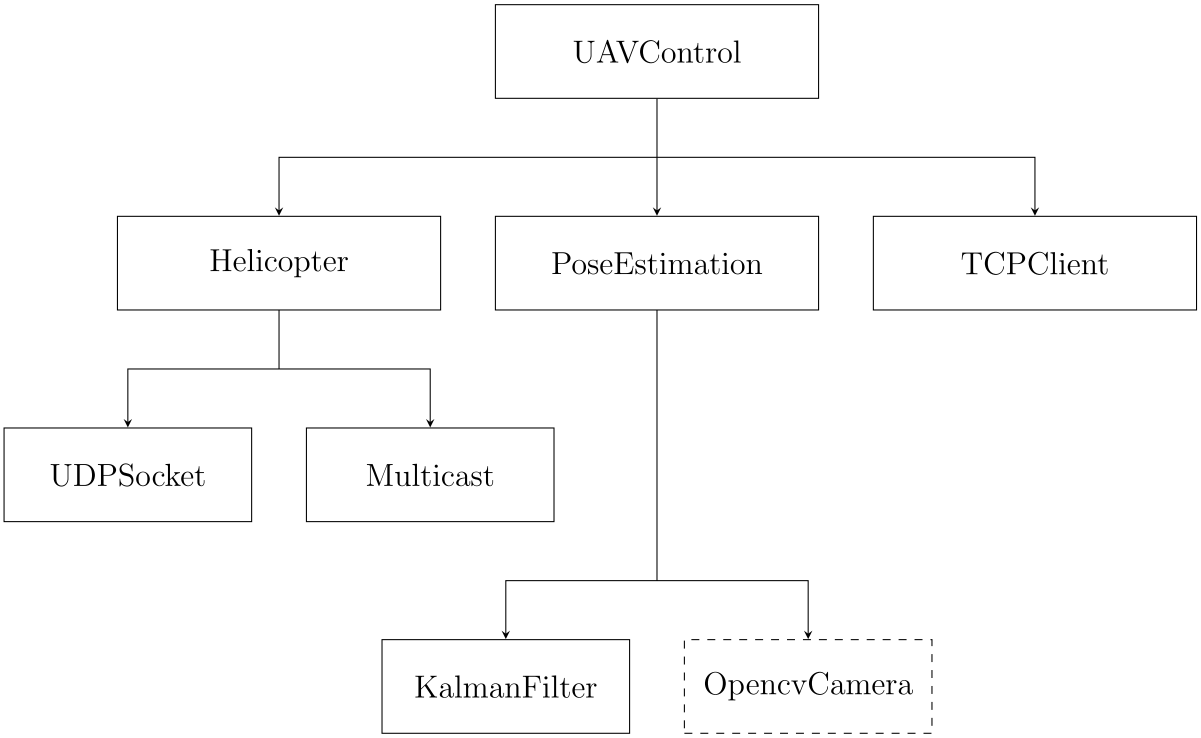

Figure 2.4.1: High-level class hierarchy

Helicopter Class The classes have been designed in the true object-oriented sense. The Helicopter class for instance, contains member variables that fully describe a helicopter's parameters, sensor values and kinematic state. A struct is defined that consists of raw sensor data such as gyroscope, accelerometer, magnetometer, barometer, battery voltage, ultrasonic, motor speed and temperature information. The kinematic state and error-covariance used in the optimal state-estimation is maintained within this class. The *UDPSocket* class and ancillary member functions help facilitate the establishment and handling of the network connection between the computer and the helicopter. The raw binary telemetry which is transmitted over WiFi is also decoded and logged by this class.

OpencvCamera Class The OpencvCamera class was designed to create an abstracted camera object that holds all the parameters relating to a particular camera in the flying volume. Some of these *camera specific* parameters are intrinsic, distortion and extrinsic matrices, resolution, frame rate, focal length and the image sensor principle axis location. See Chapter 4.1 for description of these parameters. These specific parameters are obtained using calibration routines. An auto calibration routine was included in this class for calibration from the user application. Although the primary use of this class is in the image processing server units, it is instantiated as virtual cameras in the base station software to hold camera specific information that is used in the pose estimation algorithm. For the server units, this class captures a frame of the scene with minimal latency and also undistorts the image before passing to its calling function. The *getRay* function parameterises a 3D ray given a point on the imager. This allows higher-level image processing functions to solve contention issues (via epipolar geometry (Hartley & Zisserman 2003)) when there is more than one blob in the scene.

Pose Estimation Class The Pose Estimation class is responsible for determining and maintaining the current pose estimate of each helicopter in the system. As data is received from the server units, it is stored in data structures within the virtual OpencvCamera objects in this class. The blob contention problem is solved in this class. The blob contention problem is: How does one allocate the blobs to particular helicopter's when there is more than one helicopter in the scene? The first-level approximate solution is to assume the last pose (translation and attitude) was sufficiently accurate and the helicopter has not moved too far from the last pose. The last pose is projected back into the scene of each camera and blob allocation to a particular helicopter is done based on the 2-norm between the projected and measured blobs. If the conditions do not permit the use of this method (velocity too fast or too many occlusions) then the use of epipolar geometry is used to solve the contention issue. The 3D ray of any blob is projected onto every image plane (resulting in a line), the blobs closest in distance over all mappings is the most likely candidate. Colour segmentation hugely reduces the computation complexity of this process.

TCP Client Class and UDP Socket Class The TCP Client class handles communication between the master computer and the server units. As the name suggests, it is a TCP/IP protocol. Since the computers are connected over wired ethernet cable, jitter and lost packets are not a problem with the local network and hence TCP/IP is a suitable communications protocol. The UDP socket class handles communication between the computer and the helicopters. These channels use the UDP/IP protocol. The reason for using a connectionless protocol such as UDP over this link is because the data is transmitted over WiFi and dropped packets are expected - especially with the helicopter position varying. Data is transferred at five times the rate at which the state-propagation is done, so that even if some packets are dropped, the most recent fused data is available for the control algorithm.

Multicast Class Useful information regarding the state of the helicopters are transmitted to a subnet within the local network. A multicast routing system over a broadcast routing system was chosen to share the information between nodes on the network to keep traffic to a minimum (Karaoglu & Heinzelman 2010). A dedicated computer is used for displaying vital experiment information. It simply listens for multicast packets and plots useful graphs (real-time) to facilitate testing. An Android application was also written to listen and display helicopter information for mobility.

Chapter 3

Modelling

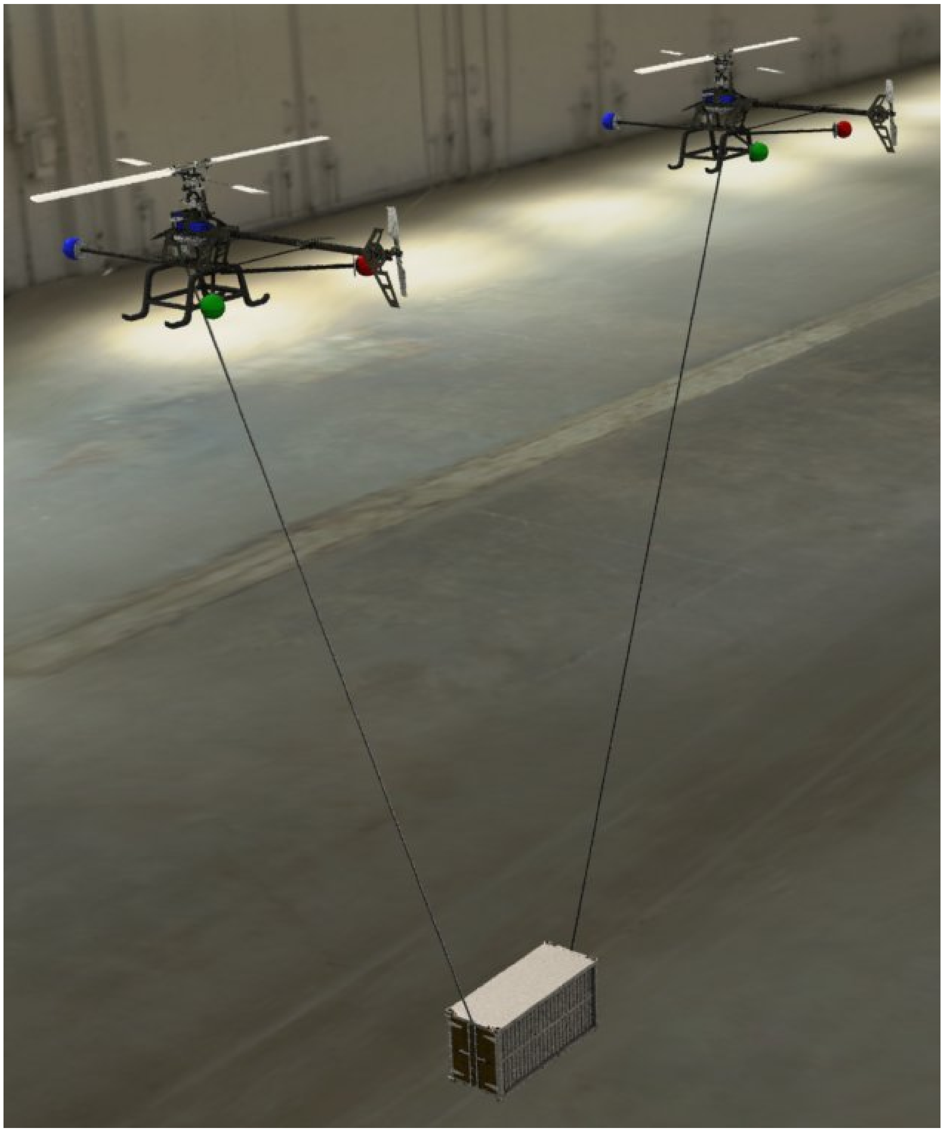

In this chapter, the twin-helicopter slung load transportation system model is developed. First, a high-fidelity model of a single helicopter from actuator inputs to kinematic outputs is derived. To estimate the parameters that characterise the helicopter model, system identification of the single helicopter plant is performed. The set of parameters obtained are used to form an uncertain set of plants that will be used later on in the QFT design. A linearised analysis of the single helicopter model in the hover condition is done to gain insight into the plant and aid in the control system design. Since the plant is multivariable, a sensible input-output pairing is assessed. Modal analysis is performed on the linearised plants to determine the source of unexpected resonant modes. The multi-body twin-helicopter slung load model is then derived using two single helicopter models, a simple 6DOF load model and the tethering constraint. Finally, the analysis of the twin-helicopter slung load model is performed to facilitate the controller design Chapter 5.2.

The contribution in this section is in the verification of a very high-fidelity model of a small-helicopter through testing and analysis. The development of a twin-helicopter slung load model that includes the inelastic tether constraint. And lastly, insight is gained into the dynamics of the individual helicopters and the twin-helicopter slung load system, through the application of Modal analysis.

3.1 Helicopter Model

This section describes the modelling of a small-scale helicopter. The derivation of the dynamic model of the helicopter has been adapted from the work done by Hald et al. (2006) and Bisgaard et al. (2009) from the University of Aalborg. In order to design an *optimal controller*, a high fidelity model of the plant is required. *Optimal control* is used here in the context of Quantitative Feedback Theory, where it means that the controller generates the *minimum control effort* required to meet the specifications for the uncertain plant set (Horowitz 1993). Control effort refers to percentage of capacity in amplitude and rate that is required by the actuators to meet the design specification. A reduction in scale of the helicopter is typically accompanied by an increase in the plant bandwidth (Mettler et al. 1999), due to three significant factors:

- reduction in mass and inertia of the body result in higher bandwidth (low-pass) filtering of the body dynamics
- reduction in the mass and inertia of the rotor blades reduces rotor time constant
- the non-linearly scaled increase in rotor angular velocity (to compensate for lift generation lost by reduced rotor diameter) reduces rotor time constant

The higher bandwidth response in small-scale helicopters is expected to come from the rotor dynamics. In full-scale helicopters, the rotor dynamics may be filtered so much through the body kinematics that high fidelity modelling of the rotor system may not be of much use for control design. The helicopter model is broken up into multiple sections shown in Fig. 3.1.1, according to the flow of signal from the pilot to the body kinematics.

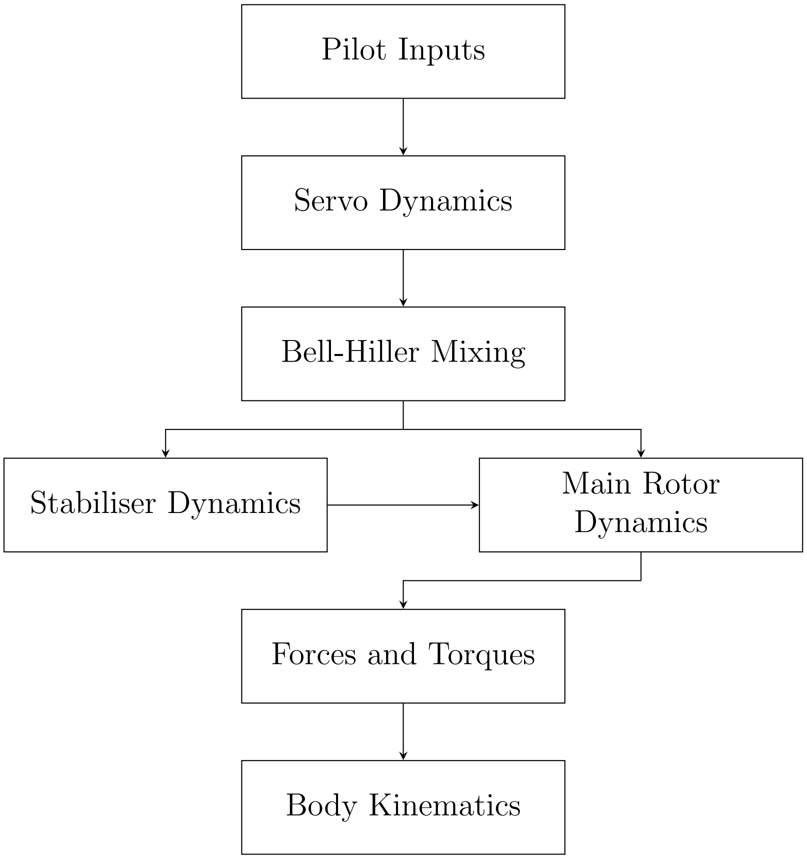

Figure 3.1.1: High-level overview of subsystems in the model

A Modelling Overview The pilot inputs consists of collective, lateral and longitudinal inputs and yaw rate reference input. The collective input refers to the input that generates a change in the blade collective pitch. This is primarily responsible for the force in the helicopter z-axis. The collective input also maps to the ESC input for speed control of the main rotor. The mapping is done so that the main rotor speed remains close to the nominal as the collective pitch changes. The lateral and longitudinal inputs refers to inputs that generate blade pitch angles primarily responsible for roll and pitch moments on the helicopter respectively. The mixer in the radio converts the collective, lateral and longitudinal inputs to individual actuator commands based on the geometry of the rotor-servo setup. All of these inputs are PWM signals with "on times" between 1000 µs and 2000 µs. The servo commands are transmitted via the radio system to the receiver on the helicopter. After a worst-case delay of 22 ms, it is decoded and shifted out of the receiver as PWM signals to the servos and the speed controller. The servos move accordingly to generate the thrust vectoring via the rotor head assembly. The rotor head is of a Bell-Hiller type. The Bell-Hiller mixing system generates a pitch on the main rotor blades as a function of the pilot's input, and a feedback signal generated through the stabiliser bar. It was pointed out in a conversation with Trevor Lorimer (June 2013) that the damping of the attitude dynamics is achieved by mechanical feedback via the stabiliser bar. The blade pitch input as a function of the azimuth position result in flapping dynamics and thrust vectoring. The forces and torques on the main and the tail rotor systems are then mapped to the center of mass, and the kinematics of the six degree-of-freedom model is computed.

3.1.1 Plant Inputs and Servo Dynamics

The pilot control inputs denoted by $\vec{\boldsymbol{T}} = [T_{lat}, T_{lon}, T_{col}, T_{yaw}]^T$ are the lateral and longitudinal cyclic, main collective and tail collective controls measured in microseconds with a range of $[1000 - 2000]$µs. The convention chosen for these signals is shown in Table. 3.1.1. The T-Rex 250SE has a 120° cyclic head system with three servos controlling the cyclic and collective movement. Experimentally, it was found that the pilot input signals get mapped to the servo input signals via the following equation,

Signal (+ve)	Interpretation
T_{col}	Positive thrust in body z-axis
T_{lat}	Negative roll
T_{lon}	Negative pitch
T_{yaw}	Positive yaw

Table 3.1.1: Pilot input convention defined with respect to the helicopter body frame (right-hand rule)

$$\vec{\boldsymbol{\Delta}}_{servo} = \begin{bmatrix} \delta_{left} \\ \delta_{right} \\ \delta_{rear} \\ \delta_{rud} \end{bmatrix} = \begin{bmatrix} K_{col} & -K_{lat} & -K_{lon} & 0 \\ K_{col} & K_{lat} & -K_{lon} & 0 \\ K_{col} & 0 & 2K_{lon} & 0 \\ 0 & 0 & 0 & K_{rud} \end{bmatrix} \vec{\boldsymbol{T}} \tag{3.1.1}$$

where K_{col}, K_{lat}, K_{lon} and K_{rud} are the pitch, lateral, longitudinal and rudder mixing gains. The deflections on the servo $\vec{\boldsymbol{\Delta}}_{servo}$, get scaled via the mixing gains on the RC transmitter to control the range of actuation. The input data used for system identification was at the servo input level, hence the mixing stage characterisation is not required for the control design. It is however included to verify the open-loop performance of the simulator. The servo was modelled using a second-order model. The Simulink model used to model the servo subsystem and the mapping to the main rotor and stabiliser bar inputs is shown in Fig. 3.1.2. The model for representing the second-order dynamics for the individual servos is given in LTI form in (3.1.2) and shown in Fig. 3.2.2 with internal rate-limit. The servo DC gain is represented by K, natural frequency given by ω_n, the damping factor by ζ and a pure delay of T_d seconds.

$$P_{servo} = \frac{K e^{-sT_d}}{(s/\omega_n)^2 + 2s\zeta/\omega_n + 1} \tag{3.1.2}$$

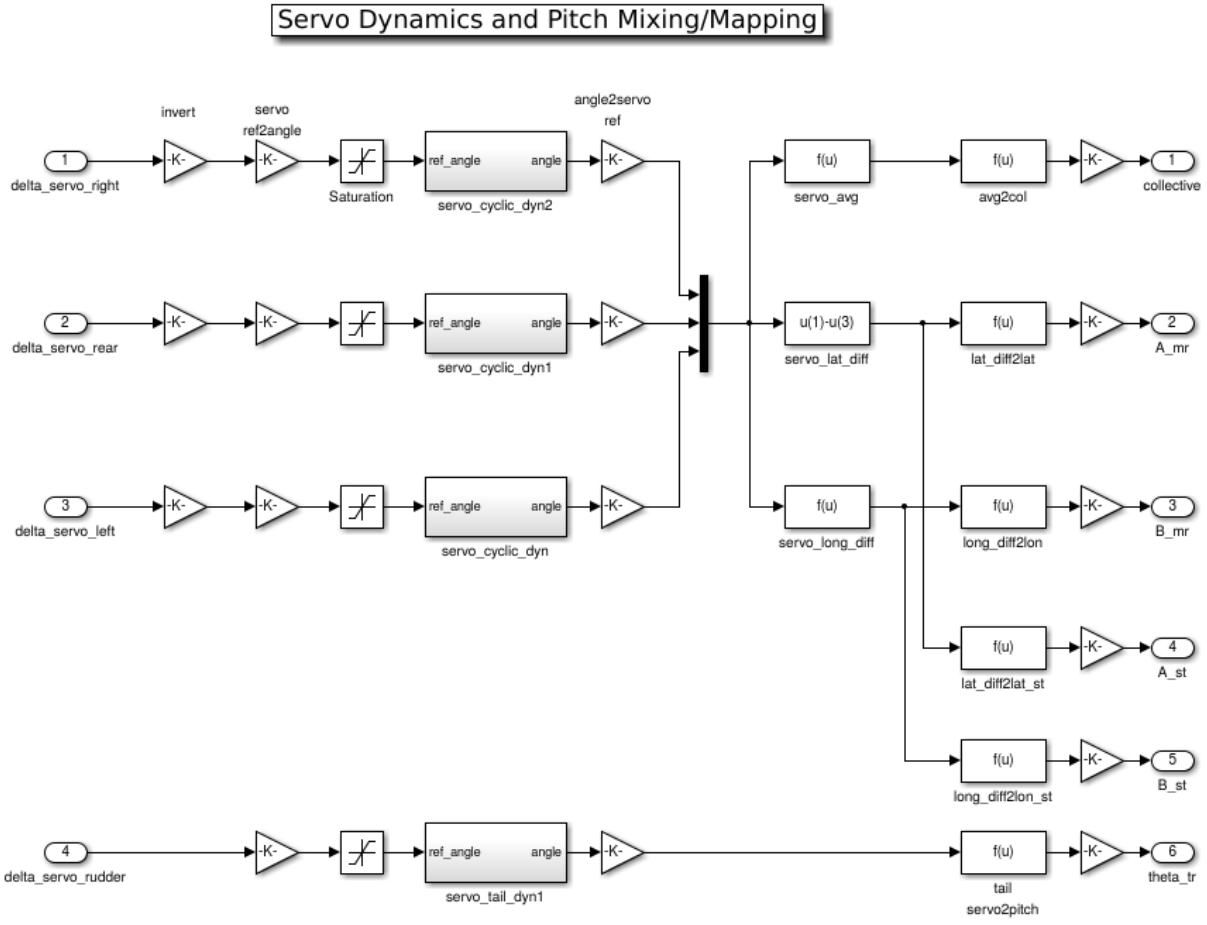

Figure 3.1.2: Simulink model of the servo subsystem and mapping to main rotor and stabiliser inputs

3.1.2 Bell-Hiller Mixing and Rotor Dynamics

A common feature among small-scale helicopters is the Bell-Hiller mixing system. This mechanism slows down the the main rotor dynamics and provides damping to body rate disturbances. The blade pitch angle in a Bell-Hiller mixing configuration is a function of the pilot inputs as well as the flapping angles of the stabiliser bar. The flapping angle (β) of the stabiliser bar is the angle that the stabiliser bar makes with the xy-plane of the swash plate (which is level with the xy-plane of the helicopter this is illustrated in Fig. 3.1.3). The blade pitch θ, as a function of the blade position (azimuth Ψ shown in Fig. 3.1.5), with respect to the rear (clockwise rotation as positive viewed from above) of the helicopter may be written as (Hald et al. 2006),

$$\theta_{mr}(\Psi) = {T'}_{col} - {T'}_{lat}\cos(\Psi) - {T'}_{lon}\sin(\Psi) \tag{3.1.3}$$

where ${T'}_{col}$ is the collective blade pitch, ${T'}_{lat}$ is the blade pitch due to a lateral command, and ${T'}_{lon}$ is the blade pitch due to a longitudinal command. The blade pitch vector $\boldsymbol{T'}$, is a function of the servo positions as well as the stabiliser bar flapping angle shown by

(3.1.5) and (3.1.6). The first harmonic approximation of the flapping angle may be written as (ibid.),

$$\beta(\Psi = \Omega t) = a_0 - a_1 \cos(\Psi) + b_1 \sin(\Psi) \tag{3.1.4}$$

where the bias component a_0 is the coning angle, a_1 is the longitudinal flapping angle, b_1 is the lateral flapping angle, and Ω is the rotor angular speed. The cyclic inputs of the Bell-Hiller mixing system may be expressed as,

$$T'_{lat} = \tilde{T}_{lat} - b_{1,st} K_h \tag{3.1.5}$$

$$T'_{lon} = \tilde{T}_{lon} - a_{1,st} K_h \tag{3.1.6}$$

where K_h is the Hiller gain which represents the gain from stabiliser bar flapping angle to main rotor pitch, and $b_{1,st}$ and $a_{1,st}$ are the lateral and longitudinal flapping angles of the stabiliser bar. The cyclic blade pitch components $\tilde{T}_{lat}$ and $\tilde{T}_{lon}$ may be reconstructed by solving for $\vec{\boldsymbol{T}}$ in (3.1.1), and then finding the mapping to $\tilde{\boldsymbol{T}}$; this relationship was found to be linear ($\tilde{\boldsymbol{T}} = diag(\vec{\boldsymbol{b}})\vec{\boldsymbol{T}} + \vec{\boldsymbol{c}}$) through measurement. The parameters $\vec{\boldsymbol{b}}$ and $\vec{\boldsymbol{c}}$ are specific for the servo linkage lengths (geometry). The stabiliser bar is a teetering type of rotor (Padfield 2008) (Seddon & Newman 2011). Hence there is no collective input and no coning ($a_0 = 0$ in (3.1.4)).

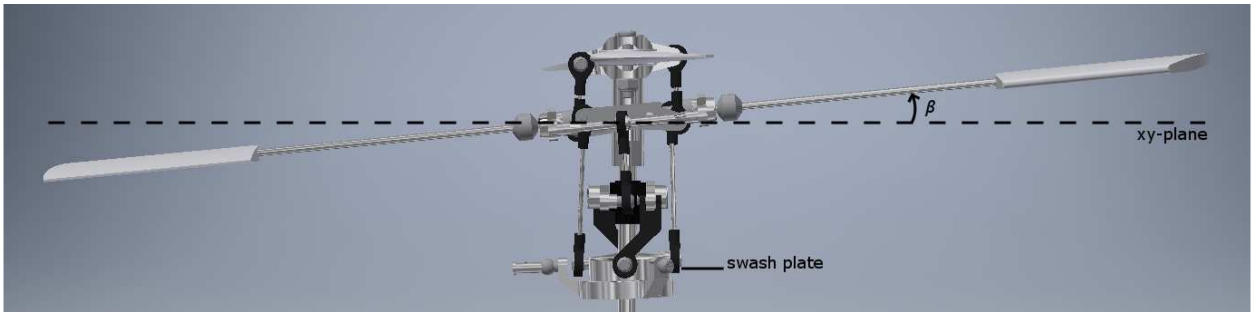

Figure 3.1.3: Side view of the rotor head showing flapping angle β of the stabiliser bar

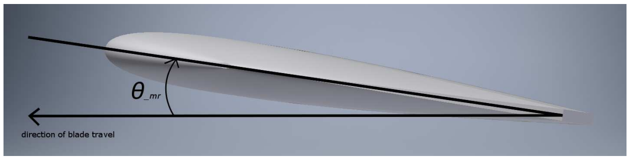

Figure 3.1.4: Main rotor blade showing pitch angle θ_{mr}

The rotor flapping dynamics are obtained by writing the torque balance equation for the blade about the flapping point (the virtual hinge),

$$I_b \ddot{\beta} = \sum_i \tau_i \tag{3.1.7}$$

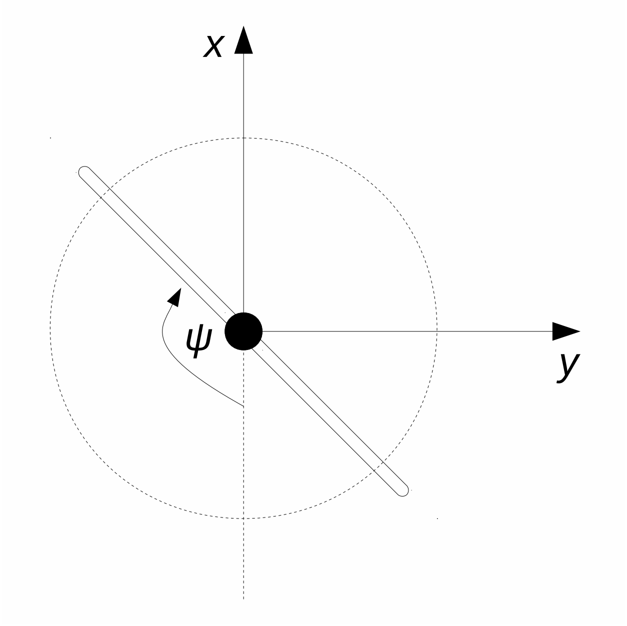

Figure 3.1.5: Drawing of the rotor view from the top showing the azimuth reference

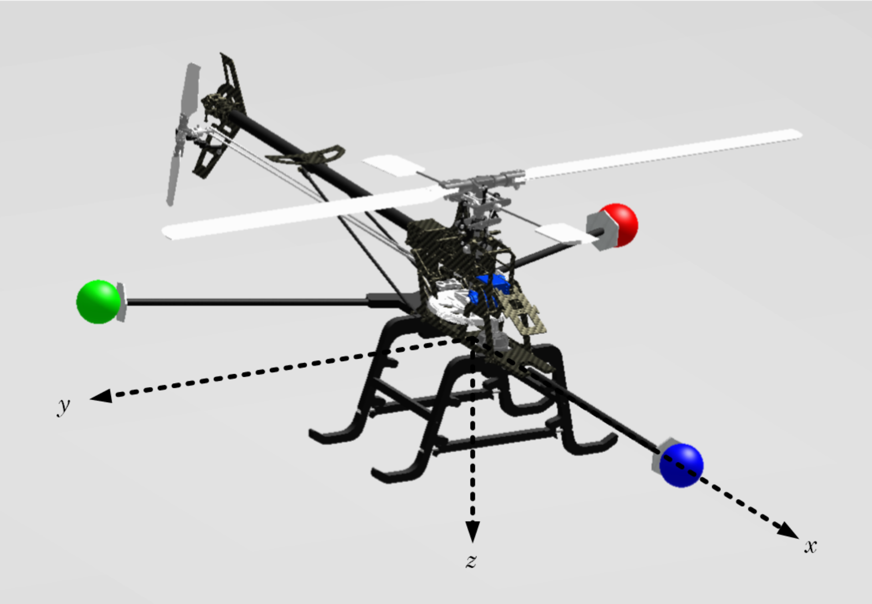

Figure 3.1.6: Reference frame of helicopter

where I_b is the blade moment of inertia about the virtual hinge (In the equations below, generic variables that apply to both the stabiliser bar and the main rotor are written without subscripts. In the equations derived for the helicopter, listed in Appendix C.1 and C.3, subscripts st denote stabiliser bar variables and subscript mr denote main rotor variables). The torque components that are contained in the the model are listed below. The classical aircraft body reference frame is used, where the x-axis points forward (from the perspective of a pilot in the cockpit), the z-axis points down and the y-axis completes the set of orthogonal axes. Positive roll is defined with positive rotation about the x-axis. Positive pitch is defined with positive rotation about the y-axis. Positive yaw is defined with positive rotation about the z-axis. For a complete derivation of the torque components shown below see Hald et al. (2006).

- **Aerodynamic torque:** Generated by the aerodynamic lift for blade element dL given by
  $$d\tau_{aero} = r\ dL \tag{3.1.8}$$
  where
  $$dL = \frac{1}{2}\rho C_l c V_b^2 dr, \tag{3.1.9}$$
  dL is the elemental lift derived from *blade element theory*, r is the displacement from the hinge axis, C_l is the coefficient of lift, ρ is the air density, c is the chord length of the blade (assumed constant with respect to r), and V_b is the blade velocity with respect to the air.

- **Restraint torque:** The torque due to the restoring force caused when the blade flaps is
  $$\tau_{res} = K_{smr}\beta \tag{3.1.10}$$
  where K_{smr} is the virtual hinge spring constant, and β is the flapping angle.

- **Centrifugal torque:** The differential torque due to the centrifugal force that results when the blade rotates is given by
  $$d\tau_{cf} = r\ dF_{cf}\sin(\beta) \tag{3.1.11}$$
  where
  $$dF_{cf} = -\Omega^2\left(e_{mr} + r\cos(\beta)\right)dM_b, \tag{3.1.12}$$
  e_{mr} is the displacement between the center of rotation and the virtual hinge, dM_b is the mass of a differential blade element.

- **Body angular torque:** An angular acceleration of the body gets reflected as a linear acceleration of blade elements which result in torque on the blade about the hinge axis. The elemental force responsible for this is
  $$dF_{ba} = r\left(-\ddot{\phi}\sin(\Omega) + \ddot{\theta}\cos(\Omega)\right)dM_b \tag{3.1.13}$$
  where $\ddot{\phi}$ and $\ddot{\theta}$ are the accelerations in roll and pitch respectively.

- **Body normal torque:** The body normal torque is the torque on the blade with respect to the hinge due to body normal acceleration. The elemental force responsible for this is
  $$dF_{bn} = \left(\ddot{z} - \dot{x}\dot{\theta} + \dot{y}\dot{\phi}\right)dM_b \tag{3.1.14}$$

- **Coriolis torque:** The torque due to a fictitious force that is apparent when a particle moves in a rotating frame of reference. The rotating frame of reference is due to body rotation and the particle velocity is due to rotor rotation. The elemental force responsible for this is

$$dF_{corr} = -2\Omega\left(\dot{\phi}\cos(\Omega) + \dot{\theta}\sin(\Omega)\right)(e_{mr} + r\cos(\beta))\,dM_b \tag{3.1.15}$$

The restraint torque is the only component that is non-existent in the stabiliser bar model because it is a teetering rotor. After all torque components have been integrated over the length of the blade, the higher-order trigonometric functions are approximated using first-order harmonics. In most cases, a first-order model for the flapping dynamics is sufficient as used in (Mettler et al. 1999). The model above gives second-order dynamics for coning, lateral and longitudinal flapping. This may be obtained by substituting the second time derivative of (3.1.4) into (3.1.7). The Matlab® Mupad tool was used to integrate and simplify the flapping equations. The flapping equations for the main rotor and stabiliser bar are given in Appendix C.1 and C.2, respectively.

The tail rotor only has a collective input, thus lateral and longitudinal flapping are taken to be zero. Due to the tail rotor speed being much higher than the main rotor (4.28 times for the T-Rex 250), the coning behaviour for the tail rotor was not modelled as its bandwidth is much higher than the control bandwidth of the related channels. Hence the tail force/torque response is limited by the tail servo bandwidth.

Induced Velocity The blade velocity in (3.1.9) is a function of the induced velocity. In order to calculate the thrust generated by the rotary wing, the induced velocity must be calculated. Momentum theory is used to calculate the thrust generated by the rotary wing. Assuming a uniform inflow, it is shown in Seddon & Newman (2011) that the induced velocity is related to the thrust by,

$$v_i = \frac{T}{2\rho A\|\vec{\boldsymbol{v}}_{bi}\|} \tag{3.1.16}$$

where $\|\vec{\boldsymbol{v}}_{bi}\| = \left\| \mathbf{v}_h^b - \begin{bmatrix} 0 \\ 0 \\ v_i \end{bmatrix} \right\|$ is the inlet velocity with respect to the induced velocity and A is cross-sectional area of the rotor disk perpendicular to the inflow. This approximation of the induced velocity results in an algebraic loop. The induced velocity is solved using the Newton-Raphson method (Ypma 1995) for the simulation. An algebraic loop is formed from (3.1.16) for the solution of the induced velocity. In order to speed up the simulation the induced velocity is passed through a low-pass filter with a corner frequency of 1000 rad/s, which is much higher in bandwidth than the rotor dynamics. This results in an additional state to the system state vector.

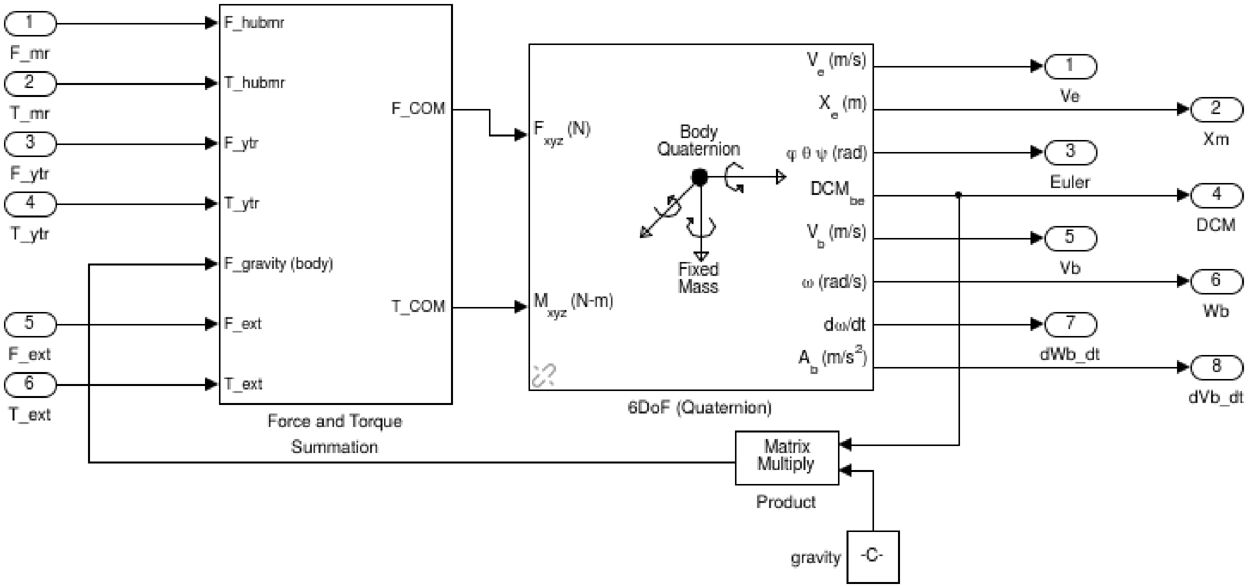

Figure 3.1.7: Simulink subsystem that handles the body kinematics. F_mr and T_mr are the forces and torques on the main rotor (main rotor frame); F_ytr and T_ytr are the force and torques on the tail rotor (tail rotor frame); the equations for the elements of the forces and torques are given in Section C.3. F_ext and T_ext are signals to accommodate external forces and torques on the helicopter (body frame). The tail rotor and main rotor are aligned with the helicopter body frame but displaced from the center of mass. The output dVb_dt is the acceleration of the helicopter in the body frame of the helicopter and corresponds to (3.1.17); dWb_dt is the angular acceleration of the helicopter in the body frame of the helicopter and corresponds to (3.1.18)

3.1.3 Force/Torque and Kinematics

The forces and torques generated by the rotor are a result of aerodynamic lift and drag of the blades. The restraint torque is an additional torque that is significant in the main rotor dynamics. To get the total force and torque on the rotor hub, the elemental forces and torques are integrated along the length of the blade and averaged for one revolution. The lateral and longitudinal torque for the main rotor hub is computed by averaging the reflected force at the virtual hinge and restraint torque over one revolution of blade travel. The derived equations for the force and torque generated by the main rotor, using Matlab's ® Mupad for symbolic manipulation, is presented in Section C.3 and Section C.4 respectively. Since there is no cyclic actuation of the tail rotor, only the force and torque about the rotor axis is considered. All the forces and torques of the main and tail rotor are mapped onto the center of mass. The rigid body six degree-of-freedom kinematic equations describe the center of mass body motion as a function of the forces and torques. The Simulink model for the kinematics is shown in Fig. 3.1.7. The kinematic equation for body linear and angular acceleration are given by the following equations,

$$\dot{\vec{\boldsymbol{v}}}_b = \frac{1}{M_h}\vec{\boldsymbol{F}}_b - (\vec{\boldsymbol{\omega}}_b \times \vec{\boldsymbol{v}}_b) \tag{3.1.17}$$

$$\dot{\vec{\boldsymbol{\omega}}}_b = \boldsymbol{I}_h^{-1}\left(\vec{\boldsymbol{T}}_b - (\vec{\boldsymbol{\omega}}_b \times \boldsymbol{I}_b \vec{\boldsymbol{\omega}}_b)\right) \tag{3.1.18}$$

where $\vec{\boldsymbol{v}}_b$ is the vector of linear velocity in the body frame, $\vec{\boldsymbol{F}}_b$ is the force on the center of mass in the body frame, M_h is the mass of the helicopter, $\vec{\boldsymbol{\omega}}_b$ is the vector of body rates, $\boldsymbol{I}_h$ is the helicopter mass inertia matrix and $\vec{\boldsymbol{T}}_b$ is the torque applied to the helicopter in the body frame.

To avoid the gimbal-lock phenomenon, the quaternion representation of the attitude of the helicopter is used. The quaternion can be obtained through integrating,

$$\dot{\vec{\boldsymbol{q}}} = \frac{1}{2}\,\vec{\boldsymbol{q}} \otimes \vec{\boldsymbol{\omega}}_q \tag{3.1.19}$$

where $\vec{\boldsymbol{q}} = [q_0, q_1, q_2, q_3]^T = q_0 + \hat{\boldsymbol{\imath}} \cdot q_1 + \hat{\boldsymbol{\jmath}} \cdot q_2 + \hat{\boldsymbol{k}} \cdot q_3$, $\vec{\boldsymbol{\omega}}_q = [0, \omega_x, \omega_y, \omega_z]^T$ the body angular velocity in quaternion form, and the operator $\otimes$ is the quaternion product (see (4.3.7) for definition).

3.1.4 Plant States

The complete model of the helicopter consist of a large number of state variables. A summary of the state variables are given below.

Stabiliser flapping states 4 states

$a_{lon,st}$ Longitudinal flapping angle (rad)

$b_{lat,st}$ Lateral flapping angle (rad)

$\dot{a}_{lon,st}$ Longitudinal flapping angle velocity (rad/s)

$\dot{b}_{lat,st}$ Lateral flapping angle velocity (rad/s)

Main rotor flapping states 6 states

$a_{con,mr}$ Coning angle (rad)

$a_{lon,mr}$ Longitudinal flapping angle (rad)

$b_{lat,mr}$ Lateral flapping angle (rad)

$\dot{a}_{con,mr}$ Coning angle velocity (rad/s)

$\dot{a}_{lon,mr}$ Longitudinal flapping angle velocity (rad/s)

$\dot{b}_{lat,mr}$ Lateral flapping angle velocity (rad/s)

Body kinematics 13 states

$\vec{\boldsymbol{x}}^e$ Position in the inertial frame [3 × 1] (m)

$\vec{\boldsymbol{v}}^b$ Velocity in the body frame [3 × 1] (m/s)

$\vec{\boldsymbol{q}}$ Quaternion [4 × 1] (unit)

$\vec{\boldsymbol{\omega}}^b$ Angular velocity in body frame [3 × 1] (rad/s)

Servo dynamics 8 states (2 × 4 servos)

δ Angular position (rad)
$\dot{\delta}$ Angular velocity (rad/s)

Thrust 1 state

v_i Induced velocity (m/s)

The state vector consist of a total of 32 states.

3.2 System Identification

The two main classes of system identification are the nonparametric time and frequency domain methods and the parameter estimation methods (Ljung 1998). In the nonparametric method, an input-output approximation is extracted from the impulse response or frequency response (using the empirical data) without a strict structure imposed from the physical system. The parameter estimation method involves selecting a model based on the physical system first, then using the empirical data to refine the parameter selection so that the error between the measured response and the simulation response to the common input is minimised in the least squares sense. This is illustrated in Fig. 3.2.1.

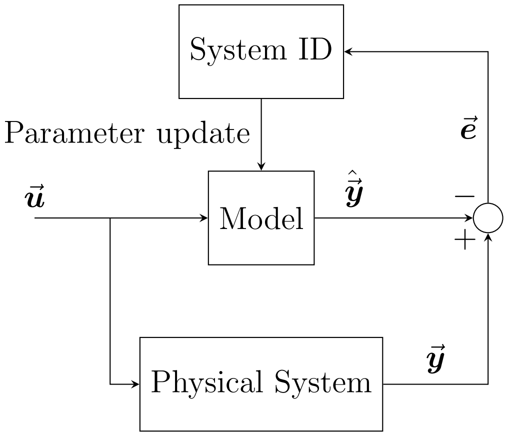

Figure 3.2.1: Functional block diagram of system identification methodology

For the helicopter model, all the significant dynamics were considered in the model so that the *model structure* is capable of capturing the salient features of the plant. Due to uncertainty in difficult to model subsystems and difficult to measure parameters, the simulation may not match the physical plant satisfactorily. The parameter estimation method was chosen to reconcile the mathematical model. By sensibly bounding the parameters to be estimated, one can obtain a better approximation of the physical plant while retaining the meaning of the physical parameters.

To simplify the system identification task, the servos were identified separately from the rest of the helicopter. This was not too challenging because most of the servo states can be measured easily. The Matlab® Optimization Toolbox was used for estimating parameters using the nonlinear least-squares method.

3.2.1 Servo Dynamics

The servo dynamics were the first to be estimated since it can be easily isolated from the rest of the system. A second-order model with rate-limits (i.e. limits on the velocity) describe the servo reference to output dynamics. A Simulink model of a generic second-order system is shown in Fig. 3.2.2 with the following free parameters: DC gain K_s, natural frequency $\omega_s n$,

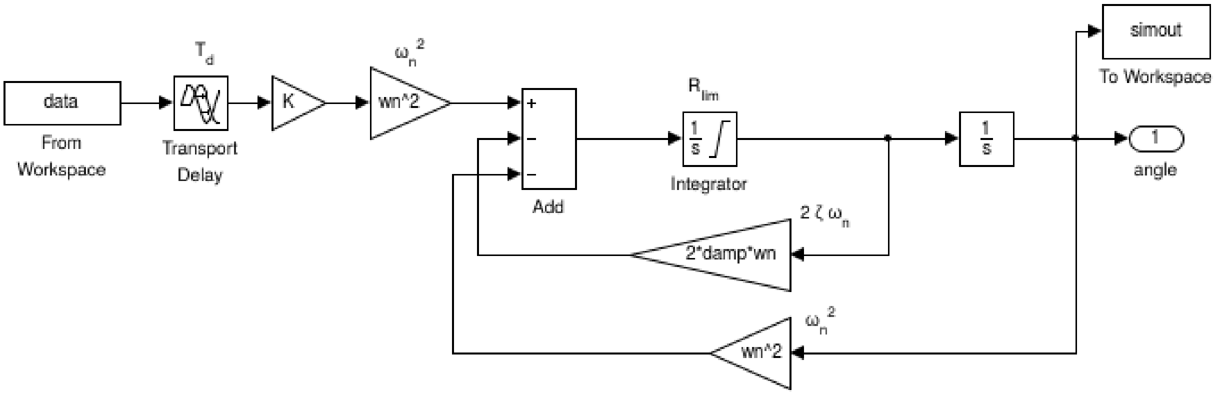

Figure 3.2.2: Simulink model of a second-order system with rate-limits; ω_{sn} is represented by $\mathrm{w_n}$, K_s is represented by K, T_{sd} is represented by $\mathrm{T_d}$, R_{slim} is represented by $\mathrm{R_{lim}}$ and ζ_s represented by ζ in the Figure above.

damping factor ζ_s, dead-time T_{sd} and angular velocity limits R_{slim}. A pulse reference (angle) was given to the servo, and the potentiometer voltage was logged for parameter estimation. The Matlab® Optimisation Toolbox was used on the model in Fig. 3.2.2 with the logged data to find the set of parameters that minimised the average error over the experiment timespan.

For economic reasons, two types of servos are used in RC helicopters. The servos responsible for cyclic control are usually analog, and slower compared to the tail collective servo (digital). The simulation angle output using the optimal parameters for the analog servo is shown in Fig. 3.2.3, along with measured response. The values of the parameters obtained from the optimisation are given in Table 3.2.1.

Table 3.2.1: Identified second-order parameters for the analog (DS410) and digital (DS420) servos

Characteristic	DS410	DS420
Gain, K_s	75.8	75.8
Damping ratio, ζ_s	0.85	0.85
Natural frequency, ω_{sn} (rad/s)	35	45
Rate-limit, R_{slim} (°/s)	413	672

3.2.2 Rotor Drive Dynamics

To simplify the control system, the motor speed was assumed to be fixed at 3500 rpm. In order to design a controller for the rotor drive dynamics, a reasonable representation of the plant was required. Step tests were done on the rotor (including the torque disturbance/-damping from the blades) to model the response. A plot of the step response is shown in

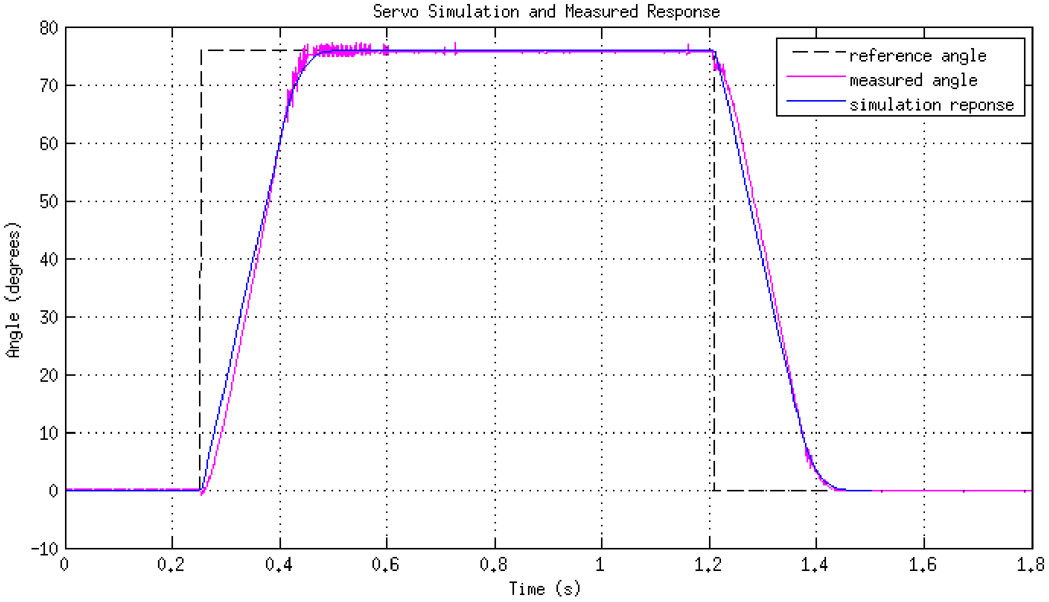

Figure 3.2.3: Measured servo angle output and simulation angle output to a step angle reference (for the analog servo)

Fig. 3.2.4. The mid-to-high frequency signal response observed in Fig. 3.2.4 is believed to be due to the aerodynamic disturbance that originate from the main rotor wake, as tests were done in a confined space. A first order plant with delay, given by,

$$P_m = k_{mp}\frac{e^{-sT_{md}}}{s/\omega_{mn}+1} \tag{3.2.1}$$

was found to be sufficient to capture the dynamics of the rotor system. A least squares minimisation was done to find the parameters that fit the data, shown in Table 3.2.2. Since the motor controller design is ancillary to the control system design, it is contained in Section E.1.

Table 3.2.2: Identified parameters for the rotor drive system

Parameter	Value
Gain, k_{mp}	3.0
Dead-time, T_{md} (ms)	120
Natural frequency, ω_{mn} (rad/s)	2.3

3.2.3 Single Helicopter

Due to space constraints, only hover operation could be safely investigated. The helicopter was flown manually within the flight volume, multiple times, with forced excitation on in-

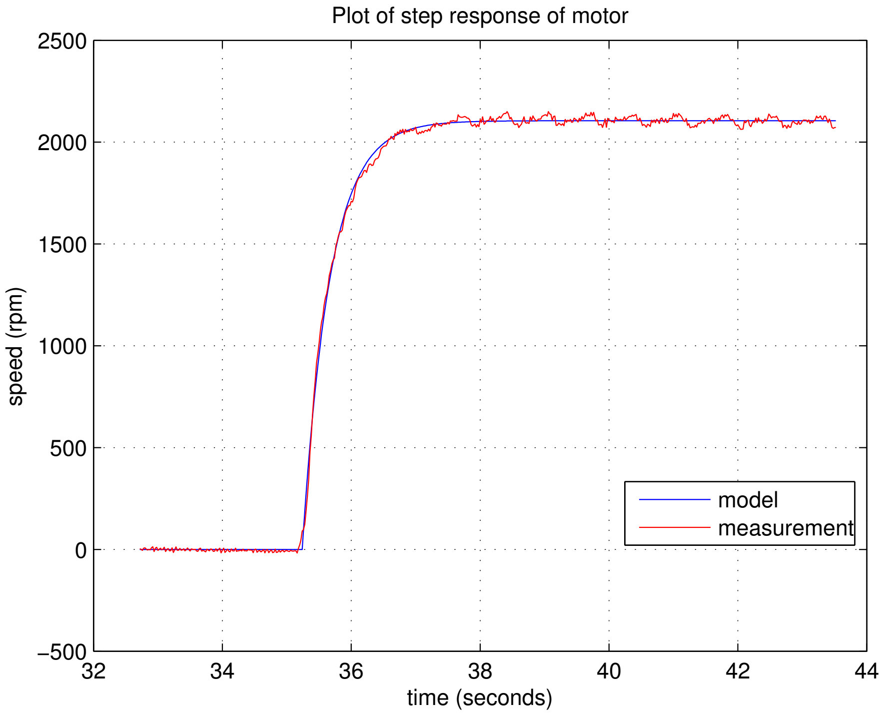

Figure 3.2.4: Step response of rotor drive system showing model response and measured data

dividual and combined channels. The input signals that were logged for the system identification process was the reference angles to each servo, the commanded yaw rate and the speed of the rotors. The output signals that were logged were the body angular and linear velocities. The Simulink model that interfaces to the measured data is shown in Fig. 3.2.5.

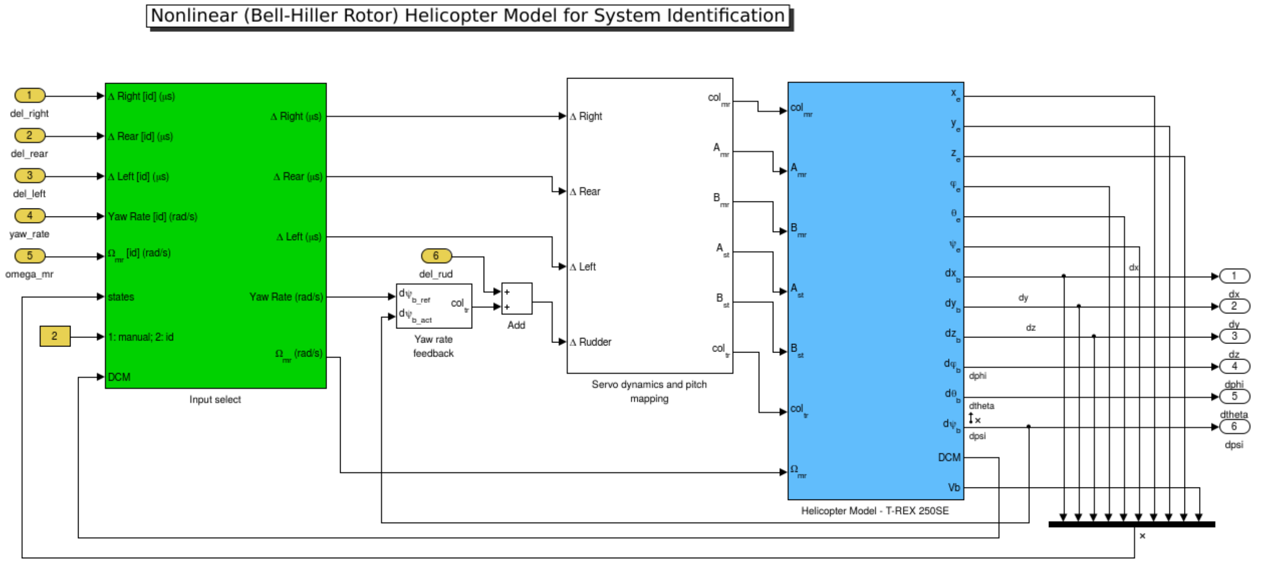

Figure 3.2.5: Simulink model of helicopter model showing system identification inputs and outputs

To get an idea of the bandwidth over which system identification would be necessary, a frequency domain assessment of the body kinematics was made. Digital filters on the IMU was configured to pre-filter the body rate measurements with a corner frequency of 98 Hz. The body angular rates were logged on-board at 200 Hz during a flight. After identifying chunks of hover flight data, a discrete Fourier transform was done for varying lengths of data. The power spectral density of the angular rates for a 10 second flight is shown in Fig. 3.2.6. The analysis showed that most of the plant dynamics were under 20 Hz. The peak power near 50 Hz is from the main rotor rotation frequency (with the blades not perfectly balanced and interaction with the non-symmetric fuselage). The roll channel was found to have the least attenuation of the vibration from the main rotor. This is not surprising, as the smallest inertia was expected to be along the roll axis.

Since the closed-loop bandwidth was expected to be under 20 Hz, the output of the optimal state-estimator (which uses the visual tracking information and the IMU data) was used capture the kinematics data. The output of the estimator produces high bandwidth angular rates with the biases removed and linear velocity estimates based on the optimal fusion of the integral of the IMU acceleration and the derivative of the visual position information. After segments of meaningful data were isolated, the data was preprocessed to remove noise and outliers. The data was then “chopped” into time ranges. The reason for this is because identification over different time spans produces an optimal fitting for specific frequency spans. The underlying problem here is that biased uncertainty in input collective, lateral and longitudinal angles gets mapped to biases in forces and torques on the helicopter body. These signals, once integrated, result in drift in the body angular and linear velocities. It seems that this is an inevitable challenge in open-loop system identification with high-fidelity models.

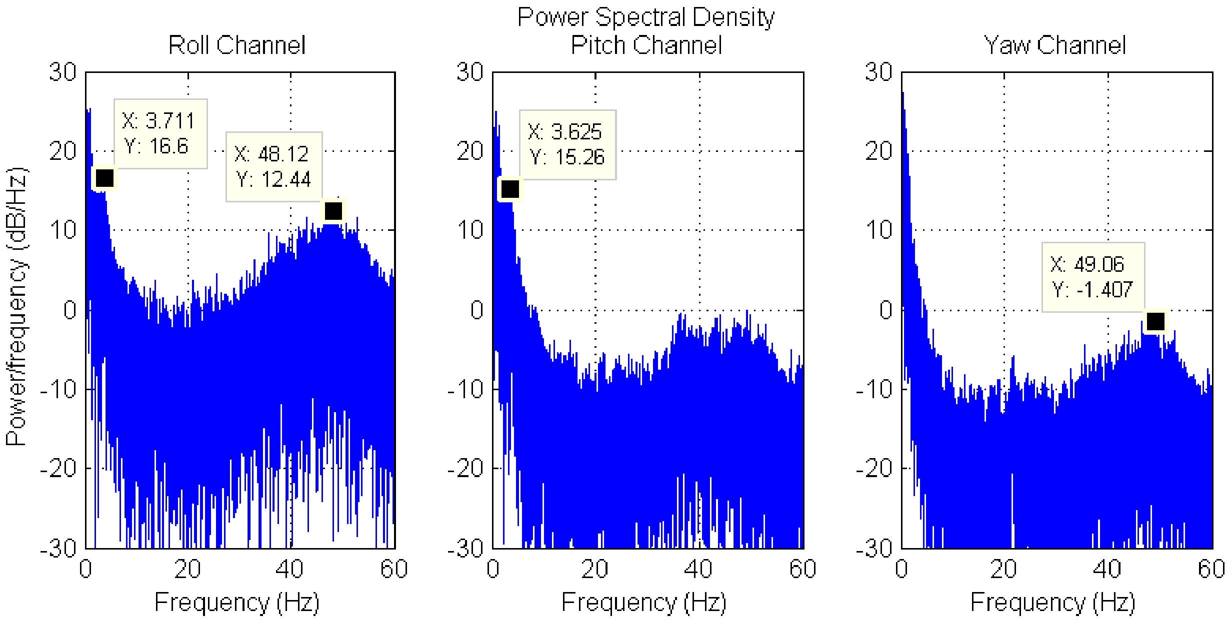

Figure 3.2.6: Power spectral density (PSD) of the angular rate signals for 10 seconds of hover flight with the magnitude calculated using $10\log_{10}(\ldots)$

The variables shown in Table 3.2.3 are parameters that are difficult to measure, thus formed part of the parameter space across which the optimisation took place. Initial values of parameters were chosen based on laboratory measurements and estimation using CAD models (for the case of mass inertia). Measuring the mapping from servo angle to blade pitch was done by analysing images taken with a camera in a static setup. Due to varying degrees of mechanical play of the rotor head, a gain and bias terms were added to the parameter space for each servo input to compensate for the poorly measured input mapping. Due to the physical plant not having much damping in the yaw dynamics, input uncertainty in the tail collective angle easily gets propagated to yaw rate drift. To compensate for this, a low-gain proportional-integral (PI) controller is used to additionally drive the tail rotor collective angle so that the simulation body yaw rate output converges to the physical plant output. Since the identification was performed using data from the helicopter already in motion, the initial conditions for the rotor dynamics (flapping initial states) were not known and therefore were added to the set of parameters to estimate.

3.2.4 Results

To highlight the fidelity of the model, the body angular rates (measured and simulated) for an experiment with identification time of 10 seconds is shown in Fig. 3.2.7. Although, poor approximation of the higher frequency dynamics is seen in the pitch channel. The least-squares error approach to parameter estimation produced results that lost accuracy of the higher frequency components with increasing *identification time*. The experiments done with lower identification times capture the higher frequency dynamics much better. Figures 3.2.8 and 3.2.9 show the time domain simulation and measured responses for different flights of

Table 3.2.3: Uncertain helicopter parameters

Parameter	Interpretation
I_{xx}, I_{yy}, I_{zz}	Moment of inertia about the x, y and z axes ($\mathrm{kg\,m^2}$)
K_{vmr}	Vertical component of center of mass from main rotor (m)
K_{hmr}	Horizontal component of center of mass from main rotor (m)
e_{mr}	Displacement from center of rotation to virtual hinge of main rotor (m)
K_{smr}	Main rotor effective spring constant (N m/rad)
C_{lmr}	Lift coefficient for main rotor
C_{lst}	Lift coefficient for stabiliser bar
C_{ltr}	Lift coefficients for tail rotor
C_{dmr}	Drag coefficient for the main rotor
C_{dtr}	Drag coefficient for the tail rotor

15 and 20 seconds identification times respectively. After running the system identification procedure over multiple flights, with different identification times, a set of parameters was extracted that capture the near-hover flight condition. The parameter set with uncertainty bounds are shown in Table 3.2.4. By assessing the parameter values and the uncertainty, it is evident that the results from the optimisation produced parameters that are sensible from the physical point of view. Nine flight test were done to generate the uncertain set of plants. After the outliers were removed, the uncertainty bounds were derived by assessing the distribution of the data. The uncertainty bounds make physical sense and are not far-fetched, as may be the case if the model structure was inconsistent with the physical system.

Table 3.2.4: Identified helicopter parameters

Parameter	Unit	Minimum	Maximum
I_{xx}	$\mathrm{kg\,m^2}$	2.134×10^{-3}	5.894×10^{-3}
I_{yy}	$\mathrm{kg\,m^2}$	3.471×10^{-3}	5.650×10^{-3}
I_{zz}	$\mathrm{kg\,m^2}$	5.627×10^{-3}	64.846×10^{-3}
K_{smr}	$\mathrm{N\,m/rad}$	166.7×10^{-3}	609.0×10^{-3}
e_{mr}	m	1.06×10^{-3}	7.83×10^{-3}
C_{lmr}		5.498	5.707
C_{lst}		1.0	1.352
C_{ltr}		1.048	1.138
C_{dmr}		28.82×10^{-3}	52.08×10^{-3}
C_{dtr}		30.38×10^{-3}	52.59×10^{-3}

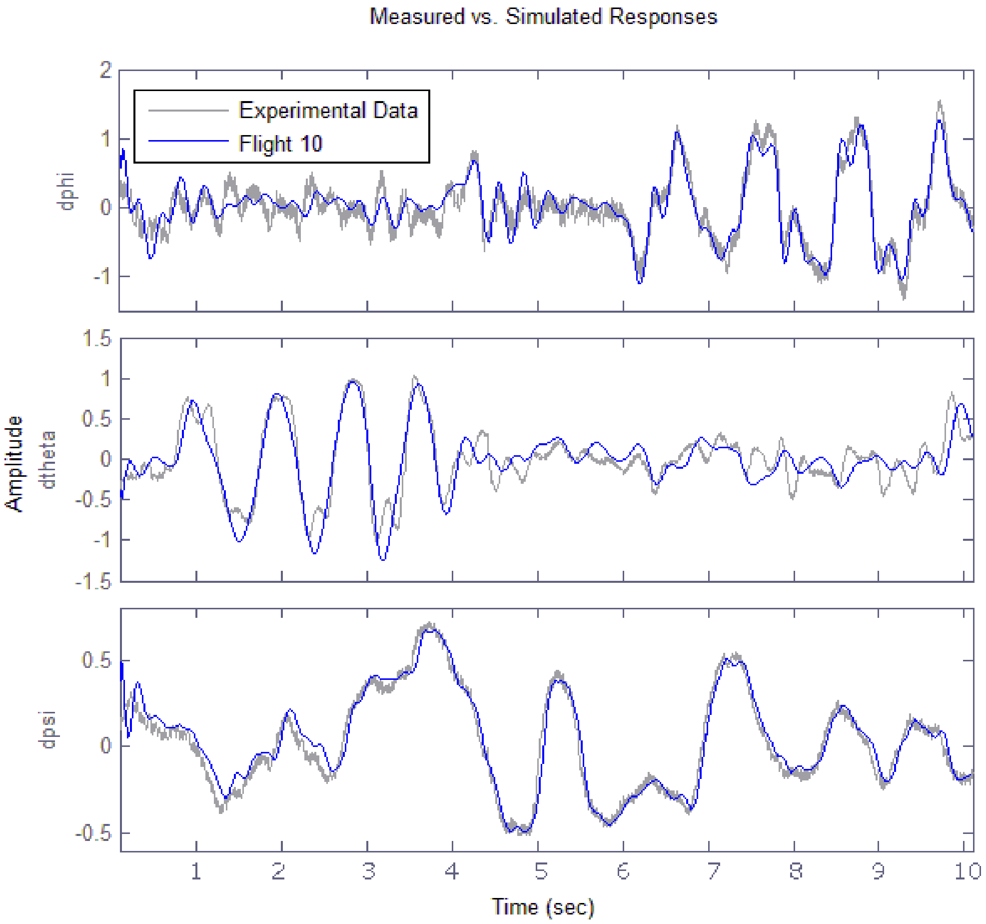

Figure 3.2.7: Simulation output and flight data for roll rate (dphi), pitch rate (dtheta), and yaw rate (dpsi) shown in rad/s for 10 seconds-parameters optimise lower frequency characteristics

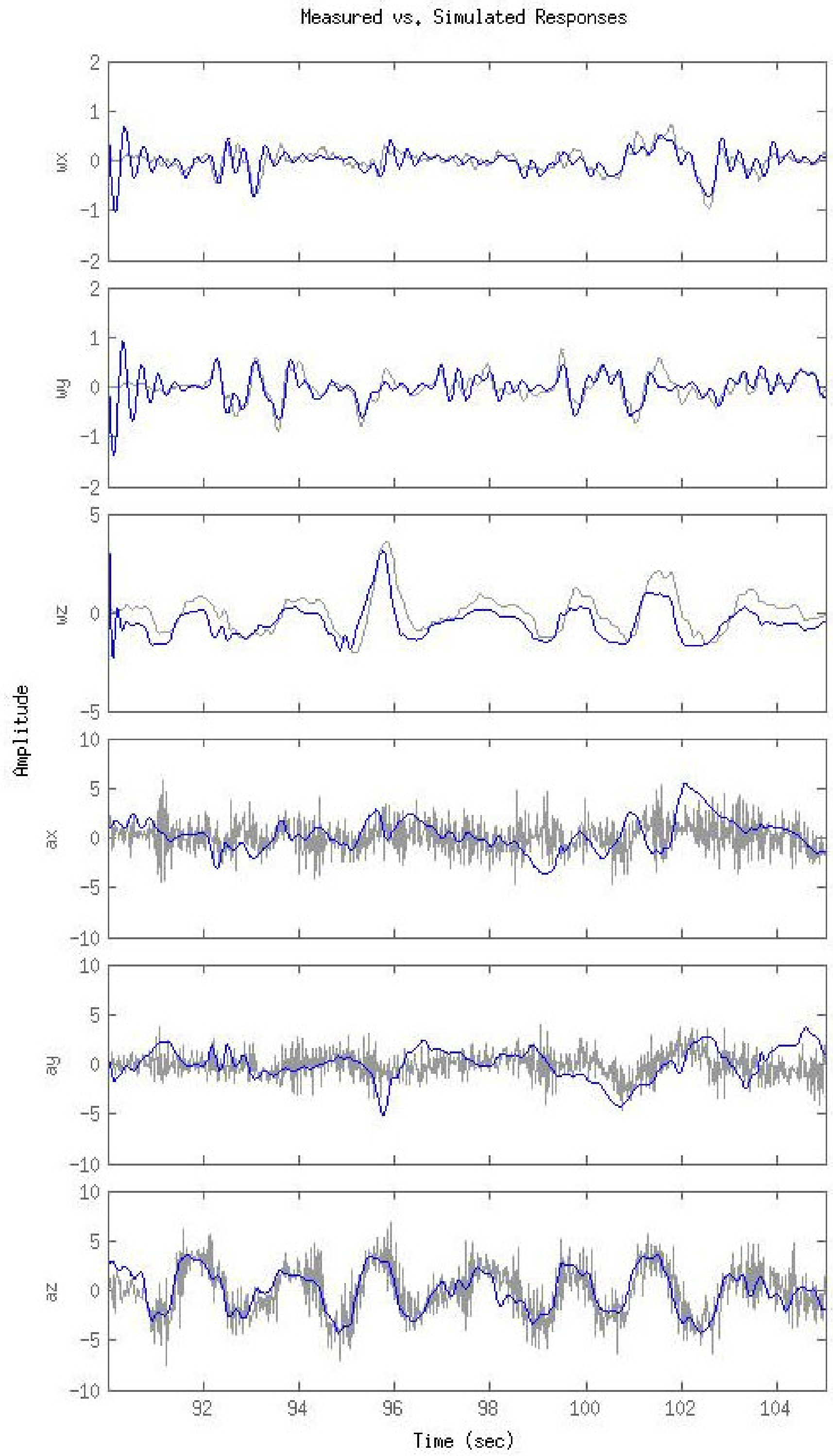

Figure 3.2.8: Simulation (blue) versus measurement (grey) (15s): FLTDATA01. Body angular rates wx, wy, wz represent roll rate, pitch rate and yaw rate in rad/s, respectively; Body linear acceleration ax, ay, az represent acceleration in the x-axis, y-axis and z-axis in m/s^2, respectively

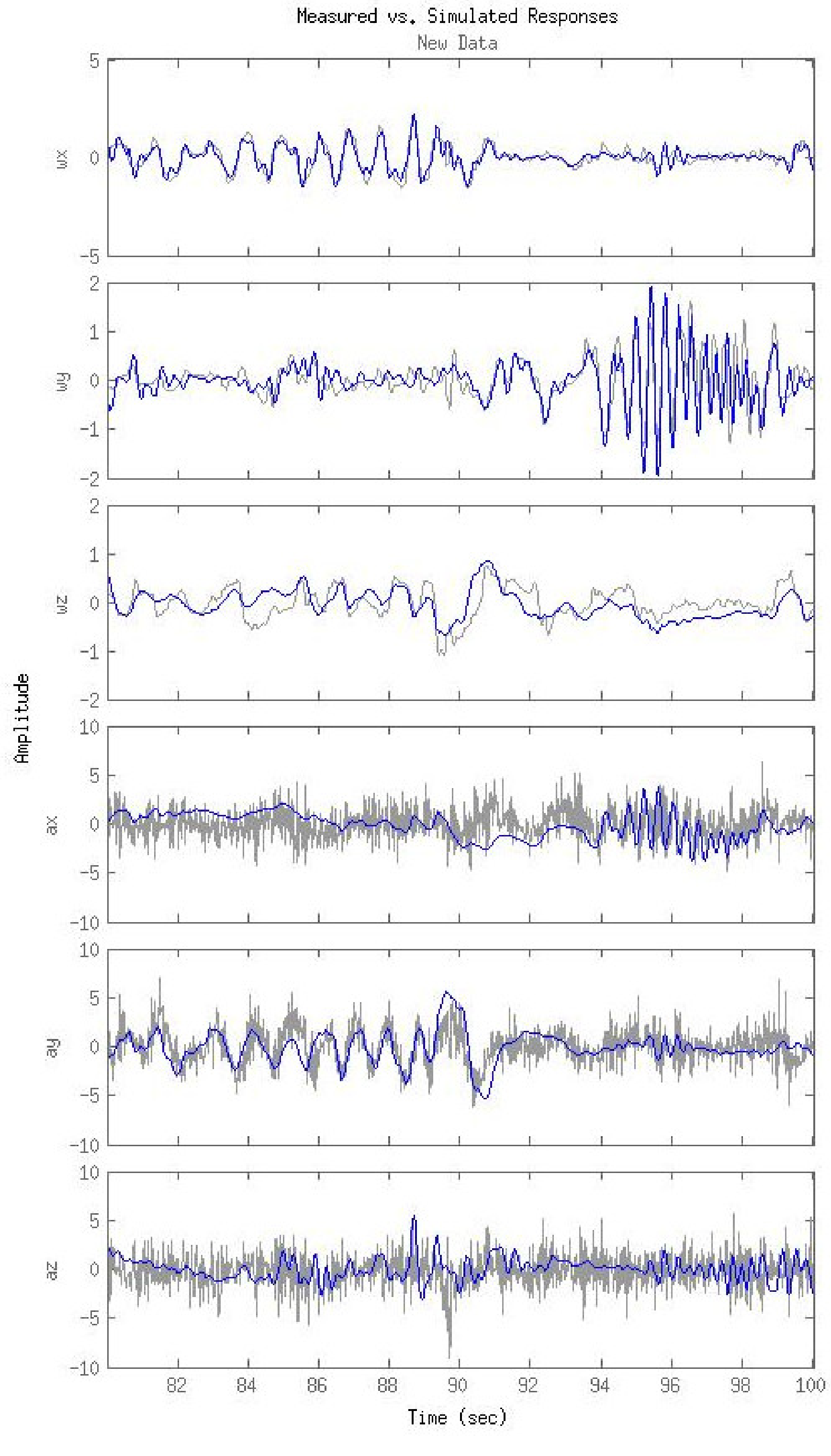

Figure 3.2.9: Simulation (blue) versus measurement (grey) (20s): FLTDATA03 Body angular rates wx, wy, wz represent roll rate, pitch rate and yaw rate in rad/s, respectively; Body linear acceleration ax, ay, az represent acceleration in the x-axis, y-axis and z-axis in m/s^2, respectively

3.3 Helicopter Model Analysis

Due to the complexity of the nonlinear system, linearised models were generated around the hover operating condition to assess resonant modes, the affect of uncertainty, interaction and the equivalence of linear models (to the nonlinear system) near hover condition. The robust controller design methodology chosen was Quantitative Feedback Theory (QFT), which also required a set of uncertain linear time-invariant (LTI) plants. A further justification for using linearised models is because the flight tests that were done, were done with excitation in the hover condition.

3.3.1 Linearised Models

The nonlinear plant was linearised at hover for parameter sets that were obtained from nine different flight tests. To simplify the design process, the helicopter control system was broken-down to subsystems based on the observed control authority. Figure 3.3.1 shows a Bode magnitude plot of the linearised responses from the plant input to body rates and vertical acceleration. It can be seen that there is significant cross-coupling between most channels at the resonant mode frequency around 22 rad/s. A comparison between the magnitude plot in Fig. 3.3.1 and the frequency domain responses in Mettler et al. (1999) confirms that the general behaviour is correct (in terms of resonance, system order), and that there is an increase in bandwidth with scale reduction. A detailed assessment and interpretation of the bandpass region of the open-loop responses (between 1 rad/s to 40 rad/s) of Fig. 3.3.1 is given below.

Heave and yaw responses The yaw-rate is strong coupling to both the rudder input and the main rotor collective input. The heave dynamics are strongly coupled to the main rotor collective. The rudder has an effect on the roll due to the location of the rudder being slightly higher than the center of mass. Pitching response from the rudder is minimal and due mainly to the drag of the blades. The main rotor collective input is the dominant control input for z-axis acceleration. The magnitude response shows that the gain from collective input (from drag torque on main rotor) to yaw-rate is just as large as for the rudder inputs. Due to this strong coupling it was decided to treat the heave/yaw dynamics as a MIMO subsystem (although there is strong cross-coupling, the system is triangular) with collective/rudder inputs.

Roll and pitch responses It is clear from Fig. 3.3.1 that the lateral and longitudinal inputs have the most control authority over the roll-rate and pitch-rate respectively. Also evident, is that actuation in the lateral and longitudinal inputs affects the z-axis acceleration (a deceleration from phase plot not shown). The lateral and longitudinal inputs have negligible effect on the yaw-rate response. Due to the cross-coupling that exists between the lateral/longitudinal inputs to the roll/pitch rates (Padfield 2008), the roll and pitch dynamics was selected as the second MIMO subsystem.

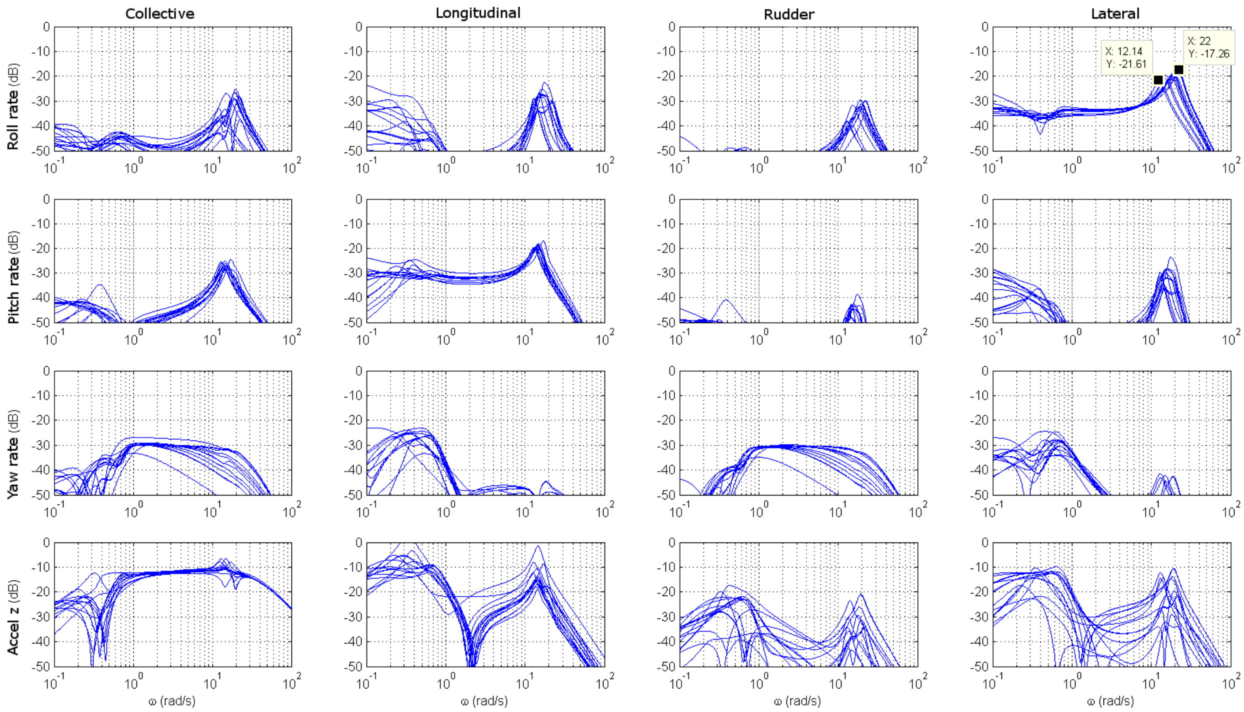

Figure 3.3.1: Bode magnitude plot of the linearised responses for the uncertain helicopter model (attitude rate in rad/s, acceleration in m/s^2, plant inputs defined in Section 3.1.1 as percentage of full-scale range)

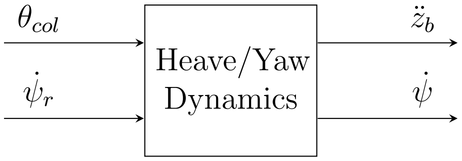

Figure 3.3.2: Heave/yaw subsystem

Linearised heave and yaw dynamics To simplify the control system, the standard RC yaw-rate controller was not disabled. The yaw-rate controller is simply yaw-rate feedback with adjustable gain (the gain was kept fixed throughout testing). For the heave/yaw subsystem, the inputs are the main rotor collective and the *yaw rate* reference (to the rate gyroscope), with the respective outputs being the heave rate and the actual yaw-rate. The uncertain system is shown in Fig. 3.3.4.

Linearised roll and pitch dynamics The lateral and longitudinal signals to the servo subsystem (which is eventually remapped to the rotor head) are used as inputs to the roll/pitch subsystem. Figure 3.3.5 show the bode plot of the lateral/longitudinal inputs to the roll and pitch rate. Dominant response from lateral-to-roll rate and longitudinal-to-pitch rate is as expected. There is coupling between the channels at the resonant frequencies. The

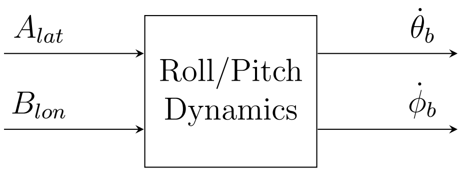

Figure 3.3.3: Roll/pitch subsystem

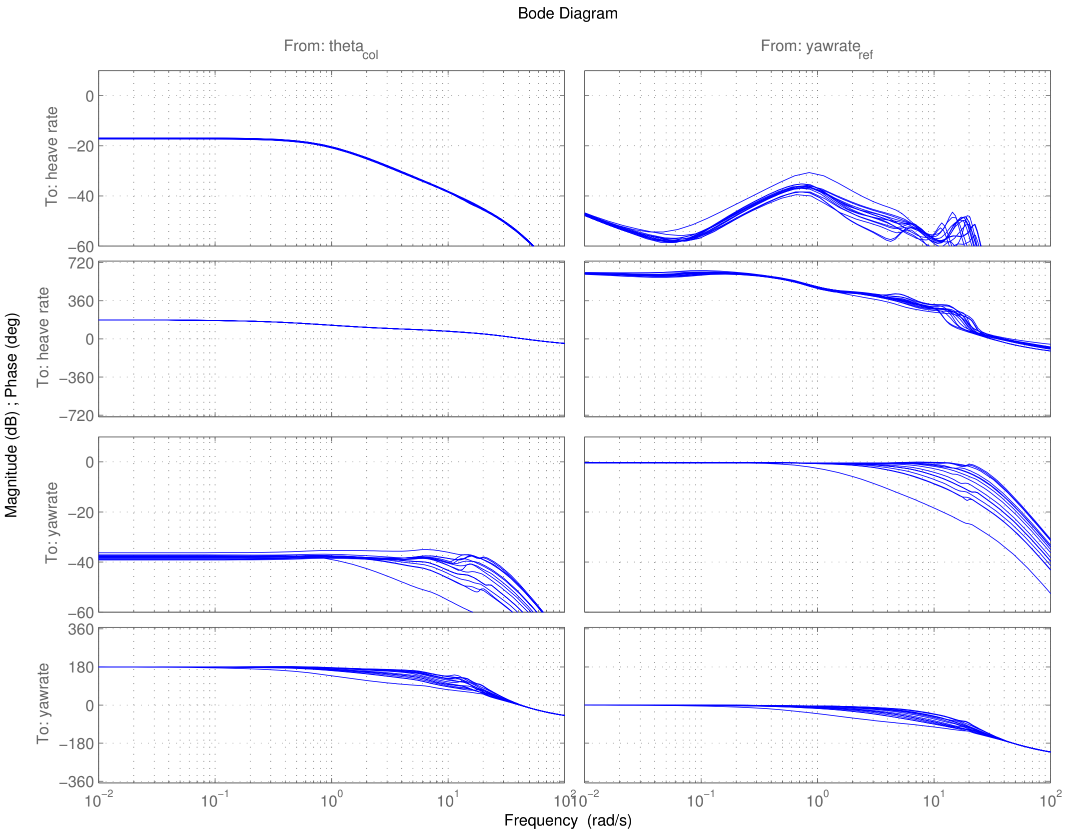

Figure 3.3.4: Bode plot of collective and yaw rate inputs to the heave rate and yaw rate

higher resonant mode frequency is between 12 rad/s - 25 rad/s. The lower resonant mode frequency is at about 0.25 rad/s. The higher resonant frequency is accordance with what is described in Mettler et al. (1999) for small helicopters; this is due to the flapping of the main rotor blades. The lower frequency resonant mode was not expected as details on the lower frequency behaviour has not been found in the literature. At first it was believed that the lower frequency mode was an artefact of linearisation, but during closed-loop tests the lower frequency resonant mode was clearly evident.

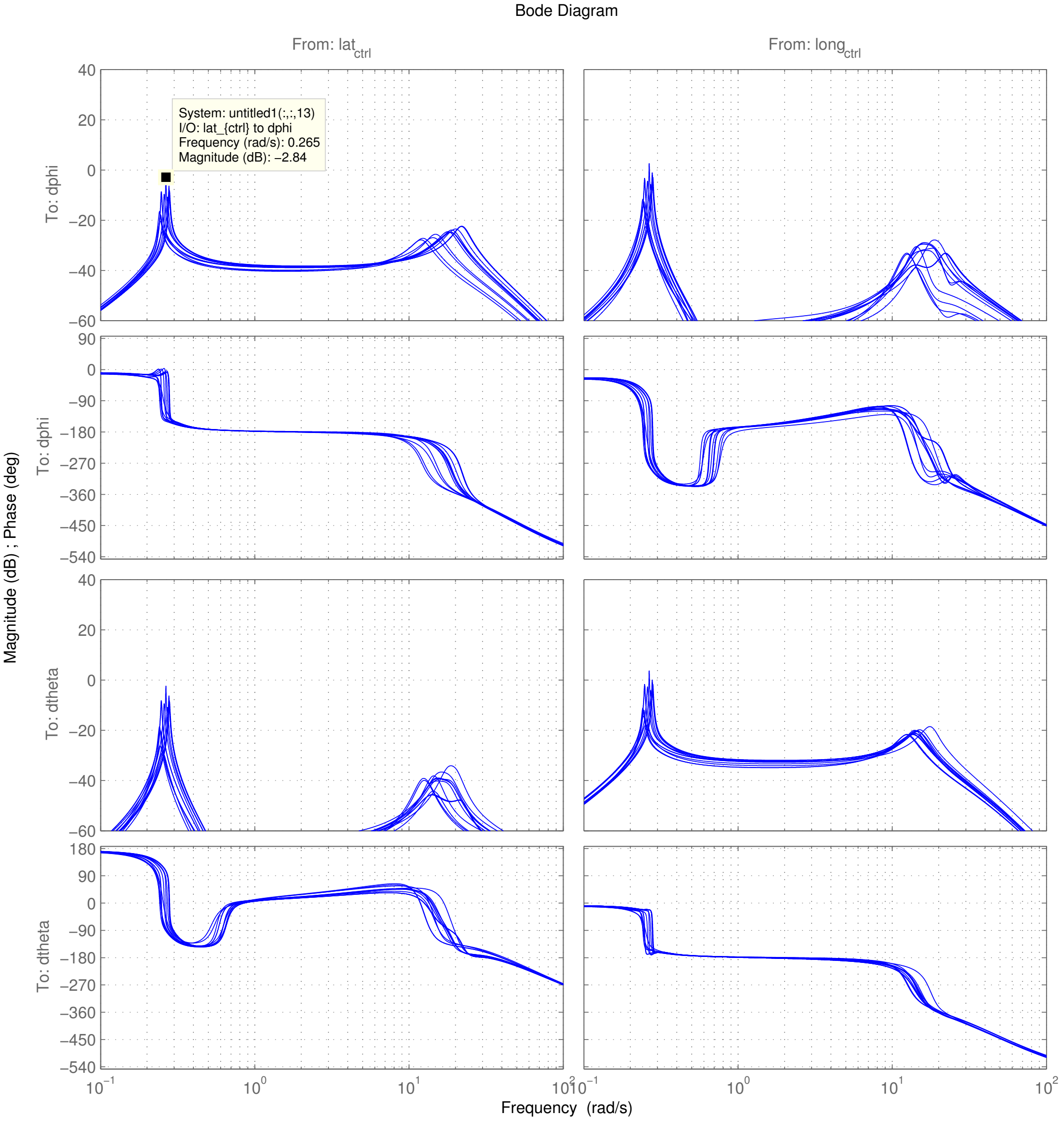

Figure 3.3.5: Bode plot of lateral and longitudinal inputs to the roll rate and pitch rate

3.3.2 Modal Analysis

The physical cause of the lower frequency mode was unclear. In order to determine the underlying cause, modal analysis was used. Modal analysis is mostly used by structural and power system engineers to investigate poorly damped resonant modes commonly encountered in their field. From a dynamic system perspective, it is used to determine the (energy) contribution to a (resonant) mode by particular state variables - thus also referred to as participation factor analysis (Garofalo et al. 2002). Given an autonomous linear time-invariant system,

$$\dot{\vec{\boldsymbol{x}}}(t) = \boldsymbol{A}\vec{\boldsymbol{x}}(t) \tag{3.3.1}$$

where $\vec{\boldsymbol{x}} \in \mathbb{R}^n$ and $\boldsymbol{A} \in \mathbb{R}^{n \times n}$ with n distinct eigenvectors, the participation matrix is (Kundur et al. 1994):

$$\boldsymbol{P} = [\vec{\boldsymbol{p}}_1 \, \vec{\boldsymbol{p}}_2 \, \ldots \, \vec{\boldsymbol{p}}_n] \tag{3.3.2}$$

with

$$\vec{\boldsymbol{p}}_i = \begin{bmatrix} p_{1i} \\ p_{2i} \\ \vdots \\ p_{ni} \end{bmatrix} = \begin{bmatrix} \phi_{1i}\psi_{i1} \\ \phi_{2i}\psi_{i2} \\ \vdots \\ \phi_{ni}\psi_{in} \end{bmatrix} \tag{3.3.3}$$

where

ϕ_{ki} = kth entry of right eigenvector $\vec{\boldsymbol{\phi}}_i$ of $\boldsymbol{A}$

ψ_{ki} = kth entry of left eigenvector $\vec{\boldsymbol{\psi}}_i$ of $\boldsymbol{A}$

The participation factor $p_{ki} = \phi_{ki}\psi_{ik}$ is a measure of the relative participation of the kth state variable in the ith mode.

The transition matrix of the subsystem plotted in Fig. 3.3.5 was analysed to determine which state variables contributed to the low frequency resonant mode (0.25 rad/s). The participation factor for the low frequency resonant mode versus the state variables is shown in Fig. 3.3.6-the extra states were added to slow down very fast dynamics (and algebraic loops).

The participation factor assessment shows that there are six states that strongly contribute to the low frequency resonant mode. The first two states that contribute to the mode are the second and third element of the quaternion (attitude). The last two states that contribute equally to the mode energy are the body linear velocities in the x and y directions. To a much lesser effect, the lateral and longitudinal flapping of the *stabiliser bar* also contributes to the low frequency resonant mode. In nominal attitude, the quaternion elements referred to above, are coupled to roll and pitch rotations. The overall participation factor analysis suggest that the low frequency resonant mode is due to coupling of the lateral movement to the stabiliser bar which induces the observed low frequency resonant mode. This mode is reflected as “interaction” in interaction index shown Fig. 5.1.2. The interaction is at a low enough frequency that the roll and pitch controllers can attenuate the effect of the mode (as may be inferred from sensitivity plots Fig. E.2.1 and Fig. E.2.2). This low frequency mode is unlike the common aircraft dynamic modes (phugoid, dutch roll mode, spiralling). It manifest its self in as a simultaneous roll and pitch with a period of around 25 s.

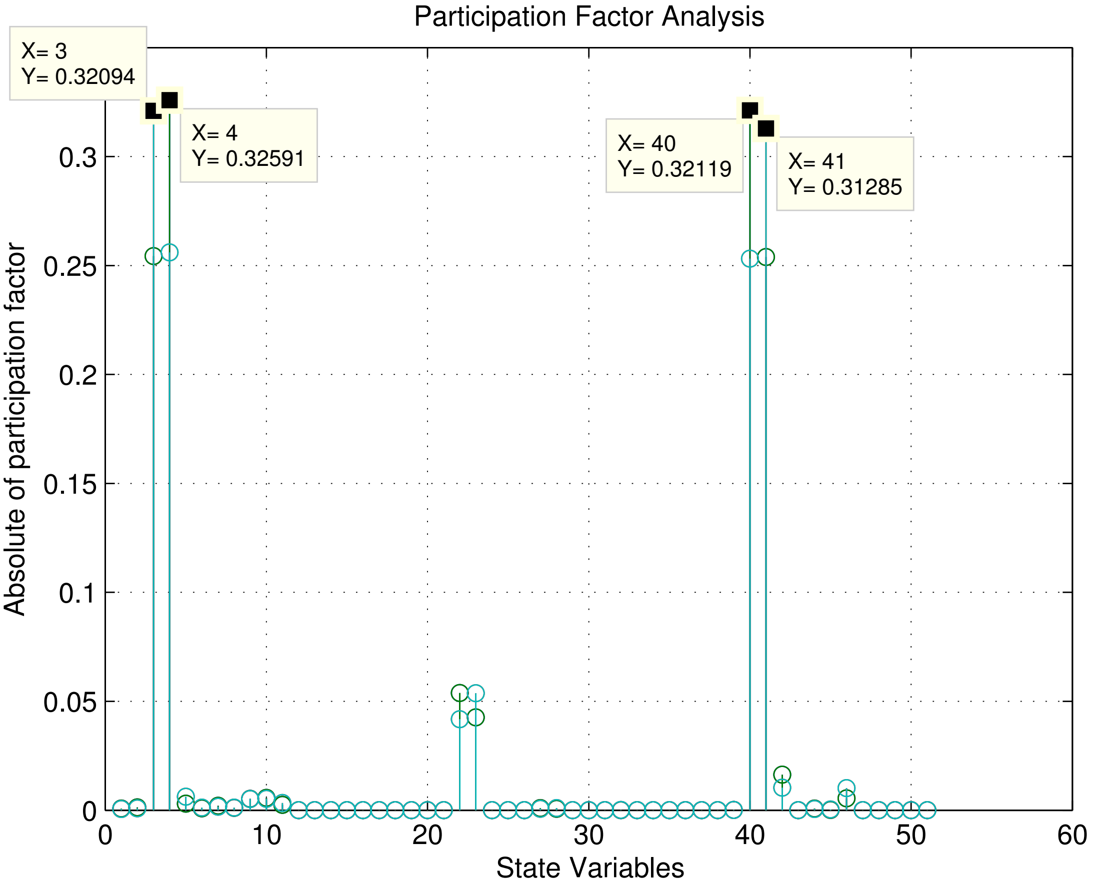

Figure 3.3.6: Magnitude of participation factors that contribute to the resonant mode 0.25 rad/s

3.4 Twin-Helicopter Slung Load System Model

This section describes the mathematical modelling of the twin-helicopter system incorporating the load. The twin-helicopter system consists of two 6 degree-of-freedom helicopter models that are tethered to each other via a load. Unlike Bisgaard et al. (2009) and Bernard & Kondak (2009), the attitude control of the load in this project is of importance, so the load is modelled as a six degree-of-freedom body as well. The forces and torques act as external inputs to the helicopter model from the common load; this is the main source of interaction of the twin-helicopter slung load transportation system. By using a realistic load such as a crate with particular attachment points makes the interaction problem more practical (and hence difficult). A rendering of the twin-helicopter slung load transportation system is shown in Fig. 3.4.1.

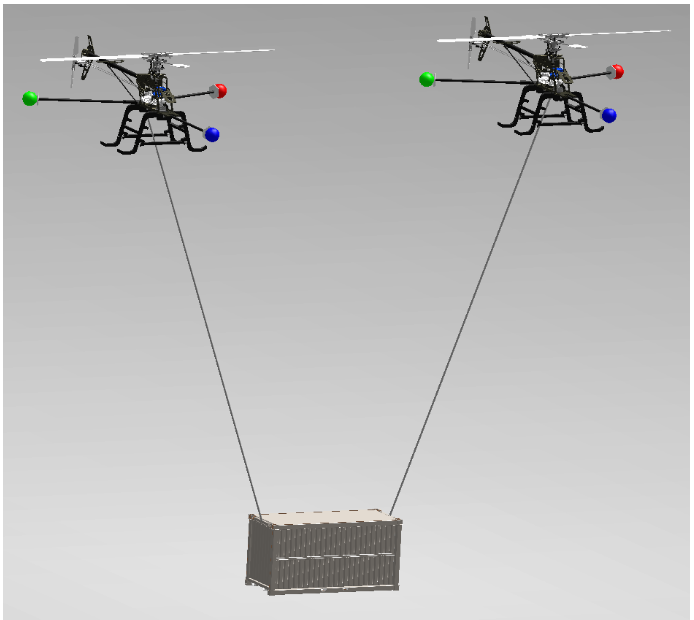

Figure 3.4.1: Rendering of twin-helicopter slung load system

Due to the complexity of the individual helicopter models, it was desired to retain the helicopter model as a separate entity that interacts with other modules. The most common way observed in the literature to model multi-body systems is the Newton-Euler approach. When the number of bodies become large, the trend is to use the principle of virtual work and Lagrange multiplers (Goldstein 1965). The Udwadia and Kalaba equation was used in Bisgaard et al. (2009) to obtain the dynamic equations for different configurations of helicopters attached to the load.

Solving for the constraint forces by assuming an inelastic interconnection (holonomic constraint) is difficult given three 6 degree-of-freedom bodies. The author's supervisor suggested a simpler and physically plausible approach to account for the helicopter-load interaction.

The suggestion was to decouple the interconnecting systems using a spring-dashpot subsystem. This approach is better because it is a closer representation of the interconnecting dynamics (as opposed to being completely rigid). The solution to the rigid interconnection may be approached progressively by increasing the stiffness of the spring-dashpot system; the greater the "stiffness" of the coupling, the greater the simulation trouble.

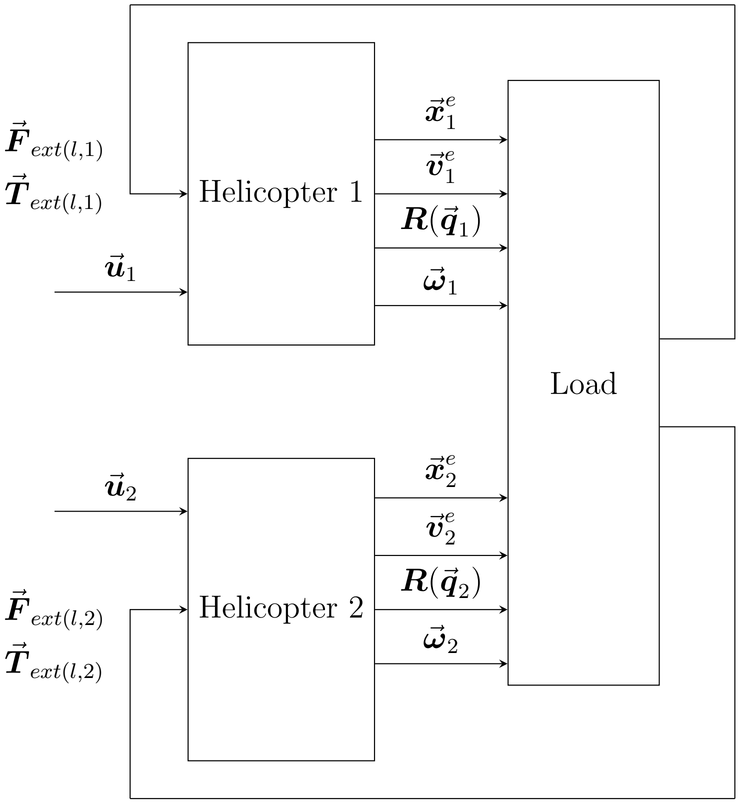

Figure 3.4.2: Functional block diagram of the twin-helicopter slung load system including the load connection

Figure 3.4.2 shows the functional block diagram of the interaction between the helicopters and the load. The helicopter blocks have pilot commands as inputs ($\vec{\boldsymbol{u}}_i$). The forces and torques due to the load are denoted as $\vec{\boldsymbol{F}}_{ext(l,i)}$ and $\vec{\boldsymbol{T}}_{ext(l,i)}$ for $i = 1, 2$. The load block receives the position, velocity, Direction Cosine Matrix (DCM) and the angular body rates of each helicopter as inputs and generates the external forces and torques that exist on each helicopter.

By using the above approach to solve the multi-body problem, a modelling solution is attained through feedback. The tension is solved in the direction of the cable by modelling the cable as a spring-dashpot system. Summing the forces acting on the cable,

$$\sum \vec{F} = -k\Delta\vec{r} - b\Delta\dot{\vec{r}} \tag{3.4.1}$$

where $\Delta\vec{r}$ is the relative deviation in displacement from the natural cable length. The spring constant is k, and mechanical damping is b. The tension in the cable is given by (3.4.1) assuming negligible cable mass and aerodynamic forces on the cable. By using the decoupling approach above, the load is abstracted as a separate kinematic system with force and torque signals that interface with the rest of the model. The default configuration for the attachment of the load to the cable from the helicopters is shown in Fig. 3.4.4. This configuration gives the twin-helicopter system the ability of controlling both the translation and attitude of the load, although, to a more limited extent the latter. The attachment configuration gives greater controllability in the roll and yaw channel of the load than the pitch channel. Controllability of the load pitch is a function of the displacement from the center of mass of the load to the attachment in the z-axis (no torque is developed when the attachment is in line with the center of mass in the z-axis). The six degree-of-freedom kinematic equations for the load are,

$$\dot{\vec{\boldsymbol{v}}}_l^b = \frac{1}{M_l}\left(\vec{\boldsymbol{F}}_{l,g}^b + \vec{\boldsymbol{F}}_{l,c1}^b + \vec{\boldsymbol{F}}_{l,c2}^b + \vec{\boldsymbol{F}}_{drag}^b\right) - \left(\vec{\boldsymbol{\omega}}_l^b \times \vec{\boldsymbol{v}}_l^b\right) \tag{3.4.2}$$

$$\dot{\vec{\boldsymbol{\omega}}}_l^b = \boldsymbol{I}_l^{b^{-1}}\left(\vec{\boldsymbol{T}}_{l,c1}^b + \vec{\boldsymbol{T}}_{l,c2}^b - \left(\vec{\boldsymbol{\omega}}_l^b \times \boldsymbol{I}_l^b \vec{\boldsymbol{\omega}}_l^b\right)\right) \tag{3.4.3}$$

The torque as a result of the force from helicopter i not acting about the center of mass of the load is given by,

$$\vec{\boldsymbol{T}}_{l,ci}^b = \vec{\boldsymbol{r}}_{l,i}^b \times \vec{\boldsymbol{F}}_{l,ci}^b \tag{3.4.4}$$

The position of the attachment point with respect to the center of mass of the load is $\vec{\boldsymbol{r}}_{l,i}^b$. The attachment points are $\vec{\boldsymbol{r}}_{l,1}^b = [0, l/2, -h/2]^T$ for helicopter 1 and $\vec{\boldsymbol{r}}_{l,2}^b = [0, -l/2, -h/2]^T$ for helicopter 2. A damping effect on the swing of the load results from the aerodynamic drag given by,

$$\vec{\boldsymbol{F}}_{drag}^b = \frac{1}{2}\rho C_d^l A \left(\vec{\boldsymbol{v}}_l^b\right)^2 \tag{3.4.5}$$

where ρ is the air density, C_d^l is the coefficient of drag for the load and A is the surface area in the direction of the velocity. The load geometry was chosen to be symmetric, so that the center of pressure (for the drag force) acts close enough to the center of mass resulting in negligible torque due to drag. The load is modelled as a rectangular prism with the following mass moment of inertia (Srinivasulu & Vaidyanathan 1976),

$$\boldsymbol{I}_l = \begin{bmatrix} \frac{M_l}{12}(h^2 + l^2) & 0 & 0 \\ 0 & \frac{M_l}{12}(w^2 + h^2) & 0 \\ 0 & 0 & \frac{M_l}{12}(w^2 + l^2) \end{bmatrix} \tag{3.4.6}$$

The parameters chosen for the twin-helicopter slung load configuration is given in Table 3.4.1. The nominal load mass was chosen to be 50 % of an individual helicopter mass, with an uncertainty of 70 %.

The attachment point on the helicopter is z_a below the center of mass, $\vec{\boldsymbol{r}}_h^b = [0, 0, 0.1]^T$. To calculate the tension in the cable, the attachment positions are transformed to the inertial

Parameter	Definition	
l	Width of the load	2 m
h	Height of the load	0.1 m
w	Depth of the load	0.1 m
z_a	Length from helicopter center of mass to attachment point	0.1 m
M_l	Mass of the load	0.120 ±70% kg

Table 3.4.1: Twin-helicopter slung load configuration parameters

frame of reference. The position of the helicopter attachment in the inertial frame is given by,

$$\vec{\boldsymbol{r}}^e_{h,a} = \vec{\boldsymbol{x}}^e_h + \boldsymbol{R}^{eb}_h \vec{\boldsymbol{r}}^b_h \tag{3.4.7}$$

where $\boldsymbol{R}^{eb}_h$ is the rotation matrix from helicopter body to the inertial frame of reference. Similarly, the position of the load attachment in the inertial frame is given by,

$$\vec{\boldsymbol{r}}^e_{l,a} = \vec{\boldsymbol{x}}^e_l + \boldsymbol{R}^{eb}_l \vec{\boldsymbol{r}}^b_l \tag{3.4.8}$$

where $\boldsymbol{R}^{eb}_l$ is the rotation matrix from the load body to the inertial frame of reference. The velocity of the helicopter attachment in the inertial frame is given by,

$$\vec{\boldsymbol{v}}^e_{h,a} = \vec{\boldsymbol{v}}^e_h + \boldsymbol{R}^{eb}_h \left(\vec{\boldsymbol{\omega}}^b_h \times \vec{\boldsymbol{r}}^b_h\right) \tag{3.4.9}$$

where $\vec{\boldsymbol{\omega}}^b_h$ is the angular rotation vector of the helicopter referenced to the body frame. Similarly, the velocity of the load attachment in the inertial frame is given by,

$$\vec{\boldsymbol{v}}^e_{l,a} = \vec{\boldsymbol{v}}^e_l + \boldsymbol{R}^{eb}_l \left(\vec{\boldsymbol{\omega}}^b_l \times \vec{\boldsymbol{r}}^b_l\right) \tag{3.4.10}$$

where $\vec{\boldsymbol{\omega}}^b_l$ is the angular rotation vector of the load referenced to the body frame.
The length of the cable is given by,

$$l = \|\vec{\boldsymbol{x}}^e_h - \vec{\boldsymbol{x}}^e_l\| \tag{3.4.11}$$

The time derivative of the cable length using dot product notation is,

$$\frac{dl}{dt} = \frac{(\vec{\boldsymbol{v}}^e_h - \vec{\boldsymbol{v}}^e_l) \cdot (\vec{\boldsymbol{x}}^e_h - \vec{\boldsymbol{x}}^e_l)}{\|\vec{\boldsymbol{x}}^e_h - \vec{\boldsymbol{x}}^e_l\|} \tag{3.4.12}$$

The magnitude of the tension can then be computed by adding the effect of the spring and damper system as,

$$|T| = \begin{cases} b \cdot \frac{dl}{dt} + k \cdot (l - l_0) & l > l_0 \\ 0 & l \leq l_0 \end{cases} \tag{3.4.13}$$

where b, k is as defined previously, and l_0 is the natural length of the cable (when $T = 0$). It is assumed that there is no compression of the cable. Converting the tension to a vector in the body frame,

$$\vec{\boldsymbol{F}}_t^b = \pm\,|T| \left(\boldsymbol{R}_l^{eb}\right)^T \frac{\vec{\boldsymbol{x}}_h^e - \vec{\boldsymbol{x}}_l^e}{\|\vec{\boldsymbol{x}}_h^e - \vec{\boldsymbol{x}}_l^e\|} \tag{3.4.14}$$

Finally, the applied torque can then be calculated given the tension and the displacement from the center of mass as,

$$\vec{\boldsymbol{T}}_t^b = \vec{\boldsymbol{r}}_l^b \times \vec{\boldsymbol{F}}_t^b \tag{3.4.15}$$

Summary of the Equations of Motion for the Twin-helicopter Load Lift System
The equations defining the helicopter kinematics for $i = 1, 2$,

$$M_{h,i}\dot{\vec{\boldsymbol{v}}}_h^{b,i} = \vec{\boldsymbol{F}}_{h,h}^{b,i} + \vec{\boldsymbol{F}}_{h,g}^{b,i} + \vec{\boldsymbol{F}}_{h,c}^{b,i} - \left(M_{h,i}\vec{\boldsymbol{v}}_h^{b,i} \times \vec{\boldsymbol{\omega}}_h^{b,i}\right) \tag{3.4.16}$$

$$\boldsymbol{I}_{h,i}\dot{\vec{\boldsymbol{\omega}}}_h^{b,i} = \vec{\boldsymbol{T}}_{h,h}^{b,i} + \vec{\boldsymbol{T}}_{h,c}^{b,i} - \left(\vec{\boldsymbol{\omega}}_h^{b,i} \times \boldsymbol{I}_{h,i}\vec{\boldsymbol{\omega}}_h^{b,i}\right) \tag{3.4.17}$$

$$\dot{\vec{\boldsymbol{q}}}_h^i = \frac{1}{2}\,\vec{\boldsymbol{q}}_h^i \otimes \begin{bmatrix} 0 \\ \vec{\boldsymbol{\omega}}_h^{b,i} \end{bmatrix} \tag{3.4.18}$$

$$\vec{\boldsymbol{v}}_h^{e,i} = \vec{\boldsymbol{q}}_h^i \otimes \begin{bmatrix} 0 \\ \vec{\boldsymbol{v}}_h^{b,i} \end{bmatrix} \otimes \vec{\boldsymbol{q}}_h^{*i} \tag{3.4.19}$$

$$\vec{\boldsymbol{x}}_h^{e,i} = \int_0^\infty \vec{\boldsymbol{v}}_l^{e,i}\; dt \tag{3.4.20}$$

where the symbol definitions are as follows,

$M_{h,i}$	Mass of helicopter i (kg)
$\vec{\boldsymbol{v}}_h^{b,i}$	Velocity of helicopter i in the body frame of helicopter i (m/s)
$\vec{\boldsymbol{v}}_h^{e,i}$	Velocity of helicopter i in the inertial frame (m/s)
$\vec{\boldsymbol{x}}_h^{e,i}$	Position of helicopter i in the inertial frame (m)
$\vec{\boldsymbol{F}}_{h,h}^{b,i}$	Force in the body frame of helicopter i due to the main and tail rotor (N)
$\vec{\boldsymbol{F}}_{h,g}^{b,i}$	Force in the body frame of helicopter i due to gravity (N)
$\vec{\boldsymbol{F}}_{h,c}^{b,i}$	Force in the body frame of helicopter i due to the cable - load attachment (N)
$\vec{\boldsymbol{T}}_{h,h}^{b,i}$	Torque in the body frame of helicopter i due to the main and tail rotor (N m)
$\vec{\boldsymbol{T}}_{h,c}^{b,i}$	Torque in the body frame of helicopter i due to the cable - load attachment (N m)
$\vec{\boldsymbol{\omega}}_h^{b,i}$	Angular rate of helicopter i measured in the body frame (rad/s)
$\vec{\boldsymbol{q}}_h^i$	Quaternion representing the rotation from inertial to body frame for helicopter i

In the above equations, the quaternion conjugate of $\vec{\boldsymbol{q}}$ is denoted by $\vec{\boldsymbol{q}}^*$, and $\otimes$ represents the quaternion product (definition in Section 4.3). Similar to the kinematic equations above, the load kinematics are defined by,

$$M_l \dot{\vec{\boldsymbol{v}}}_l^b = \vec{\boldsymbol{F}}_{l,c1}^b + \vec{\boldsymbol{F}}_{l,c2}^b + \vec{\boldsymbol{F}}_{l,g}^b - \left(M_l \vec{\boldsymbol{v}}_l^b \times \vec{\boldsymbol{\omega}}_l^b \right) \tag{3.4.21}$$

$$\boldsymbol{I}_l \dot{\vec{\boldsymbol{\omega}}}_l^b = \vec{\boldsymbol{T}}_{l,c1}^b + \vec{\boldsymbol{T}}_{l,c2}^b - \left(\vec{\boldsymbol{\omega}}_l^b \times \boldsymbol{I}_l \vec{\boldsymbol{\omega}}_l^b \right) \tag{3.4.22}$$

$$\dot{\vec{\boldsymbol{q}}}_l = \frac{1}{2}\, \vec{\boldsymbol{q}}_l \otimes \begin{bmatrix} 0 \\ \vec{\boldsymbol{\omega}}_l^b \end{bmatrix} \tag{3.4.23}$$

$$\vec{\boldsymbol{v}}_l^e = \vec{\boldsymbol{q}}_l \otimes \begin{bmatrix} 0 \\ \vec{\boldsymbol{v}}_l^b \end{bmatrix} \otimes \vec{\boldsymbol{q}}_l^* \tag{3.4.24}$$

$$\vec{\boldsymbol{x}}_l^e = \int_0^\infty \vec{\boldsymbol{v}}_l^e \; dt \tag{3.4.25}$$

where,

M_l	Mass of load (kg)
$\vec{\boldsymbol{v}}_l^b$	Velocity of the load in the body frame (m/s)
$\vec{\boldsymbol{v}}_l^e$	Velocity of the load in the inertial frame (m/s)
$\vec{\boldsymbol{x}}_l^e$	Position of the load in the inertial frame (m)
$\vec{\boldsymbol{F}}_{l,ci}^b$	Force in the body frame of the load due to the cable attachment between helicopter i and load (N)
$\vec{\boldsymbol{F}}_{l,g}^b$	Force of gravity in the body frame of load (N)
$\vec{\boldsymbol{T}}_{l,ci}^b$	Torque in the body frame of load due to helicopter i cable - load attachment (N m)
$\vec{\boldsymbol{\omega}}_l^b$	Angular rate of load measured in the body frame (rad/s)
$\vec{\boldsymbol{q}}_l$	Quaternion representing the rotation from inertial to body frame for the load

The cable forces and torques are resolved using (3.4.19), (3.4.20), (3.4.24) and (3.4.25) in the tension computation of the spring-damper model (3.4.26). This is done in the inertial frame and then transformed to the respective body frame.

$$\vec{\boldsymbol{F}}_{l,ci}^e = \begin{cases} -\left[b\frac{(\vec{\boldsymbol{v}}_h^{e,i} - \vec{\boldsymbol{v}}_l^e)\cdot(\vec{\boldsymbol{x}}_h^{e,i} - \vec{\boldsymbol{x}}_l^e)}{\|\vec{\boldsymbol{x}}_h^{e,i} - \vec{\boldsymbol{x}}_l^e\|} + k\left(\|\vec{\boldsymbol{x}}_h^{e,i} - \vec{\boldsymbol{x}}_l^e\| - l_0 \right) \right] \frac{\vec{\boldsymbol{x}}_h^{e,i} - \vec{\boldsymbol{x}}_l^e}{\|\vec{\boldsymbol{x}}_h^{e,i} - \vec{\boldsymbol{x}}_l^e\|} & \|\vec{\boldsymbol{x}}_h^{e,i} - \vec{\boldsymbol{x}}_l^e\| > l_0 \\ \vec{\boldsymbol{0}} & \|\vec{\boldsymbol{x}}_h^{e,i} - \vec{\boldsymbol{x}}_l^e\| \le l_0 \end{cases} \tag{3.4.26}$$

The force on the load in the body frame of the load is given by,

$$\vec{\boldsymbol{F}}_{l,ci}^b = \vec{\boldsymbol{q}}_l^* \otimes \begin{bmatrix} 0 \\ \vec{\boldsymbol{F}}_{l,ci}^e \end{bmatrix} \otimes \vec{\boldsymbol{q}}_l \tag{3.4.27}$$

The force on the helicopter in the body frame of the helicopter is given by,

$$\vec{\boldsymbol{F}}_{h,c}^{b,i} = \vec{\boldsymbol{q}}_h^{*i} \otimes \begin{bmatrix} 0 \\ -\vec{\boldsymbol{F}}_{l,ci}^{e} \end{bmatrix} \otimes \vec{\boldsymbol{q}}_h^{i} \tag{3.4.28}$$

A simulation study of the twin-helicopter slung load system was undertaken to verify the modelling. The controllers for the individual helicopters were implemented as designed in Section 5.1 and tethered to the load *without* coordinated control. Figure 3.4.5 shows an animation of the twin-helicopter lift system carrying a load of a width of one meter.

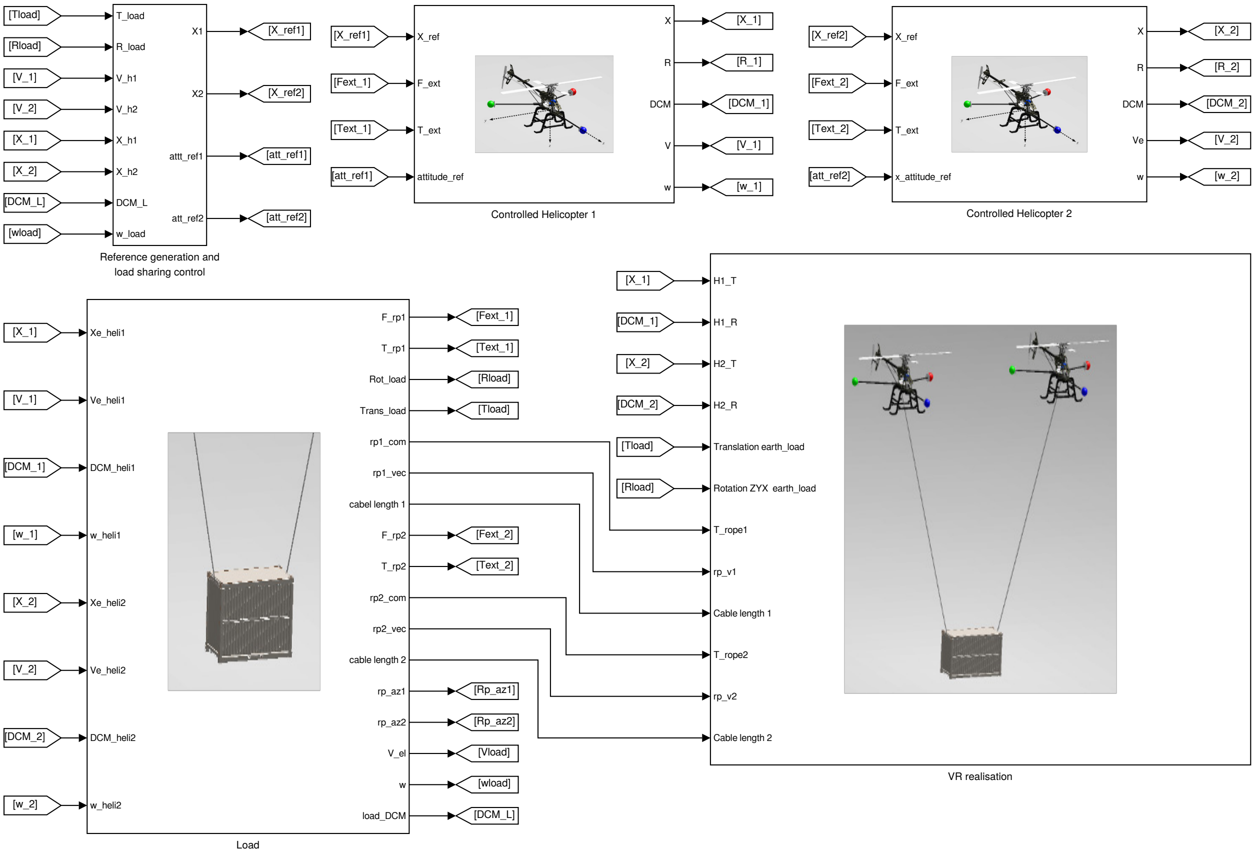

Figure 3.4.3: High-level Simulink model of the twin-helicopter lift system. Labels: In "Reference generation and load sharing control" block - Tload: load position (m) in inertial frame, Rload: ZYX sequence Euler angles (rad) of the load, V_[1/2]: velocity (m/s) of helicopter [1/2] in inertial frame, X_[1/2]: position (m) of helicopter [1/2] in inertial frame, DCM_L: Direction Cosine Matrix of load from inertial to body frame, wload: load angular velocity (rad/s) in body frame, X_ref[1/2]: Helicopter [1/2] reference position (m) in inertial frame (only used for "independent control" mode), att_ref[1/2]: roll, pitch and yaw Euler angle (rad) references for helicopter [1/2] using ZYX sequence (used in "coordinated control" mode). "Controlled Helicopter [1/2]" - R_[1/2]: roll, pitch and yaw Euler angles (rad) in ZYX sequence for helicopter [1/2], DCM[1/2]: DCM from inertial to body frame for helicopter [1/2], w_[1/2]: helicopter [1/2] body rates (rad/s) in the body frame, Fext_[1/2]: external force (N) on helicopter [1/2] in the inertial frame, Text_[1/2]: external torque (N m) on helicopter [1/2] in the inertial frame. "Load" - Vload: Velocity (m/s) of the load in inertial frame, rp[1/2]_com: cable [1/2] center of mass position (m) in inertial frame, rp[1/2]_vec: cable [1/2] position (m) vector, cable length [1/2]: cable [1/2] length (m), Rp_az[1/2]: cable [1/2] change in length (m/s).

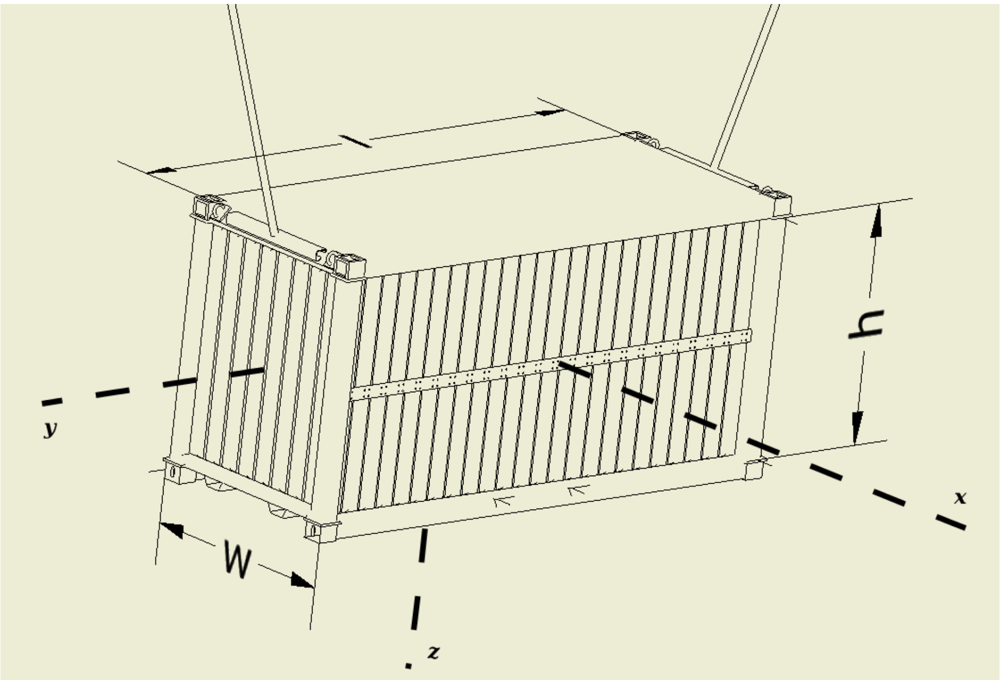

Figure 3.4.4: Representation of the load showing the dimensions and the cable attachment locations

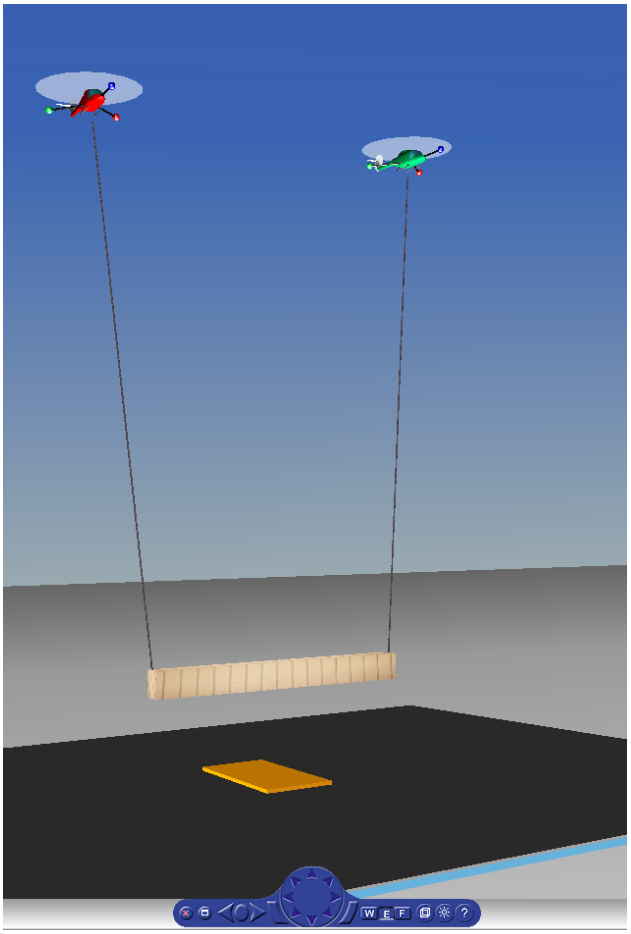

Figure 3.4.5: Simulink VRML engine output showing simulation output of the twin-helicopter slung load system (see `https://youtu.be/kzLWpIqW9lA` - independent control)

3.5 Twin-Helicopter Slung Load System Model Analysis

In order to determine a strategy for controlling the twin-helicopter system, a set of linearised plants was required in the nominal configuration. Using the stabilising controller for the individual helicopters (*see* Section 5.1), the system was forced into the nominal hover condition carrying the load. The resulting states in the nominal condition was then used to generate linearised models of the twin-helicopter system. The chosen input for analysis was the helicopter roll and pitch attitude and the helicopter altitude. The chosen output of interest was the load translation, roll, yaw and the separation distance δ, between the helicopters. The separation distance is a useful quantity to regulate because it can be used to prevent the helicopters from getting too close to each other. The rotor wake interaction may significantly affect the performance of each helicopter if they get too close (for example, in the case of a high load roll angle requirement). Also, the farther away from keeping the cable vertical, the greater the steady-state helicopter attitude that is required which will affect the comfort of the pilot and passengers. The separation distance is defined to be the displacement between the two helicopters projected onto the xy-plane,

$$\delta = \left\| \begin{bmatrix} x^e_{h1} \\ y^e_{h1} \end{bmatrix} - \begin{bmatrix} x^e_{h2} \\ y^e_{h2} \end{bmatrix} \right\| \tag{3.5.1}$$

The fixed cable length allows for the helicopter to move along an arc and still maintain the load translation and attitude, this is illustrated in Fig. 3.5.2. Although the relative position of the helicopters are controllable along a 3D arc, the yaw attitude of the load is limited to small angles. The reason for the limitation is because the linearised set of plants lose validity as the yaw angle increases. This does not pose a limitation in the ability to manoeuvre the load though. A change in the load yaw angle in the inertial frame can still be accommodated by yawing the individual helicopters and maintaining zero relative yaw between the load and helicopters, as depicted in Fig. 3.5.3. By using this approach the linearised models are still valid.

The purpose of the section is to make sense of the resonant modes visible in the linearised response. In this way, insight is gained on the understanding of the plant dynamics which will help in the frequency domain design approach later. The magnitude response of the nominal plant (using load parameters from Table 3.4.1) is shown in Fig. 3.5.4. It is well known that the resonant frequency of a simple pendulum is given by,

$$\omega_p = \sqrt{g/L} \tag{3.5.2}$$

where $g = 9.81\,\mathrm{m\,s^{-2}}$ is the gravitational acceleration on earth and L is the length of the cable between the center of mass and the pivot point. Using the nominal length of 2 m, results in an expected resonant mode of 2.2 rad/s for a *simple pendulum.* Fig. 3.5.4 shows a resonant mode around 2.3 rad/s. This mode is believed to be due to the pendulous nature of the system and is found to be coupled to all channels. Because this mode is most strongly related to the length of the cable, it is not expected to shift significantly given plant uncertainty unless the length of the cable changes.

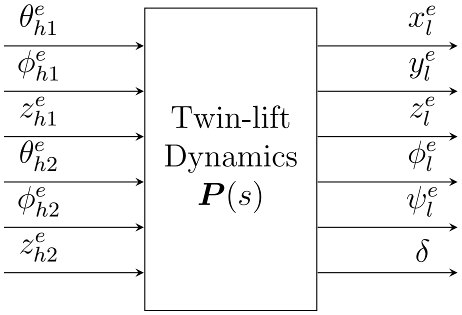

Figure 3.5.1: Twin-lift model inputs and outputs (6 × 6 plant). The helicopter pitch, roll and altitude are represented by θ^e_{hi} (rad), ϕ^e_{hi} (rad) and z^e_{hi} (m) respectively for helicopter $i \in 1, 2$. The pitch and roll are Euler angles using the ZYX sequence (yaw first, then pitch and lastly roll). The altitude is in the inertial frame. The load position is given by x^e_l, y^e_l and z^e_l in meters in the inertial frame. The load roll is given by ϕ^e_l and yaw given by ψ^e_l, also in the ZYX sequence. The separation distance is represented by δ (m)

To determine the source of the resonant mode at 0.69 rad/s, modal analysis (*see* Section 3.3.2) was done on the linearised plant. The twin-helicopter model was tedious to analyse due to the large number of states - a total of 131 states. In spite of this, it was found that four states contributed significantly to the mode. The participation factors for the 0.69 rad/s mode is shown in Fig. 3.5.5. The four states are the roll dynamics of each the helicopter and the corresponding body velocities. This correlates strongly with peak resonance of the separation output shown in 3.5.4. This is best interpreted to be the pendulous mode due to the constrained coupling in the roll dynamics of the twin-helicopter system. This mode is also unlikely to shift significantly under plant uncertainty since there is feedback in the roll dynamics in inner loops of the control system.

The last resonant mode that appeared in the linearised response which had an unclear source was the mode at 8.59 rad/s. Figure 3.5.6 shows the participation factor for the 8.59 rad/s mode. The states that correspond to the mode are the yaw angle and yaw rate of the load. This can be interpreted to be the rotational vibratory mode of the load about the yaw. This mode will be a function of the load inertia in the z-axis and the cable coupling dynamics to the helicopters.

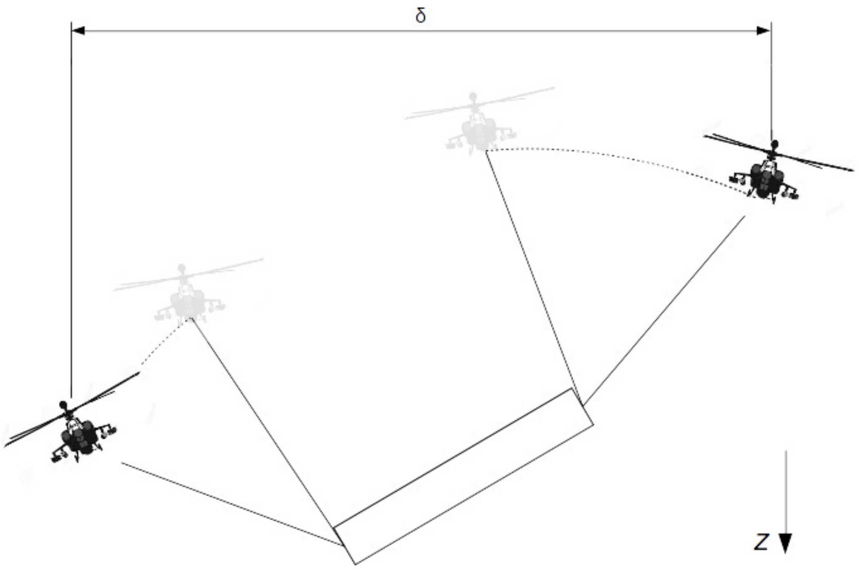

Figure 3.5.2: Illustration of how the helicopter positions are controllable with fixed length cable

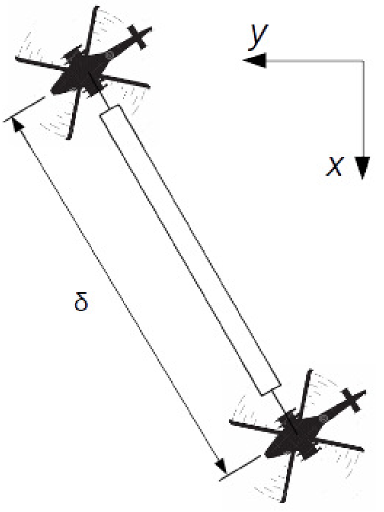

Figure 3.5.3: Illustration showing how inertial yaw capability can be achieved without diverging from the linearised models

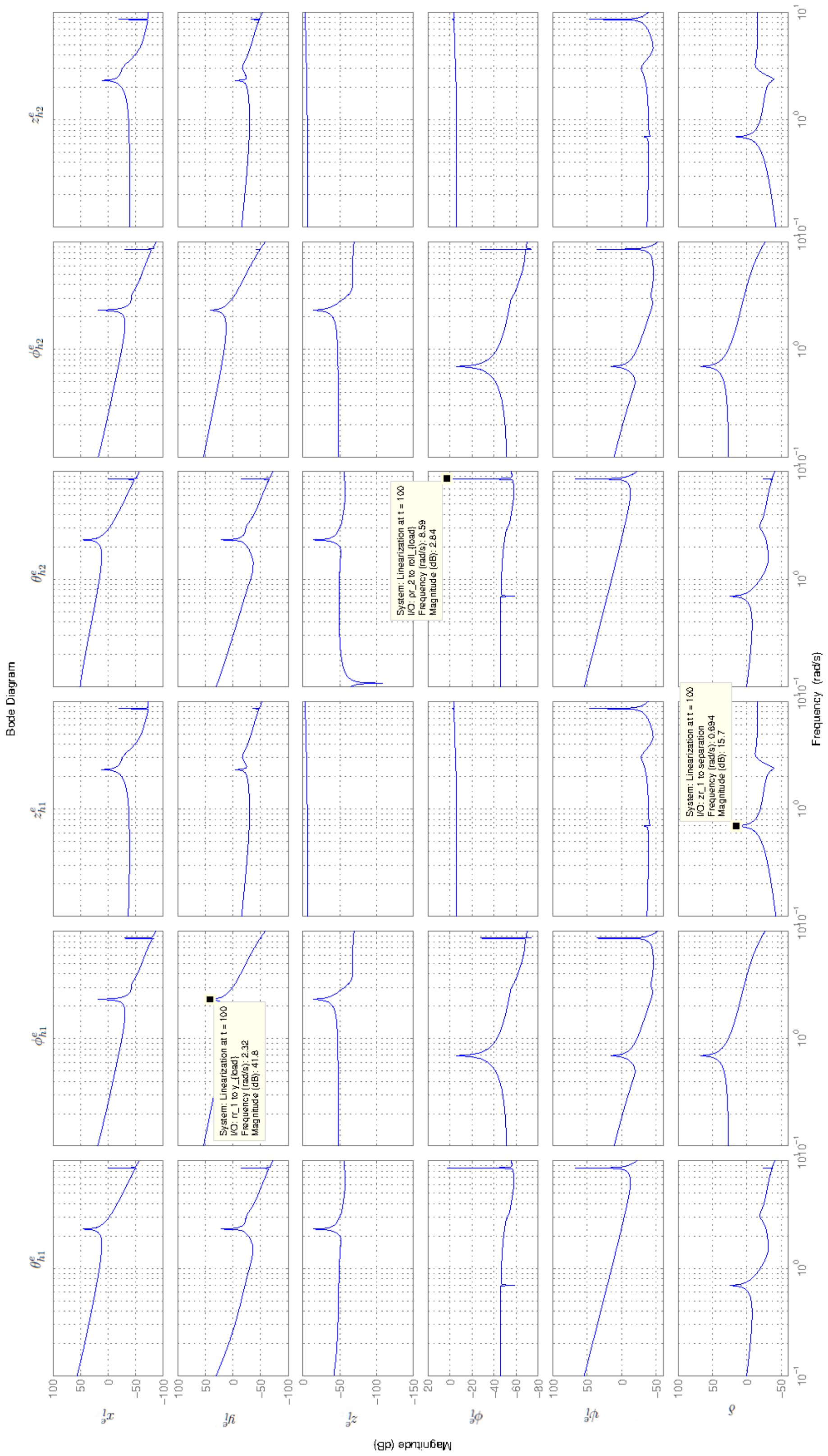

Figure 3.5.4: The Bode magnitude plot of the twin-helicopter system (depicted in Fig. 3.5.1) showing cross-coupling and resonant points.

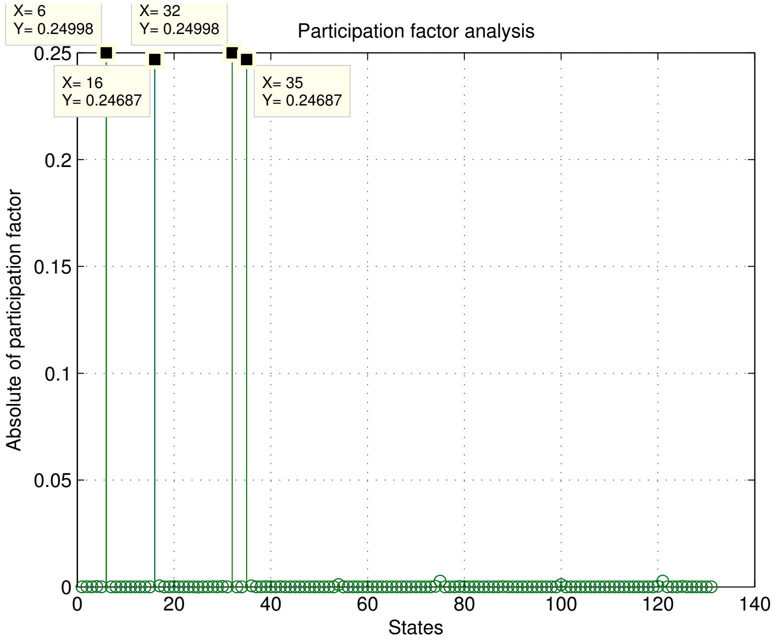

Figure 3.5.5: Magnitude of participation factors that contribute to the resonant mode at 0.69 rad/s

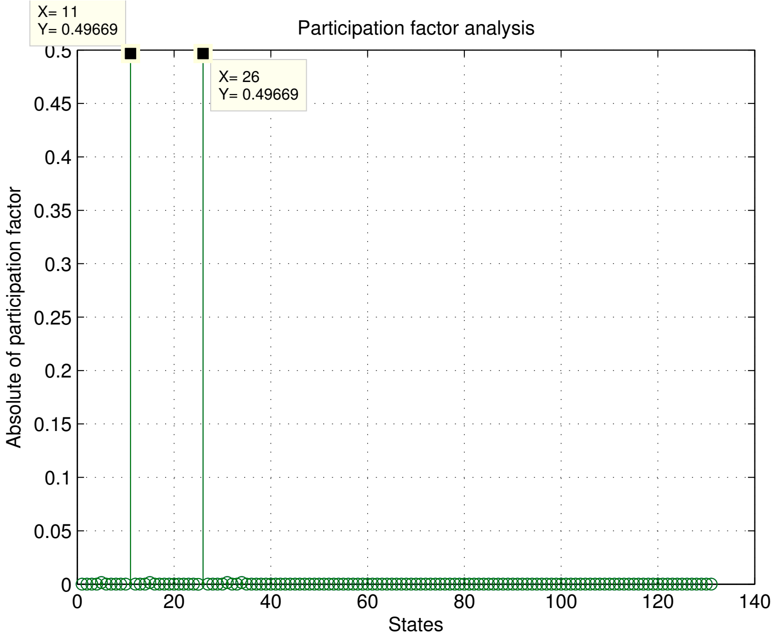

Figure 3.5.6: Magnitude of participation factors that contribute to the resonant mode at 8.59 rad/s

Chapter 4

Estimation

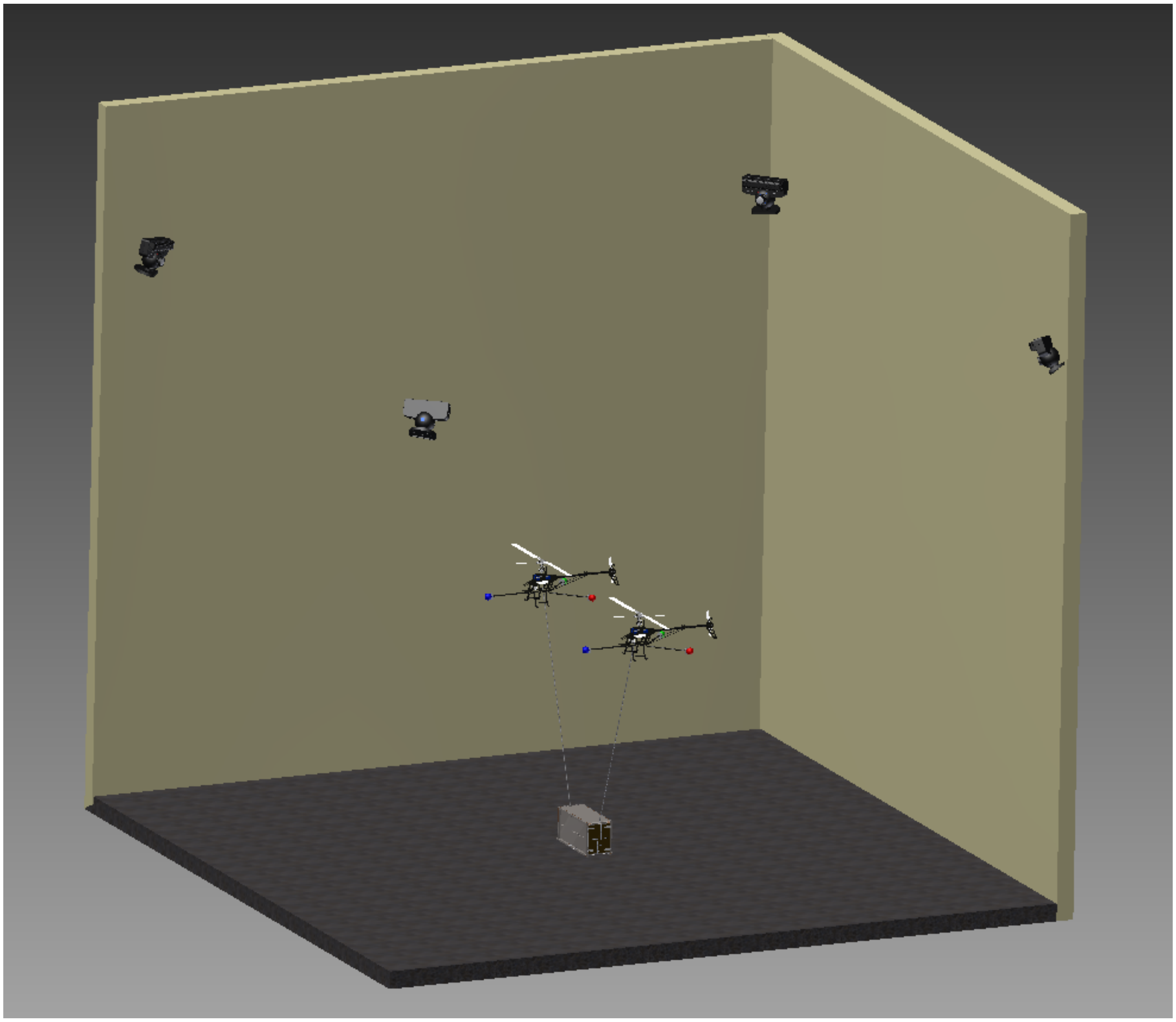

In this chapter, the estimation of the kinematic state variables is investigated. An overview of the architecture of the motion capture system is described, as well as the description of the image processing that was performed. The Extended Kalman Filter (EKF) is used to fuse the inertial body frame measurements and the motion capture data to optimally estimate the kinematic state variables. The *state propagation equations* are described that propagate the inertial measurements to the kinematic state variables. Thereafter, the state variables are mapped to the data in each camera frame of reference to form the *measurement equations*. After the development of the equations, the performance of the EKF in fusing the data is presented.

4.1 Overview

Performing the experiments indoor made the sensor requirements more challenging. Most UAV applications are outdoor (Wendel et al. 2006) where Global Positioning System (GPS) is available. In order to determine the kinematic state variables in the laboratory, many institutions use off-the-shelf motion capture systems, such as the Vicon® Motion capture system. These systems were originally developed for film animation and cost more than US$50 000 (Delaney 1998). Institutions such as UPENN, ETH and MIT use the Vicon motion capture system for position and attitude determination of their aerial vehicles. An off-the-shelf motion capture system was not an option in this study due to financial constraints. For this project, a low-cost motion capture system was developed that gives satisfactory reliability, resolution and frame rate for indoor aerial vehicle control.

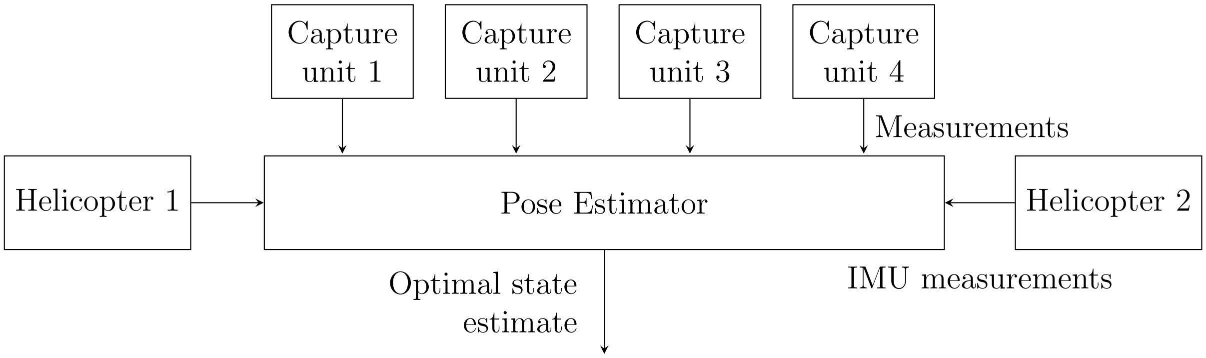

Figure 4.1.1: An overview of pose estimation elements

The pose tracking system is responsible for optimal estimation of the kinematic state variables of the helicopters for feedback control and system identification. Figure 4.1.1 shows an overview of the elements of the pose estimation system. The capture unit is defined as the device responsible capturing and processing the scene. Upon a request from the client, the capture unit returns the position of the red, green and blue fiducial markers in the scene (see Fig. 2.3.2), in the respective camera frame of reference. These are the *measurements* of the state-estimator. There is a total of four capture units, each located in the upper corner of the flying volume. Body angular rate and linear acceleration measurements are done in the body frame of the helicopters using rate gyroscopes and accelerometers. These measurements are used to propagate the kinematic state variables. The gyroscope and accelerometer measurements are high bandwidth, but noisy and suffer from low frequency errors which vary with environmental conditions. The motion capture system does not have as high bandwidth information as the gyroscope and accelerometer but after calibration, provides accurate low frequency information. The Extended Kalman filter is used to fuse the measurements in an optimal manner to estimate the linear and angular position and velocity states of the helicopter in the room coordinate frame.

Tracking more than one helicopter complicates matters due to the possible ambiguity when using the same colour fiducial markers. Based on the camera chosen, it was found that distinguishing more than the primary colours was very difficult. The exposure of the camera was set to the minimum value that allowed detection of the markers in the scene. This helped in reducing affect of varying ambient light on the segmentation result. In spite of this, the observed colour of the fiducial markers covered a large range in changing ambient lighting conditions. Thus, there was no other option than to resolve the ambiguity between the helicopters in software. This was done by assuming sufficient initial separation to track helicopters individually. Upon subsequent estimation iterations, the previous pose was used to project the fiducial markers back into the scene. Based on an upper velocity limit, the maximum possible displacement was used to allocate markers to the correct helicopter in the scene. As a last resort, epipolar geometry is used to resolve the contention (Hartley & Zisserman 2003).

Figure 4.1.2: Capture unit condensed to Raspberry Pi

Old, unused desktop computers were used in the capture unit for collecting and pre-processing the image data. Although bulky, there were a zero cost and a convenient solution at the time. Plans are in place to migrate the software to single-board computers such as the Raspberry Pi and BeagleBone. The Linux kernel used has been patched with the PREEPMT_RT (Real-Time Linux 2010) patch which gives minimal latency in the capture and data transport process. A jitter of less than 5 µs was measured which is considered negligible for the bandwidth of this project. For further portability, UDP over WiFi may be used transport the data between the Capture units and the base station. This will allow the use of the motion capture units in larger spaces with only power supply cables to the capture units. This low-cost design opens up the possibility of new applications.

4.2 Image Processing

The image processing task is a simple segmentation problem. The *measurements* required for the state-estimator are the positions of the fiducial points in the camera frame of reference. Due to imperfections in the sensor and lens manufacturing, the cameras needed to be calibrated. The *Camera Calibration Toolbox for Matlab* (Bouguet 2008) was used to estimate the lens distortion coefficients and the CMOS offset from the center of the lens. The OpenCV library is used to perform the basic image processing operations. Gonzalez & Woods (2002) was used as a general reference for understanding the segmentation process. The following sequence of operations are performed to extract the fiducial points:

1. Capture image
2. Convert to Hue, Saturation, Value (HSV) space
3. Segment image by colour range
4. Perform Gaussian smoothing
5. Find blob area and filter based on expected area
6. Find center of mass with subpixel interpolation for valid blobs
7. Undistort fiducial points based on distortion mapping coefficients

After this process is complete, a region of interest is formed to make subsequent searches quicker. The region of interest grows as the blobs move apart. This way the blobs are tracked. If the blobs are no longer in the scene, the region of interest defaults to the entire frame. The remapping of the pixels using the distortion map is a computationally expensive operation. A huge improvement in performance was obtained by undistorting only the points of interest instead of the entire frame as is usually done.

4.3 State and State-Error Covariance Propagation

Although a full estimate of the helicopter state variables can be developed, it was decided to estimate only the kinematic state variables of the plant. This decision was made due to the complexity of the helicopter plant; the large number of state variables (32; *see* Section 3.1.4), in addition to the complicated nonlinearities that will make the computational cost very large. The propagation equations are developed below, similar to that found in Van Der Merwe & Wan (2004).

The rotation matrix in terms of the quaternion, from the body frame to the inertial frame is given by (Diebel 2006),

$$\boldsymbol{R}_{eb}(\vec{\boldsymbol{q}}) = \begin{bmatrix} q_1^2+q_2^2-q_3^2-q_4^2 & 2(q_2q_3-q_1q_4) & 2(q_2q_4+q_1q_3) \\ 2(q_2q_3+q_1q_4) & q_1^2-q_2^2+q_3^2-q_4^2 & 2(q_3q_4-q_1q_2) \\ 2(q_2q_4-q_1q_3) & 2(q_3q_4+q_1q_2) & q_1^2-q_2^2-q_3^2+q_4^2 \end{bmatrix} \tag{4.3.1}$$

The state vector to be estimated is $\vec{\boldsymbol{x}}_k = [\vec{\boldsymbol{p}}_k^T, \vec{\boldsymbol{v}}_k^T, \vec{\boldsymbol{q}}_k^T, \vec{\boldsymbol{\omega}}_{b,k}^T, \vec{\boldsymbol{a}}_{b,k}^T]^T$, where $\vec{\boldsymbol{p}}_k$ is the position in the inertial frame, $\vec{\boldsymbol{v}}_k$ is the velocity in the inertial frame, $\vec{\boldsymbol{q}}_k$ is the quaternion that represents the attitude of the body frame with respect to the inertial frame, $\vec{\boldsymbol{\omega}}_{b,k}$ and $\vec{\boldsymbol{a}}_{b,k}$ are the gyroscope and accelerometer measurement biases. The subscript k indicates the kth discrete sample.

Assuming constant velocity and acceleration during the time between samples Δt, the position and the velocity state-difference equations are,

$$\vec{\boldsymbol{p}}_{k+1} = \vec{\boldsymbol{p}}_k + \Delta t \cdot \vec{\boldsymbol{v}}_k + \Delta t \cdot \vec{\boldsymbol{\eta}}_{p_k} \tag{4.3.2}$$

$$\vec{\boldsymbol{v}}_{k+1} = \vec{\boldsymbol{v}}_k + \Delta t \cdot \vec{\boldsymbol{a}}_k + \Delta t \cdot \vec{\boldsymbol{\eta}}_{v_k} \tag{4.3.3}$$

where Δt is the time between propagating the state. The acceleration $\vec{\boldsymbol{a}}_k$ in (4.3.3) is the acceleration in the inertial frame which is given by,

$$\vec{\boldsymbol{a}}_k = \boldsymbol{R}_{eb}(\vec{\boldsymbol{q}}_k)\vec{\tilde{\boldsymbol{a}}}_k - \vec{\boldsymbol{g}} \tag{4.3.4}$$

$$\vec{\tilde{\boldsymbol{a}}}_k = \vec{\boldsymbol{a}}_{accel,k} - \vec{\boldsymbol{a}}_{b,k} + \vec{\boldsymbol{\eta}}_{accel,k} \tag{4.3.5}$$

where $\vec{\boldsymbol{g}}$ is the acceleration due to gravity in the inertial frame, $\vec{\boldsymbol{a}}_{accel,k}$ is the accelerometer output (rad/s^2) in the body frame and $\vec{\boldsymbol{\eta}}_{accel,k}$ is the accelerometer noise.

The quaternion derivative is given by (Marins et al. 2001),

$$\dot{\vec{\boldsymbol{q}}} = \frac{1}{2}\vec{\boldsymbol{q}} \otimes [0 \; \vec{\boldsymbol{\omega}}^T]^T \tag{4.3.6}$$

where the quaternion product is defined as,

$$\vec{\boldsymbol{q}}^A \otimes \vec{\boldsymbol{q}}^B = \begin{bmatrix} q_1^A q_1^B - q_2^A q_2^B - q_3^A q_3^B - q_4^A q_4^B \\ q_1^A q_2^B + q_2^A q_1^B + q_3^A q_4^B - q_4^A q_3^B \\ q_1^A q_3^B - q_2^A q_4^B + q_3^A q_1^B + q_4^A q_2^B \\ q_1^A q_4^B + q_2^A q_3^B - q_3^A q_2^B + q_4^A q_1^B \end{bmatrix} \tag{4.3.7}$$

alternatively, (4.3.7) can be re-written (Trawny & Roumeliotis 2005) as,

$$\vec{\boldsymbol{q}}^A \otimes \vec{\boldsymbol{q}}^B = \begin{bmatrix} q_1^B & -q_2^B & -q_3^B & -q_4^B \\ q_2^B & q_1^B & q_4^B & -q_3^B \\ q_3^B & -q_4^B & q_1^B & q_2^B \\ q_4^B & q_3^B & -q_2^B & q_1^B \end{bmatrix} \begin{bmatrix} q_1^A \\ q_2^A \\ q_3^A \\ q_4^A \end{bmatrix} = \begin{bmatrix} q_1^A & -q_2^A & -q_3^A & -q_4^A \\ q_2^A & q_1^A & -q_4^A & q_3^A \\ q_3^A & q_4^A & q_1^A & -q_2^A \\ q_4^A & -q_3^A & q_2^A & q_1^A \end{bmatrix} \begin{bmatrix} q_1^B \\ q_2^B \\ q_3^B \\ q_4^B \end{bmatrix} \tag{4.3.8}$$

Discretising (4.3.6) using Explicit Euler (first-order) integration,

$$\vec{\boldsymbol{q}}_{k+1} = \vec{\boldsymbol{q}}_k + \Delta t \cdot \frac{1}{2}\vec{\boldsymbol{q}}_k \otimes [0\ \tilde{\vec{\boldsymbol{\omega}}}_k^T]^T \tag{4.3.9}$$

where $\tilde{\vec{\boldsymbol{\omega}}}_k^T$ represents the gyroscope reading (rad/s) with the biases removed. Expanding (4.3.9),

$$\vec{\boldsymbol{q}}_{k+1} = \frac{1}{2}\Delta t \begin{bmatrix} q_{1,k} & -q_{2,k} & -q_{3,k} & -q_{4,k} \\ q_{2,k} & q_{1,k} & -q_{4,k} & q_{3,k} \\ q_{3,k} & q_{4,k} & q_{1,k} & -q_{2,k} \\ q_{4,k} & -q_{3,k} & q_{2,k} & q_{1,k} \end{bmatrix} \begin{bmatrix} 2/\Delta t \\ \tilde{\omega}_{x,k} \\ \tilde{\omega}_{y,k} \\ \tilde{\omega}_{z,k} \end{bmatrix} \tag{4.3.10}$$

The quaternion is normalised on each computation step to prevent skewness that may result through an accumulation of numerical errors.

The gyroscope and accelerometer *biases* evolve with the following state-difference equations (Van Der Merwe & Wan 2004),

$$\vec{\boldsymbol{\omega}}_{b,k+1} = \vec{\boldsymbol{\omega}}_{b,k} + \Delta t \cdot \vec{\boldsymbol{\eta}}_{\omega b,k} \tag{4.3.11}$$

$$\vec{\boldsymbol{a}}_{b,k+1} = \vec{\boldsymbol{a}}_{b,k} + \Delta t \cdot \vec{\boldsymbol{\eta}}_{ab,k} \tag{4.3.12}$$

$$\tilde{\vec{\boldsymbol{\omega}}}_k = \vec{\boldsymbol{\omega}}_{gyro,k} - \vec{\boldsymbol{\omega}}_{b,k} + \vec{\boldsymbol{\eta}}_{gyro,k} \tag{4.3.13}$$

The a priori state-error covariance is calculated by propagating the previous state-error covariance through the linearisation of the state-difference equation for the Extended Kalman filter operation (Brown & Hwang 1997). The nonadditive process noise also needs to be considered in the state-error propagation. The propagation is given by (ibid.) as,

$$\boldsymbol{P}_{k+1}^- = \boldsymbol{A}_k \boldsymbol{P}_k^- \boldsymbol{A}_k^T + \boldsymbol{W}_k \boldsymbol{Q} \boldsymbol{W}_k^T \tag{4.3.14}$$

where $\boldsymbol{A}_k = \left.\frac{\partial \vec{\boldsymbol{f}}}{\partial \vec{\boldsymbol{x}}}\right|_k$ and $\boldsymbol{W}_k = \left.\frac{\partial \vec{\boldsymbol{f}}}{\partial \vec{\boldsymbol{\eta}}}\right|_k$. The noise vector $\vec{\boldsymbol{\eta}}_k = [\vec{\boldsymbol{\eta}}_{p,k}^T, \vec{\boldsymbol{\eta}}_{v,k}^T, \vec{\boldsymbol{\eta}}_{a,k}^T, \vec{\boldsymbol{\eta}}_{\omega,k}^T, \vec{\boldsymbol{\eta}}_{\omega_{b,k}}^T, \vec{\boldsymbol{\eta}}_{a_{b,k}}^T]^T$ consists of the position noise, velocity noise, accelerometer noise, gyroscope noise, gyroscope bias noise and accelerometer bias noise respectively; with the error covariance of $\vec{\boldsymbol{\eta}}_k$ represented by $\boldsymbol{Q}$. The expansion of matrices $\boldsymbol{A}_k$ and $\boldsymbol{W}_k$ are given in Appendix D.1.

4.4 State-Error Correction

The measurements used to correct the state error is the information from the camera. Since the mappings from the image frame to three dimensional space is overdetermined for the chosen setup, precomputing the pose will yield a less complicated correction phase. Although this may simplify the correction phase, the measurement equation was chosen to be described explicitly for accurate estimation of the measurement covariance. Homogeneous coordinates are used to describe the mapping from three dimensional space in the inertial frame to the image plane as,

$$\lambda \begin{bmatrix} u_i \\ v_i \\ 1 \end{bmatrix} = \boldsymbol{M}_i \boldsymbol{R}_{cr,i}(\vec{\boldsymbol{P}}_o - \vec{\boldsymbol{T}}_{cr,i}) + \vec{\boldsymbol{\nu}}_i = \boldsymbol{K}_i \vec{\boldsymbol{B}}_i + \vec{\boldsymbol{\nu}}_i \tag{4.4.1}$$

where $\boldsymbol{M}_i$ is the camera intrinsic matrix of the ith camera, $\boldsymbol{R}_{cw,i}$ is the rotation matrix from the inertial frame to camera i, $\vec{\boldsymbol{P}}_o$ is an object point in the inertial frame, $\vec{\boldsymbol{T}}_{cr,i}$ is the translation from the inertial frame to camera i, and u_i and v_i are the coordinates in the image plane (pixels) of camera i. The pixel measurement noise represented by $\vec{\boldsymbol{\nu}}_i$, is zero-mean with covariance $\boldsymbol{R}_k$. For brevity, define $\boldsymbol{K}_i \in \mathbb{R}^{3\times 3}$ and $\vec{\boldsymbol{B}}_i \in \mathbb{R}^3$. The variable λ is a scaling variable that corresponds to the distance between the camera and the point (a single point on the image can be projected to a line in 3D). The fiducial points defined by the position of the LED beacons (Fig. 2.3.2) may be mapped to the inertial frame of reference by,

$$\vec{\boldsymbol{P}}_o = R_{eb}(\vec{\boldsymbol{q}})\vec{\boldsymbol{P}}_{op} + \vec{\boldsymbol{T}}_{rp} \tag{4.4.2}$$

where $\vec{\boldsymbol{P}}_{op}$ (LED position) is a point with respect to the platform frame and $\vec{\boldsymbol{T}}_{rp}$ is the translation from the platform to the inertial frame origin (center of floor in flying space). Expanding (4.4.1) in scalar form,

$$u_i = \frac{K_{11,i}B_{1,i} + K_{12,i}B_{2,i} + K_{13,i}B_{3,i}}{K_{31,i}B_{1,i} + K_{32,i}B_{2,i} + K_{33,i}B_{3,i}} + \nu_x \tag{4.4.3}$$

$$v_i = \frac{K_{21,i}B_{1,i} + K_{22,i}B_{2,i} + K_{23,i}B_{3,i}}{K_{31,i}B_{1,i} + K_{32,i}B_{2,i} + K_{33,i}B_{3,i}} + \nu_y \tag{4.4.4}$$

The measurement equation is given by,

$$\begin{bmatrix} u_i \\ v_i \end{bmatrix} = \vec{\boldsymbol{h}}_i(\vec{\boldsymbol{x}}) \tag{4.4.5}$$

The scalar expansion of $\vec{\boldsymbol{B}}_i$ is,

$$B_{1,i} = (q_1^2 + q_2^2 - q_3^2 - q_4^2)X + 2(q_2q_3 - q_1q_4)Y + 2(q_2q_4 + q_1q_3)Z + p_x - t^{cr}_{x,i} \tag{4.4.6}$$

$$B_{2,i} = 2(q_2q_3 + q_1q_4)X + (q_1^2 - q_2^2 + q_3^2 - q_4^2)Y + 2(q_3q_4 - q_1q_2)Z + p_y - t^{cr}_{y,i} \tag{4.4.7}$$

$$B_{3,i} = 2(q_2q_4 - q_1q_3)X + 2(q_3q_4 + q_1q_2)Y + (q_1^2 - q_2^2 - q_3^2 + q_4^2)Z + p_z - t^{cr}_{z,i} \tag{4.4.8}$$

The Kalman gain and corrected (post-priori) state-error covariance are given below (Brown & Hwang 1997),

$$\boldsymbol{K}_k = \boldsymbol{P}_k^- \boldsymbol{C}_k (\boldsymbol{C}_k \boldsymbol{P}_k^- \boldsymbol{C}_k^T + \boldsymbol{R}_k)^{-1} \tag{4.4.9}$$

$$\boldsymbol{P}_k^+ = (\boldsymbol{I} - \boldsymbol{K}_k \boldsymbol{C}_k)\, \boldsymbol{P}_k^- \tag{4.4.10}$$

$\boldsymbol{C}_k$ is the Jacobian of (4.4.1) (a function of the state variable $\vec{\boldsymbol{q}}$). The derivation of the Jacobian is given in Appendix D.2.

4.5 State Estimation Results

The optimal state-estimation results that fuse the inertial sensors and motion capture data are shown below. The Extended Kalman Filter (EKF) states are compared to nonlinear least squares solution from the motion capture data alone. That solution is obtained by forming an overdetermined set by stacking equations of the form (4.4.1) for each identified blob and camera; the nonlinear least squares solution was found through iteration. The nonlinear least squares solution is a good benchmark to check whether the estimator is correcting the affect of inertial measurement biases. Figure 4.5.1 shows the EKF and nonlinear least squares estimate of the translation of a helicopter during a test flight (subject to rotor vibrations). The EKF results lies almost completely over the least-squares estimates.

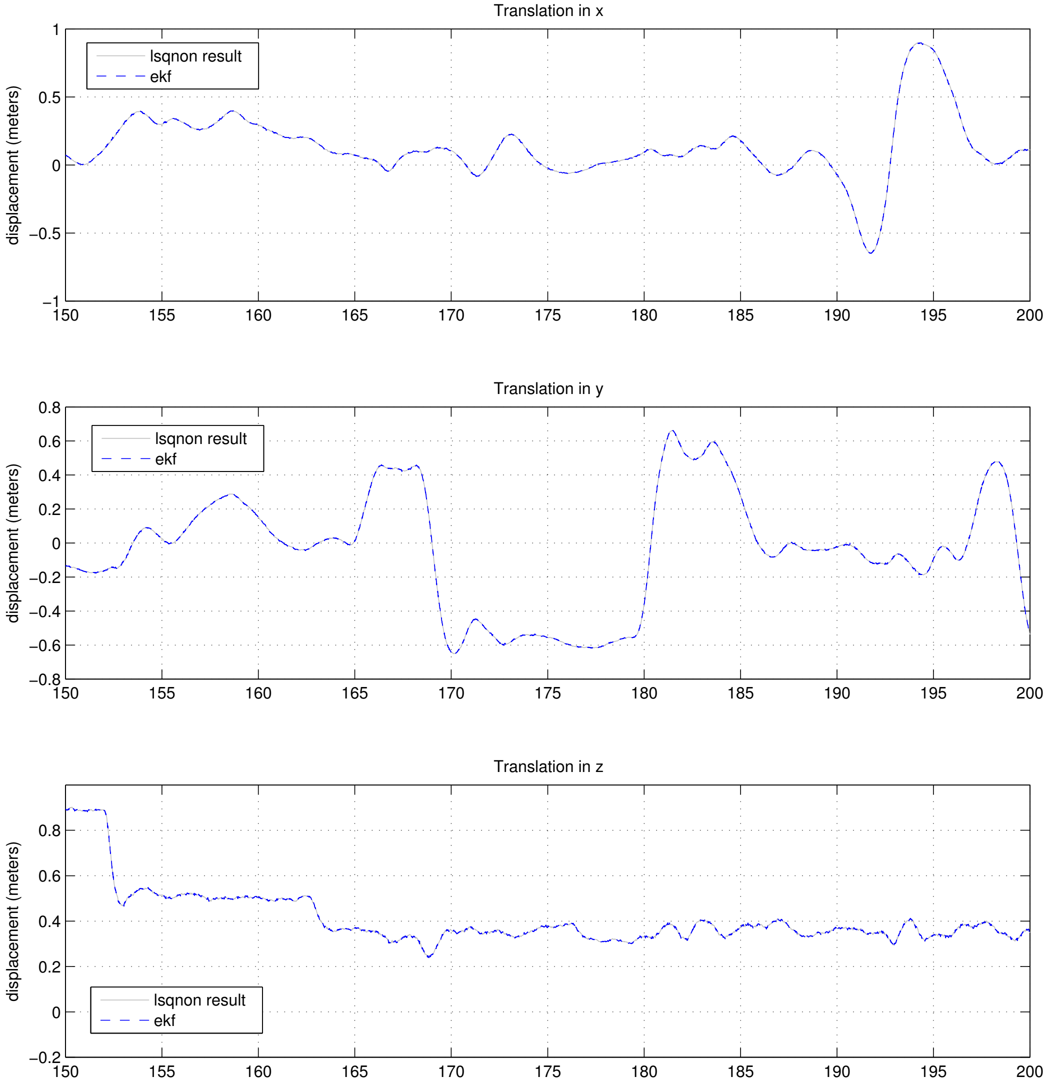

Figure 4.5.1: Translation estimation using the extended Kalman filter versus result from nonlinear least squares estimate

The roll, pitch and yaw of the helicopter during the test flight is shown in Fig. 4.5.2. It can be seen that the output of the EKF is smoother than the least squares estimation - this is a result of the optimal fusion of the gyroscope and accelerometer data with the motion capture data.

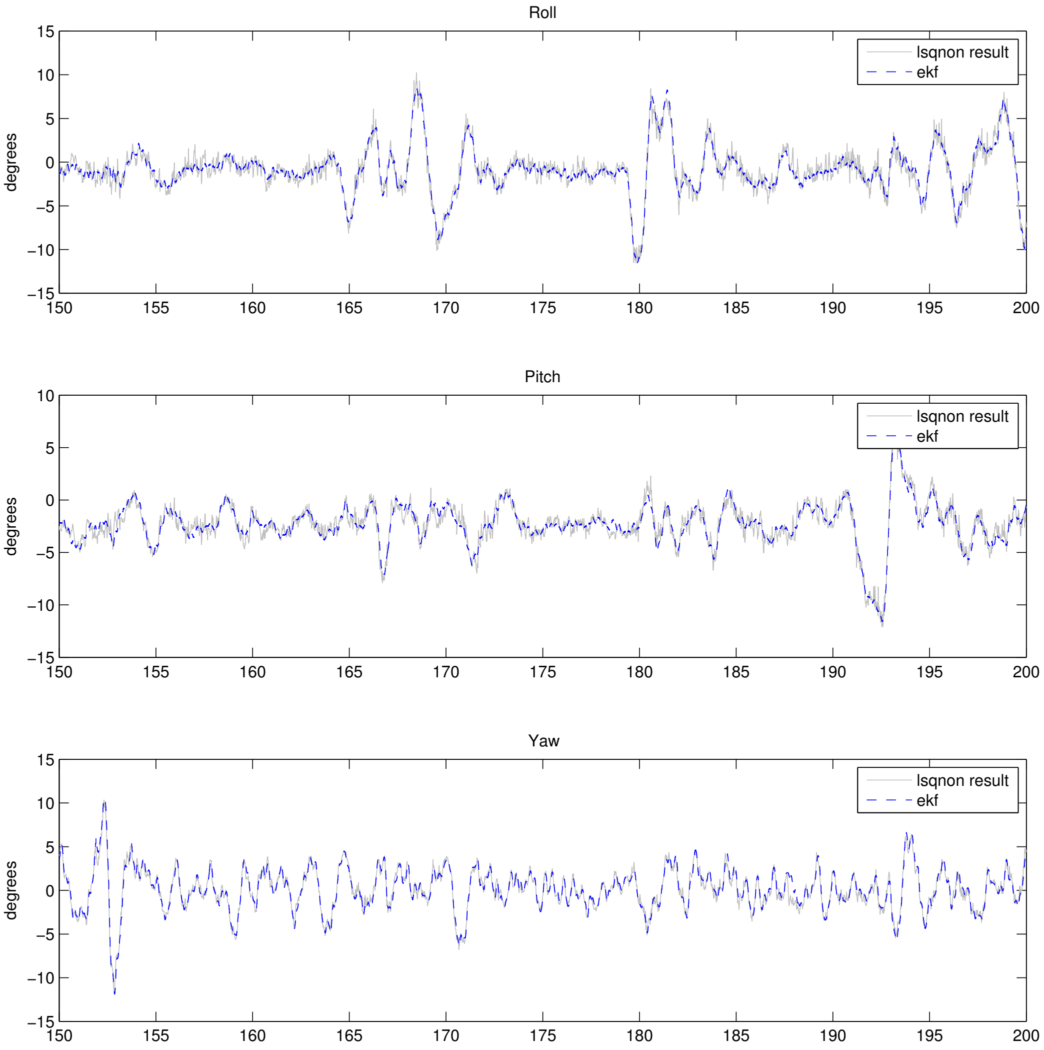

Figure 4.5.2: Roll, pitch and yaw output of the extended Kalman filter estimate versus result from nonlinear least squares estimate

Figure 4.5.3 shows the estimated velocity in x, y and z of the helicopter in the earth-fixed frame. Again, it can be seen the the EKF yields a smoother response due to the fusion with the accelerometer.

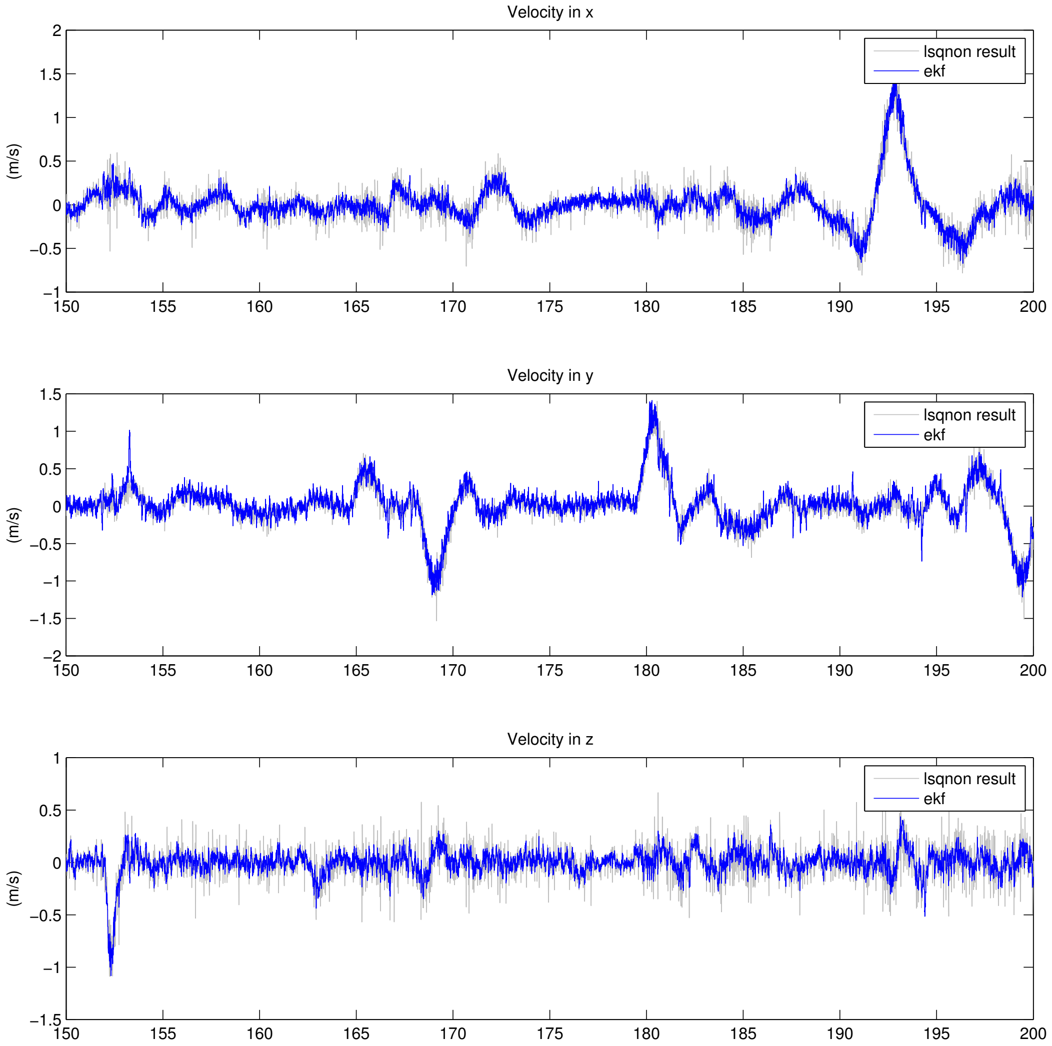

Figure 4.5.3: Velocity estimate using the extended Kalman filter versus result from nonlinear least squares estimate

Chapter 5

Control

In this chapter, the controller designs are presented. The chapter is split into two sections. The first section is labelled *Independent Helicopter Control*, and the second is labelled *Coordinated Helicopter Control*. As a fall-back control strategy, the helicopters must be safely controlled independently when not attached to the load. This will be required if the system goes unstable due to large disturbances. The helicopters will need to quickly release the load to prevent collision, and then land safely. A robust controller is designed using Quantitative Feedback Theory (QFT) in the Independent Helicopter Control section for attitude and position control of the helicopters. Strategies around solving the attitude and translation control of the load using the twin-helicopter slung load system is investigated, and a solution is presented using QFT in the Coordinated Helicopter Control section.

5.1 Independent Helicopter Control

Independent Helicopter Control mode is used to describe the mode of operation when the helicopters are not connected to the load. Quantitative Feedback Theory is used to design a robust controller for the helicopter when operating independently. This was required to test the state-estimation system, as well as the general system architecture. It was also desired to use independent control as a performance benchmark for testing the load-sharing control system. Due to the limited testing space, the controller is designed for the hover operating condition (lower linear velocities) only.

The aim of the control system design is to control the position of the helicopter in the inertial frame of reference. The plant is linearised about level attitude and zero linear body velocity. After the linear analysis done in Section 3.3.1, it was found that a suitable breakdown of the dynamics is a roll/pitch subsystem and a heave/yaw subsystem based on the coupling. This is also recommended in Raptis & Valavanis (2010). The translational control requirement is met by an outer loop commanding attitude and altitude.

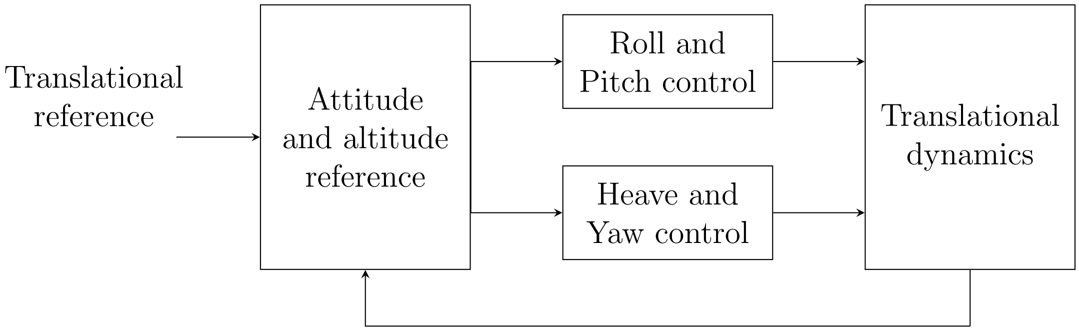

Figure 5.1.1: High-level overview of control scheme used for independent control

Using the ZYX (yaw, pitch, roll) rotation sequence, the following equation may be used to map body angular rates to Euler rates (Padfield 2008),

$$\begin{bmatrix} \dot{\theta}^e \\ \dot{\phi}^e \\ \dot{\psi}^e \end{bmatrix} = \begin{bmatrix} 1 & \sin(\phi^e)\tan(\theta^e) & \cos(\phi^e)\tan(\theta^e) \\ 0 & \cos(\phi^e) & -\sin(\phi^e) \\ 0 & \sin(\phi^e)\sec(\theta^e) & \cos(\phi^e)\sec(\theta^e) \end{bmatrix} \begin{bmatrix} \dot{\theta}^b \\ \dot{\phi}^b \\ \dot{\psi}^b \end{bmatrix} \tag{5.1.1}$$

For small roll and pitch angles which is applicable in the hover case, the mapping in (5.1.1) becomes close to diagonal. This is the justification for using the Euler angles as feedback signals. In order to determine whether a non-diagonal controller will be required, an assessment of the interaction index is performed.

5.1.1 Cross-coupling

The Perron root of the interaction matrix may be used to assess the cross-coupling in the plant (Boje 2002). For a diagonal splitting of the plant, as used in MIMO QFT design (*see* (5.2.7)), the interaction matrix is given by,

$$\boldsymbol{X} = \left(\hat{\boldsymbol{P}}^*_D + \boldsymbol{G}_D\right)^{-1} \hat{\boldsymbol{P}}^*_O \tag{5.1.2}$$

where $\hat{\boldsymbol{P}}^*_D$ and $\hat{\boldsymbol{P}}^*_O$ are the diagonal and off-diagonal splittings of $\hat{\boldsymbol{P}}^* = \boldsymbol{P}^{-1} = (\boldsymbol{PK})^{-1}$ and $\boldsymbol{K}$ is the decoupling pre-compensator. For a 2 × 2 plant, the closed-loop interaction index is given by (Reddi & Boje 2012),

$$\gamma_c(\boldsymbol{X}) = \underset{P \in \boldsymbol{P}}{max} \left\{ \sqrt{abs\left[\frac{q^*_{11}q^*_{22}}{q^*_{12}q^*_{21}} \frac{1}{(1+l^*_1)(1+l^*_2)}\right]} \right\} \tag{5.1.3}$$

where q^*_{ij} are equivalent plants with pre-compensation and l^*_i are diagonal loop gains. There are two motivations for reducing the interaction index. The first is with regard to *design* of multivariable systems for stability by reducing the Perron root of the interaction matrix to less than unity for all frequencies, stability may be guaranteed by ensuring that the individual loops are stable (a diagonal dominance criteria (Boje 2002)). The second implication for reducing the interaction index is that there is a reduction in the over-design in the QFT design methodology (*see* (5.2.7), (5.2.9) ...).

Roll and Pitch

Figure 5.1.2 shows the open-loop interaction index for the roll/pitch *rate* plant. It can be seen that the interaction index is marginally larger than unity at frequencies near 0.2 rad/s, which is significantly lower than the bandwidth of the roll/pitch rate plant. Equation (5.1.3) shows that the interaction index may be reduced via feedback from high individual loop gain. The high gain from the kinematic integrators (controlling body angular position not rate) will reduce the interaction index around 0.2 rad/s to below unity. Hence a pre-compensator is not necessary for the roll/pitch rate loop.

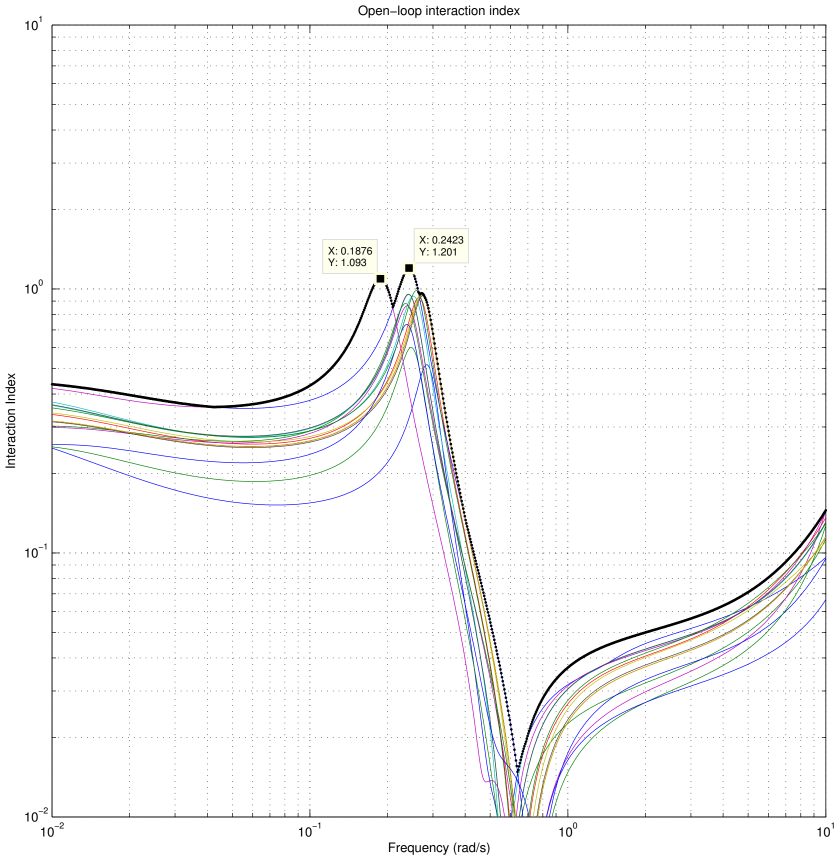

Figure 5.1.2: Open-loop interaction index for roll/pitch rate plant across uncertainty set ($l_1^* = l_2^* = 0$)

Heave and Yaw

The interaction index for the heave/yaw plant is shown in Fig. 5.1.3. The interaction index is very low for the heave/yaw plant. This is expected due to the triangular magnitude response of the system (*see* Section 3.3.1). The low peak *interaction index* in this subsystem does not imply the that *interaction* is low, but rather that the interaction will not cause stability issues in the multivariable system.

5.1.2 Digital Design

The avionics instrumentation samples the state of the helicopters at 50 Hz. The controller is implemented digitally on the on-board avionics. To design for the *effect of sampling*, the design is done in the w-domain (Eitelberg 1988). It is shown in Eitelberg (1988) that the effect of sampling a continuous-time process is to *approximately* add a right-hand plane zero, $(1 - wT_s/2)$, where T_s is the sampling period. The approximation requires that the sampling rate be much higher than the highest frequency pole in the plant. Using a sampling rate

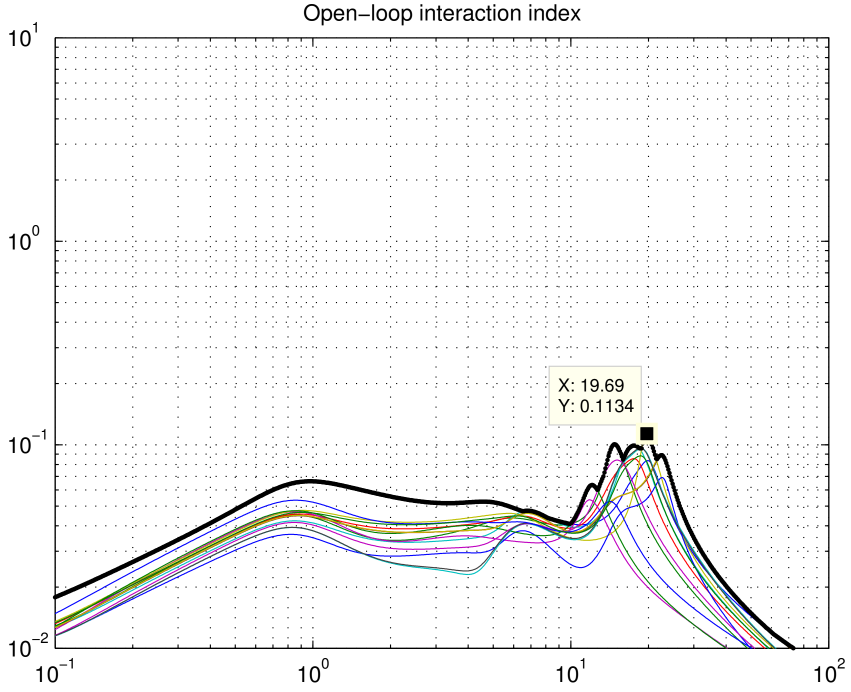

Figure 5.1.3: Open-loop interaction index for heave/yaw plant across uncertainty set

of 1/50 s, the non-minimum phase effect of the sampled system is to add (non-minimum) phase lag of 45° and +3dB of gain at 100 rad/s. The fastest loops in the design are the attitude loops, with no bandwidth exceeding 10 rad/s. This is 10 times less than the effective non-minimum pole frequency that comes from the effect of sampling and thus makes the approximation valid. The effect of sampling and implementation delay T_d, may thus be captured in an equivalent plant $P'(w)$,

$$P'(w) \approx P(s)\Big|_{s=w} (1 - wT_s/2)\frac{1 - wT_d/2}{1 + wT_d/2} \tag{5.1.4}$$

The worst-case lumped implementation delay was measured to be 5 ms. The effect of sampling is taken in all the design cases to follow. As the design seeks to maximise achievable bandwidth, the fastest sampling of the helicopter state was chosen (50 Hz). In other designs, the lowest sampling rate that allow specifications to be achieved may be required. In that case, $(1 - wT_s/2)$ may be used as a looping shaping element and the minimum sampling time that meets specifications may be extracted. By loop shaping $L(w) = P'(w)G(w)$, an accurate representation of the *performance* and *stability* of the *sampled system* is reflected in familiar Inverse Nichols plots.

5.1.3 Roll/Pitch Controller Design

Multivariable QFT was chosen as the robust controller design methodology. Simplified studies (see Section 5.2.3 and 5.2.4) suggested that attitude and heave control bandwidth limitation may result in there being no solution of the coordinated control problem. For this reason, the control specification was to maximise the bandwidth for the roll and pitch channels while meeting stability requirements across the uncertain set of plants. Preliminary plant input analysis suggested that the performance is limited by stability constraints rather than actuator limits.

The robust stability specification is,

$$\left|\frac{1}{1+l_i}\right| \leq 6dB \quad \forall\, \omega \quad i = 1, 2.$$

where $l_i = p_i g_i$ is the ith loop gain. The robust stability margin of 6 dB was chosen to get additional bandwidth, with acceptable overshoot in the worst-case plant case. The low interaction index within the required closed-loop bandwidth made it unnecessary to implement a non-diagonal controller. Therefore a diagonal controller structure was chosen and sequential loop closing procedure applied (Eitelberg 1999). Since both loops have similar bandwidth and symmetric cross-coupling the choice of the first loop does not matter. The roll loop controller was designed first, followed by the pitch loop (taking into account the closed-loop roll dynamics). The roll and pitch loops were shaped to meet the stability bounds. Figure 5.1.4 and Fig. 5.1.5 are inverse Nichols plots of the nominal open-loop gain of the roll and pitch loops. For each "design frequency", the point on the nominal loop is shown together with the corresponding design bounds. The bounds consists of upper and lower bounds that must be satisfied by the nominal loop to ensure that the specifications are met for the plant set. The resulting controller for the roll loop is,

$$g_{roll}(w) = -720\ \frac{(w/15.45)^2 + 2 \cdot 0.2 \cdot (w/15.45) + 1}{(w/15.5)^2 + 2 \cdot 2 \cdot (w/15.5) + 1} \tag{5.1.5}$$

and for the pitch loop,

$$g_{pitch}(w) = -295\ \frac{(w/14.5)^2 + 2 \cdot 0.2 \cdot (w/14.5) + 1}{(w/18.5)^2 + 2 \cdot 1.4 \cdot (w/18.5) + 1} \tag{5.1.6}$$

The aim was to maximise the roll and pitch loop gain cross-over frequency. The gain cross-over frequency achieved for the nominal plant was 5.3 rad/s for the roll loop; and 6.3 rad/s for the pitch loop. Due to the similar channel dynamics, both controllers result in the same complex lead-lag structure. Damping factors were constrained to be greater than 0.2 to prevent numerical implementation issues. The magnitude of the sensitivity for the roll and pitch loops are shown in Fig. E.2.1 and Fig. E.2.2 in Appendix E.

5.1.4 Heave/Yaw Controller Design

The same procedure as carried out for the roll/pitch subsystem is done for the heave/yaw subsystem. The specification is robust stability limit of 6 dB for the heave and yaw channels with maximum gain cross-over frequency. A further requirement is that there is zero steady-state error in both channels to a unit step reference.

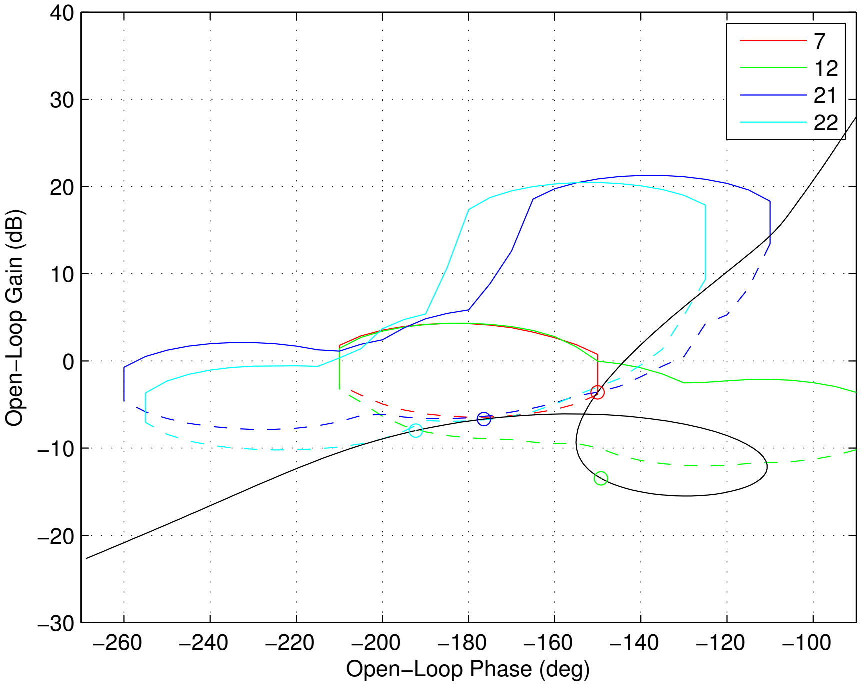

Figure 5.1.4: Controller design $g_{roll}(w)$, for the roll control loop

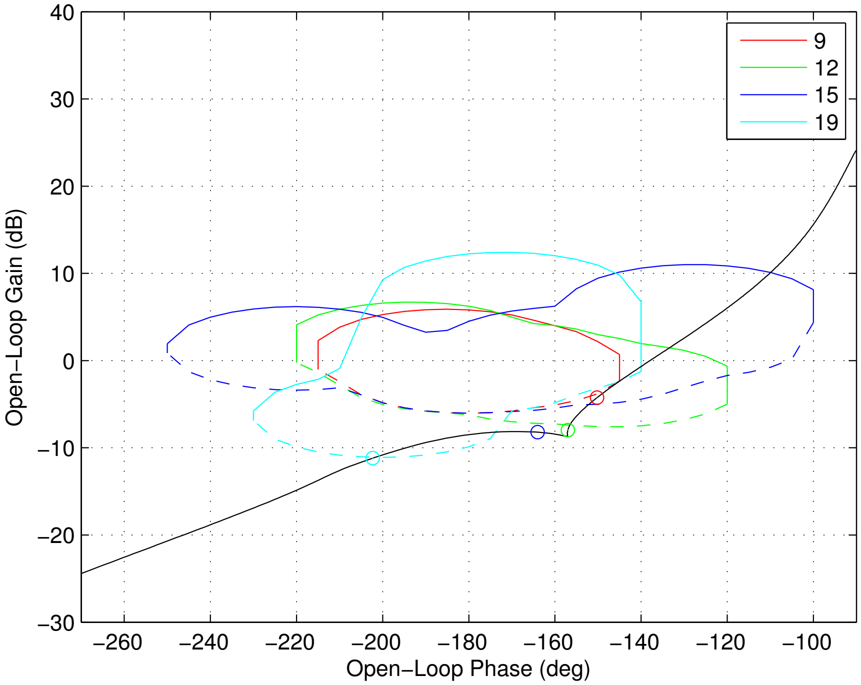

Figure 5.1.5: Controller design $g_{pitch}(w)$, for the pitch control loop

The controller design for the yaw loop is shown in Fig. 5.1.6. The yaw angular position controller is given in (5.1.7). The controller that achieved the specifications for the heave loop is shown in (5.1.8). Both controllers have a PID structure. The gain cross-over frequency achieved for the nominal plant was 2 rad/s for the yaw loop; and 4 rad/s for the heave loop. The step response of the closed-loop system for the reference yaw and heave are shown in Fig. E.2.3 and Fig. E.2.4.

$$g_{yaw}(w) = 150\;\frac{w/2+1}{w}\;\frac{w/2+1}{w/30+1} \tag{5.1.7}$$

$$g_{heave}(w) = -100\;\frac{w/1+1}{w}\;\frac{w/1.5+1}{w/30+1} \tag{5.1.8}$$

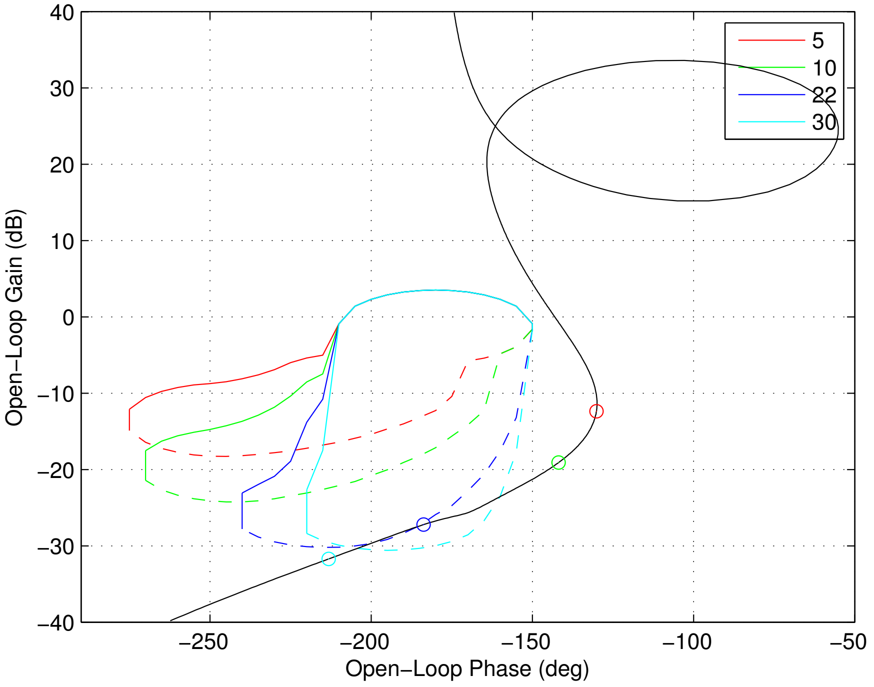

Figure 5.1.6: Controller design $g_{yaw}(w)$, for the yaw control loop

5.1.5 Velocity Controller Design

When the attitude and altitude control loops are closed, translational control can easily be achieved through rolling and pitching the helicopter. To illustrate this idea, consider the following steady-state behaviour. Assume a nose-down pitch command is given, naturally there is a reduction in the force opposite to gravity. The heave control loop increases the collective thrust to maintain altitude. The thrust increase must be greater than the weight of the helicopter to maintain altitude with non-level pitch. The force component in the inertial x-axis due to the pitch angle results in acceleration in the x-axis. This is illustrated in Fig.

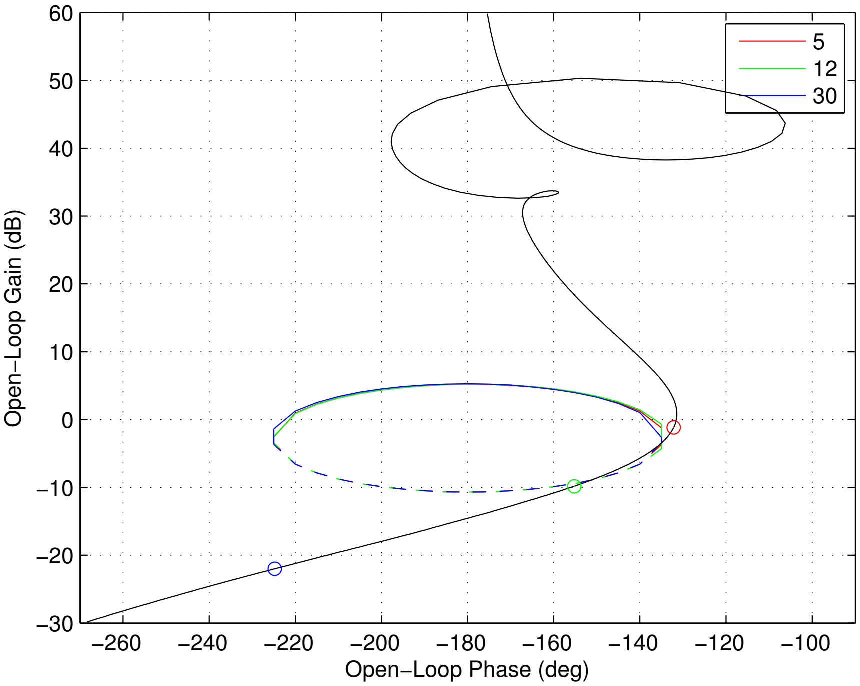

Figure 5.1.7: Controller design $g_{heave}(w)$, for the heave control loop

5.1.8. Similarly, translation in the y-axis is achieved by rolling the helicopter.

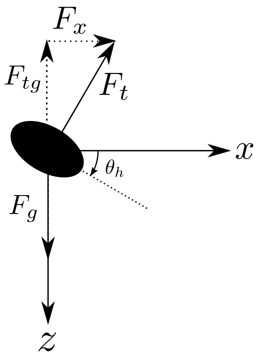

Figure 5.1.8: Illustration of inertial force in the x-axis when pitched nose-down

The analysis of the geometry in Fig. 5.1.8 yields that the force in the x-axis is,

$$F_x = \sqrt{F_{tg}^2 + F_x^2}\sin(\theta_h) \tag{5.1.9}$$

Given that the altitude is maintained ($F_{tg} = F_g$), (5.1.9) may be solved to obtain,

$$F_x = F_g \tan(\theta_h) \tag{5.1.10}$$

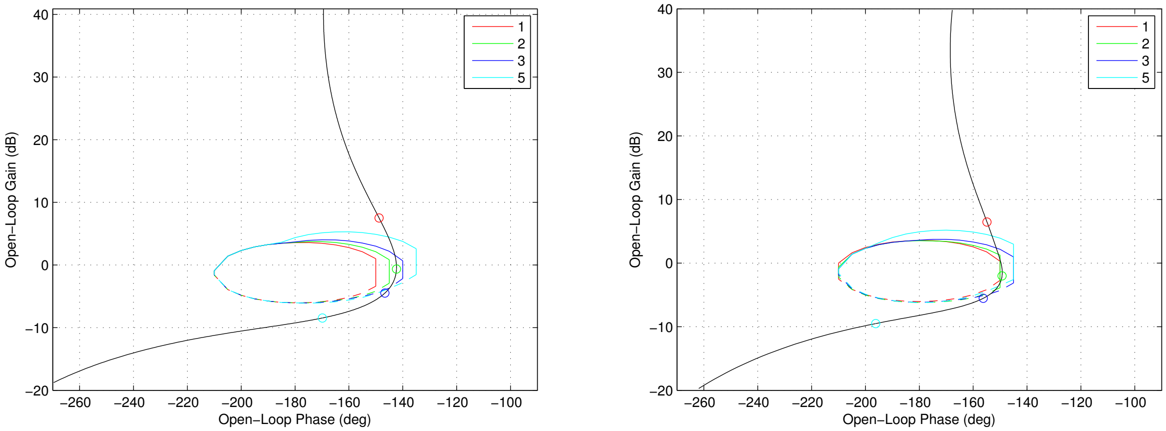

(a) Velocity loop for body x-axis

(b) Velocity loop for body y-axis

Figure 5.1.9: Controller design for the velocity loops

The acceleration will be,

$$a_x = g\tan(\theta_h) \tag{5.1.11}$$

Similarly, the acceleration in the y-axis will be,

$$a_y = g\tan(\phi_h) \tag{5.1.12}$$

The translation control mode is required as a fall-back if more complicated (load sharing) control laws fail. For instance, if there is a cable break, the control system will revert to basic translational control. Then the helicopter will automatically be commanded to return to the landing platform. The reference commands are given in the room frame of reference. The translational controller is designed to control the position error in the body frame of reference.

In order to constrain the velocity and simplify the control design, a controller was designed for the body x and y velocities. From (5.1.11) and (5.1.12) the plant is expected to be essentially an integrator (neglecting the actuator model).

In the event of an unhandled failure in the system, the helicopters must respond fast enough to prevent a crash. Hence, maximum bandwidth while meeting robust stability limit of 6 dB was chosen as the specification. The designed velocity controllers are,

$$g_{vx}(w) = -0.18\,\frac{w/1.1+1}{w} \tag{5.1.13}$$

$$g_{vy}(w) = 0.17\,\frac{w/1.3+1}{w} \tag{5.1.14}$$

The velocity loop design showing the robust stability bounds are shown in Fig. 5.1.9. The magnitude of the sensitivity for the velocity loops given the uncertain plant is shown in Fig. 5.1.10.

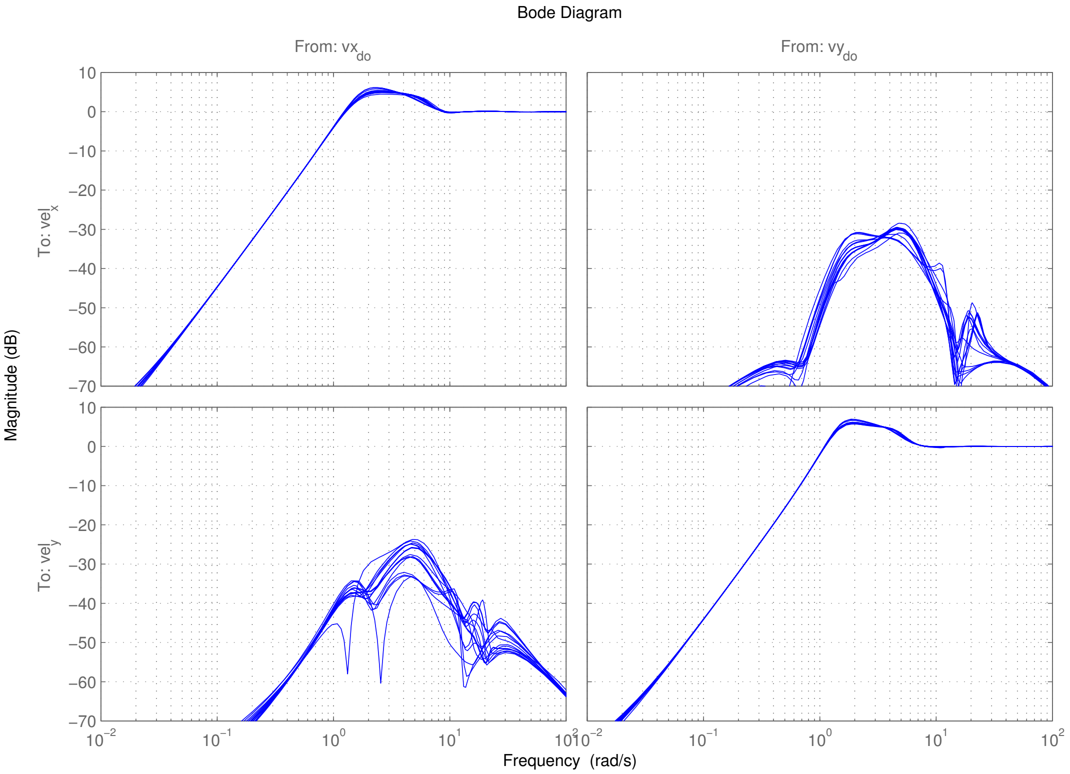

Figure 5.1.10: Magnitude plot of the sensitivity of the velocity loops

5.1.6 Position Controller Design

A cascaded velocity/position loop design approach was taken. In addition to being able to add velocity limits in the velocity loop, the cascaded approach offers a reduction of uncertainty in the inner loop, easing the design of the outer loop (Eitelberg 1999). With the inner velocity loops closed, the position loop controllers were designed to satisfy the 3 dB robust stability requirement with maximum bandwidth. The position loop is only required at startup before the coordinated control scheme takes over. A larger robust stability margin was used in the position loop which also minimises the excitation of the inner loops. The position controller designs are shown in Fig. 5.1.11; the controllers given in (5.1.15) and (5.1.16).

$$g_x(w) = 0.146\,\frac{w/0.53+1}{w} \tag{5.1.15}$$

$$g_y(w) = 0.145\,\frac{w/0.50+1}{w} \tag{5.1.16}$$

In order to command the position independently of the yaw, the position error is mapped into the body frame using the estimated rotation matrix. For small roll and pitch angles,

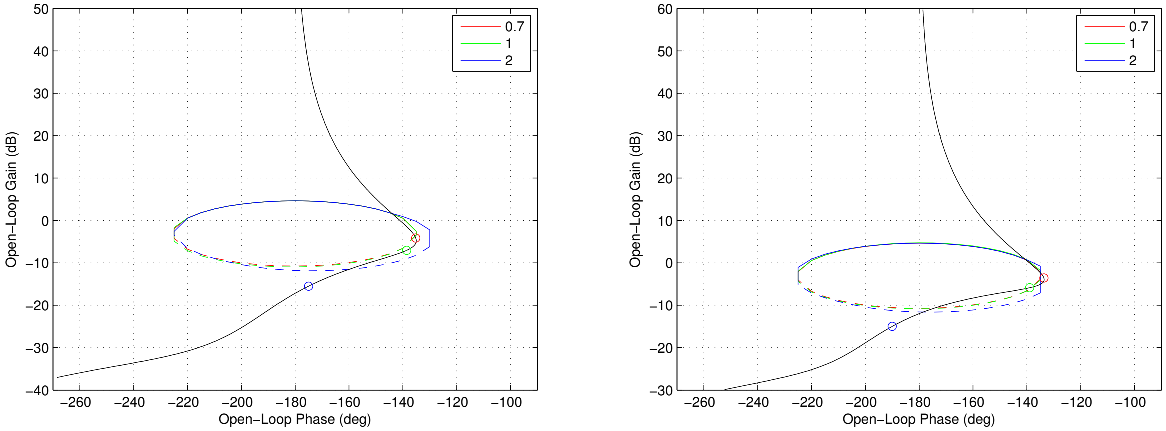

(a) Position loop for body x-axis

(b) Position loop for body y-axis

Figure 5.1.11: Controller design for the position loops

the mapping is,

$$\mathbf{e}_{\mathbf{x}}^{b} \approx \begin{bmatrix} \cos(\psi^e) & -\sin(\psi^e) & 0 \\ \sin(\psi^e) & \cos(\psi^e) & 0 \\ 0 & 0 & 1 \end{bmatrix} \mathbf{e}_{\mathbf{x}}^{e} \tag{5.1.17}$$

where $\mathbf{e}_{\mathbf{x}}^{b}$ is the position error in the body frame.

To test the controllers, the designed controllers were implemented discretely on the on-board computer by applying the Tustin transform (Eitelberg 2000),

$$g(z) = g(w)\Bigg|_{w=\frac{2}{T_s}\ \frac{z-1}{z+1}}$$

to obtain the algorithm. Reference trajectories were given from the base station for position. The telemetry was recorded from the optimal state estimate using the motion capture data and the inertial sensors described in Section 4. The results from one of the tests is shown in Fig. 5.1.12. The first closed-loop test that was done was recorded and can be seen here `https://youtu.be/7Kq4-oiGThU`.

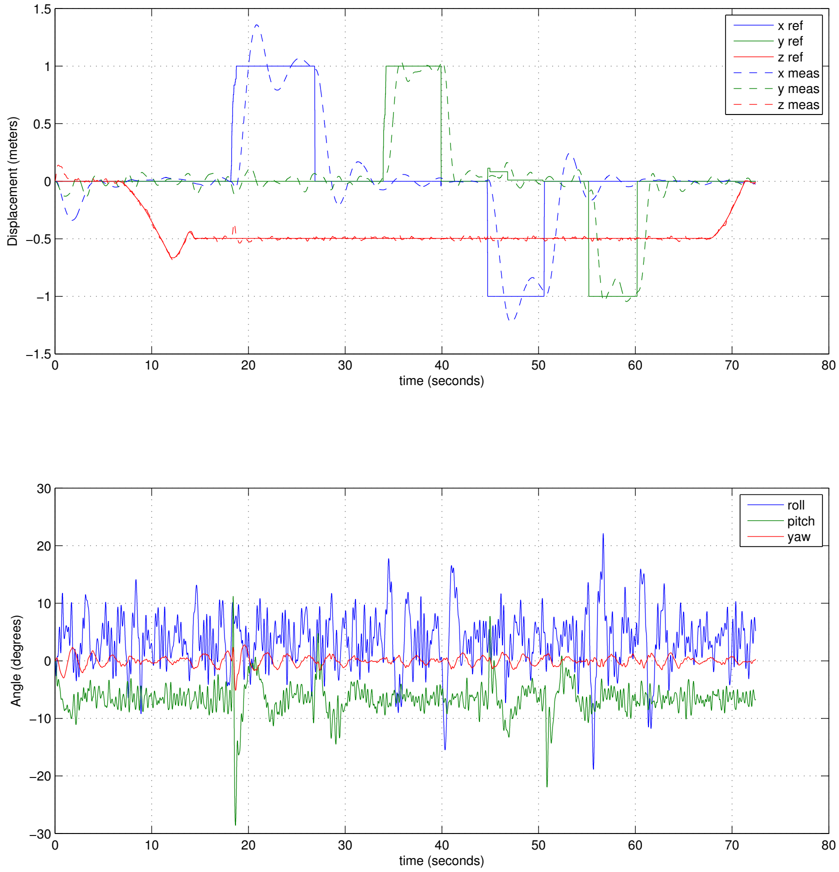

Figure 5.1.12: Helicopter position tracking response; corresponding Euler angles

Figure 5.1.13: A snapshot from an experiment testing position control *see* `https://youtu.be/7Kq4-oiGThU`

5.2 Coordinated Helicopter Control

In this section, a solution for the twin-helicopter slung load transportation system is investigated. The high-level user requirements are presented as guidelines for the design. At first, the approach to an effective solution was not obvious, thus a *trivial solution* was investigated to gain insight into the system dynamics. The trivial solution is presented which consisted of using position control independently on each helicopter to control the load. To gain further insight into the multivariable plant, a *simplified model* of the twin-helicopter slung load system was investigated. In the simplified model, the helicopter dynamics are neglected. The design for the simplified model, suggested using a pre-compensator. This led to the investigation of an optimal *decoupler design*. After the decoupler design, the plant was framed into a 6×6 multivariable plant that allowed for MIMO *QFT design* methodology to be applied. Lastly, in *design discussion*, the results of the design are presented and discussed.

5.2.1 Requirements

A practical way to finding a solution (gradually) to the complicated twin-helicopter slung load system, is a multi-loop control design approach. Although an elaborate controller design (with the least over-design) can be made to act at the actuator inputs, the benefit of abstracting the twin-helicopter load transportation problem at the level of the individual helicopter attitude and altitude control makes it easy to adapt the solution to production helicopters. The aeronautical design standard specification for military rotorcraft ADS-33E, include an Attitude Command/Attitude Hold Response (ACAH) mode (Baskett 2000), this is essentially the lowest level of control that the twin-helicopter load transportation system is divided into. Since some helicopters have this Stability Augmentation System (SAS), it is a matter of convenience to retain the attitude and heave control loops (done in Section 5.1).

The solution should meet the following high-level mission requirements:

1. A means to control the separation distance between the center of mass of the helicopters shall be made available for safety and performance reasons.
2. The operator shall be able to supply reference translational commands for the load to follow.
3. The operator shall be able to supply reference attitude commands for the load to follow.
4. Contention between control should not exist between the pilots.
5. The multi-lift augmentation system (MLAS) shall be able to easily be applied to current stability augmentation systems.

5.2.2 Trivial Solution: Feedback to Helicopter Position

The simplest approach to achieving load translation and attitude control is to command the position of the helicopters such that the reference translation and attitude of the load is achieved. The performance of this strategy may be acceptable if the helicopter control system is capable of sufficiently rejecting the cable force disturbances. Provided that the pendulous mode is sufficiently damped, the position and attitude of the load can be computed from the geometry made between the helicopters and the load. So, feedback is not *required* to achieve the objective. But to accommodate changes in the length of the cable, length of the load and default separation distances, the load error is fed back to drive the helicopter position references.

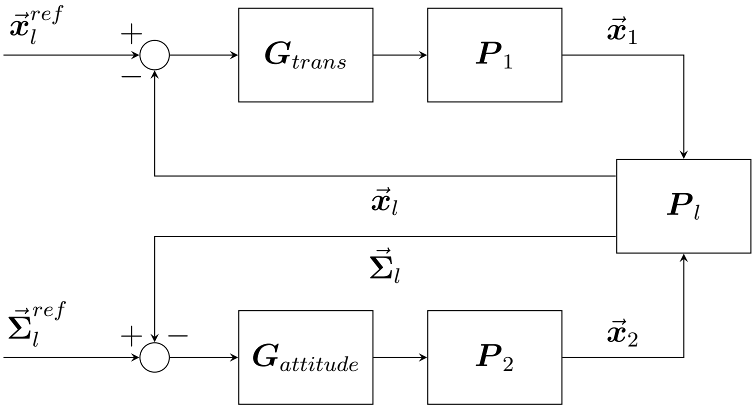

Figure 5.2.1: Control scheme for feeding back load error to helicopter position

The load sharing is resolved by allocating helicopter 1 to control the position of the load, and helicopter 2 to control the attitude of the load. To handle the pendulous mode, an input shaping filter can be implemented. For the parameters of the experiment, it was found through simulation (random load trajectories; high/low bandwidth excitation) that the pendulous mode is sufficiently damped by the combination of aerodynamic drag, the elastic cable and the closed-loop response of the helicopter. The feedback structure for the *trivial solution* is shown in Fig. 5.2.1.

The controller $\boldsymbol{G}_{trans}$ is a diagonal PI controller (parallel form) which generates position reference in the inertial x,y and z axes for helicopter 1. The gains which gave the fastest response (highest closed-loop bandwidth in tracking) are $K_p = 0.1$, $K_i = 0.05$ (any further attempt to increase performance resulted in destabilising the system for sensible step reference inputs). Only the load roll and yaw are actively controlled in this scheme. The controller $\boldsymbol{G}_{attitude}$ is a diagonal PI controller consisting of roll and yaw controllers $\boldsymbol{G}_{attitude} = diag\left([G_{yaw}, 0, G_{roll}]\right)$. The yaw controller gains are $K_p = 0.3$, $K_i = 0.25$ and the roll controller gains are $K_p = 0.4$, $K_i = 0.20$. The roll error generates a reference to the altitude of helicopter 2 and the yaw error generates a reference to the inertial x position of helicopter 2. This asymmetric scheme of controlling the load position with helicopter 1, and the load attitude with helicopter 2, works by regulating the load attitude sufficiently well by helicopter 2. By driving helicopter

1 as a response to a load translation error, a load attitude error is generated. If the attitude error is regulated with sufficient bandwidth both translation and attitude requirements can be met. This *asymmetric* strategy of control allows for helicopters of differing performance to be used; with the higher performing one used for attitude regulation. The disadvantage of this method is that the pendulous modes in the system are not controlled. The other disadvantage is that by design, the translation and attitude responses are coupled. The greatest value of this trivial control mechanism was to get the twin-helicopter load transportation system in a stable nominal configuration where linearisation could be performed to obtain a set of uncertain plants for robust controller design.

The simulation results for a step change in load roll angle is shown in Fig. 5.2.2. The strong coupling in attitude and translation is evident in Fig. 5.2.2. The 3D visualisation of the steady-state pose is shown in Fig. 5.2.3. The highest bandwidth that could be achieved (across all channels) without the system going unstable was approximately 0.1 rad/s in the roll loop with this control strategy.

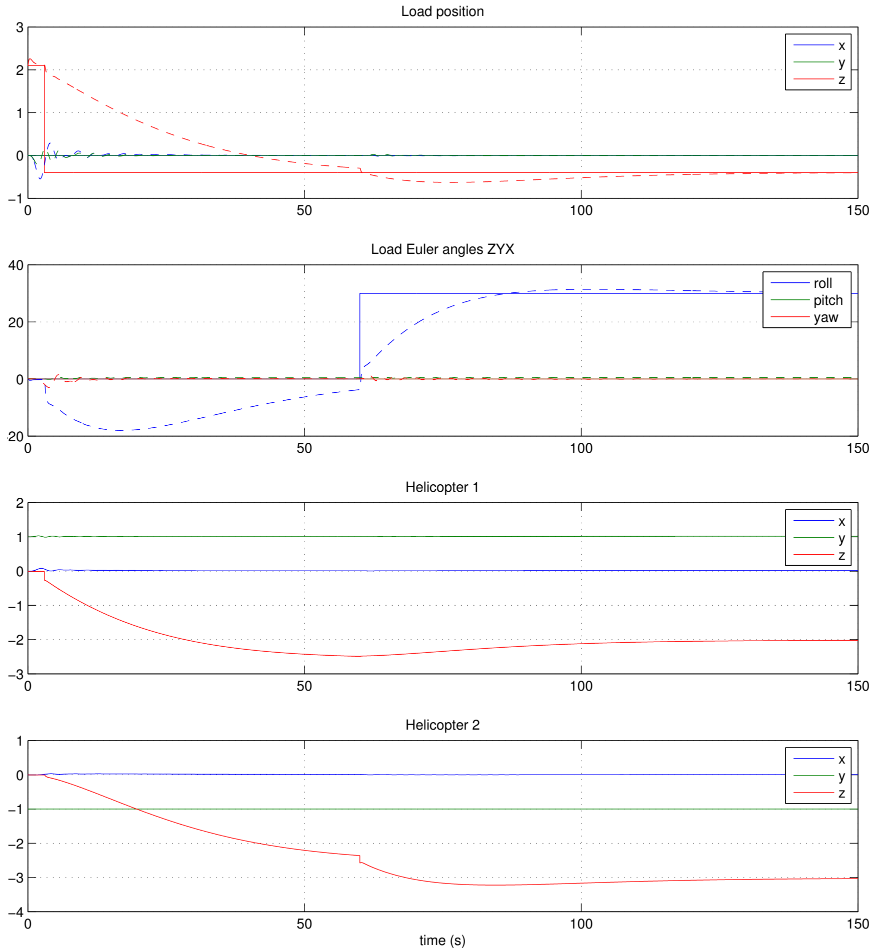

Figure 5.2.2: Simulation response of load control using feedback to helicopter positions; Load position and Euler angles (ZYX - yaw, pitch, roll sequence) show the reference in solid lines

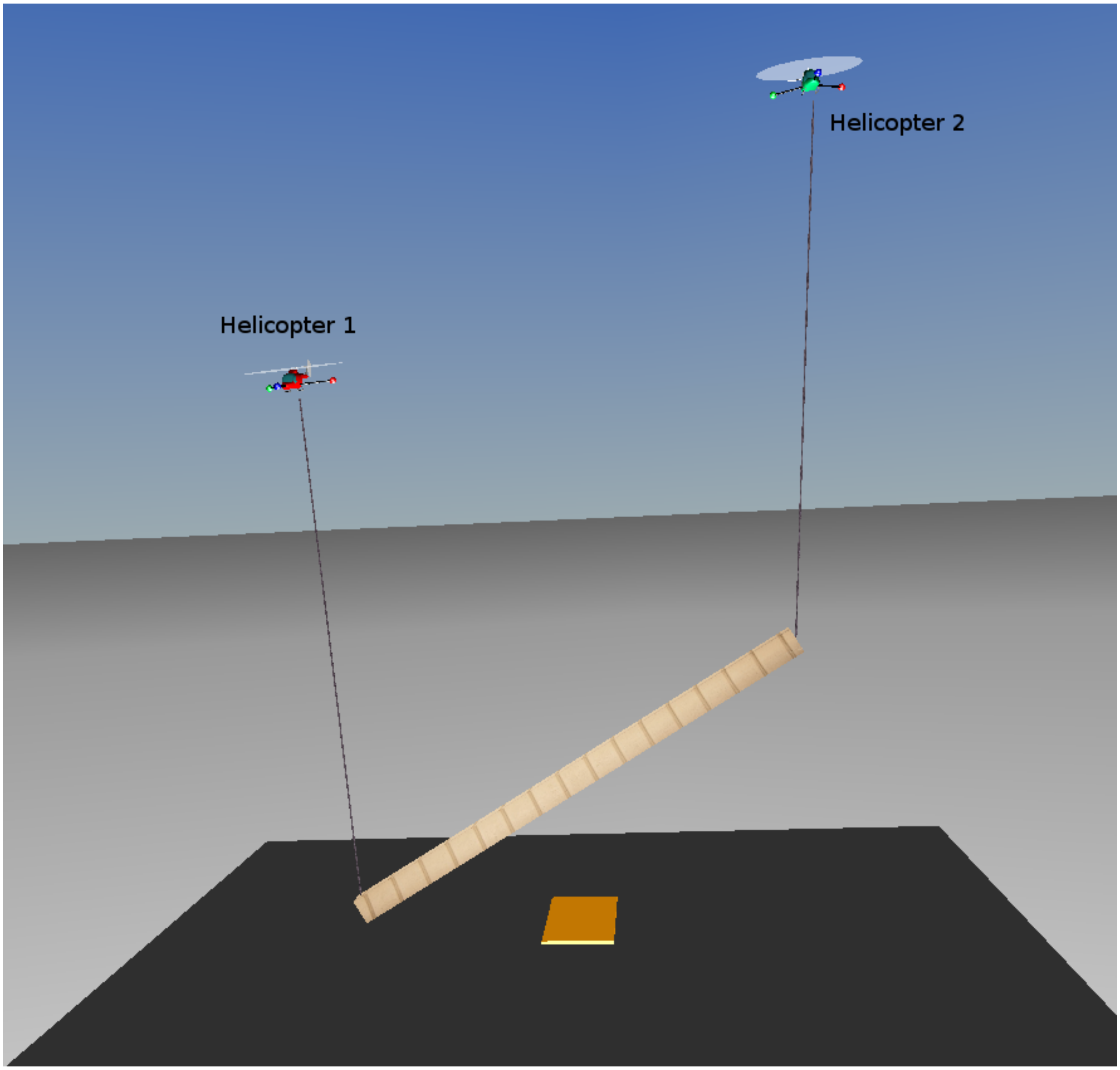

Figure 5.2.3: Animation of simulation showing steady state pose

5.2.3 Simplified Model

To investigate a control structure that could possibly work for the twin-helicopter load transportation system, a simplified model of the system was studied. The helicopters were replaced with point masses with force inputs. In this way, the load sharing problem can be investigated without the complexity of the helicopter dynamics.

The objective is to control the load translation and attitude. A top-down approach is taken in solving the problem. Starting of with the translation, Newtonian mechanics require that a resultant force be applied to the center of the mass of the load. A controller can be designed to generate the required force on the load to meet some performance criteria. Implementation of the force on the load may now be considered. Since there is a cable attached to each end of the load in a *symmetric manner*, it is sensible to split the translation force requirement equally. Going one step lower, the implementation of the force at each attachment point must be considered. Assuming the that the force requirement can be tracked with sufficiently high bandwidth, the outer loop translation requirements will be met.

Similarly, a net torque at the center of mass of the load is required to generate an attitude change. To accommodate this, a form of differential control can be done to the force signal generated from the translation controller. This will allow for both attitude and translation requirements to be achieved provided that the inner loop is capable of tracking the force requirements. This control scheme is illustrated in Fig. 5.2.4. Block $\boldsymbol{K}$ can be thought of as a static decoupler in the scheme.

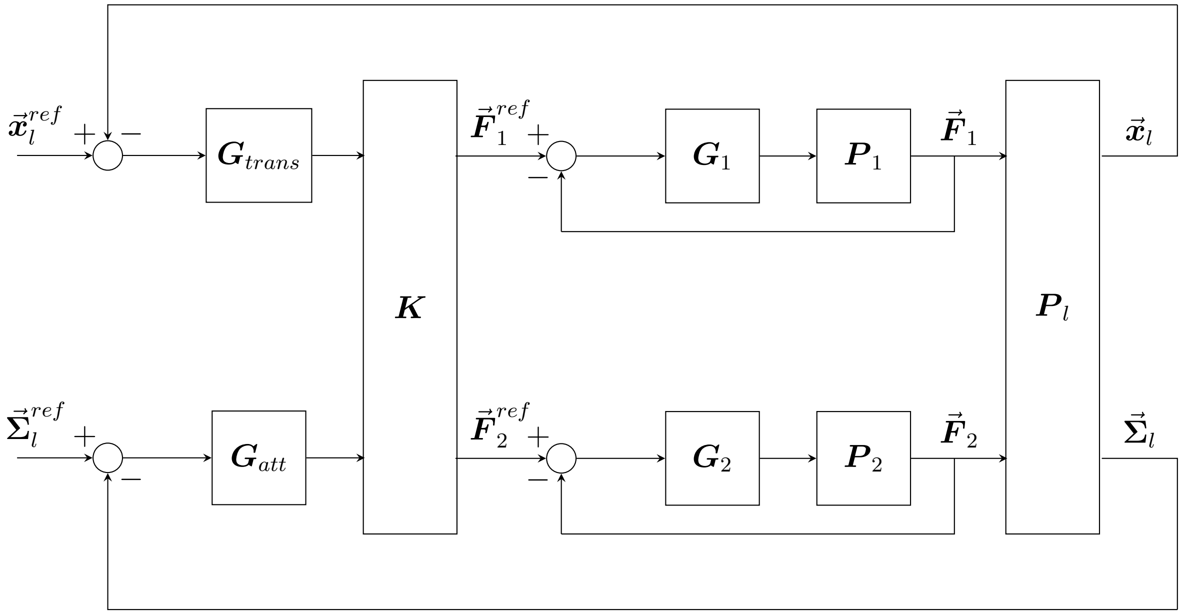

Figure 5.2.4: Control scheme: differential control with force tracking

The feedback loops $\boldsymbol{L}_1 = \boldsymbol{P}_1\boldsymbol{G}_1$ and $\boldsymbol{L}_2 = \boldsymbol{P}_2\boldsymbol{G}_2$ are the force control loops. The simplified plants are given by $\boldsymbol{P}_i = M_{h,i}\ diag(\dot{\vec{\boldsymbol{v}}}_h^{e,i})$ for $i = 1, 2$ in the inertial frame. The static decoupler (or mixer) can be represented in matrix form as,

$$\boldsymbol{K} = \begin{bmatrix} 0.5 & 0 & 0 & 0 & 1 & -1 \\ 0 & 0.5 & 0 & 0 & 0 & 0 \\ 0 & 0 & 0.5 & 1 & 0 & 0 \\ 0.5 & 0 & 0 & 0 & 1 & 1 \\ 0 & 0.5 & 0 & 0 & 0 & 0 \\ 0 & 0 & 0.5 & -1 & 0 & 0 \end{bmatrix} \tag{5.2.1}$$

with the following input order $\vec{\boldsymbol{u}} = [u_x,\ u_y,\ u_z,\ u_\phi,\ u_\theta,\ u_\psi]^T$ and output order $\vec{\boldsymbol{y}} = \left[\vec{\boldsymbol{F}}_1^{ref^T},\ \vec{\boldsymbol{F}}_2^{ref^T}\right]^T$. In the above control structure, the dynamics of the twin-lift system gets contained in the force control loops. The cross-coupling is significant at this level and large loop gain is required to decouple the system, which may not be possible with the helicopters in the loop. Figure 5.2.5 shows a bode plot of the controller (diagonal and equal for each channel) required to stabilise the inner force loops. A stabilising solution was found by designing controllers with a notch filter around the pendulous resonant frequency, phase lead and gain for the inner force loops. Stabilising the outer position loops just requires phase lead at the gain cross-over frequency. The simplified problem was investigated to find a possible control structure that could be applied to the twin-helicopter load transportation

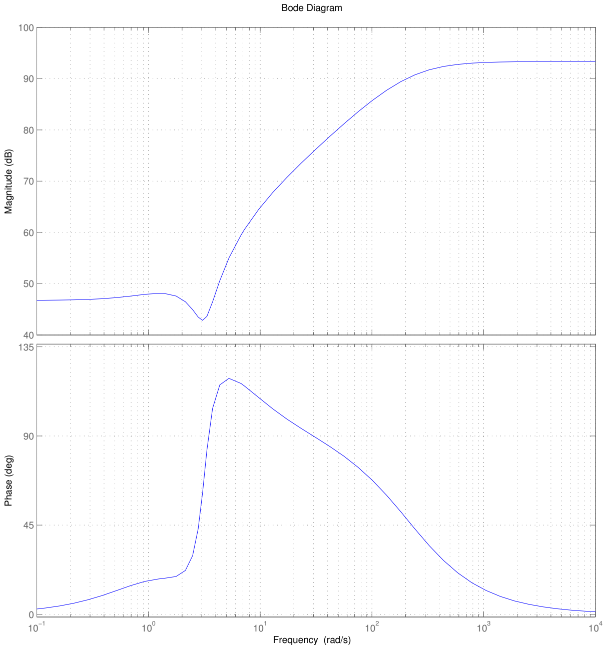

Figure 5.2.5: Bode plot of force controller

system. Figure 5.2.6 shows the tracking response for both translation and attitude. The stabilisation using this control structure shows that if the bandwidth limitations of helicopters are not severe, a similar control structure may be feasible.

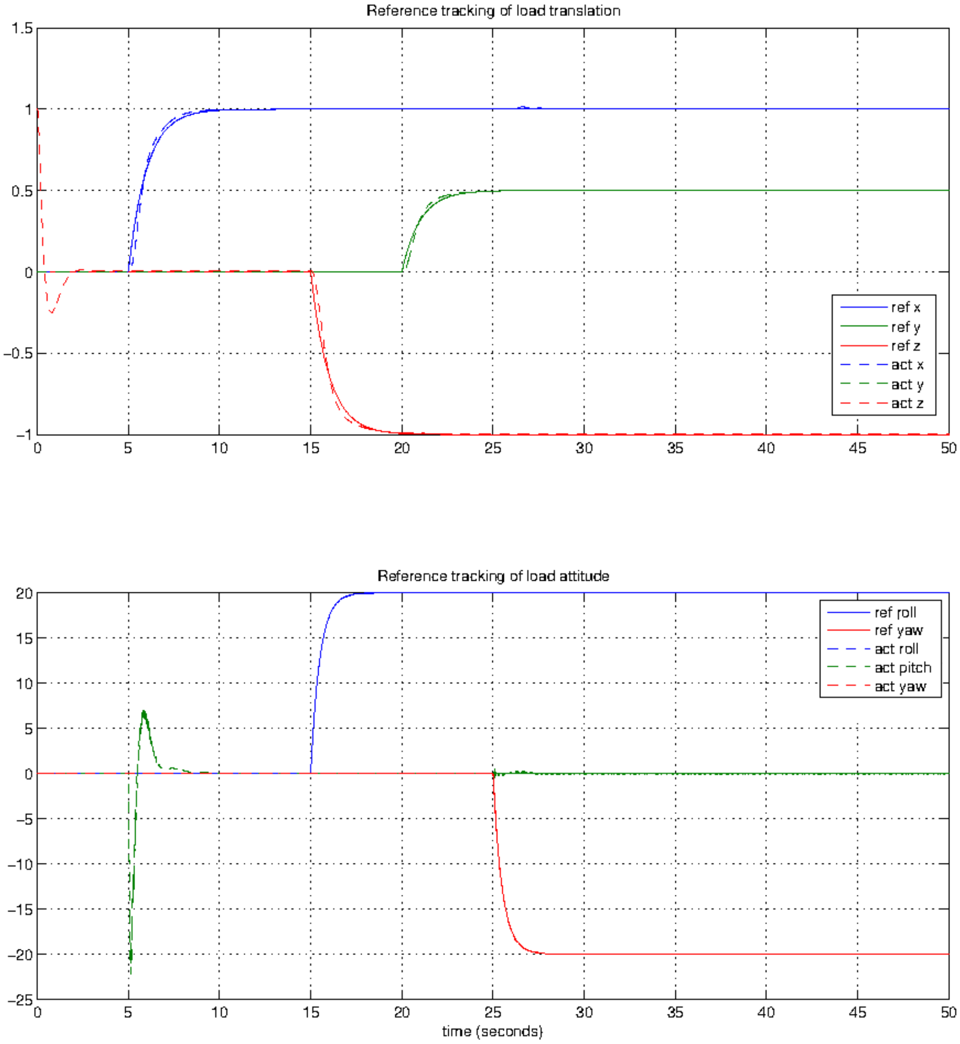

Figure 5.2.6: Simulation response of simplified model showing stable tracking

Decomposing the problem into two major loops seems beneficial to the implementation in the real system as well. Individual helicopters may embed tension sensors in the cable attachment mechanism and the attitude can be controlled to track the tension (with appropriate frame of reference mapping). A decentralised controller can generate the required force to be tracked and transmitted to the force controllers of each helicopter.

5.2.4 Decoupler Design

A stabilising solution using the tension tracking approach described in Section 5.2.3 to the twin-helicopter load transportation system was not found. This is due to the bandwidth limitations of the helicopters. The cross-coupling in the twin-helicopter system was too high and insufficient bandwidth was available (due to delay) to decouple the dynamics, which was not the case with the simplified model. Thus, the force loops were removed.

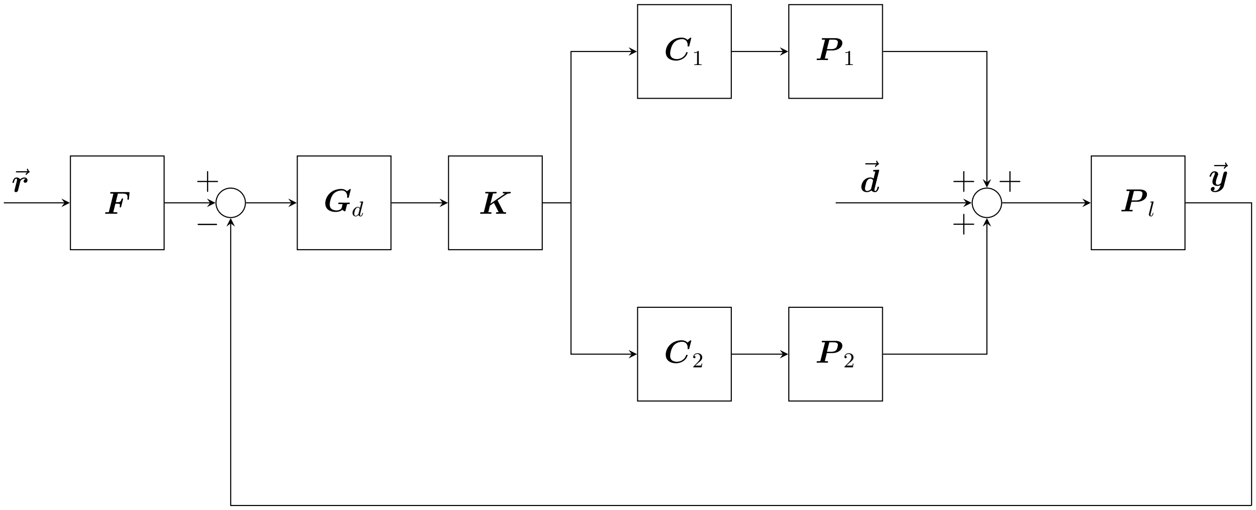

Figure 5.2.7: Coordinated load sharing control structure

A classical coordinated load sharing control structure, adopted from Eitelberg (1999), shown in Fig. 5.2.7, was believed to be a plausible architecture for solving the twin-helicopter slung load system. The helicopter plants are represented by $\boldsymbol{P}_1$ and $\boldsymbol{P}_2$, the decentralised controller $\boldsymbol{G}_d$, static decoupler $\boldsymbol{K}$, the load dynamics $\boldsymbol{P}_l$ and the pre-filter $\boldsymbol{F}$. The possibly dynamic feedback blocks $\boldsymbol{C}_1$ and $\boldsymbol{C}_2$ distribute the control effort between supply plants as described in Eitelberg (1999). Considering the helicopters as supply plants with interaction, one may view general interaction in terms of a clever sketch by Eitelberg (2003), shown in Fig. 5.2.8.

The role of the interaction index in multivariable control design was explained in Section 5.1.1. The equivalent plant excluding the pre-compensator in Fig. 5.2.7 is given by,

$$\boldsymbol{P}_e = \boldsymbol{P}_l\left(\boldsymbol{P}_1 + \boldsymbol{P}_2\right), \ldots \boldsymbol{C}_1 = \boldsymbol{C}_2 = \boldsymbol{I} \tag{5.2.2}$$

The open-loop interaction index of the uncertain plant set of the equivalent plant $\boldsymbol{P}_e$ (with helicopter parameter uncertainty and load mass uncertainty) is shown in Fig. 5.2.9. The spectral radius of the interaction matrix (5.1.2), is much larger than unity and hence the plant is far from exhibiting *diagonally dominance* (Boje 2002).

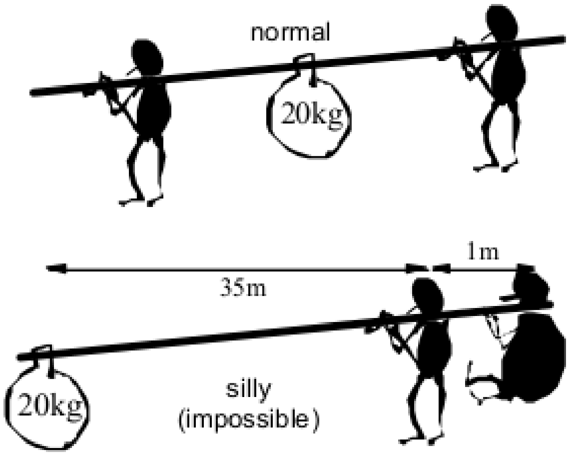

Figure 5.2.8: Load sharing example of “low and high interaction” (Eitelberg 2003)

Based on the control authority allocation done in Section 5.2.3, the plant was pre-compensated using differential control in the form of the pre-compensator,

$$\boldsymbol{K} = \begin{bmatrix} 0.5 & 0 & 0 & 0 & 1 & 0 \\ 0 & 0.5 & 0 & 0 & 0 & 1 \\ 0 & 0 & 0.5 & 1 & 0 & 0 \\ 0.5 & 0 & 0 & 0 & 1 & 0 \\ 0 & 0.5 & 0 & 0 & 0 & -1 \\ 0 & 0 & 0.5 & -1 & 0 & 0 \end{bmatrix} \tag{5.2.3}$$

for the augmented plant (addition of separation control output). A much lower peak and average interaction index over the plant uncertainty was obtained, this is shown in Fig. 5.2.10. The interaction index in the frequency range of interest was significantly reduced, although not less than unity.

Due to the reduction in the interaction index obtained from using a general differential decoupler, it was decided to investigate finding an *optimal* static pre-compensator (optimal in the sense of maximum cross-coupling reduction near the gain cross-over frequency through mixing rather than high gain). The benefit of interaction index reduction is a reduction in the required loop gain to achieve performance specifications as well as a justification for closed-loop stability (Boje 2002). If the spectral radius (interaction index) of the interaction matrix 5.1.2, is less than unity for all frequencies, instability cannot come from the cross-coupling. The methodology found in Boje & Nwokah (1999) was used to find the optimal static pre-compensator. The nominal plant was inverted across a set of frequencies close to the expected gain cross-over frequency. The inverse of the plant at $\omega = 0.954\,\text{rad/s}$ was found to produce the *best reduction* in the interaction index near the gain cross-over frequency (over uncertainty). The ALIGN algorithm of Kouvaritakis’ (Maciejowski 1989), (Skogestad & Postlethwaite 2007) was then used to find a real approximation of the complex static pre-compensator. The real approximation to the static pre-compensator found is,

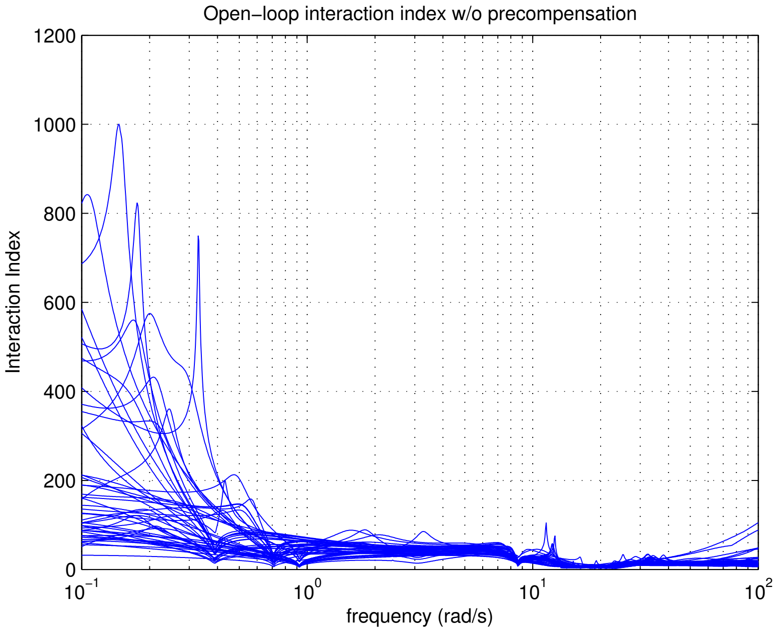

Figure 5.2.9: Open-loop interaction index of the uncertain plant set without precompensation

$$\begin{aligned}\boldsymbol{K} &= \text{ALIGN}\left(\boldsymbol{P}(j0.954)^{-1}\right)\\ &= \begin{bmatrix} 0.0753 & 0 & -0.0012 & -0.0010 & -0.0851 & 0 \\ 0.0002 & -0.0720 & -0.0011 & 0.0009 & -0.0325 & -0.0224 \\ -0.0004 & -0.0007 & 0.9872 & 0.9665 & 0.0001 & 0.0031 \\ 0.0753 & 0 & -0.0012 & 0.0010 & 0.0815 & 0 \\ 0.0002 & -0.0720 & -0.0011 & 0.0010 & -0.0320 & 0.0224 \\ -0.0004 & -0.0007 & 0.9874 & -0.9667 & -0.0003 & -0.0032 \end{bmatrix}\end{aligned} \tag{5.2.4}$$

The resulting interaction index using the optimal pre-compensator is shown in Fig. 5.2.11 for the uncertain plant set. The pre-compensator reduces the interaction index to below unity for frequencies up to 13.3 rad/s. The reduction in interaction index using the optimal pre-compensator is significantly greater than that of the *differential decoupler*.

An alternative perspective on the interaction can be gained from assessing the Bristol gains. The Bristol gain matrix is defined as (Eitelberg 2006),

$$\boldsymbol{B}(s) = \boldsymbol{P}(s) \times \left[\boldsymbol{P}^{-1}(s)\right]^{T} \tag{5.2.5}$$

where × in the above equation represents the Hadamard product (element-by-element product) and $\boldsymbol{P}$ is the plant. Bristol (1966) argued that the element $[\boldsymbol{B}(s)]_{ij}$ is a measure of the interaction from the *jth* input to the *ith* output. The Bristol gain plot (envelope across uncertainty) shown in Fig. 5.2.12, shows that after pre-compensation, the diagonal elements become close to unity in the frequency range of interest.

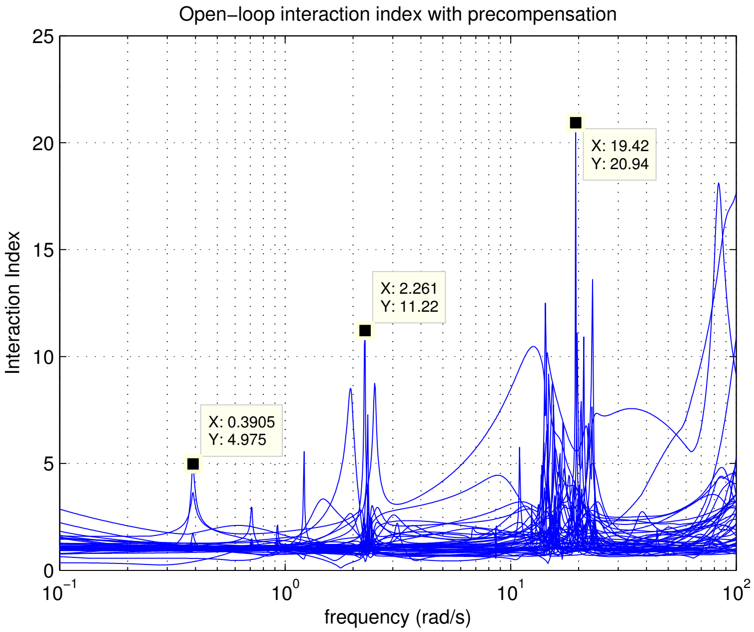

Figure 5.2.10: Open-loop interaction index of the uncertain plant set using the *intuitive* decoupler

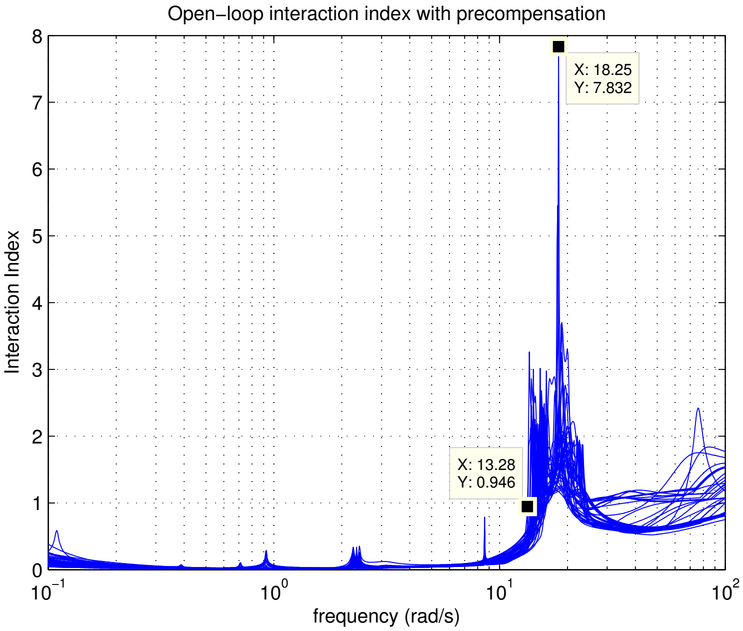

Figure 5.2.11: Open-loop interaction index of the uncertain plant set using the optimal static pre-compensator

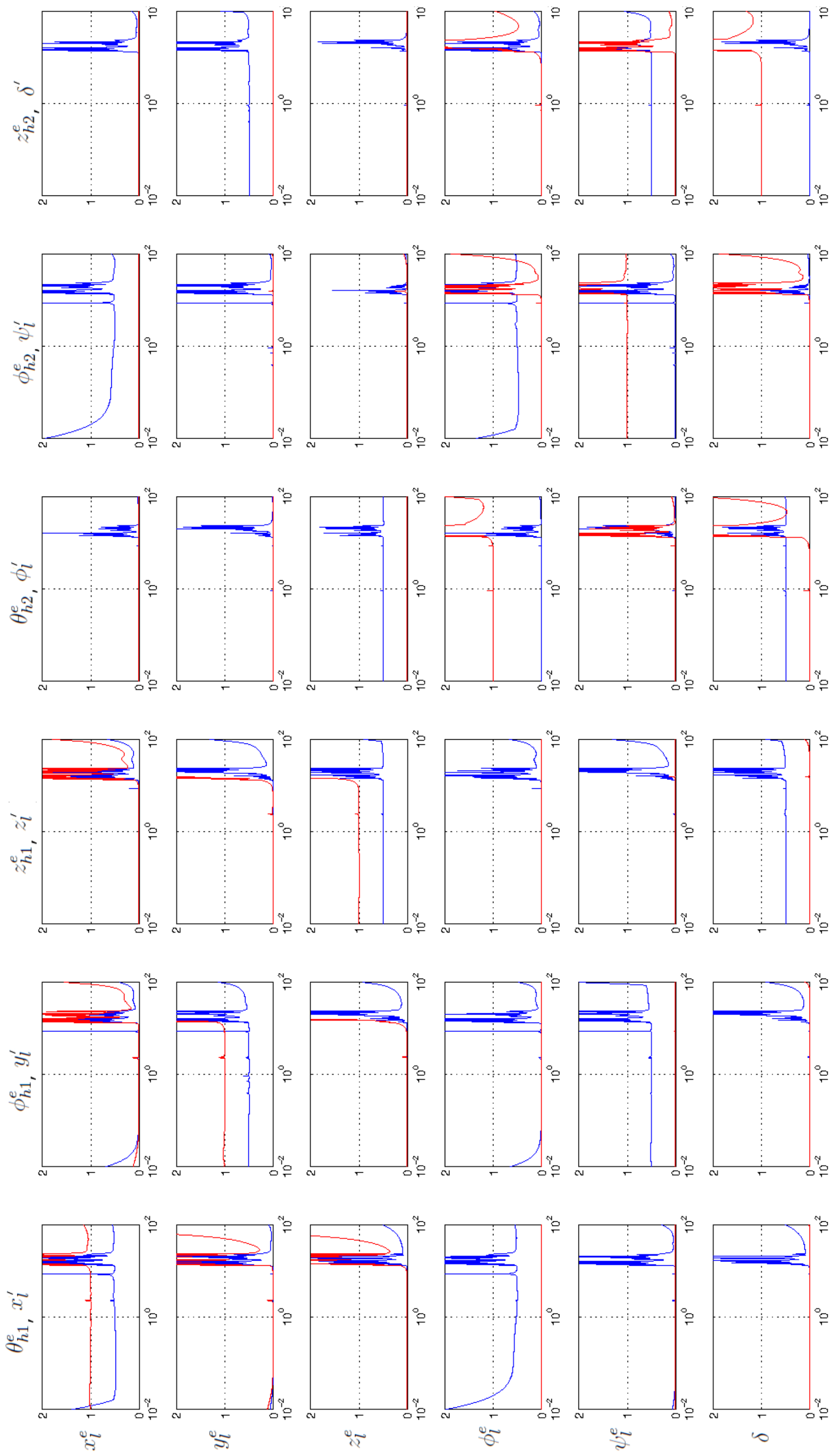

Figure 5.2.12: Plot of the Bristol gains (maximum values across uncertainty set) before (blue) and after pre-compensation (red); x-axis represents frequency in rad/s. Primed inputs depicted, represent the pre-compensated plant inputs.

5.2.5 Multivariable QFT Controller Design

It was shown in Section 5.2.4, that a static pre-compensator $\boldsymbol{K}$, exists that significantly reduces the cross-coupling across the uncertain plant set. Now, a decentralised controller will be designed using QFT. The resulting controller $\boldsymbol{G} = \boldsymbol{K}\boldsymbol{G}_d$, is non-diagonal. The effect of cross-coupling, parameter uncertainty and delay on the multi-resonant mode plant make the control design difficult. QFT is used in this regard to gain transparency to the effect of loop shaping (in particular the phase response) on the robust stability of the system. The specification for design is to meet plant output disturbance rejection specification for the uncertain system. A Bode magnitude plot of the uncertain *pre-compensated* plant set is shown in Fig. E.3.1.

The uncertainty in the twin-helicopter slung load plant comes from the individual helicopter parameter uncertainty as well as for designing for a particular load mass range. The effect of the helicopter parameter uncertainty is reduced as a result of the inner attitude loops of the helicopters. The load mass uncertainty is 70% of its nominal value; this corresponds to a load mass uncertainty of between (approximately) 6% − 36% of the mass of a single helicopter. The mass distribution across the load was assumed to be uniform, hence the load inertia becomes an uncertain parameter too.

Design Specifications

Due to the difficulty of the design, aim was to find a robust stability solution that maximised the bandwidth for the uncertain plant set - no further constraints where imposed. The output disturbance rejection specifications is,

$$\left|\boldsymbol{T}(j\omega)\right|_{ij} = \left|(\boldsymbol{I} + \boldsymbol{L}(j\omega))^{-1}\right|_{ij} \leq \left|\boldsymbol{A}(j\omega)\right|_{ij} \tag{5.2.6}$$

where $\boldsymbol{L}(j\omega) = \boldsymbol{P}(j\omega)\boldsymbol{K}\boldsymbol{G}_d(j\omega),\ \boldsymbol{P}(j\omega) \in \mathbb{P}$. The equivalent plant $\boldsymbol{P}_e$ in (5.2.2) is represented in this section by $\boldsymbol{P}$. The dependence on the complex variable $s = j\omega$ is omitted for brevity in the following section. The output disturbance rejection specification for each channel $\left|\boldsymbol{A}(j\omega)\right|_{ij}$, is given in Eqs. E.3.1 - E.3.36.

MIMO QFT Design Equations

A comprehensive development of the current state of the art of multivariable QFT can be found in Yaniv (2013) or Houpis et al. (2006). The design equation for disturbance rejection using a *diagonal splitting* (Horowitz 2001), (Horowitz 1982) is given by,

$$\begin{aligned}\boldsymbol{T} &= \left(\hat{\boldsymbol{P}}^{*}{}_{D} + \boldsymbol{G}_d\right)^{-1}\hat{\boldsymbol{P}}^{*} - \left(\hat{\boldsymbol{P}}^{*}{}_{D} + \boldsymbol{G}_d\right)^{-1}\hat{\boldsymbol{P}}^{*}{}_{O}\boldsymbol{T} \\ &= \left(\hat{\boldsymbol{P}}^{*}{}_{D} + \boldsymbol{G}_d\right)^{-1}\hat{\boldsymbol{P}}^{*} - \boldsymbol{X}\boldsymbol{T}\end{aligned} \tag{5.2.7}$$

where $\hat{\boldsymbol{P}}^{*} = (\boldsymbol{P}\boldsymbol{K})^{-1}$ is the inverse of the pre-compensated plant. The *diagonal splitting*, splits the equivalent plant $\hat{\boldsymbol{P}}^{*}$, into $\hat{\boldsymbol{P}}^{*}{}_{D} + \hat{\boldsymbol{P}}^{*}{}_{O}$, where $\hat{\boldsymbol{P}}^{*}{}_{D}$ contains the diagonal elements of $\hat{\boldsymbol{P}}^*$, and $\hat{\boldsymbol{P}}^*{}_O$ contains the off-diagonal elements of $\hat{\boldsymbol{P}}^*$. The design equations in scalar form may be written as,

$$t_{ij} = \frac{q_{ii}^*}{1+g_i q_{ii}^*}\left(\frac{1}{q_{ij}^*} - \sum_{k=1,k\neq i}^{n} \frac{1}{q_{ik}^*} t_{kj}\right), \qquad i,j = 1,\ldots,6. \tag{5.2.8}$$

where t_{ij} is the (i,j) element of $\boldsymbol{T}$, and $q_{ij}^* = 1/[\hat{\boldsymbol{P}}^*]_{ij}$. The design equations are implicit in the *specifications*, and since t_{kj} are not known a priori, they are bounded by the specifications during design process. This is a source of conservatism in the design methodology. As loops are designed, the known t_{kj} can be substituted into subsequent loop design equations to reduce conservatism. By applying the Schwarz inequality to (5.2.8), the design equations for row one are:

$$\begin{aligned} t_{11} &\leq \left|\frac{1}{1+l_1^*}\right| \left(1 + \left|\frac{q_{11}^*}{q_{12}^*}\right| |t_{21}| + \left|\frac{q_{11}^*}{q_{13}^*}\right| |t_{31}| + \left|\frac{q_{11}^*}{q_{14}^*}\right| |t_{41}| + \left|\frac{q_{11}^*}{q_{15}^*}\right| |t_{51}| + \left|\frac{q_{11}^*}{q_{16}^*}\right| |t_{61}|\right) \\ &\leq |t_{11}| \end{aligned} \tag{5.2.9}$$

$$\begin{aligned} t_{1j} &\leq \left|\frac{1}{1+l_1^*}\right| \left(\left|\frac{q_{11}^*}{q_{1j}^*}\right| + \left|\frac{q_{11}^*}{q_{12}^*}\right| |t_{2j}| + \left|\frac{q_{11}^*}{q_{13}^*}\right| |t_{3j}| + \left|\frac{q_{11}^*}{q_{14}^*}\right| |t_{4j}| + \left|\frac{q_{11}^*}{q_{15}^*}\right| |t_{5j}| + \left|\frac{q_{11}^*}{q_{16}^*}\right| |t_{6j}|\right) \\ &\leq |t_{1j}| \qquad j = 2,\ldots,6. \end{aligned} \tag{5.2.10}$$

The *genbnds(10,...)* command from Matlab's ® QFT Toolbox (Borghesani et al. 1994) computes the nominal loop bounds for a linear fractional inequality of the form,

$$\left|\frac{A+BG}{C+DG}\right| < W_s \tag{5.2.11}$$

where G is the controller and W_s represent the weight obtained from the specifications. The latest QFT toolbox is available from (Garcia-Sanz 2008-2017). The design equations (5.2.9), (5.2.10), are then mapped to (5.2.11) to generate the nominal loop gain bounds. Unlike in the H$_\infty$ design methodology, the choice of the nominal plant for a QFT design does not affect the performance (Sidi 2001). For convenience, the first plant of the set was used as the nominal plant $\boldsymbol{P}_0(s)$.

Initial Controller Design

The loop design of the load translation in x was investigated first. It was noted, that the loop bounds were too constrained and was impossible to meet without using impractical controller elements (damping factors of less than 0.001). The reduction of the interaction index in the expected gain cross-over frequency range via static pre-compensation was the best that could be achieved. There was no obvious means known to further reduce the conservativeness of the initial loop design. It became apparent upon a re-analysis of the Bristol gains plotted in Fig. 5.2.12, that after pre-compensation, the load translational dynamics were largely decoupled from the attitude and separation dynamics. To determine whether it was possible to break the plant into two 3×3 plants and still achieve stability, a block diagonal splitting was performed on the plant. If the 6×6 plant could be stabilised by two diagonal controllers, that would reduce the conservativeness of the bounds for the sub-plants, although the 6×6 disturbance specifications would not be expected to be met completely. The benefit of this approach is that an initial stabilising controller can be obtained. Through iteration, the controller can be tuned to meet the original specifications (if possible).

Performing the *block diagonal* splitting for output disturbance rejection one gets,

$$\begin{aligned} \boldsymbol{T} &= \left(\hat{\boldsymbol{P}}^{*}{}_{BD} + \boldsymbol{G}_{Bd}\right)^{-1} \hat{\boldsymbol{P}}^{*} - \left(\hat{\boldsymbol{P}}^{*}{}_{BD} + \boldsymbol{G}_{Bd}\right)^{-1} \hat{\boldsymbol{P}}^{*}{}_{BO}\boldsymbol{T} \\ &= \left(\hat{\boldsymbol{P}}^{*}{}_{BD} + \boldsymbol{G}_{Bd}\right)^{-1} \hat{\boldsymbol{P}}^{*} - \boldsymbol{X}_{BD}\boldsymbol{T} \end{aligned} \tag{5.2.12}$$

with $\hat{\boldsymbol{P}}^{*} = \left[\begin{array}{c|c} \hat{\boldsymbol{P}}^{*}{}_{11} & \hat{\boldsymbol{P}}^{*}{}_{12} \\ \hline \hat{\boldsymbol{P}}^{*}{}_{21} & \hat{\boldsymbol{P}}^{*}{}_{22} \end{array}\right]$, $\boldsymbol{G}_{Bd} = \left[\begin{array}{c|c} \boldsymbol{G}_{11} & \boldsymbol{0} \\ \hline \boldsymbol{0} & \boldsymbol{G}_{22} \end{array}\right]$, $\boldsymbol{P}^{\hat{*}}_{BD} = \left[\begin{array}{c|c} \hat{\boldsymbol{P}}^{*}{}_{11} & \boldsymbol{0} \\ \hline \boldsymbol{0} & \hat{\boldsymbol{P}}^{*}{}_{22} \end{array}\right]$ and $\hat{\boldsymbol{P}}^{*}{}_{BO} = \left[\begin{array}{c|c} \boldsymbol{0} & \hat{\boldsymbol{P}}^{*}{}_{12} \\ \hline \hat{\boldsymbol{P}}^{*}{}_{21} & \boldsymbol{0} \end{array}\right]$. Each of the block matrices are 3×3. The *interaction index* (see Section 5.1.1) of the open-loop system with a block diagonal splitting is shown in Fig. 5.2.13. Since the interaction index for the block diagonal splitting is less than unity for all frequencies, it is a sufficiency condition that the 6×6 system will be stable, provided the two 3×3 subsystems are stable by the application of Limebeer (1982) on block diagonal splitting. Note that the comparison of interaction index in the case above, is not a relative comparison of general interaction. The application of the Perron root to the second terms in (5.2.7) and (5.2.12) allows a way to determine whether those terms can destabilise the MIMO system.

The following design is cast onto the w-domain for digital implementation. The mapping of the effect of sampling into the w-domain is explained in Section 5.1.2. The controller is shaped in the w-domain, and the digital algorithm can be obtained by applying the Tustin transform to the controller,

$$G(z) = G(w)\bigg|_{w=\frac{2}{T_s}\frac{z-1}{z+1}} \tag{5.2.13}$$

to obtain the controller in the z-domain (Eitelberg 1988).

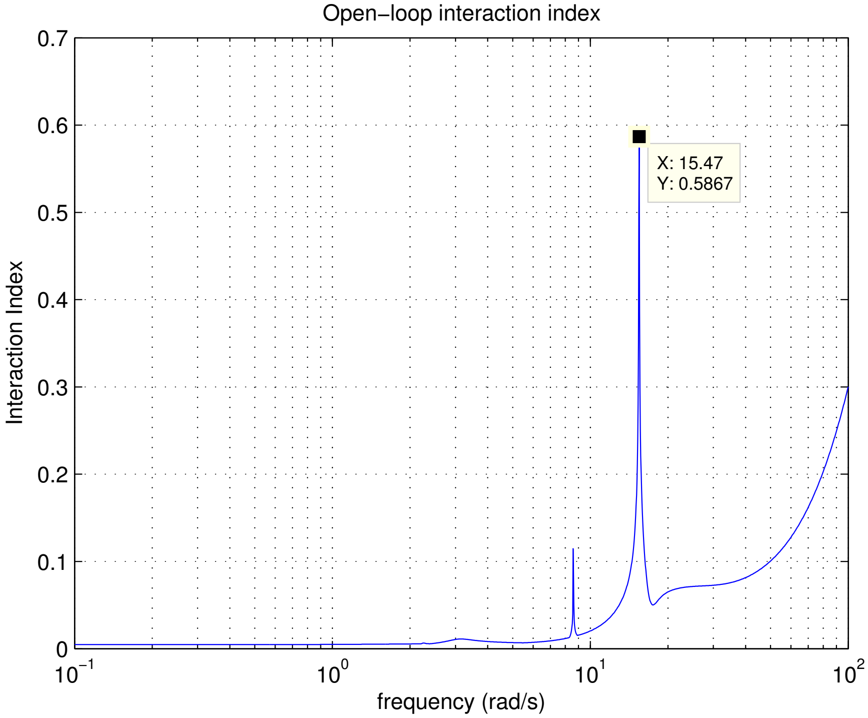

Figure 5.2.13: Open-loop interaction index of the 6×6 plant with a block diagonal splitting

Loop Shaping the Initial Controller

Using the justification above for splitting the system, an initial controller will be designed for each of the 3×3 subsystems. The translational dynamics are referred to as the *block 1* subsystem, and the attitude and separation dynamics referred to as the *block 2* subsystem.

Loop 1 of block 1: Load translation in x The controller that shapes the nominal loop to meet the bounds for the translation x loop is shown in Fig. 5.2.14. The controller is given in (5.2.14). The nominal loop gain cross-over is 0.3 rad/s.

$$g_{11a}(w) = -0.0043\,\frac{w/0.1+1}{w}\,\frac{w/0.115+1}{w/1.115+1}\,\frac{1}{(w/3)^2+2\cdot 0.707\cdot w/3+1} \tag{5.2.14}$$

Loop 2 of block 1: Load translation in y The controller that shapes the nominal loop to meet the bounds for the translation y loop is shown in Fig. 5.2.15. The controller is given in (5.2.15). The nominal loop gain cross-over is 0.32 rad/s. Low frequency over-design was required to meet specifications near the gain cross-over frequency. One can see that the delay after the 2.2 rad/s resonant mode is so large in loop 1 and 2, that the ability to get significantly larger gain cross-over frequencies is practically impossible.

$$g_{22a}(w) = -0.0047\,\frac{w/0.1+1}{w}\,\frac{w/0.095+1}{w/0.95+1}\,\frac{1}{(w/3)^2+2\cdot 0.6\cdot w/3+1} \tag{5.2.15}$$

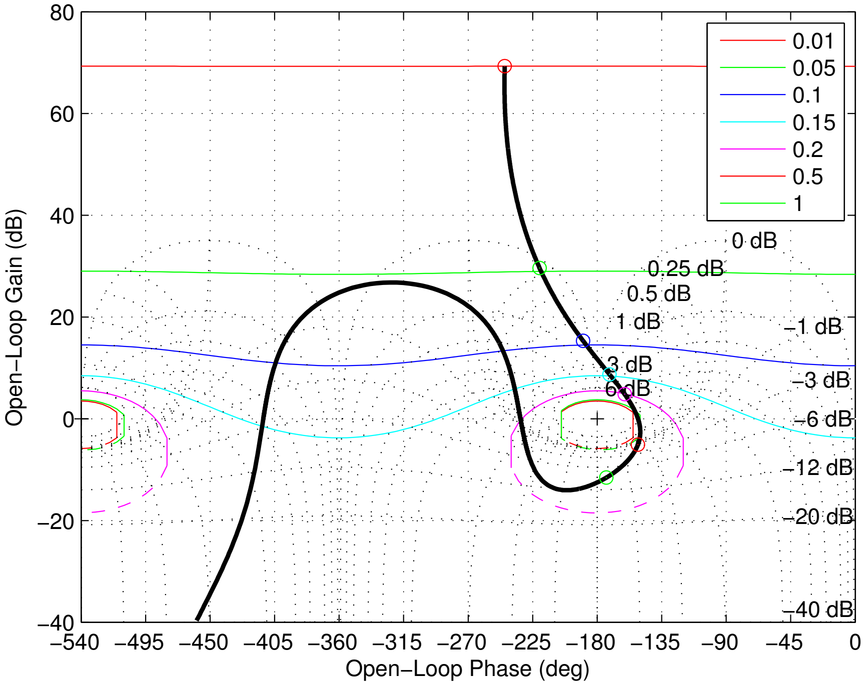

Figure 5.2.14: Load x-axis translation controller design $l_{11a}(w) = p_{11a}g_{11a}$

Loop 3 of block 1: Load translation in z Interaction around the loop gain cross-over frequency of the translation in z was manifested as very conservative loop boundaries. Horowitz' *improved method* (Horowitz 1982) was used to reduce to conservative loop boundaries. A comparison of the loop boundaries of using the exact design equations versus the over-bound design equations can be seen in Fig. 5.2.16, with the satisfying nominal loop design. The controller is given in (5.2.16). The nominal loop gain cross-over is 2.1 rad/s.

$$g_{33a}(w) = \frac{2}{w} \tag{5.2.16}$$

Loop 2 of block 2: Load yaw angle Loop 2 of block 2 was the easiest initial loop that could be stabilised with specifications mostly met. The shaped nominal loop is shown in Fig. 5.2.17. The controller is given in (5.2.17). The resonant mode at 8.59 rad/s added greatly to the phase lag making it difficult to stabilise the plant (yaw angle loop). A complex lead-lag term had to be used to get enough phase lead. It was impossible to meet the nominal loop gain requirement at 8.59 rad/s due to the delay in the system. It was hoped that the over-bounding of the specification was producing the unrealisable gain requirement. The yaw loop is re-design using the exact design equations that include the roll and separation controllers further down; there it is shown that the specifications can be met at all design frequencies. The gain cross-over frequency obtained for the nominal loop was 0.7 rad/s. To

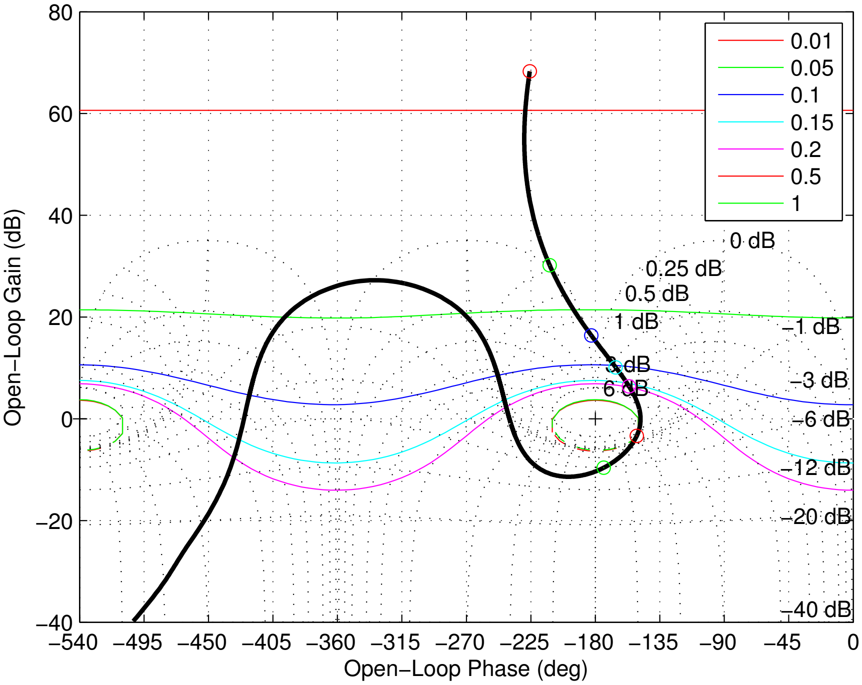

Figure 5.2.15: Load y-axis translation controller design $l_{22a}(w) = p_{22a}g_{22a}$

meet the low frequency requirement, a double integrator had to be used in the controller.

$$g_{22b}(w) = -\frac{0.0008}{w^2}\,\frac{w/0.095+1}{w/1.52+1}\,\frac{(w/0.1)^2+2\cdot 1\cdot w/0.1+1}{(w/20)^2+2\cdot 1\cdot w/20+1} \tag{5.2.17}$$

Loop 1 of block 2: Load roll angle The load roll angle requirements were easy to satisfy, although over-design at low frequency was required. The gain cross-over frequency obtained is 1.9 rad/s for the load roll angle loop. The controller that satisfies the requirement is given in (5.2.18). The shaped nominal loop is shown in Fig. 5.2.18.

$$g_{11b}(w) = 1.8\,\frac{1}{w(w/6.2+1)^2} \tag{5.2.18}$$

Loop 3 of block 2: Helicopter separation The helicopter separation controller specifications were difficult to meet and required a high-order controller. The controller that meets the nominal loop gain requirement is given in (5.2.19). The shaped nominal loop is shown in Fig. 5.2.19. A nominal gain cross-over frequency of 0.84 rad/s was obtained for the separation loop.

$$\begin{aligned} g_{33b}(w) = -0.0092\,\frac{w/0.025+1}{w^2}\,&\frac{(w/0.41)^2+2\cdot 0.2\cdot w/0.41+1}{(w/0.308)^2+2\cdot 0.7\cdot w/0.308+1}\,\cdot \\ &\cdot\frac{(w/0.5)^2+2\cdot 1\cdot w/0.5+1}{(w/19)^2+2\cdot 0.7\cdot w/19+1} \end{aligned} \tag{5.2.19}$$

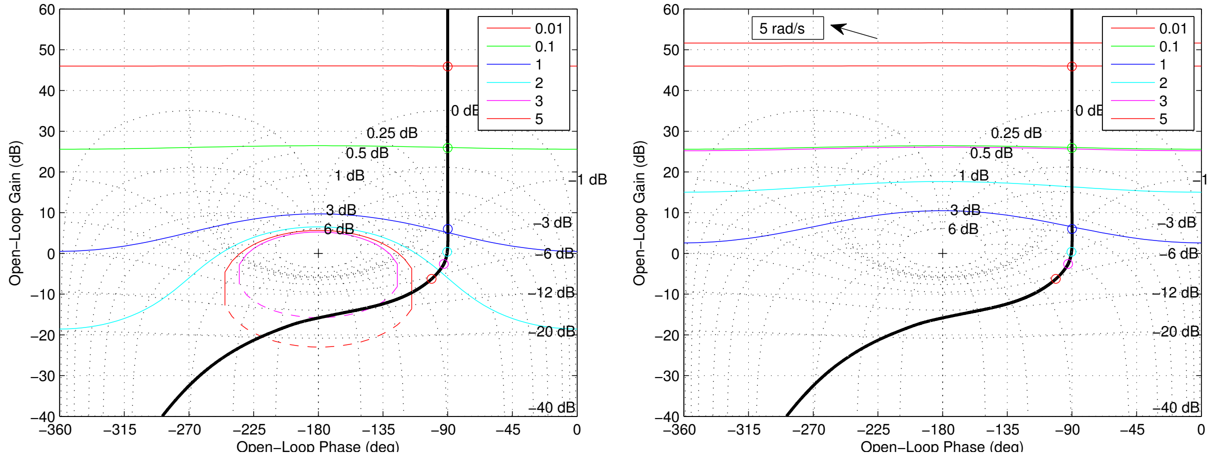

(a) Loop boundaries using the *improved method* (b) Loop boundaries using the original method

Figure 5.2.16: Load z-axis translation controller design $l_{33a}(w) = p_{33a}g_{33a}$

Yaw Loop Re-design The resonant mode in the yaw loop at 8.59 rad/s was particular troublesome in the design. The re-design using the exact design equations (including the design of row 1 and row 2) is shown in Fig. 5.2.20. A comparison with Fig. 5.2.17, show that the initial bounds were conservative, particular around the resonant mode (reduction from about 50 dB to about 18 dB). The re-designed yaw loop controller is given in (5.2.20).

$$g_{22b}(w) = -\frac{0.00095}{w^2}\,\frac{w/0.095+1}{w/3.42+1}\,\frac{(w/0.1)^2+2\cdot 1\cdot w/0.1+1}{(w/20)^2+2\cdot 1\cdot w/20+1} \tag{5.2.20}$$

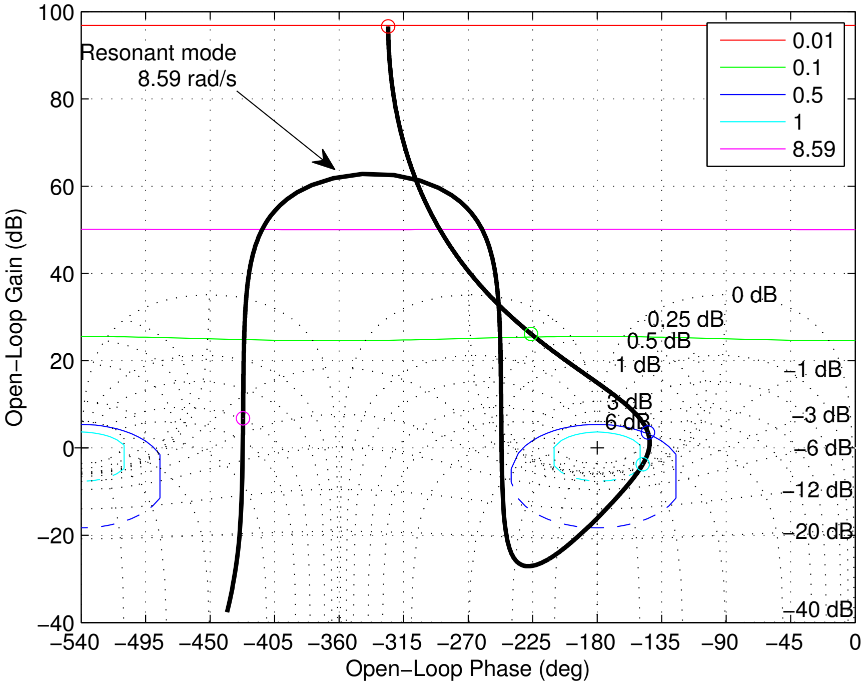

Figure 5.2.17: Load yaw angle controller design $l_{22b}(w) = p_{22b}g_{22b}$

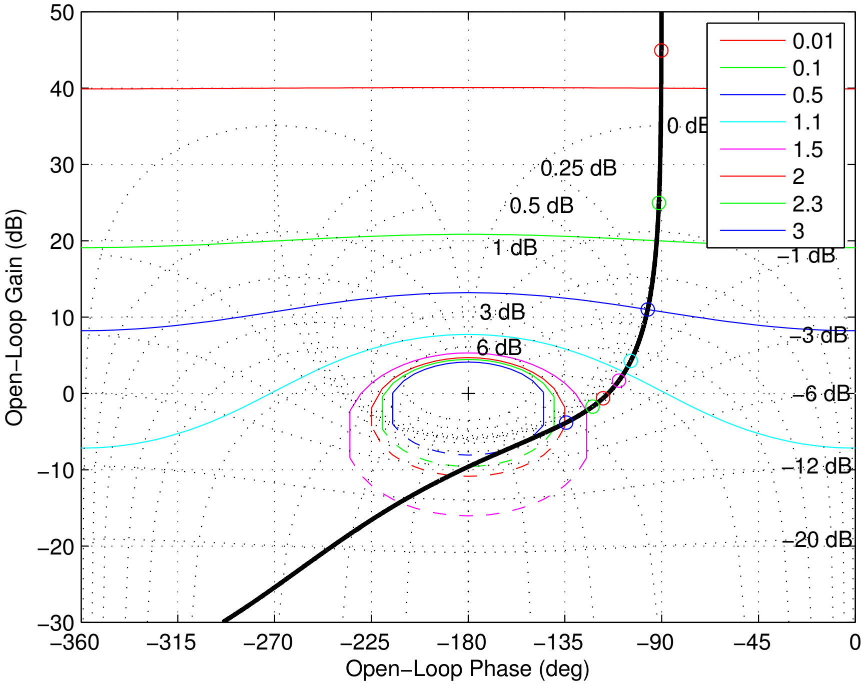

Figure 5.2.18: Load roll angle controller design $l_{11b}(w) = p_{11b}g_{11b}$

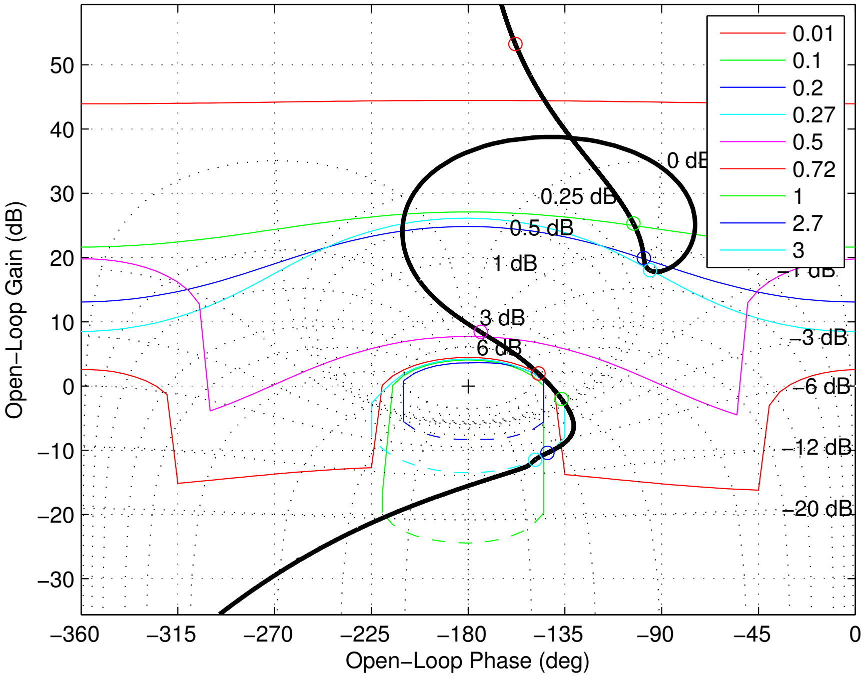

Figure 5.2.19: Helicopter separation distance controller design $l_{33b}(w) = p_{33b}g_{33b}$

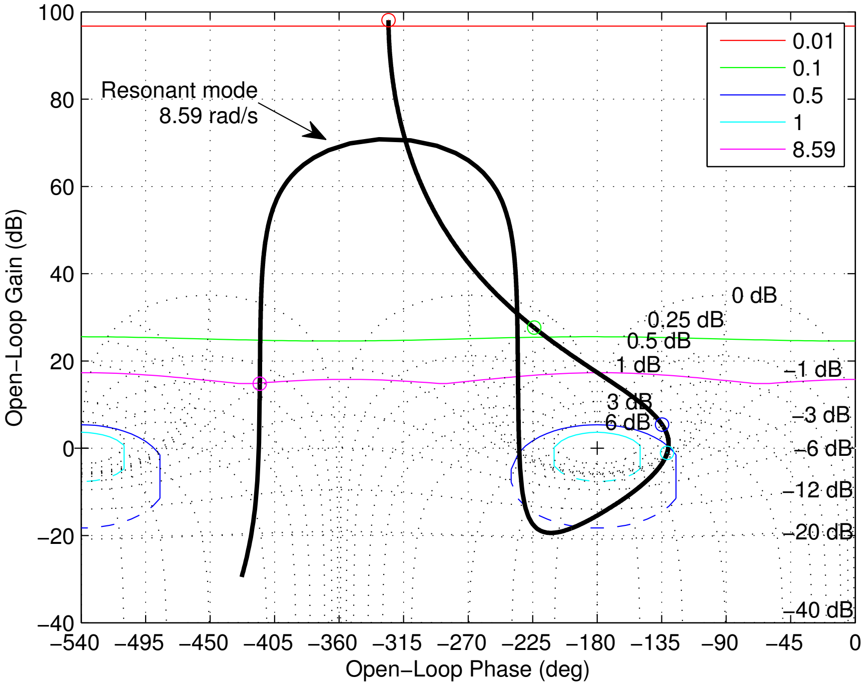

Figure 5.2.20: Re-design of load yaw angle controller design $l_{22b}(w) = p_{22b}g_{22b}$

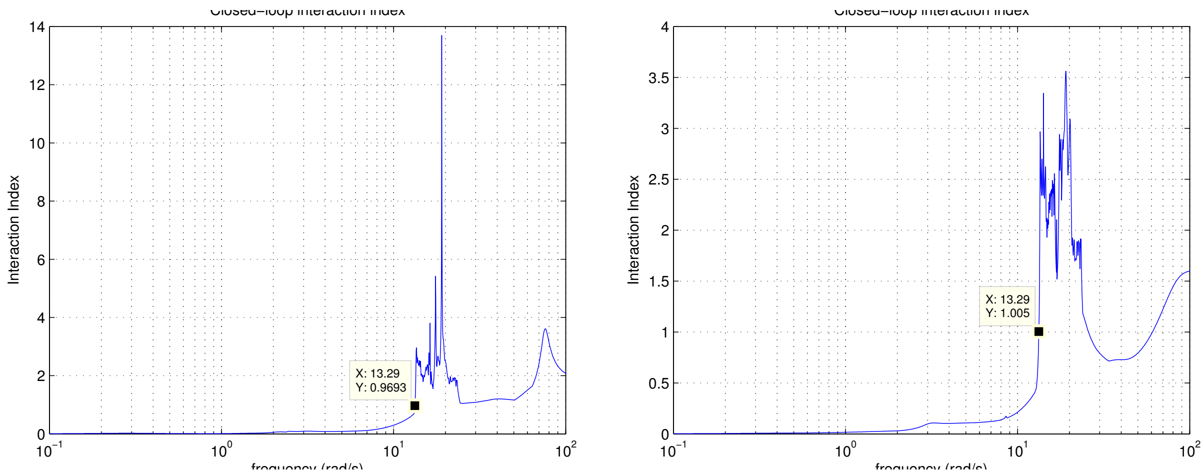

(a) Closed-loop interaction index of subsystem 1 (b) Closed-loop interaction index of subsystem 2

Figure 5.2.21: Closed-loop interaction index of subsystems

Improving the Initial Controller

Due to the difficulty of the design (coming from conservative bounds), the 6×6 plant was broken into two 3×3 plants. Assessing the Perron root of the interaction matrix, for a block diagonal splitting, showed that it was sufficient to stabilise the two 3×3 systems to ensure stability of the 6×6 system. The design for the 3×3 systems had much less conservative bounds, which made finding an *initial stabilising controller* possible. The initial stabilising controller is given by,

$$\boldsymbol{G}_1' = \boldsymbol{K}\boldsymbol{G}_1 \ = \boldsymbol{K} \begin{bmatrix} g_{11a}(w) & 0 & 0 & 0 & 0 & 0 \\ 0 & g_{22a}(w) & 0 & 0 & 0 & 0 \\ 0 & 0 & g_{33a}(w) & 0 & 0 & 0 \\ 0 & 0 & 0 & g_{11b}(w) & 0 & 0 \\ 0 & 0 & 0 & 0 & g_{22b}(w) & 0 \\ 0 & 0 & 0 & 0 & 0 & g_{33b}(w) \end{bmatrix} \tag{5.2.21}$$

The closed-loop interaction index of each subsystem is shown in Fig. 5.2.21. Since the closed-loop interaction index not less than unity for all frequencies, it *cannot* be guaranteed that stability of the system is given by the stability of the individual loops (Limebeer 1982). The individual loops were designed to be stable and the spectral radius of the interaction matrix is less than unity at least until 13 rad/s, this suggests that there are no unstable closed-loop poles (in the right-half plane of the s-plane) for frequencies below 13 rad/s; in other words, destabilisation can only come from closed-loop poles moving across the imaginary axis at frequencies above 13 rad/s. Due to the improbability of this in the practical system, the design proceeds without a clear *stability design* methodology. To confirm MIMO stability, the closed-loop system will be *assessed* after the controller design for stability. The closed-loop (using the initial controller) Bode magnitude plot of the output disturbance response is shown in Fig. 5.2.22. The green markings show were the specifications are violated for the 6×6 system. The violation is mainly due to the cross-coupling not taken into account in the subsystem design (the other cause is not using design frequencies where violations occurred). The initial stabilising controller $\boldsymbol{G}_1$, can now be tuned for each row using the *exact design equations* so that the specifications of the 6×6 system is achieved. Solving for the exact design equations symbolically can be a very tedious task for a 6×6 system. Fortunately, Yaniv (2013) has showed that a multidimensional linear fractional mapping on the controller (to be modified) may be given by,

$$\boldsymbol{T}(j\omega) = \frac{\boldsymbol{C}_k^{-1} + g_k \boldsymbol{C}_k^{-1}\left(\boldsymbol{e}_k^T \boldsymbol{C}_k^{-1} \boldsymbol{p}_k \boldsymbol{I} - \boldsymbol{p}_k \boldsymbol{e}_k^T \boldsymbol{C}_k^{-1}\right)}{1 + g_k \boldsymbol{e}_k^T \boldsymbol{C}_k^{-1} \boldsymbol{p}_k} \leq |\boldsymbol{A}(j\omega)|, \tag{5.2.22}$$

where

$$\begin{aligned} \boldsymbol{C}_k &= \boldsymbol{I} + \boldsymbol{P}\left(\boldsymbol{G} - \boldsymbol{G}_k\right), \\ \boldsymbol{G}_k &= diag(0, \ldots, 0, g_k, \ldots, 0), \\ \boldsymbol{p}_k &= \left(p_{1k}, p_{2k}, \ldots, p_{6k}\right)^T, \end{aligned}$$

and

$$\boldsymbol{e}_k^T = [0, \ldots, 0, 1, 0, \ldots, 0],$$

with 1 in the position of k, and g_k is the controller to be designed, p_{ij} is (i, j) element of the plant $\boldsymbol{P}$, given all other loops are designed.

Controller Tuning Using (5.2.22) one may tune the initial controller to try to meet the 6×6 output disturbance rejection specifications. The list of violations of the specifications using the initial controller is shown in Table 5.2.1. The design strategy is to try to first correct severe violations of the specifications by appropriately tuning the *right* controller, then going through one iteration of design to minimise the over-design (find minimum loop gain for each controller that meets specifications' *if possible*).
Table 5.2.1 shows that specifications are violated on the following load output variables, y-axis position, z-axis position and the roll output. From (5.2.8), it can be seen that the magnitude of $t_{ij}(w)$ may be reduced through three means; firstly, by having a large enough loop gain in channel i; secondly, by reducing the ratios $\left|\frac{q_{ii}^*}{q_{ik}^*}\right|$ for $k = 1, \ldots, 6$; and lastly by reducing the magnitude of the other output disturbance responses for the *respective column.* By the application of the Schwarz inequality to (5.2.8), the means to meeting the specifications described above is conservative (i.e. not independent). Reducing the ratios $\left|\frac{q_{ii}^*}{q_{ik}^*}\right|$, can be achieved through the introduction of dynamic cross-feed elements in the controller (Boje 2002). It should also be clear that altering the loop gain of row i, will change the response of every column in row i, and from (5.2.8), every row in the system gets altered (because every element is a function of the elements in it's column). By the application of the Schwarz inequality on (5.2.8), one should understand that an increase in $|t_{ij}(j\omega_1)|$ *may* result in an increase in the magnitude of the disturbance response of any other input-output pair at ω_1. A further consideration to be noted when tuning is of the Bode integral for a stabilised system, which implies that a decrease of sensitivity at some frequencies will result in an increase in sensitivity at other frequencies (Horowitz 1993) -

Table 5.2.1: Violations of specification

Element	Response	Violation Description
$\lvert t_{25}(j\omega)\rvert$	Yaw output disturbance to y position output	Around resonant mode 2.2 rad/s
$\lvert t_{26}(j\omega)\rvert$	Separation output disturbance to y position output	Around resonant mode 2.2 rad/s; Low frequency specifications not met
$\lvert t_{31}(j\omega)\rvert$	x position output disturbance to z position output	Around resonant mode 2.2 rad/s
$\lvert t_{32}(j\omega)\rvert$	y position output disturbance to z position output	Around resonant mode 2.2 rad/s
$\lvert t_{34}(j\omega)\rvert$	Roll output disturbance to z position output	Around resonant mode 2.2 rad/s; Low frequency specifications not met
$\lvert t_{35}(j\omega)\rvert$	Yaw output disturbance to z position output	Around resonant mode 2.2 rad/s
$\lvert t_{36}(j\omega)\rvert$	Separation output disturbance to z position output	Around 25 rad/s; Low frequency specifications not met
$\lvert t_{45}(j\omega)\rvert$	Yaw output disturbance to roll output	Around 25 rad/s

the waterbed effect. This suggests that in tuning a particular loop, if it is suspected that there will be an increase in sensitivity at particular frequencies, it should be approached with caution if there is insufficient room between the specification and response envelope of the column responses.

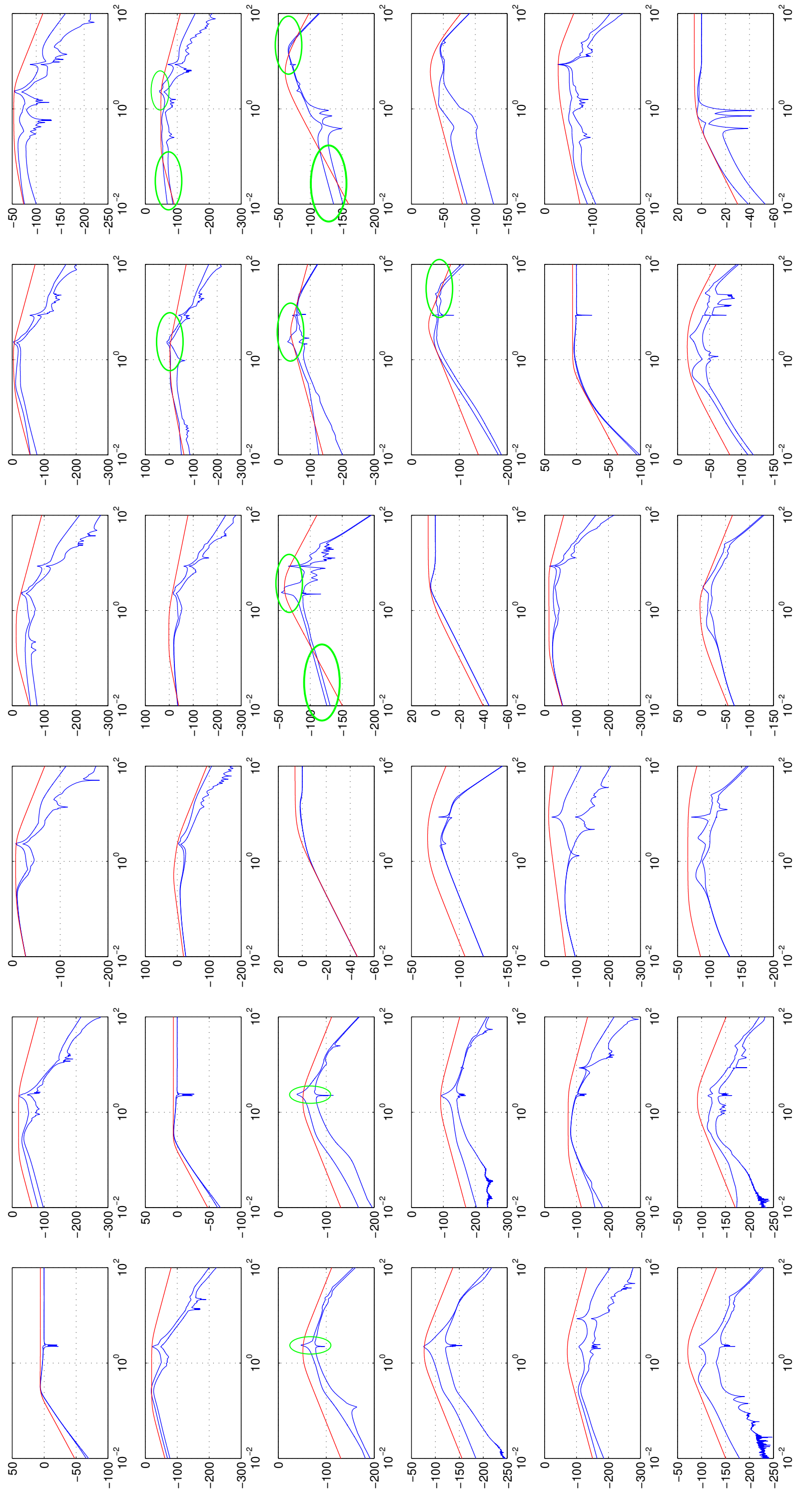

Figure 5.2.22: Bode magnitude plot of the minimum and maximum sensitivity envelope of the closed-loop system (blue) with the initial controller; sensitivity specifications (red); highlighting sensitivity violation (green); x-axis: frequency in rad/s; y-axis: magnitude in dB

Tuning load z position controller Since most of the violations occurred on the z position output variable, and it was known that a higher loop bandwidth was possible, $\boldsymbol{G}_1(3,3)$ was chosen first for tuning. A second integrator was added to improve low frequency regulation. To target the 2.2 rad/s resonant mode, the loop gain was increased around the resonant mode. This required an increase in the gain cross-over frequency from 2.1 rad/s to 10.4 rad/s. The "cost" of reduction in sensitivity at the resonant frequency 2.2 rad/s was an unavoidable increase in sensitivity around 25 rad/s in channels $t_{35}(w)$ and $t_{36}(w)$, shown in Fig. E.3.2. This added violation is attended to later in the design. The tuned controller is given by (5.2.23). The high frequency violation is less than -60 dB in both channels, thus for practical reasons it is an acceptable violation. The increase in sensitivity at around the new gain cross-over frequency (10.4 rad/s) of loop 3, has resulted in an increase in the envelope of the response in some of the rows of column 3 - through the mechanism explained earlier. In particular, $t_{63}(w)$ violates the specification. Since the peak is around -60 dB, it is not a major concern but will be considered in the following design steps.

$$g_{33}(w) = 0.326 \; \frac{w/0.032+1}{w^2} \; \frac{(w/16.4)^2 + 2\cdot 0.46 \cdot w/16.4 + 1}{(w/30)^2 + 2\cdot 1 \cdot w/30 + 1} \tag{5.2.23}$$

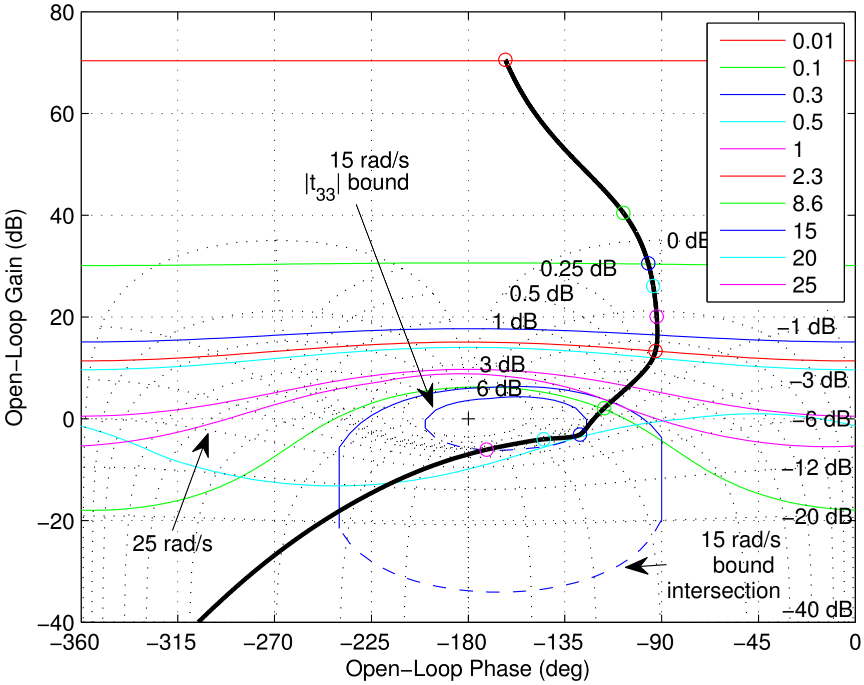

Figure 5.2.23: Controller design $g_{33}(w)$

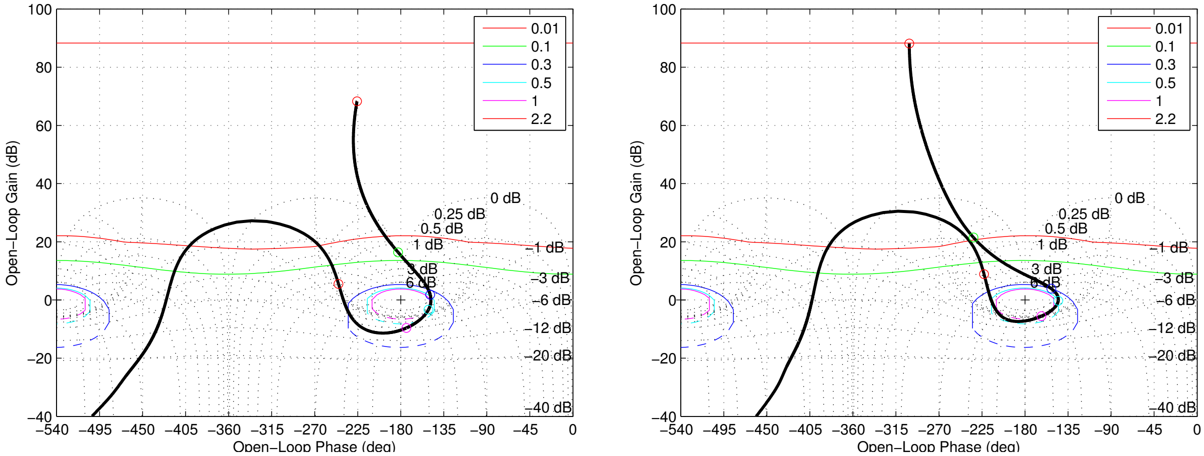

(a) Loop design of controller $g_{22a}(w)$

(b) Loop design of controller $g_{22}(w)$

Figure 5.2.24: Loop design of y position loop with exact bounds

Tuning load y position controller Since the second most violations occurred in the y position loop output, the second controller that is was chosen to be tuned is $\boldsymbol{G}_1(2,2)$. The violations at around 2.2 rad/s in channels $t_{25}(w)$ and $t_{26}(w)$ can be solved by increased loop gain in g_{22} or by reducing the cross-coupling from the yaw and separation output. The low frequency coupling in $t_{26}(w)$ can be solved with increased low frequency gain without much difficulty. The tuned controller is given in (5.2.24). It was not possible to achieve the required loop gain around the resonant mode (2.2 rad/s), but an improvement in regulation was possible from the initial design. The initial and tuned y position loop design is shown in Fig. 5.2.24 with the exact bounds.

$$g_{22}(w) = -0.000434\,\frac{w/0.025+1}{w^2}\,\frac{(w/0.157)^2+2\cdot 0.6\cdot w/0.157+1}{(w/1.7)^2+2\cdot 0.9\cdot w/1.7+1} \tag{5.2.24}$$

Although the tuned controller improves the design at the targeted frequencies, an updated plot of the sensitivity shown in Fig. E.3.3, shows that the improvement is accompanied with a violation at high frequencies of $t_{36}(w)$.

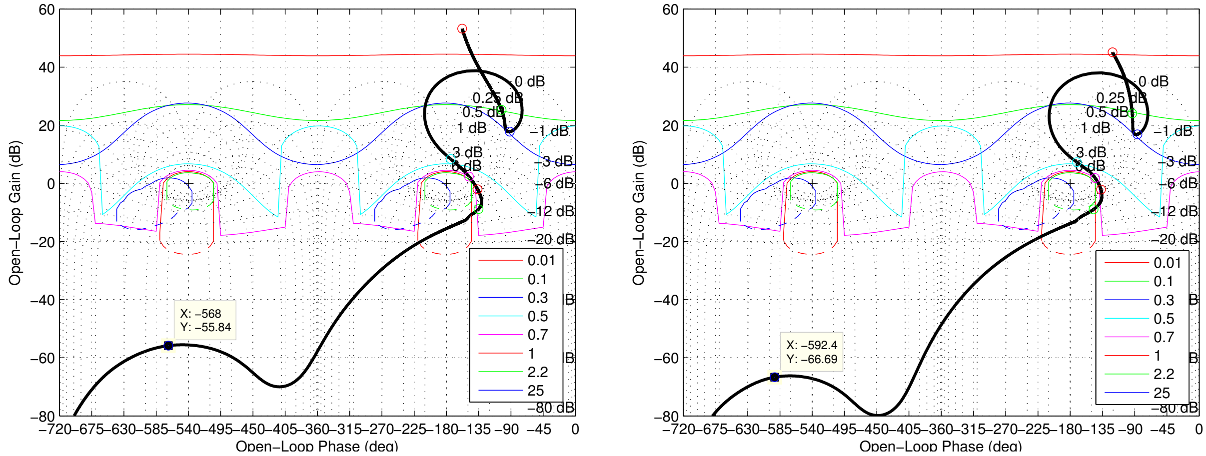

(a) Loop design of controller $g_{33b}(w)$ (b) Loop design of controller $g_{66}(w)$

Figure 5.2.25: Loop design of separation loop with exact bounds

Tuning load separation controller After tuning the z position controller, it was noted that a high frequency violation of $t_{36}(w)$ occurred. The separation controller is modified to try and fix this violation. Since the specifications of the separation output is broadly met, a reduction in the cross-coupling does not require large loop gain. Sufficient roll-off after the gain cross-over frequency of the separation loop may reduce the cross-coupling into channel $t_{36}(w)$. Figure E.3.4 shows the separation output specifications being met together with channel $t_{36}(w)$ specifications being met. The separation controller that fixes the violation is given in (5.2.25). Figure 5.2.25 shows the initial and the tuned controller with the exact bounds. A reduction in loop gain around 25 rad/s is also highlighted.

$$\begin{aligned} g_{66}(w) = -0.002\,\frac{w/0.006+1}{w^2}\,&\frac{(w/0.42)^2+2\cdot 0.2\cdot w/0.42+1}{(w/0.326)^2+2\cdot 0.78\cdot w/0.326+1}\cdot \\ &\cdot\frac{(w/0.48)^2+2\cdot 1\cdot w/0.48+1}{(w/10)^2+2\cdot 1\cdot w/10+1} \end{aligned} \tag{5.2.25}$$

Tuning load yaw angle controller The next violations that were attempted to be resolved was the high-frequency cross-coupling from the yaw input to the z position and roll angle of the load. The yaw loop controller also had to be tuned slightly to meet the 8.59 rad/s resonance requirement. This can be seen in Fig. 5.2.27. To reduce the high-frequency cross-coupling into the other channels, the controller was tuned to start roll-off earlier, this is shown in Fig. 5.2.26. The result on the sensitivity improvement in $t_{35}(w)$ and $t_{45}(w)$ can be seen in E.3.5. The final yaw loop controller is given in (5.2.26).

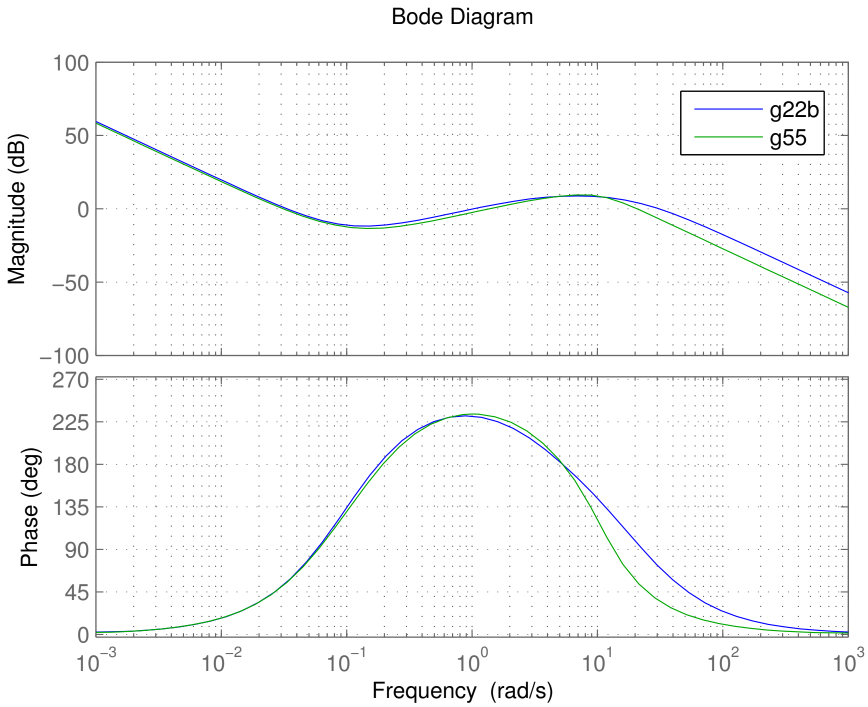

Figure 5.2.26: Comparison between initial and tuned yaw controller

$$g_{55}(w) = -\frac{0.00083}{w^2}\;\frac{w/0.066+1}{w/5+1}\;\frac{(w/0.13)^2+2\cdot 1\cdot w/0.13+1}{(w/10.8)^2+2\cdot 0.64\cdot w/10.8+1} \tag{5.2.26}$$

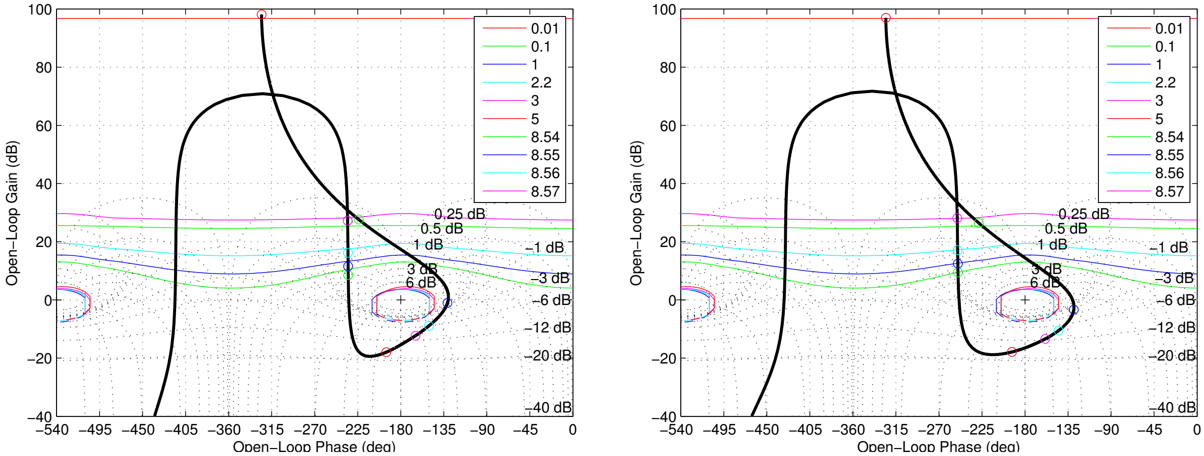

(a) Loop design of controller $g_{22b}(w)$

(b) Loop design of controller $g_{55}(w)$

Figure 5.2.27: Loop design of yaw loop with exact bounds

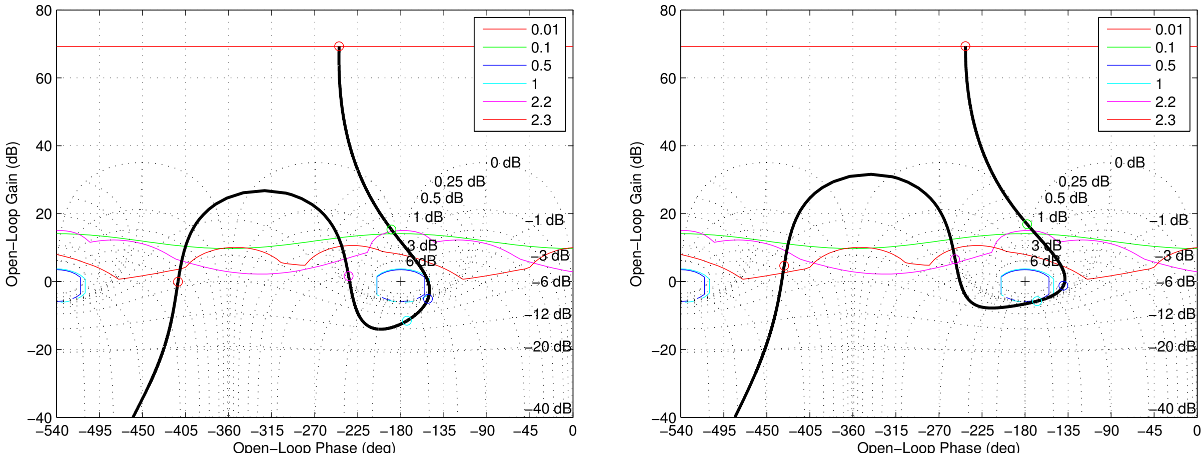

(a) Loop design of controller $g_{11a}(w)$ (b) Loop design of controller $g_{11}(w)$

Figure 5.2.28: Loop design of x position loop with exact bounds

Tuning load x position controller Tuning of the other loops resulted in the x position loop responses to be violated slightly near the 2.2 rad/s resonant mode. The x position loop controller only needed to be modified slightly near the resonant mode and have sufficient roll-off at high-frequency to prevent transmission into other rows. The tuned controller is given in (5.2.27). The exact bounds for loop 1 is shown in Fig. 5.2.28 with both initial and tuned design. The sensitivity response after tuning the x position loop is given in Fig. E.3.6.

$$g_{11}(w) = -\frac{0.00043}{w}\ \frac{(w/0.09)^2 + 2\cdot 1\cdot w/0.09 + 1}{(w/1.56)^2 + 2\cdot 0.6\cdot w/1.56 + 1}\cdot \\ \cdot\frac{1}{(w/6.7)^2 + 2\cdot 0.707\cdot w/6.7 + 1} \tag{5.2.27}$$

Tuning load roll angle controller The remaining loop that may be tuned is the load roll angle loop. Figure 5.2.29 shows the sensitivity response after tuning all controllers except the roll angle controller. It can be seen that the only violation in the roll output response, is with respect to the x position output disturbance around the 2.2 rad/s resonant mode. Trying to attenuate this mode further requires larger loop gain at higher frequencies, which increases the cross-coupling into other channels. Hence, it was decided that the violation at 2.2 rad/s is acceptable, especially with it being attenuated to −60 dB.

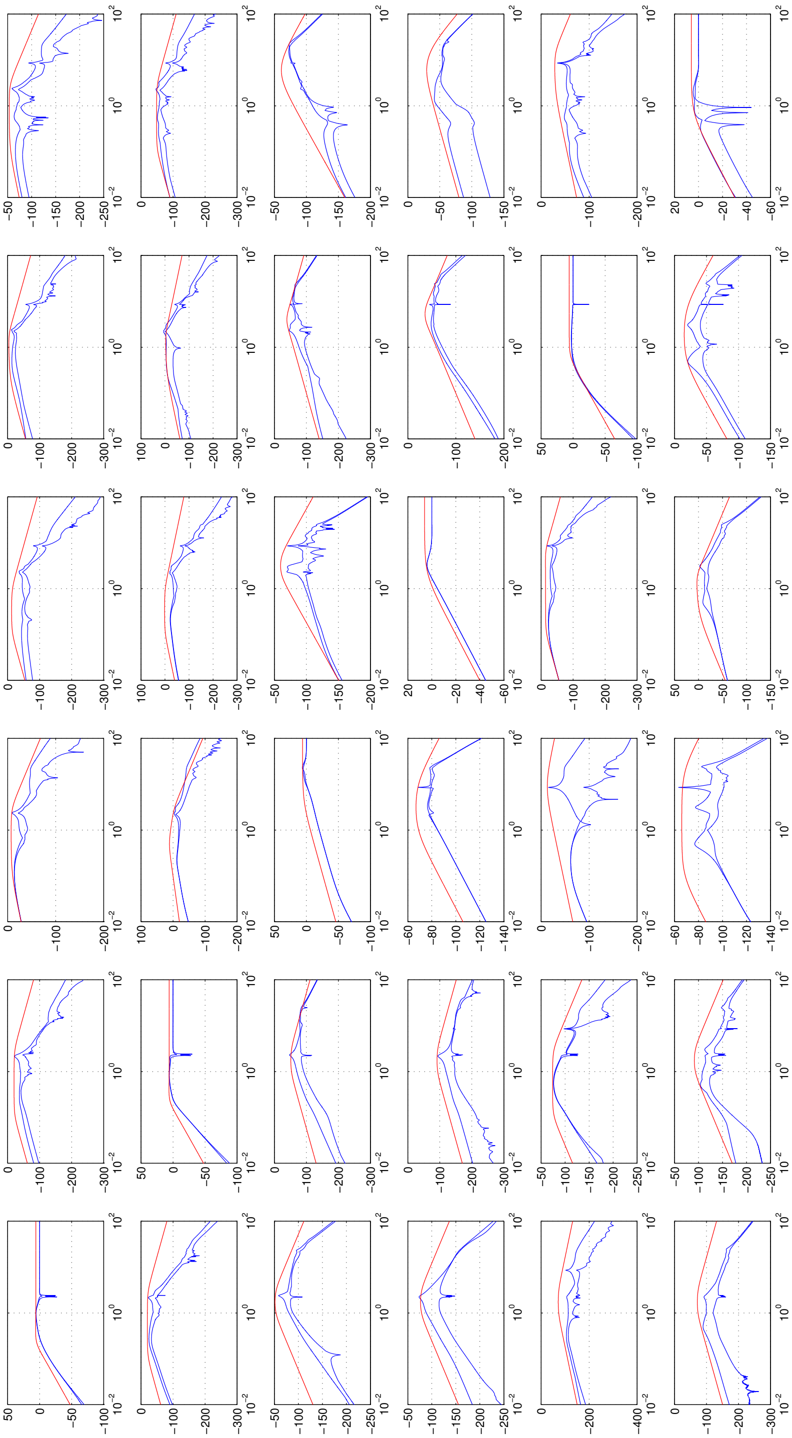

Figure 5.2.29: Bode magnitude plot of the minimum and maximum sensitivity envelope of the closed-loop system (blue) *after* tuning of the initial controller; sensitivity specifications (red); x-axis: frequency in rad/s; y-axis: magnitude in dB

Reduce Interaction Figure 5.2.29 shows that the tuned controller almost satisfies the specifications completely - there are some frequencies where minor violation of the specifications occur. It may be possible to reduce the cross-coupling further by designing dynamic cross-feed terms for targeted frequencies. The methodology of designing dynamic cross-feed terms in the QFT framework is shown in Boje (2002). It was not possible to reduce the interaction with a post-compensator $\boldsymbol{K}_2$, given the uncertainty, to improve the output disturbance response significantly. The post-compensator is located before the feedback controller $\boldsymbol{G}_d$, as depicted in Fig. 5.2.30. After post-compensation the loop gain will by

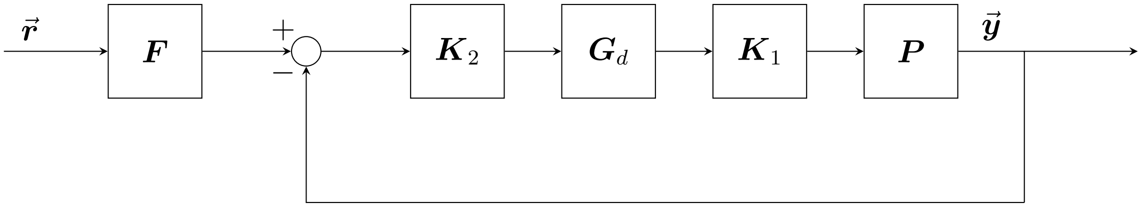

Figure 5.2.30: Control block diagram showing post-compensator

$\boldsymbol{L} = \boldsymbol{P}\boldsymbol{K}_1\boldsymbol{G}_d\boldsymbol{K}_2 = \boldsymbol{P}^*\boldsymbol{K}_2$. A reduction in the cross-coupling will occur if the the ratio of the diagonal to the off-diagonal terms in $\boldsymbol{L}$ are reduced. By applying the methodology in Boje (2002) to an effective plant $\boldsymbol{P}' = \boldsymbol{P}^*\boldsymbol{K}_2$, one can obtain a linear fractional mapping on the elements of $\boldsymbol{K}_2$ which can be used to design the dynamic cross-feed terms. To illustrate this, the reduction in cross-coupling at 2.2 rad/s in the $t_{54}(w)$ response will be considered. Using a unimodular maxtrix $\boldsymbol{K}_2$ (ibid.), the effective plant inverse may be written as,

$$\hat{\boldsymbol{P}}' = \hat{\boldsymbol{K}}_2\hat{\boldsymbol{P}}^* \tag{5.2.28}$$

with

$$\hat{\boldsymbol{K}}_2 = \begin{bmatrix} 1 & 0 & 0 & 0 & 0 & 0 \\ 0 & 1 & 0 & 0 & 0 & 0 \\ 0 & 0 & 1 & 0 & 0 & 0 \\ 0 & 0 & 0 & 1 & 0 & 0 \\ 0 & 0 & 0 & \hat{k}_{54} & 1 & 0 \\ 0 & 0 & 0 & 0 & 0 & 1 \end{bmatrix}$$

Expanding (5.2.28) for row 5 one gets the following,

$$\hat{\boldsymbol{P}}'_{5j} = 1/q'_{5j} = 1/q^*_{5j} + \hat{k}_{54}1/q^*_{4j} \qquad j = 1,\ldots,6. \tag{5.2.29}$$

One may reduce the interaction in $t_{54}(w)$ by reducing the ratio of the diagonal to the off-diagonal (ibid.),

$$\frac{q'_{55}}{q'_{54}} = \frac{q^*_{55}}{q^*_{54}}\frac{1+\hat{k}_{54}q^*_{54}/q^*_{44}}{1+\hat{k}_{54}q^*_{55}/q^*_{45}} = \frac{q^*_{55}}{q^*_{54}}\beta \tag{5.2.30}$$

The element $\hat{k}_{54}$ is designed to force $\beta < 0.2$ through the linear fractional mapping in (5.2.30). The design showing the level curves for $\beta = 0.2$ is shown in Fig. 5.2.31. The cross-feed term designed is given in (5.2.31). The improvement in cross-coupling reduction is shown in Fig. 5.2.32.

$$\hat{k}_{54}(w) = -\frac{0.015w}{(w/2.35)^2 + 2 \cdot 0.7 \cdot w/2.35 + 1} \tag{5.2.31}$$

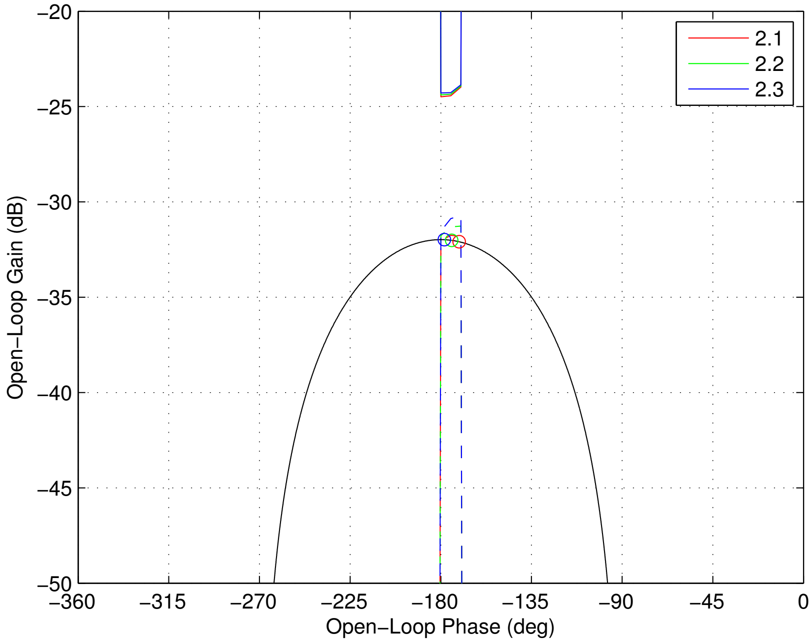

Figure 5.2.31: Design of cross-feed term $\hat{k}_{54}$

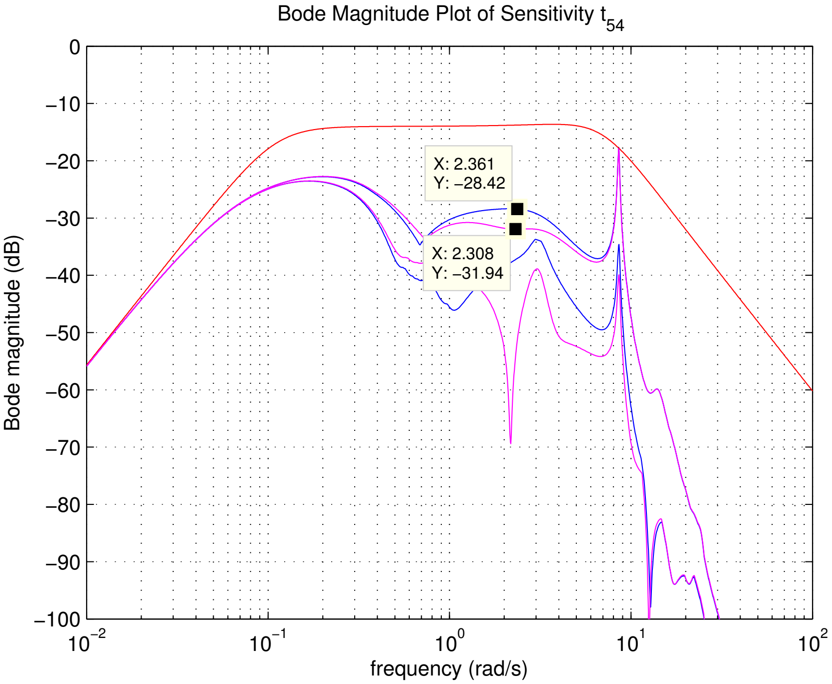

Figure 5.2.32: Sensitivity plot of $t_{54}(w)$ showing the reduction in cross-coupling obtained through cross-feed; $t_{54}(w)$ without cross-feed in blue; $t_{54}(w)$ with cross-feed in magenta; specification in red

5.2.6 System Stability

The approach to *design* for stability was to use a diagonal dominance type of argument to allow the design of the individual loop to proceed. As stated earlier, by performing a splitting of the multivariable plant *that allows design of the individual channels* and ensuring that the spectral radius of the interaction matrix is less than unity for all frequencies, stability of the multivariable system can be guaranteed by ensuring stability of the individual loops (Boje 2002).

The 6×6 plant, was broken into two 3×3 subsystems through a block diagonal splitting (after pre-compensation). The analysis of the interaction index showed that stability of the 6×6 plant will be guaranteed by the stability of the individual subsystems (*see* (5.2.12)). It was shown in Fig. 5.2.21, that the closed-loop interaction index of the individual subsystems were not less than unity for all frequencies (only up to about 13 rad/s). The stability argument was based on Limebeer (1982), which is believed to be the least restrictive stability argument for decentralised systems. To find conditions for design for stability would require a new Theorem that provides a design guideline where the applied one failed. The analysis up to 13 rad/s imply that destabilisation of the system (right-half plane closed-loop poles) *may* come from the cross-coupling above 13 rad/s (spectral radius of the interaction matrix is greater than unity above 13 rad/s). Figure 5.2.33 shows the right-half complex plane partitioned at a radius ω_x. The Theorem should generate design guidelines for $\omega > \omega_x = 13$ rad/s for the specific problem. This is left as a recommendation for further research.

Although a clear-cut design methodology for stability could not be defined, the *analysis* for stability can be shown by the time-domain response of the nonlinear system (*see* Fig. 5.2.36 and Fig. 5.2.37).

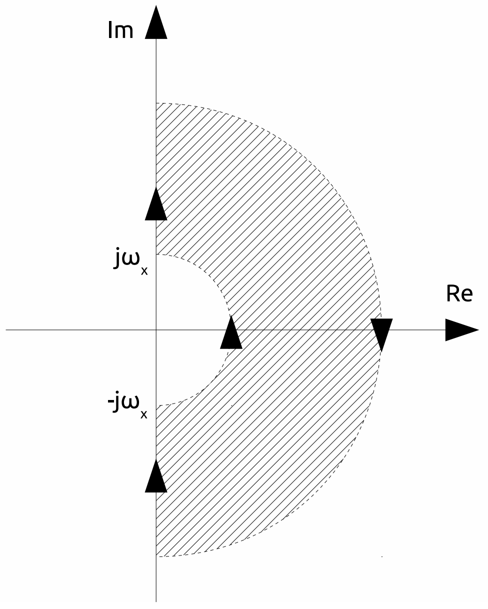

Figure 5.2.33: Complex plane showing split right-half plane

5.2.7 Results and Discussion

In this section, the time domain response of the nonlinear control system will be shown. A comparison of the MIMO QFT control scheme and the trivial solution will be analysed. Although, the controller was designed for disturbance rejection (and robust stability) specifications, the response to step inputs to the reference will be assessed to easily visualise the closed-loop bandwidth.

Step Responses to Nonlinear System

A step input to the x, y and z reference positions were given for three plant cases covering the extreme and average mass uncertainty. The result to the step inputs is shown in Fig. 5.2.34 for the system with the QFT decentralised controller. The initial excitation shown in Fig. 5.2.34 was due to the initial conditions of the twin-helicopter lift system. The overshoot in the tracking response can easily be conditioned using a pre-filter design. The same step references were given to the *trivial solution* (Section 5.2.2) and the results are shown in Fig. 5.2.35. Although, the trivial solution was not a proper feedback solution, it was the only obvious solution at the time, and was additionally intended to serve as a benchmark solution. The trivial solution showed the best tracking bandwidth that could be achieved without *destabilising the system.* From a comparison of the step response, it can be seen that the QFT decentralised solution has much higher bandwidth than the trivial solution. Figure 5.2.35 also shows that the resonant modes are not actively controlled (evident in the y position response). There was also significant coupling to the attitude using the trivial solution (although it was done by design, in retrospect it is not ideal). It is clear that the QFT decentralised solution is superior to the “trivial solution” in *achievable* loop bandwidth.

Trajectory Tracking of the Nonlinear System

A reference trajectory which excites all channels was generated to test the nonlinear system response to cross-coupled inputs. A circle trajectory for the x-y plane, ramp in z position and sinusoid reference for the roll and yaw (π rad out of phase to the roll) angle was generated. The separation reference is given by,

$$\delta^{ref} = l_0 + \cos(\phi_l) \tag{5.2.32}$$

where l_0 is the separation distance when the roll angle (ϕ_l) is zero. This way the helicopters always lie over the load attachment points. This also prevents excessive steady-state attitude angles of the helicopter which may make the pilot uncomfortable. A 3D plot of the helicopter tracking the described trajectory reference is shown in Fig. 5.2.36. The roll, yaw and separation tracking during the same simulation is shown in Fig. 5.2.37.

A complex trajectory was generated testing both translation tracking and attitude tracking was done and can be viewed on YouTube on the link `https://youtu.be/bJs7ehfYPP0`. Figure 5.2.38 shows a snapshot of the simulation.

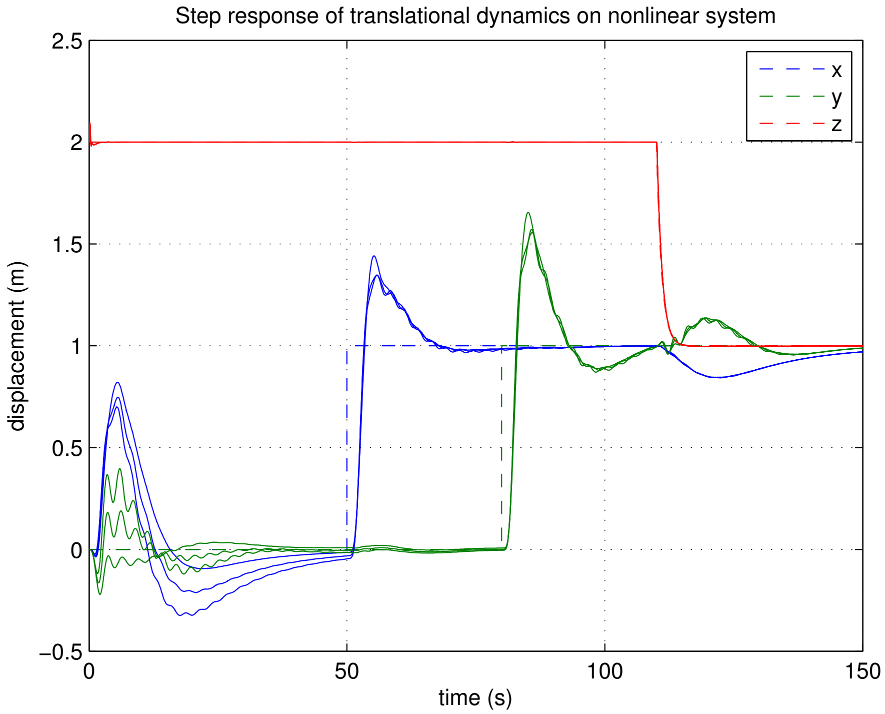

Figure 5.2.34: Nonlinear system step response for the decentralised QFT controller

Discussion

The results of the QFT controller design shows a robust controller solution to the twin-helicopter load transportation system exists. The performance gained from using a coordinated load sharing structure compared to independent helicopter control (trivial solution) for transporting the load was significant. The main purpose of the trivial solution was to be able to get the twin-helicopter load transportation system in nominal operating conditions so that linearised models of the plant could be extracted. The secondary purpose was to act as a benchmark for an improved design strategy. It is in no way a true feedback solution, as it does not actively control the dynamics of the load. The solution to the *simplified model* using force control was the first proper attempt of using feedback to solve the load sharing problem. When the concept was evaluated for the real system, it proved to be too difficult because of the bandwidth limitation from the helicopters.

The difficulty in the design stemmed from a combination the plant being multivariable, uncertain and having multiple resonant modes. The 6×6 plant has many over-bound terms which resulted in loop boundaries that were not possible to attain with the delay in the system. Decomposing the system into two 3×3 subsystems helped greatly. The uncertainty in the under-damped resonant modes reduces the solution space for a stabilising controller. The use of QFT provided transparency on how shaping one channel influenced the responses in other channels. In particular, it was found that the multivariable system (cross-coupling) was sensitive to the shaping of the loop phase near the under-damped poles of the indi-

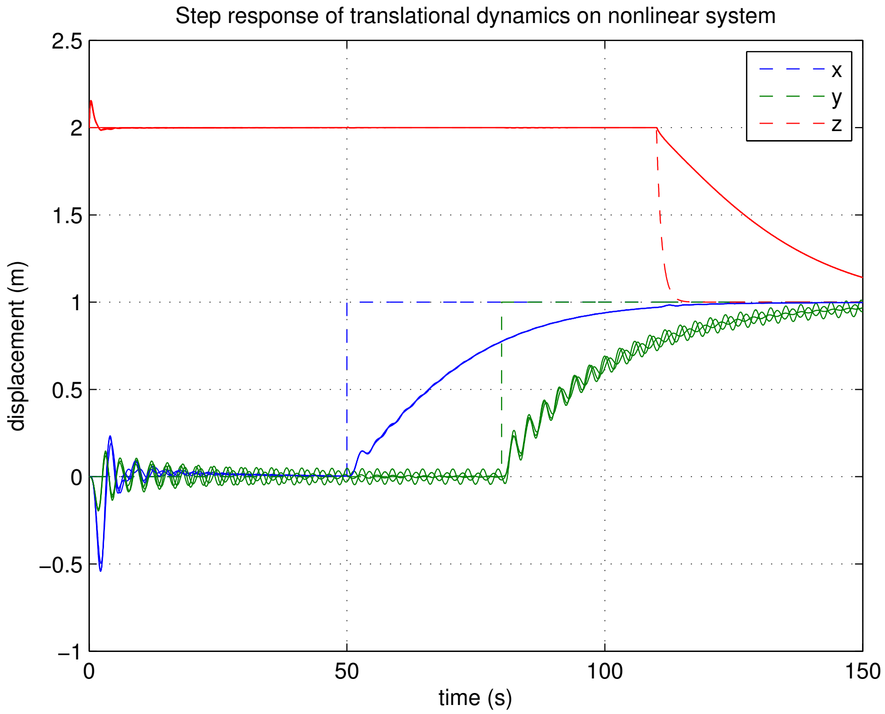

Figure 5.2.35: Nonlinear system step response for the *trivial solution*

vidual loops. Because of transparency and the level of authority in the QFT methodology, choice of the elements that made up the controller could be selected carefully to prevent possible implementation issues; for example, the damping factors were limited to 0.2, the controller order was minimised and the number of significant digits in controller elements controlled to prevent fragility. Also, the nominal loops were shaped with the insight of signal propagation from different points in the loop; for example, considering noise propagation at high-frequencies.

Through the iterative process of tuning the final controller, it became clear that a MIMO QFT toolbox that recalculates the loop boundaries of all loops as a single controller is modified will be very beneficial to tuning multivariable controllers. In trying to find a solution to the twin-helicopter load transportation system, the author was led to using a static pre-compensator from the idea of using differential control (mixing). Later on in the design, a dynamic post-compensator was suggested as an adhoc measure to reduce interaction to meet specifications. Dynamic pre-compensation using a non-diagonal control design methodology as shown in Boje (2002) would be a better approach to minimise the over-design across the operating frequency range (can target frequencies to attenuate compared with a DC pre-compensator).

Although an H_∞ controller may be high-order and possibly fragile, a possible improvement on the design may be obtained to extract a diagonal controller from an H_∞ controller as done in Reddi (2011), and tune the diagonal elements to meet QFT specifications.

Demonstration of Coordinated Control on Experimental Platform

Unfortunately, the helicopters built for testing the coordinated control crashed during early testing of the coordinated control scheme. The particular test did not engage the coordinated control, it was a test to check if the fail-safe with regards to rotor separation distance will be satisfied. One of the helicopter's sustained only minor mechanical damage. The other helicopter's electronics board was completely damaged and was non-functional after the crash, thus, detailed on-board telemetry could not be recovered. The manual override was activated to try to land the helicopter safely, but the "glitch" caused one of the helicopters to accelerate vertically, so rapidly that manual control was not sufficient to bring the helicopter down safely (a large flying volume would have greatly increased the chances of saving the helicopters).

The "accident" was so violent that it rendered one of crashed helicopter non-usable and no components could be salvaged. A lack of funding and technical human resources to build a new instrumented helicopter prevented further testing of the coordinated control scheme. Fortunately, sufficient experimental tests were done on the individual helicopters prior to the crash to confirm the high fidelity models. Given the limitations, it was agreed in consultation with the author's supervisor to proceed with testing of the coordinated control scheme using the simulator that was designed and the verified helicopter models. Due to the above circumstances, a video demonstration of the control design through *simulation* may be accessed via the link `https://youtu.be/bJs7ehfYPP0` (coordinated control demonstration starts at time 2:16).

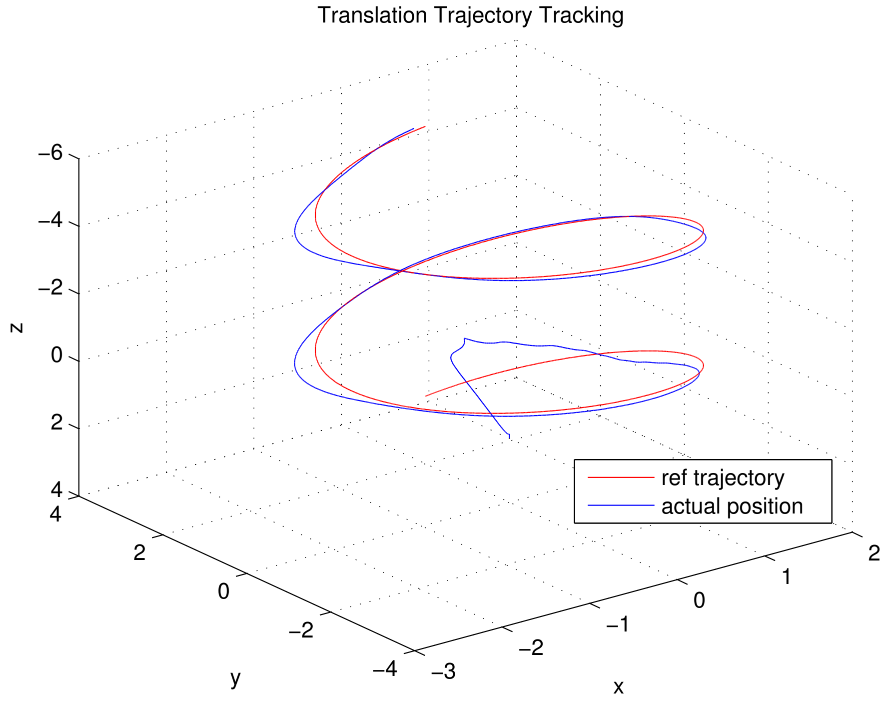

Figure 5.2.36: 3D plot of simulation results of nonlinear system following a trajectory (translation tracking shown)

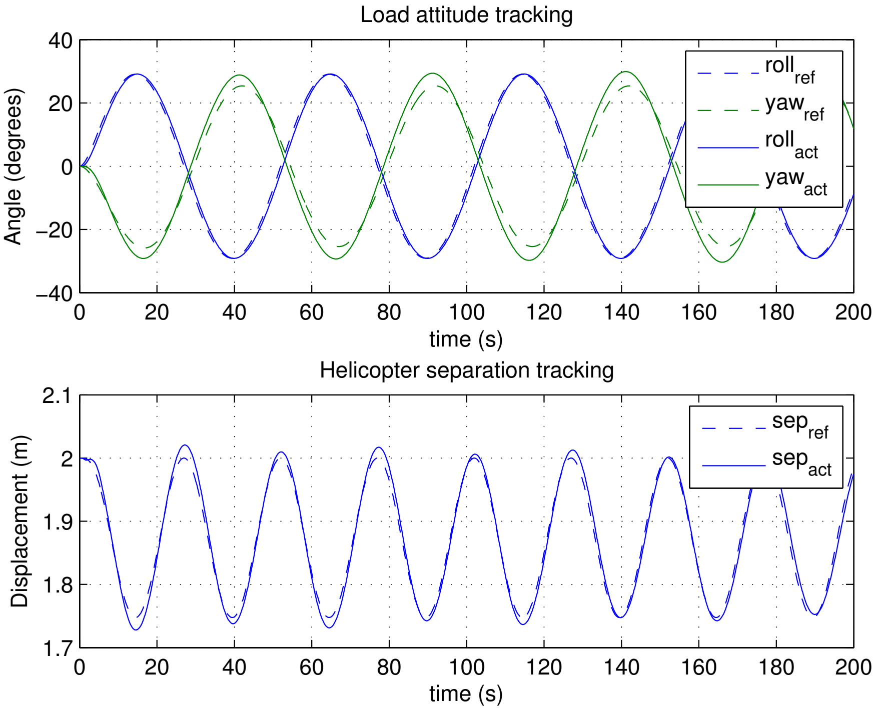

Figure 5.2.37: Simulation results of nonlinear system following a trajectory (attitude and separation tracking shown)

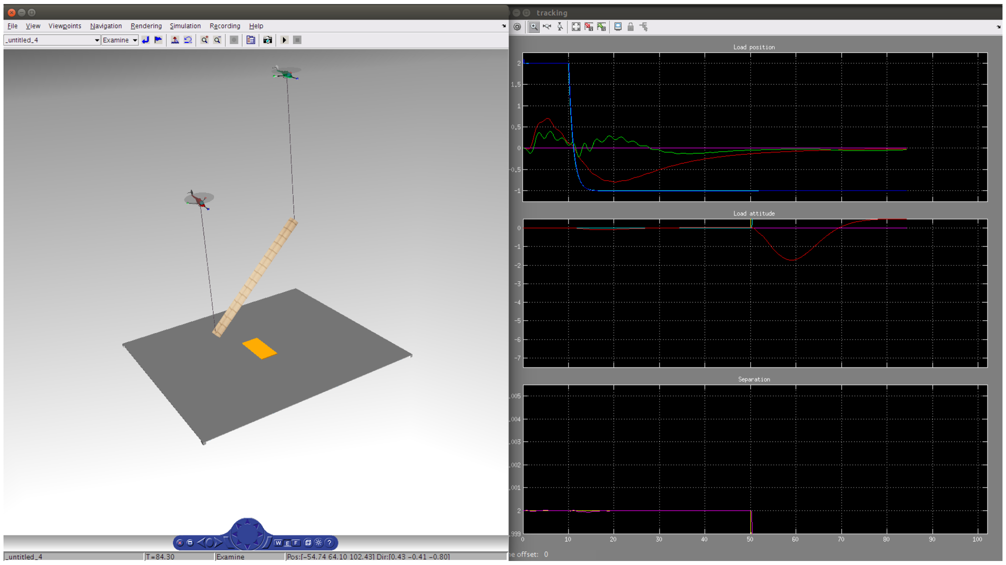

Figure 5.2.38: A snapshot from simulation testing trajectory tracking *see* `https://youtu.be/bJs7ehfYPP0`

Chapter 6

Conclusion

Increasing the number of supply plants to increase output capability is done in many process control cases, the twin-helicopter load transportation system is an application of the same idea to a mechanical (force) system. Besides the increase in carrying capacity, the twin-helicopter transportation system has added degrees of freedom which allow for not only the load translation to be controlled, but also the load attitude. This study focused on determining whether a stabilising solution exist for the twin-helicopter load transportation system in the real world with reasonable uncertainty. Through the efforts of modelling, estimation and control, a robust (QFT) solution was found. The study did not focus on what the expected increase in carrying capacity may be. In an optimal configuration, it is not unreasonable to expect the increase in carrying capacity to be slightly less than double the carrying capacity of a single helicopter, at least in steady-state. The control "energy" would need to be shared between stabilising the twin-helicopter lift system and carrying the load. So in terms of the individual helicopter thrust capability, there should be some "headroom" left for stabilising the configuration. The reasoning is sufficient to not deny the claims of approximately proportional increase in carrying capacity, although, a study looking at the extremes of load lifting capability is recommended as one would expect this to be a high-priority client requirement.

Attitude control of the load is not just a matter of convenience, for many load structures that need transportation, attitude control is necessary. The necessity may not have been visible due to the fact that there were no generic means available in the past. In the past, load attitude was not controlled, it was simply constrained through the tethering configuration as shown in Fig. 6.0.1. NWW (2016) quote wind turbine blades of lengths up to 45 m, which is more than double the length of a UH-60 Black Hawk helicopter (FAS 2000). The conventional tethering for loads such as wind turbine blades and radio masts (loads that are long and slender) may put too much tension on the supporting configuration for it to be feasible to transport. Now that it has been shown that it is feasible to control the attitude of loads by aerial means, other uses may become apparent. One of the seasonal problems in Cape Town, South Africa is the devastating damage of flora and fauna by veldfires. The twin-helicopter transportation system may be used to carry larger quantities of water and have control in the pour rate (attitude control) to put out veldfires compared with the conventional water bomber strategy.

Figure 6.0.1: Limited attitude control (Sgt. Susan Wilt 2008)

In order to determine whether it was possible to find a solution to the twin-helicopter transportation system, development in the field of instrumentation, modelling and estimation had to be done as preliminaries. Each of the preceding chapters have contributed to the knowledge of the field in the following manner. Chapter 2 described the instrumentation that was developed for autonomous control and verification of the model of the helicopters. This was essential in gaining credibility of the models used for finding the solution to the twin-helicopter slung load transportation system. The avionics and motion capture technology developed may be re-used with slight modifications, to industrialise the twin-helicopter load transportation system; moving from the laboratory environment to the outdoor where its application will find use. In the "real-world" implementation of the system, production helicopters with standard Attitude Command/Attitude Hold (ACAH) stability augmentation systems (SAS) may be used, as was envisioned in the coordinated load sharing control design. It is proposed that an interface to the SAS consisting of wireless communication to relay attitude and altitude reference be designed - called the Twin-lift Communication and Control (TCC) unit. The avionics developed, may be re-framed and placed on the load to estimate the load attitude and translation. The image processing and state-estimation concepts developed in Chapter 4 may be applied to a wide field-off-view camera "looking" towards the helicopters to estimate accurate separation distance measurements and load kinematics. The load sensor may be called the Twin-lift Load Sensor (TLS) unit. This Twin-lift Control System (TCS) architecture is depicted in Fig. 6.0.2. The coordinated load sharing controller designed in Chapter 5 may be implemented in TLS and the resulting attitude and altitude references be communicated over a real-time wireless network to the TCC units.

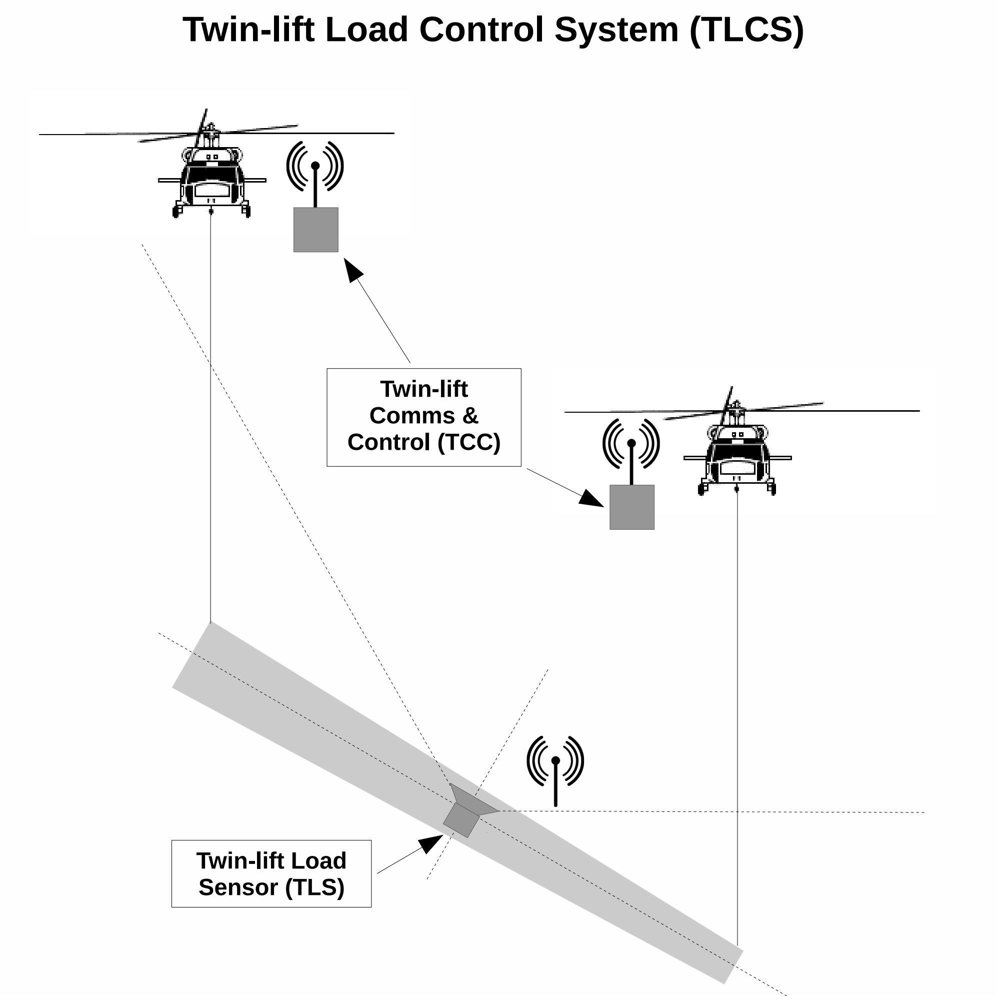

Figure 6.0.2: Twin-lift Load Control System

The effort in this thesis is the application of the state-of-the-art in control engineering towards the realisation of an “aerial crane” capable of transporting/assembling heavy loads to/in remote locations. Using quantitative robust control methodology, the solution space of a novel problem is found.

Appendix A

Electronics

A.1 Aerial Application Board

A.1.1 Communication

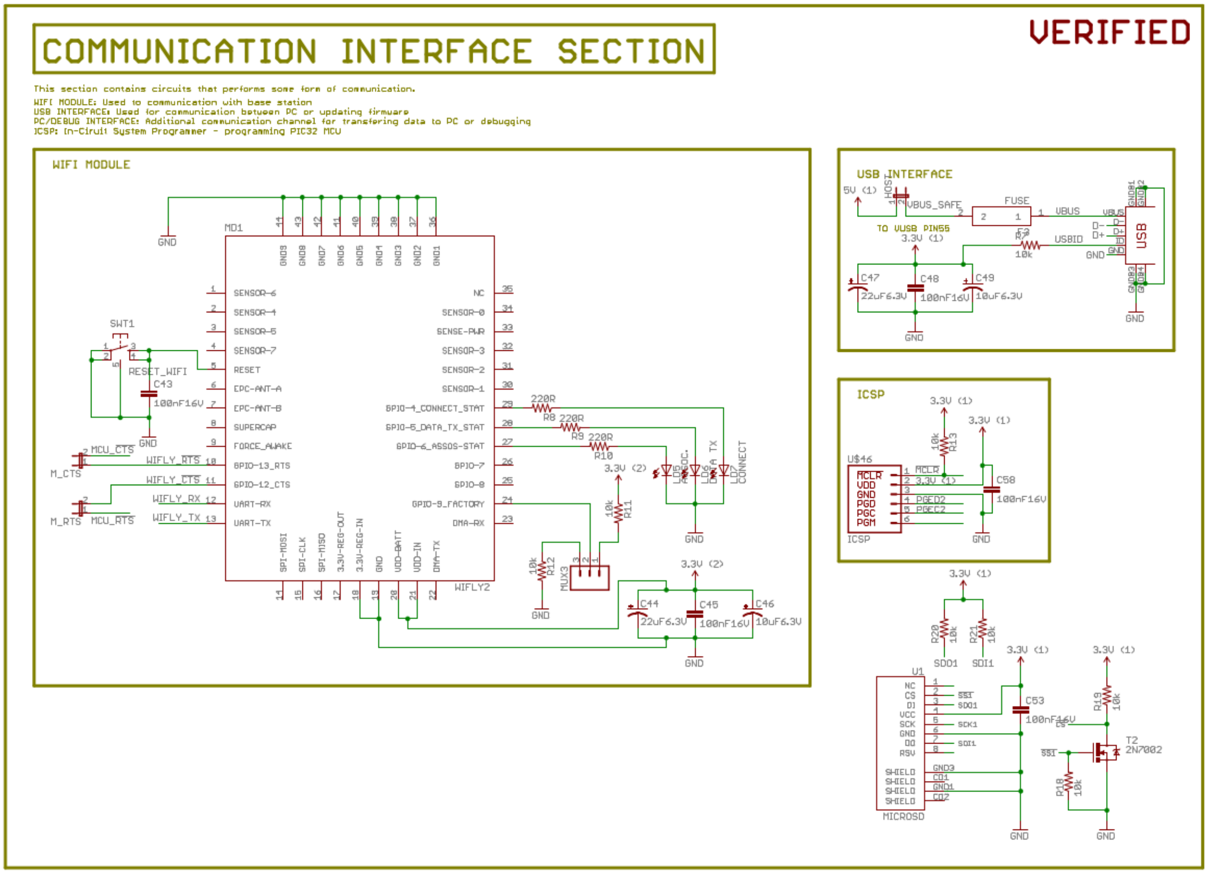

Figure A.1.1: Communication interface

A.1.2 General

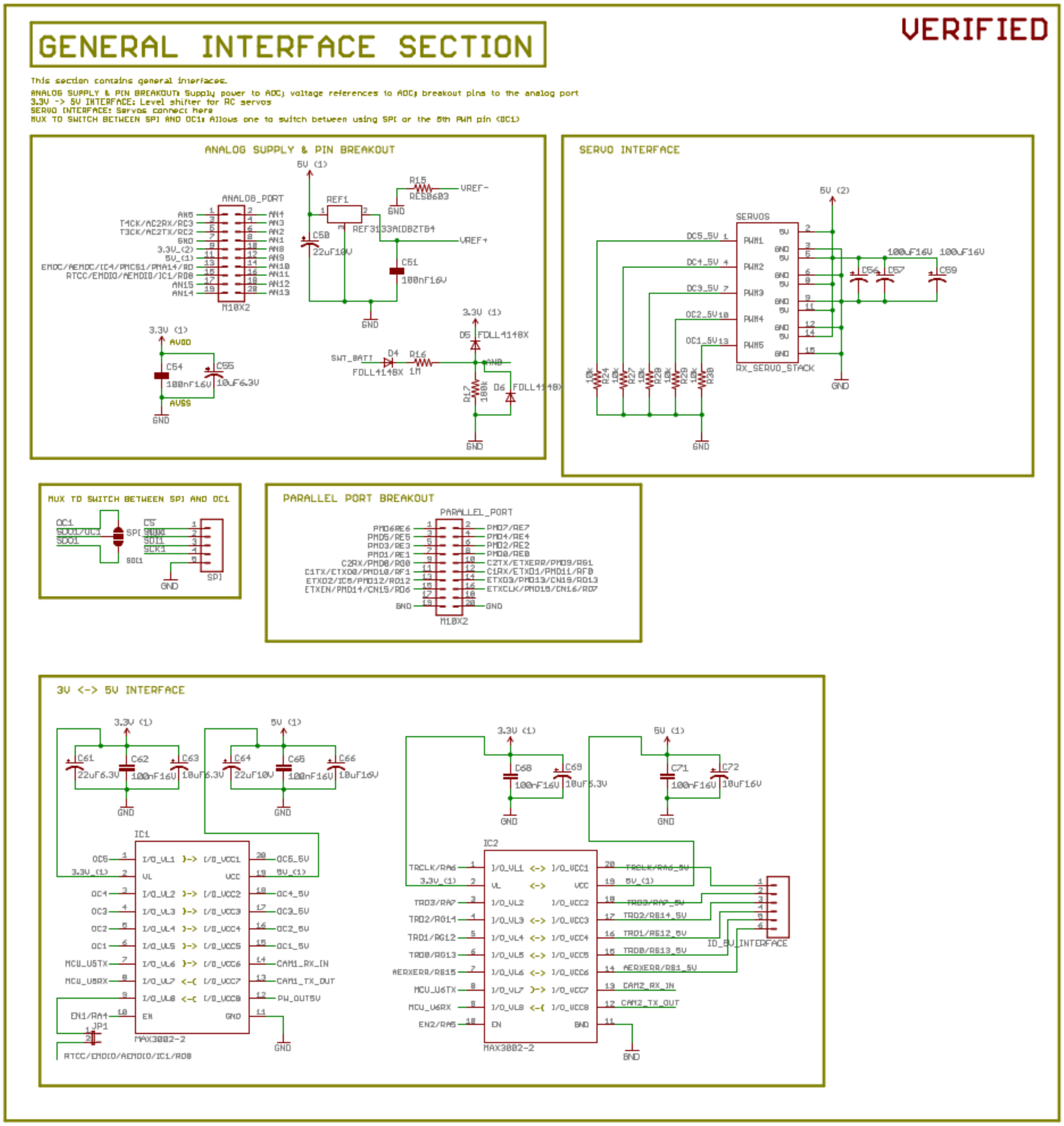

Figure A.1.2: General interface schematic

A.1.3 Microcontroller

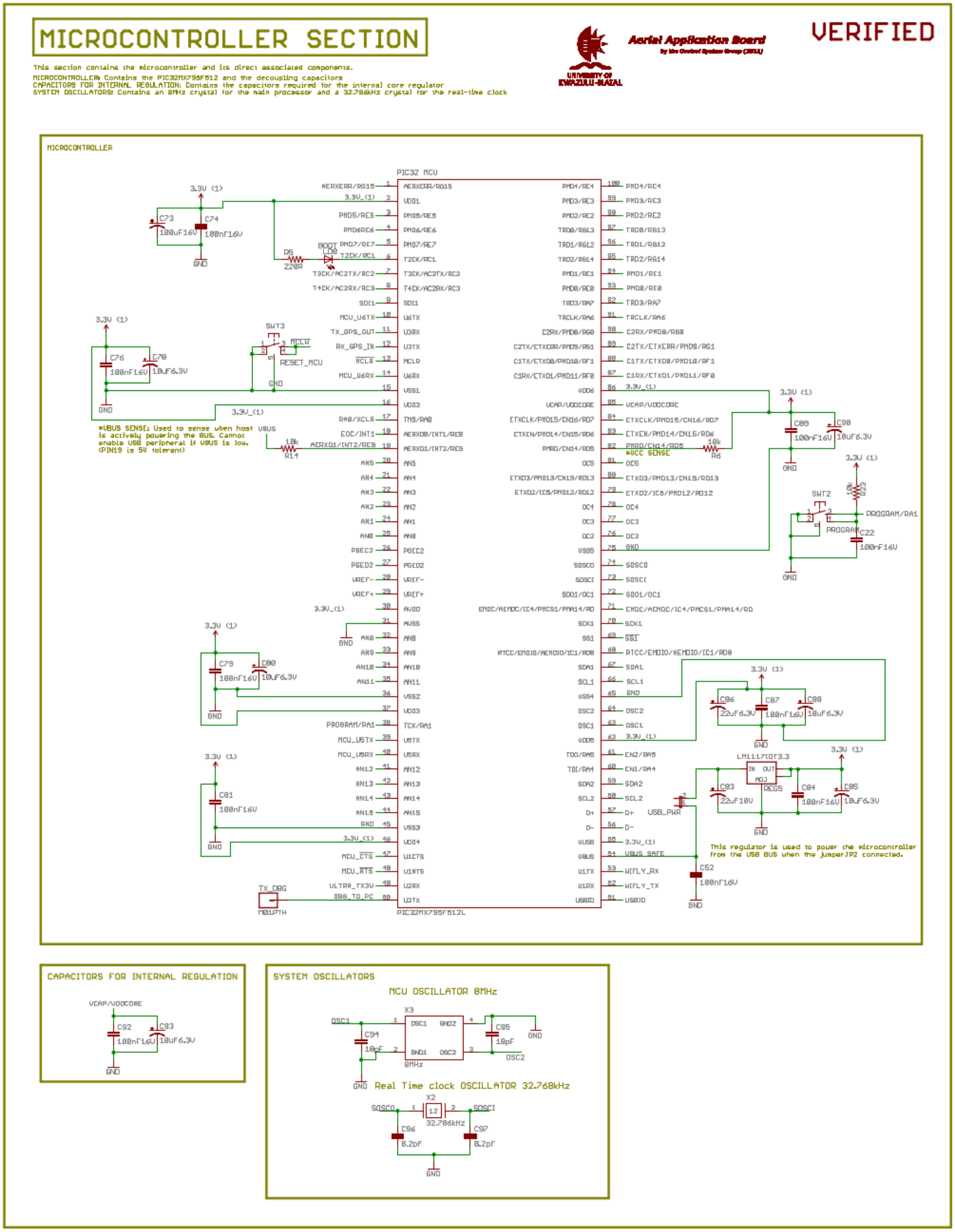

Figure A.1.3: Microcontroller schematic

A.1.4 Sensor

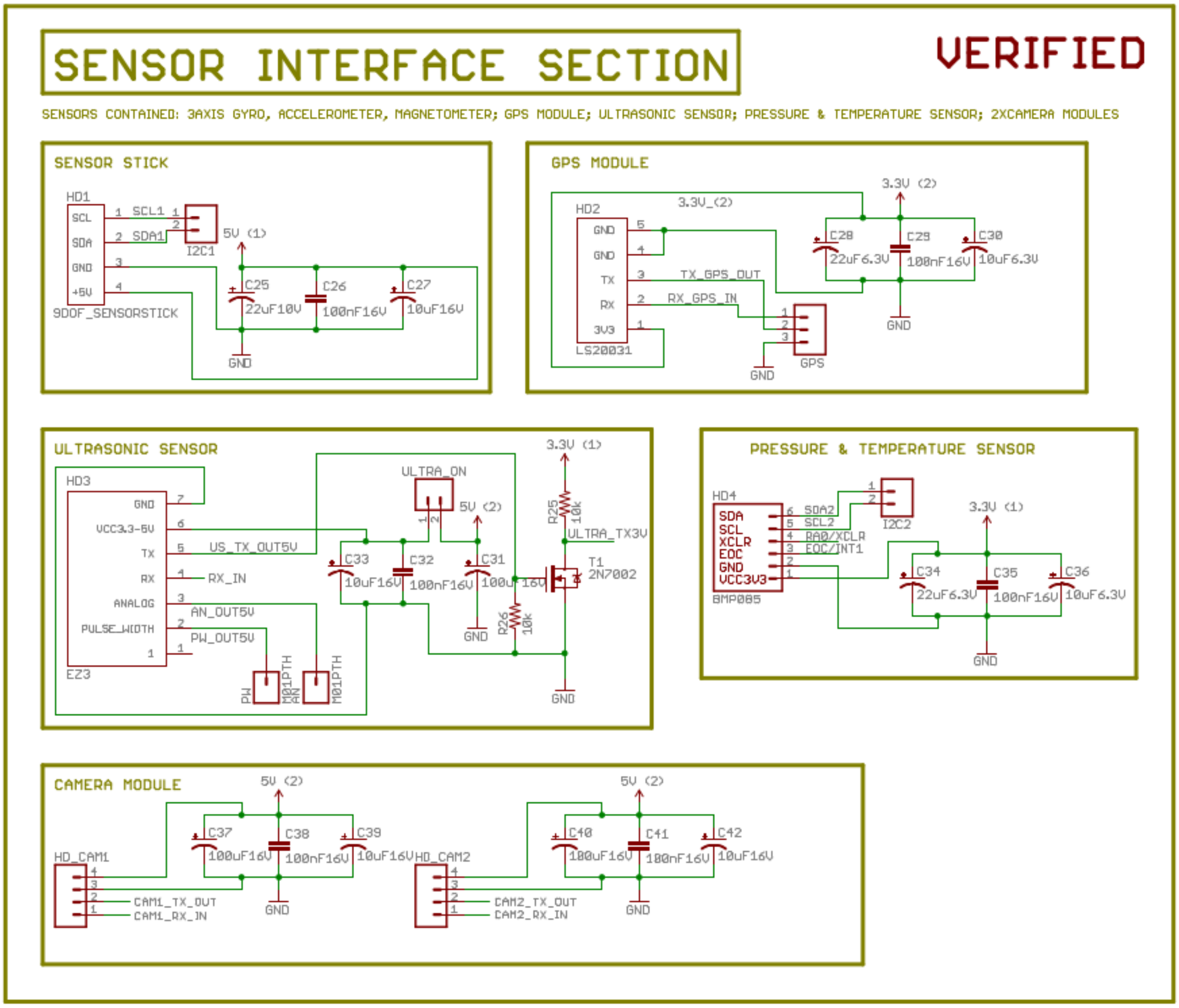

Figure A.1.4: Sensor interface schematic

A.1.5 Power

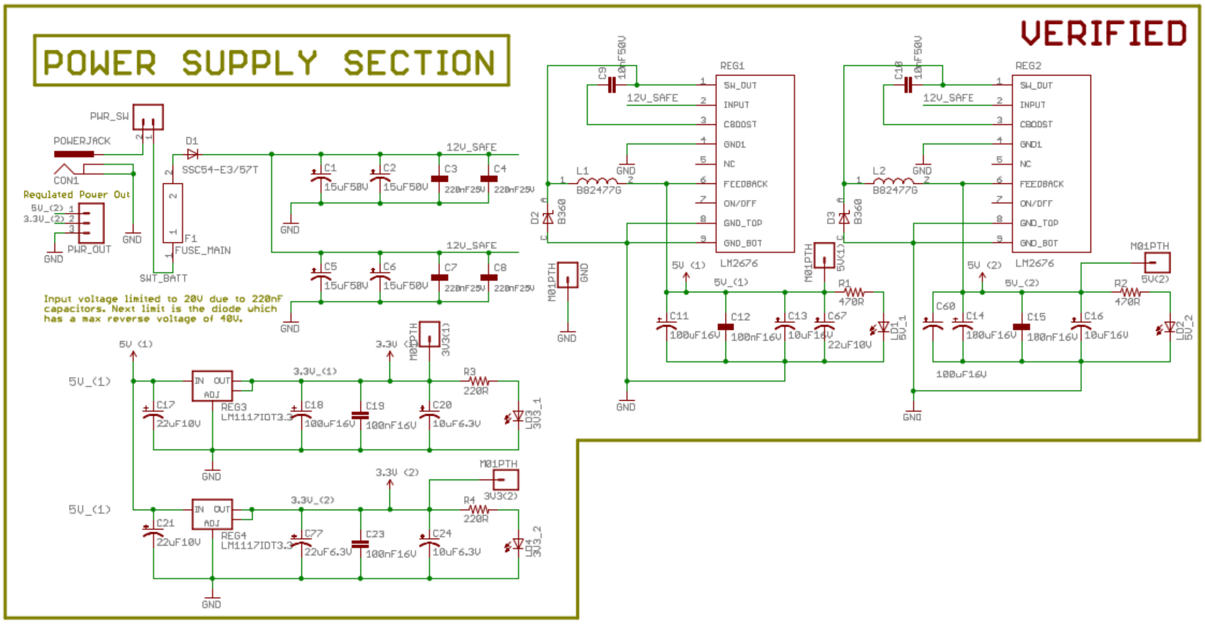

Figure A.1.5: Power supply schematic

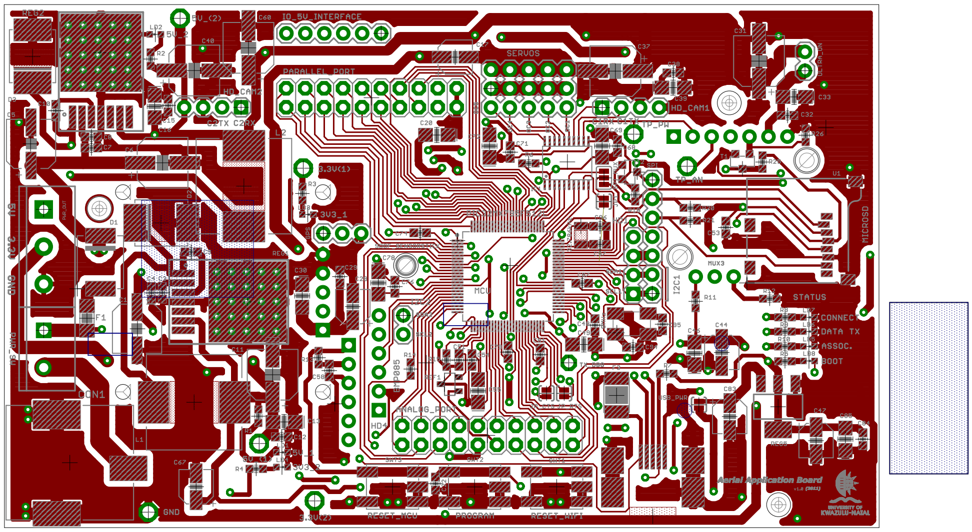

2011/09/28 11:53:44 AM f=2.22 C:\users\yashren\documents\eagle\aerial application board 2\main.brd

Figure A.1.6: Aerial Application Board Top Layout

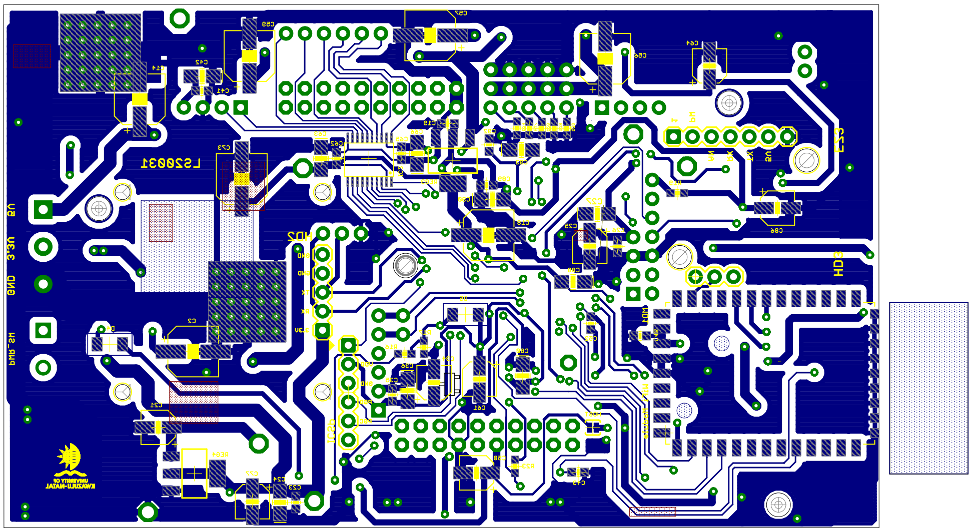

2011/09/28 11:55:15 AM f=2.22 C:\users\yashren\documents\eagle\aerial application board 2\main.brd

Figure A.1.7: Aerial Application Board Bottom Layout

A.2 PWM Multiplexer Board

A.2.1 Mux Board

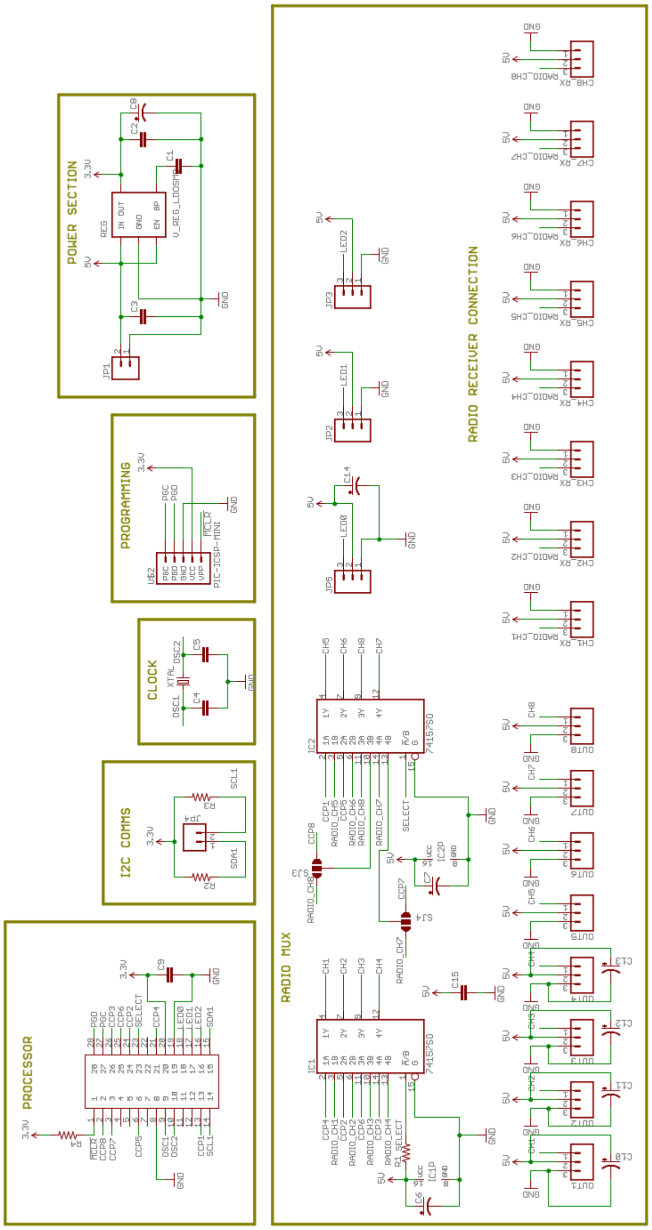

Figure A.2.1: PWM Multiplexer Board

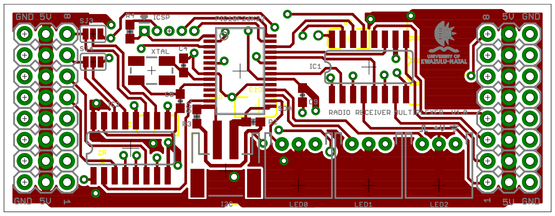

Figure A.2.2: PWM Multiplexer Board Top Layout

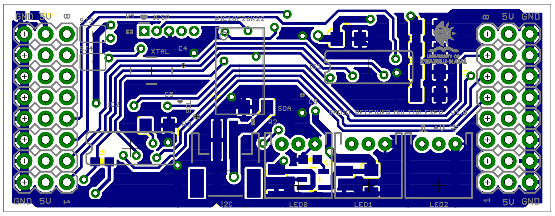

Figure A.2.3: PWM Multiplexer Board Bottom Layout

Appendix B

Mechanical

B.1 Landing Gear

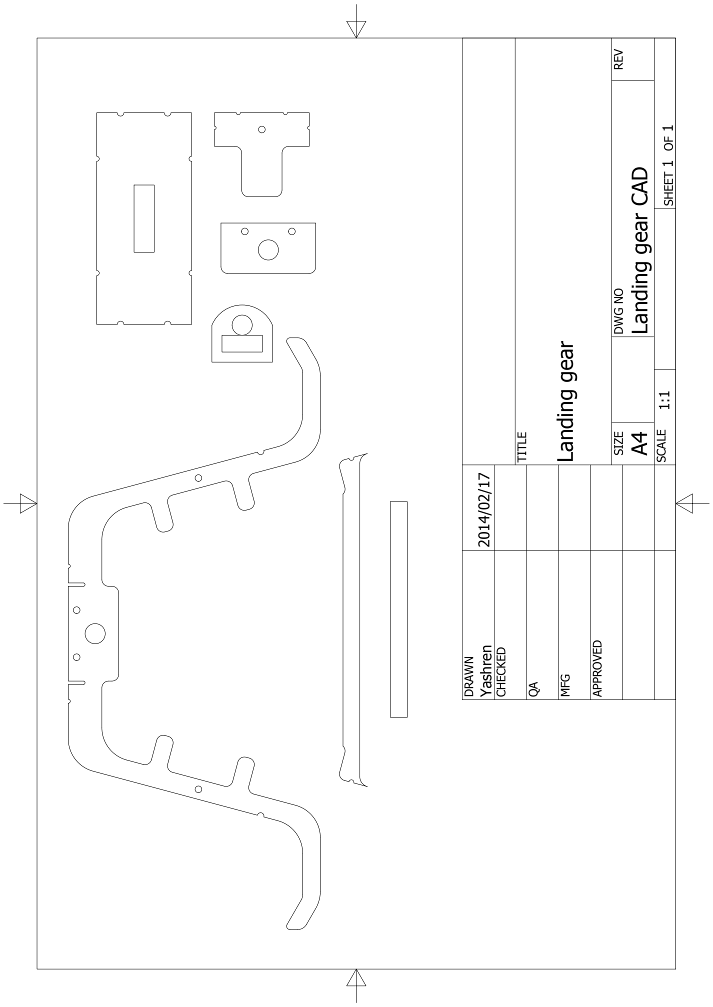

Figure B.1.1: Landing gear design

Appendix C

Modelling

C.1 Main Rotor Flapping Dynamics

$$
\begin{gathered}
\ddot{a}_0 = -\frac{1}{24\, I_{bmr}}(24\, K_{smr}\, a_0 - 24\, \ddot{z}\, M_b + 24\, \dot{\theta}\, \dot{x}\, M_b - 24\, \dot{\phi}\, \dot{y}\, M_b + 24\, \Omega^2\, I_{bmr}\, a_0 + 24\, \Omega^2\, e_{mr}\, a_0\, M_b \\
+ 2\, \rho\, R_{mr}^3\, c_{mr}\, \dot{x}\, C_{lmr}\, \dot{b}_1 + 2\, \rho\, R_{mr}^3\, c_{mr}\, \dot{y}\, C_{lmr}\, \dot{a}_1 - 3\, \Omega^2\, \rho\, R_{mr}^4\, c_{mr}\, \theta_0\, C_{lmr} - 2\, \rho\, c_{mr}\, e_{mr}^3\, \dot{x}\, C_{lmr}\, \dot{b}_1 \\
- 2\, \rho\, c_{mr}\, e_{mr}^3\, \dot{y}, C_{lmr}\, \dot{a}_1 - \Omega^2\, \rho\, c_{mr}\, e_{mr}^4\, \theta_0\, C_{lmr} - 3\, \rho\, R_{mr}^2\, c_{mr}\, \dot{x}^2\, \theta_0\, C_{lmr} - 3\, \rho\, R_{mr}^2\, c_{mr}\, \dot{y}^2\, \theta_0\, C_{lmr} \\
- 3\, \rho\, c_{mr}\, e_{mr}^2\, \dot{x}^2\, \theta_0, C_{lmr} - 3\, \rho\, c_{mr}\, e_{mr}^2\, \dot{y}^2\, \theta_0\, C_{lmr} + 2\, \dot{\phi}\, \rho\, R_{mr}^3\, c_{mr}\, \dot{x}\, C_{lmr} + 2\, \rho\, \dot{\theta}\, R_{mr}^3\, c_{mr}\, \dot{y}\, C_{lmr} \\
- 4\, \Omega\, \rho\, R_{mr}^3\, c_{mr}\, \dot{z}\, C_{lmr} + 3\, \Omega\, \rho\, R_{mr}^4\, c_{mr}\, C_{lmr}\, \dot{a}_0 + 4\, \Omega\, \rho\, R_{mr}^3\, c_{mr}\, C_{lmr}\, v_i + \dot{\phi}\, \rho\, c_{mr}\, e_{mr}^3\, \dot{x}\, C_{lmr} \\
+ \rho\, \dot{\theta}\, c_{mr}\, e_{mr}^3\, \dot{y}\, C_{lmr} - 2\, \Omega\, \rho\, c_{mr}\, e_{mr}^3\, \dot{z}\, C_{lmr} - \Omega\, \rho\, c_{mr}\, e_{mr}^4\, C_{lmr}\, \dot{a}_0 + 2\, \Omega\, \rho\, c_{mr}\, e_{mr}^3\, C_{lmr}\, v_i \\
- 3\, \dot{\phi}\, \rho\, R_{mr}^2\, c_{mr}\, e_{mr}\, \dot{x}\, C_{lmr} - 3\, \rho\, \dot{\theta}\, R_{mr}^2\, c_{mr}\, e_{mr}\, \dot{y}\, C_{lmr} + 6\, \Omega\, \rho\, R_{mr}^2\, c_{mr}\, e_{mr}\, \dot{z}\, C_{lmr} \\
- 8\, \Omega\, \rho\, R_{mr}^3\, c_{mr}\, e_{mr}\, C_{lmr}\, \dot{a}_0 - 6\, \Omega\, \rho\, R_{mr}^2\, c_{mr}\, e_{mr}\, C_{lmr}\, v_i + 4\, \Omega\, \rho\, R_{mr}^3\, c_{mr}\, \dot{x}\, B_{1,\mathrm{mr}}\, C_{lmr} \\
- 4\, \Omega\, \rho\, R_{mr}^3\, c_{mr}\, \dot{y}\, A_{1,\mathrm{mr}}\, C_{lmr} + 2\, \Omega\, \rho\, c_{mr}\, e_{mr}^3\, \dot{x}\, B_{1,\mathrm{mr}}\, C_{lmr} - 3\, \Omega\, \rho\, c_{mr}\, e_{mr}^3\, \dot{x}\, C_{lmr}\, a_1 \\
- 2\, \Omega\, \rho\, c_{mr}\, e_{mr}^3\, \dot{y}\, A_{1,\mathrm{mr}}\, C_{lmr} + 3\, \Omega\, \rho\, c_{mr}\, e_{mr}^3\, \dot{y}\, C_{lmr}\, b_1 + 6\, \rho\, R_{mr}\, c_{mr}\, e_{mr}\, \dot{x}^2\, \theta_0\, C_{lmr} \\
+ 6\, \rho\, R_{mr}\, c_{mr}\, e_{mr}^2\, \dot{x}\, C_{lmr}\, \dot{b}_1 - 6\, \rho\, R_{mr}^2\, c_{mr}\, e_{mr}\, \dot{x}\, C_{lmr}\, \dot{b}_1 + 6\, \rho\, R_{mr}\, c_{mr}\, e_{mr}\, \dot{y}^2\, \theta_0\, C_{lmr} \\
+ 6\, \rho\, R_{mr}\, c_{mr}\, e_{mr}^2\, \dot{y}\, C_{lmr}\, \dot{a}_1 - 6\, \rho\, R_{mr}^2\, c_{mr}\, e_{mr}\, \dot{y}\, C_{lmr}\, \dot{a}_1 + 4\, \Omega^2\, \rho\, R_{mr}^3\, c_{mr}\, e_{mr}\, \theta_0\, C_{lmr} \\
+ 6\, \Omega\, \rho\, R_{mr}^2\, c_{mr}\, e_{mr}^2\, C_{lmr}\, \dot{a}_0 - 6\, \Omega\, \rho\, R_{mr}^2\, c_{mr}\, e_{mr}\, \dot{x}\, B_{1,\mathrm{mr}}\, C_{lmr} + 6\, \Omega\, \rho\, R_{mr}\, c_{mr}\, e_{mr}^2\, \dot{x}\, C_{lmr}\, a_1 \\
- 3\, \Omega\, \rho\, R_{mr}^2\, c_{mr}\, e_{mr}\, \dot{x}\, C_{lmr}\, a_1 + 6\, \Omega\, \rho\, R_{mr}^2\, c_{mr}\, e_{mr}\, \dot{y}\, A_{1,\mathrm{mr}}\, C_{lmr} \\
- 6\, \Omega\, \rho\, R_{mr}\, c_{mr}\, e_{mr}^2\, \dot{y}\, C_{lmr}\, b_1 + 3\, \Omega\, \rho\, R_{mr}^2\, c_{mr}\, e_{mr}\, \dot{y}\, C_{lmr}\, b_1)
\end{gathered} \tag{C.1.1}
$$

$$
\begin{gathered}
\ddot{a}_1 = 2\, \Omega\, \dot{b}_1 + \Omega^2\, a_1 + \frac{1}{48\, I_{bmr}}(96\, \Omega\, \dot{\phi}\, I_{bmr} - 48\, K_{smr}\, a_1 - 48\, \ddot{\theta}\, I_{bmr} - 48\, \Omega^2\, I_{bmr}\, a_1 - 48\, \Omega^2\, e_{mr}\, a_1\, M_b \\
+ 96\, \Omega\, \dot{\phi}\, e_{mr}\, M_b + 12\, \rho\, R_{mr}^2\, c_{mr}\, \dot{y}\, \dot{z}\, C_{lmr} - 8\, \rho\, R_{mr}^3\, c_{mr}\, \dot{y}\, C_{lmr}\, \dot{a}_0 - 12\, \rho\, R_{mr}^2\, c_{mr}\, \dot{y}\, C_{lmr}\, v_i \\
+ 6\, \Omega^2\, \rho\, R_{mr}^4\, c_{mr}\, A_{1,\mathrm{mr}}\, C_{lmr} + 6\, \Omega^2\, \rho\, R_{mr}^4\, c_{mr}\, C_{lmr}\, b_1 + 12\, \rho\, c_{mr}\, e_{mr}^2\, \dot{y}\, \dot{z}\, C_{lmr} \\
+ 8\, \rho\, c_{mr}\, e_{mr}^3\, \dot{y}\, C_{lmr}\, \dot{a}_0 - 12\, \rho\, c_{mr}\, e_{mr}^2\, \dot{y}\, C_{lmr}\, v_i + 2\, \Omega^2\, \rho\, c_{mr}\, e_{mr}^4\, A_{1,\mathrm{mr}}\, C_{lmr} \\
- 2\, \Omega^2\, \rho\, c_{mr}\, e_{mr}^4\, C_{lmr}\, b_1 - 6\, \Omega\, \rho\, \dot{\theta}\, R_{mr}^4\, c_{mr}\, C_{lmr} + 3\, \rho\, R_{mr}^2\, c_{mr}\, \dot{x}^2\, A_{1,\mathrm{mr}}\, C_{lmr}
\end{gathered}
$$

$$\begin{aligned}
&+ 3\,\rho\,R_{mr}^2\,c_{mr}\,\dot{x}^2\,C_{lmr}\,b_1 + 9\,\rho\,R_{mr}^2\,c_{mr}\,\dot{y}^2\,A_{1,\mathrm{mr}}\,C_{lmr} - 3\,\rho\,R_{mr}^2\,c_{mr}\,\dot{y}^2\,C_{lmr}\,b_1 \\
&- 2\,\Omega\,\rho\,\dot{\theta}\,c_{mr}\,e_{mr}^4\,C_{lmr} + 3\,\rho\,c_{mr}\,e_{mr}^2\,\dot{x}^2\,A_{1,\mathrm{mr}}\,C_{lmr} + 3\,\rho\,c_{mr}\,e_{mr}^2\,\dot{x}^2\,C_{lmr}\,b_1 \\
&+ 9\,\rho\,c_{mr}\,e_{mr}^2\,\dot{y}^2\,A_{1,\mathrm{mr}}\,C_{lmr} - 3\,\rho\,c_{mr}\,e_{mr}^2\,\dot{y}^2\,C_{lmr}\,b_1 - 6\,\Omega\,\rho\,R_{mr}^4\,c_{mr}\,C_{lmr}\,\dot{a}_1 \\
&+ 2\,\Omega\,\rho\,c_{mr}\,e_{mr}^4\,C_{lmr}\,\dot{a}_1 - 24\,\rho\,R_{mr}\,c_{mr}\,e_{mr}\,\dot{y}\,\dot{z}\,C_{lmr} + 24\,\rho\,R_{mr}\,c_{mr}\,e_{mr}\,\dot{y}\,C_{lmr}\,v_i + 16\,\Omega\,\rho\,R_{mr}^3 \\
&c_{mr}\,e_{mr}\,C_{lmr}\,\dot{a}_1 + 8\,\Omega\,\rho\,R_{mr}^3\,c_{mr}\,\dot{x}\,C_{lmr}\,a_0 + 16\,\Omega\,\rho\,R_{mr}^3\,c_{mr}\,\dot{y}\,\theta_0\,C_{lmr} + 4\,\Omega\,\rho\,c_{mr}\,e_{mr}^3\,\dot{x}\,C_{lmr}\,a_0 \\
&+ 8\,\Omega\,\rho\,c_{mr}\,e_{mr}^3\,\dot{y}\,\theta_0\,C_{lmr} - 6\,\rho\,R_{mr}\,c_{mr}\,e_{mr}\,\dot{x}^2\,A_{1,\mathrm{mr}}\,C_{lmr} - 6\,\rho\,R_{mr}\,c_{mr}\,e_{mr}\,\dot{x}^2\,C_{lmr}\,b_1 \\
&- 18\,\rho\,R_{mr}\,c\,e_{mr}\,\dot{y}^2\,A_{1,\mathrm{mr}}\,C_{lmr} - 24\,\rho\,R_{mr}\,c_{mr}\,e_{mr}^2\,\dot{y}\,C_{lmr}\,\dot{a}_0 + 24\,\rho\,R_{mr}^2\,c_{mr}\,e_{mr}\,\dot{y}\,C_{lmr}\,\dot{a}_0 \\
&+ 6\,\rho\,R_{mr}\,c_{mr}\,e_{mr}\,\dot{y}^2\,C_{lmr}\,b_1 - 8\,\Omega^2\,\rho\,R_{mr}^3\,c_{mr}\,e_{mr}\,A_{1,\mathrm{mr}}\,C_{lmr} - 12\,\Omega\,\rho\,R_{mr}^2\,c_{mr}\,e_{mr}^2\,C_{lmr}\,\dot{a}_1 \\
&- 16\,\Omega^2\,\rho\,R_{mr}^3\,c_{mr}\,e_{mr}\,C_{lmr}\,b_1 - 6\,\rho\,R_{mr}^2\,c_{mr}\,\dot{x}\,\dot{y}\,B_{1,\mathrm{mr}}\,C_{lmr} + 6\,\rho\,R_{mr}^2\,c_{mr}\,\dot{x}\,\dot{y}\,C_{lmr}\,a_1 \\
&- 6\,\rho\,c_{mr}\,e_{mr}^2\,\dot{x}\,\dot{y}\,B_{1,\mathrm{mr}}\,C_{lmr} + 6\,\rho\,c_{mr}\,e_{mr}^2\,\dot{x}\,\dot{y}\,C_{lmr}\,a_1 + 8\,\Omega\,\rho\,\dot{\theta}\,R_{mr}^3\,c_{mr}\,e_{mr}\,C_{lmr} \\
&+ 12\,\Omega^2\,\rho\,R_{mr}^2\,c_{mr}\,e_{mr}^2\,C_{lmr}\,b_1 + 12\,\rho\,R_{mr}\,c_{mr}\,e_{mr}\,\dot{x}\,\dot{y}\,B_{1,\mathrm{mr}}\,C_{lmr} - 12\,\rho\,R_{mr}\,c_{mr}\,e_{mr}\,\dot{x}\,\dot{y}\,C_{lmr}\,a_1 \\
&- 12\,\Omega\,\rho\,R_{mr}^2\,c_{mr}\,e_{mr}\,\dot{x}\,C_{lmr}\,a_0 - 24\,\Omega\,\rho\,R_{mr}^2\,c_{mr}\,e_{mr}\,\dot{y}\,\theta_0\,C_{lmr})
\end{aligned} \tag{C.1.2}$$

$$\begin{aligned}
\ddot{b}_1 = {} & \Omega^2\,b_1 - 2\,\Omega\,\dot{a}_1 - \frac{1}{48\,I_{bmr}}(48\,\ddot{\phi}\,I_{bmr} + 48\,K_{smr}\,b_1 + 96\,\Omega\,\dot{\theta}\,I_{bmr} + 48\,\Omega^2\,I_{bmr}\,b_1 + 48\,\Omega^2\,e_{mr}\,b_1\,M_b \\
&+ 96\,\Omega\,\dot{\theta}\,e_{mr}\,M_b - 12\,\rho\,R_{mr}^2\,c_{mr}\,\dot{x}\,\dot{z}\,C_{lmr} + 8\,\rho\,R_{mr}^3\,c_{mr}\,\dot{x}\,C_{lmr}\,\dot{a}_0 + 12\,\rho\,R_{mr}^2\,c_{mr}\,\dot{x}\,C_{lmr}\,v_i \\
&+ 6\,\Omega^2\,\rho\,R_{mr}^4\,c_{mr}\,B_{1,\mathrm{mr}}\,C_{lmr} + 6\,\Omega^2\,\rho\,R_{mr}^4\,c_{mr}\,C_{lmr}\,a_1 - 12\,\rho\,c_{mr}\,e_{mr}^2\,\dot{x}\,\dot{z}\,C_{lmr} \\
&- 8\,\rho\,c_{mr}\,e_{mr}^3\,\dot{x}\,C_{lmr}\,\dot{a}_0 + 12\,\rho\,c_{mr}\,e_{mr}^2\,\dot{x}\,C_{lmr}\,v_i + 2\,\Omega^2\,\rho\,c_{mr}\,e_{mr}^4\,B_{1,\mathrm{mr}}\,C_{lmr} \\
&- 2\,\Omega^2\,\rho\,c_{mr}\,e_{mr}^4\,C_{lmr}\,a_1 + 6\,\Omega\,\dot{\phi}\,\rho\,R_{mr}^4\,c_{mr}\,C_{lmr} + 9\,\rho\,R_{mr}^2\,c_{mr}\,\dot{x}^2\,B_{1,\mathrm{mr}}\,C_{lmr} \\
&- 3\,\rho\,R_{mr}^2\,c_{mr}\,\dot{x}^2\,C_{lmr}\,a_1 + 3\,\rho\,R_{mr}^2\,c_{mr}\,\dot{y}^2\,B_{1,\mathrm{mr}}\,C_{lmr} + 3\,\rho\,R_{mr}^2\,c_{mr}\,\dot{y}^2\,C_{lmr}\,a_1 \\
&+ 2\,\Omega\,\dot{\phi}\,\rho\,c_{mr}\,e_{mr}^4\,C_{lmr} + 9\,\rho\,c_{mr}\,e_{mr}^2\,\dot{x}^2\,B_{1,\mathrm{mr}}\,C_{lmr} - 3\,\rho\,c_{mr}\,e_{mr}^2\,\dot{x}^2\,C_{lmr}\,a_1 \\
&+ 3\,\rho\,c_{mr}\,e_{mr}^2\,\dot{y}^2\,B_{1,\mathrm{mr}}\,C_{lmr} + 3\,\rho\,c_{mr}\,e_{mr}^2\,\dot{y}^2\,C_{lmr}\,a_1 + 6\,\Omega\,\rho\,R_{mr}^4\,c_{mr}\,C_{lmr}\,\dot{b}_1 \\
&- 2\,\Omega\,\rho\,c_{mr}\,e_{mr}^4\,C_{lmr}\,\dot{b}_1 + 24\,\rho\,R_{mr}\,c_{mr}\,e_{mr}\,\dot{x}\,\dot{z}\,C_{lmr} - 24\,\rho\,R_{mr}\,c_{mr}\,e_{mr}\,\dot{x}\,C_{lmr}\,v_i \\
&- 16\,\Omega\,\rho\,R_{mr}^3\,c_{mr}\,e_{mr}\,C_{lmr}\,\dot{b}_1 - 16\,\Omega\,\rho\,R_{mr}^3\,c_{mr}\,\dot{x}\,\theta_0\,C_{lmr} + 8\,\Omega\,\rho\,R_{mr}^3\,c_{mr}\,\dot{y}\,C_{lmr}\,a_0 \\
&- 8\,\Omega\,\rho\,c_{mr}\,e_{mr}^3\,\dot{x}\,\theta_0\,C_{lmr} + 4\,\Omega\,\rho\,c_{mr}\,e_{mr}^3\,\dot{y}\,C_{lmr}\,a_0 - 18\,\rho\,R_{mr}\,c_{mr}\,e_{mr}\,\dot{x}^2\,B_{1,\mathrm{mr}}\,C_{lmr} \\
&+ 24\,\rho\,R_{mr}\,c_{mr}\,e_{mr}^2\,\dot{x}\,C_{lmr}\,\dot{a}_0 - 24\,\rho\,R_{mr}^2\,c_{mr}\,e_{mr}\,\dot{x}\,C_{lmr}\,\dot{a}_0 + 6\,\rho\,R_{mr}\,c_{mr}\,e_{mr}\,\dot{x}^2\,C_{lmr}\,a_1 \\
&- 6\,\rho\,R_{mr}\,c_{mr}\,e_{mr}\,\dot{y}^2\,B_{1,\mathrm{mr}}\,C_{lmr} - 6\,\rho\,R_{mr}\,c_{mr}\,e_{mr}\,\dot{y}^2\,C_{lmr}\,a_1 - 8\,\Omega^2\,\rho\,R_{mr}^3\,c_{mr}\,e_{mr}\,B_{1,\mathrm{mr}}\,C_{lmr} \\
&- 16\,\Omega^2\,\rho\,R_{mr}^3\,c_{mr}\,e_{mr}\,C_{lmr}\,a_1 + 12\,\Omega\,\rho\,R_{mr}^2\,c_{mr}\,e_{mr}^2\,C_{lmr}\,\dot{b}_1 - 6\,\rho\,R_{mr}^2\,c_{mr}\,\dot{x}\,\dot{y}\,A_{1,\mathrm{mr}}\,C_{lmr} \\
&+ 6\,\rho\,R_{mr}^2\,c_{mr}\,\dot{x}\,\dot{y}\,C_{lmr}\,b_1 - 6\,\rho\,c_{mr}\,e_{mr}^2\,\dot{x}\,\dot{y}\,A_{1,\mathrm{mr}}\,C_{lmr} + 6\,\rho\,c_{mr}\,e_{mr}^2\,\dot{x}\,\dot{y}\,C_{lmr}\,b_1 \\
&- 8\,\Omega\,\dot{\phi}\,\rho\,R_{mr}^3\,c_{mr}\,e_{mr}\,C_{lmr} + 12\,\Omega^2\,\rho\,R_{mr}^2\,c_{mr}\,e_{mr}^2\,C_{lmr}\,a_1 + 12\,\rho\,R_{mr}\,c_{mr}\,e_{mr}\,\dot{x}\,\dot{y}\,A_{1,\mathrm{mr}}\,C_{lmr} \\
&- 12\,\rho\,R_{mr}\,c_{mr}\,e_{mr}\,\dot{x}\,\dot{y}\,C_{lmr}\,b_1 + 24\,\Omega\,\rho\,R_{mr}^2\,c_{mr}\,e_{mr}\,\dot{x}\,\theta_0\,C_{lmr} \\
&- 12\,\Omega\,\rho\,R_{mr}^2\,c_{mr}\,e_{mr}\,\dot{y}\,C_{lmr}\,a_0)
\end{aligned} \tag{C.1.3}$$

C.2 Stabiliser Flapping Dynamics

$$\begin{aligned}\ddot{a}_1 = -\frac{1}{16\,I_{bst}}(&16\,\ddot{\theta}\,I_{bst} + 16\,K_{smr}\,a_1 - 32\,\Omega\,\dot{\phi}\,I_{bst} - 32\,\Omega\,I_{bst}\,\dot{b}_1 + 4\,\rho\,c_{st}\,\dot{y}\,\dot{z}\,C_{lst}\,{R_i}^2 \\ &- 4\,\rho\,c_{st}\,\dot{y}\,\dot{z}\,C_{lst}\,{R_{\mathrm{st}}}^2 - 4\,\rho\,c_{st}\,\dot{y}\,C_{lst}\,{R_i}^2\,v_i + 4\,\rho\,c_{st}\,\dot{y}\,C_{lst}\,{R_{\mathrm{st}}}^2\,v_i \\ &+ 2\,\Omega^2\,\rho\,c_{st}\,A_1\,C_{lst}\,{R_i}^4 - 2\,\Omega^2\,\rho\,c_{st}\,A_1\,C_{lst}\,{R_{\mathrm{st}}}^4 + 2\,\Omega^2\,\rho\,c_{st}\,C_{lst}\,{R_i}^4\,b_1 \\ &- 2\,\Omega^2\,\rho\,c_{st}\,C_{lst}\,{R_{\mathrm{st}}}^4\,b_1 - 2\,\Omega\,\rho\,\dot{\theta}\,c_{st}\,C_{lst}\,{R_i}^4 + 2\,\Omega\,\rho\,\dot{\theta}\,c_{st}\,C_{lst}\,{R_{\mathrm{st}}}^4 \\ &+ \rho\,c_{st}\,\dot{x}^2\,A_1\,C_{lst}\,{R_i}^2 - \rho\,c_{st}\,\dot{x}^2\,A_1\,C_{lst}\,{R_{\mathrm{st}}}^2 + \rho\,c_{st}\,\dot{x}^2\,C_{lst}\,{R_i}^2\,b_1 - \rho\,c_{st}\,\dot{x}^2\,C_{lst}\,{R_{\mathrm{st}}}^2\,b_1 \\ &+ 3\,\rho\,c_{st}\,\dot{y}^2\,A_1\,C_{lst}\,{R_i}^2 - 3\,\rho\,c_{st}\,\dot{y}^2\,A_1\,C_{lst}\,{R_{\mathrm{st}}}^2 - \rho\,c_{st}\,\dot{y}^2\,C_{lst}\,{R_i}^2\,b_1 \\ &+ \rho\,c_{st}\,\dot{y}^2\,C_{lst}\,{R_{\mathrm{st}}}^2\,b_1 - 2\,\Omega\,\rho\,c_{st}\,C_{lst}\,{R_i}^4\,\dot{a}_1 + 2\,\Omega\,\rho\,c_{st}\,C_{lst}\,{R_{\mathrm{st}}}^4\,\dot{a}_1 \\ &- 2\,\rho\,c_{st}\,\dot{x}\,\dot{y}\,B_1\,C_{lst}\,{R_i}^2 + 2\,\rho\,c_{st}\,\dot{x}\,\dot{y}\,B_1\,C_{lst}\,{R_{\mathrm{st}}}^2 + 2\,\rho\,c_{st}\,\dot{x}\,\dot{y}\,C_{lst}\,{R_i}^2\,a_1 \\ &- 2\,\rho\,c_{st}\,\dot{x}\,\dot{y}\,C_{lst}\,{R_{\mathrm{st}}}^2\,a_1)\end{aligned} \tag{C.2.1}$$

$$\begin{aligned}\ddot{b}_1 = -\frac{1}{16\,I_{bst}}(&16\,\ddot{\phi}\,I_{bst} + 16\,K_{smr}\,b_1 + 32\,\Omega\,\dot{\theta}\,I_{bst} + 32\,\Omega\,I_{bst}\,\dot{a}_1 + 4\,\rho\,c_{st}\,\dot{x}\,\dot{z}\,C_{lst}\,{R_i}^2 \\ &- 4\,\rho\,c_{st}\,\dot{x}\,\dot{z}\,C_{lst}\,{R_{\mathrm{st}}}^2 - 4\,\rho\,c_{st}\,\dot{x}\,C_{lst}\,{R_i}^2\,v_i + 4\,\rho\,c_{st}\,\dot{x}\,C_{lst}\,{R_{\mathrm{st}}}^2\,v_i \\ &- 2\,\Omega^2\,\rho\,c_{st}\,B_1\,C_{lst}\,{R_i}^4 + 2\,\Omega^2\,\rho\,c_{st}\,B_1\,C_{lst}\,{R_{\mathrm{st}}}^4 - 2\,\Omega^2\,\rho\,c_{st}\,C_{lst}\,{R_i}^4\,a_1 \\ &+ 2\,\Omega^2\,\rho\,c_{st}\,C_{lst}\,{R_{\mathrm{st}}}^4\,a_1 - 2\,\Omega\,\dot{\phi}\,\rho\,c_{st}\,C_{lst}\,{R_i}^4 + 2\,\Omega\,\dot{\phi}\,\rho\,c_{st}\,C_{lst}\,{R_{\mathrm{st}}}^4 \\ &- 3\,\rho\,c_{st}\,\dot{x}^2\,B_1\,C_{lst}\,{R_i}^2 + 3\,\rho\,c_{st}\,\dot{x}^2\,B_1\,C_{lst}\,{R_{\mathrm{st}}}^2 + \rho\,c_{st}\,\dot{x}^2\,C_{lst}\,{R_i}^2\,a_1 \\ &- \rho\,c_{st}\,\dot{x}^2\,C_{lst}\,{R_{\mathrm{st}}}^2\,a_1 - \rho\,c_{st}\,\dot{y}^2\,B_1\,C_{lst}\,{R_i}^2 + \rho\,c_{st}\,\dot{y}^2\,B_1\,C_{lst}\,{R_{\mathrm{st}}}^2 \\ &- \rho\,c_{st}\,\dot{y}^2\,C_{lst}\,{R_i}^2\,a_1 + \rho\,c_{st}\,\dot{y}^2\,C_{lst}\,{R_{\mathrm{st}}}^2\,a_1 - 2\,\Omega\,\rho\,c_{st}\,C_{lst}\,{R_i}^4\,\dot{b}_1 \\ &+ 2\,\Omega\,\rho\,c_{st}\,C_{lst}\,{R_{\mathrm{st}}}^4\,\dot{b}_1 + 2\,\rho\,c_{st}\,\dot{x}\,\dot{y}\,A_1\,C_{lst}\,{R_i}^2 - 2\,\rho\,c_{st}\,\dot{x}\,\dot{y}\,A_1\,C_{lst}\,{R_{\mathrm{st}}}^2 \\ &- 2\,\rho\,c_{st}\,\dot{x}\,\dot{y}\,C_{lst}\,{R_i}^2\,b_1 + 2\,\rho\,c_{st}\,\dot{x}\,\dot{y}\,C_{lst}\,{R_{\mathrm{st}}}^2\,b_1)\end{aligned} \tag{C.2.2}$$

C.3 Main Rotor Forces

$$\begin{aligned}F_x = -\frac{1}{96}\rho\,b\,c_{mr}\,(R_{mr} - e_{mr})\,(&24\,R_{mr}\,\dot{z}\,C_{lmr}\,\dot{b}_1 - 24\,R_{mr}\,C_{lmr}\,\dot{b}_1\,v_i - 16\,\dot{\phi}\,R_{mr}^2\,C_{lmr}\,\dot{a}_0 \\ &- 24\,e_{mr}\,\dot{z}\,C_{lmr}\,\dot{b}_1 + 24\,e_{mr}\,C_{lmr}\,\dot{b}_1\,v_i + 8\,\dot{\phi}\,e_{mr}^2\,C_{lmr}\,\dot{a}_0 - 24\,\dot{x}\,\dot{z}\,\theta_0\,C_{lmr} + 72\,\dot{y}\,\dot{z}\,C_{lmr}\,a_0 \\ &+ 24\,\dot{x}\,\theta_0\,C_{lmr}\,v_i - 72\,\dot{y}\,C_{lmr}\,a_0\,v_i - 16\,R_{mr}^2\,C_{lmr}\,\dot{a}_0\,\dot{b}_1 - 16\,e_{mr}^2\,C_{lmr}\,\dot{a}_0\,\dot{b}_1 \\ &+ 24\,\dot{y}^2\,\theta_0\,C_{lmr}\,a_1 + 24\,\dot{y}^2\,A_{1,\mathrm{mr}}\,C_{lmr}\,a_0 - 48\,\dot{y}^2\,C_{lmr}\,a_0\,b_1 + 24\,\Omega\,R_{mr}\,\dot{x}\,C_d \\ &+ 24\,\dot{\phi}\,R_{mr}\,\dot{z}\,C_{lmr} - 24\,\dot{\phi}\,R_{mr}\,C_{lmr}\,v_i + 24\,\Omega\,e_{mr}\,\dot{x}\,C_d + 24\,\dot{\phi}\,e_{mr}\,\dot{z}\,C_{lmr} - 24\,\dot{\phi}\,e_{mr}\,C_{lmr}\,v_i \\ &+ 16\,\Omega^2\,R_{mr}^2\,\theta_0\,C_{lmr}\,a_1 + 8\,\Omega^2\,R_{mr}^2\,A_{1,\mathrm{mr}}\,C_{lmr}\,a_0 + 8\,\Omega^2\,R_{mr}^2\,C_{lmr}\,a_0\,b_1 + 4\,\Omega^2\,e_{mr}^2\,\theta_0\,C_{lmr}\,a_1 \\ &+ 8\,\Omega^2\,e_{mr}^2\,A_{1,\mathrm{mr}}\,C_{lmr}\,a_0 - 4\,\Omega^2\,e_{mr}^2\,C_{lmr}\,a_0\,b_1 + 8\,\dot{\phi}\,R_{mr}\,e_{mr}\,C_{lmr}\,\dot{a}_0 - 9\,\dot{\phi}\,R_{mr}\,\dot{x}\,B_{1,\mathrm{mr}}\,C_{lmr} \\ &+ 3\,\dot{\theta}\,R_{mr}\,\dot{x}\,A_{1,\mathrm{mr}}\,C_{lmr} + 3\,\dot{\phi}\,R_{mr}\,\dot{x}\,C_{lmr}\,a_1 + 3\,\dot{\theta}\,R_{mr}\,\dot{x}\,C_{lmr}\,b_1 + 3\,\dot{\phi}\,R_{mr}\,\dot{y}\,A_{1,\mathrm{mr}}\,C_{lmr} \\ &- 3\,\dot{\theta}\,R_{mr}\,\dot{y}\,B_{1,\mathrm{mr}}\,C_{lmr} - 21\,\dot{\phi}\,R_{mr}\,\dot{y}\,C_{lmr}\,b_1 - 15\,\dot{\theta}\,R_{mr}\,\dot{y}\,C_{lmr}\,a_1 \\ &+ 12\,\Omega\,R_{mr}\,\dot{z}\,B_{1,\mathrm{mr}}\,C_{lmr} + 36\,\Omega\,R_{mr}\,\dot{z}\,C_{lmr}\,a_1 - 12\,\Omega\,R_{mr}\,B_{1,\mathrm{mr}}\,C_{lmr}\,v_i - 36\,\Omega\,R_{mr}\,C_{lmr}\,a_1\,v_i\end{aligned}$$

$$
\begin{gathered}
+ 8\,\Omega\,\dot{\phi}\,R_{mr}^2\,\theta_0\,C_{lmr} - 8\,\Omega\,\dot{\theta}\,R_{mr}^2\,C_{lmr}\,a_0 - 9\,\dot{\phi}\,e_{mr}\,\dot{x}\,B_{1,\mathrm{mr}}\,C_{lmr} + 3\,\dot{\theta}\,e_{mr}\,\dot{x}\,A_{1,\mathrm{mr}}\,C_{lmr} \\
+ 3\,\dot{\phi}\,e_{mr}\,\dot{x}\,C_{lmr}\,a_1 + 3\,\dot{\theta}\,e_{mr}\,\dot{x}\,C_{lmr}\,b_1 + 3\,\dot{\phi}\,e_{mr}\,\dot{y}\,A_{1,\mathrm{mr}}\,C_{lmr} \\
- 3\,\dot{\theta}\,e_{mr}\,\dot{y}\,B_{1,\mathrm{mr}}\,C_{lmr} - 21\,\dot{\phi}\,e_{mr}\,\dot{y}\,C_{lmr}\,b_1 - 15\,\dot{\theta}\,e_{mr}\,\dot{y}\,C_{lmr}\,a_1 + 12\,\Omega\,e_{mr}\,\dot{z}\,B_{1,\mathrm{mr}}\,C_{lmr} \\
- 12\,\Omega\,e_{mr}\,\dot{z}\,C_{lmr}\,a_1 - 12\,\Omega\,e_{mr}\,B_{1,\mathrm{mr}}\,C_{lmr}\,v_i + 12\,\Omega\,e_{mr}\,C_{lmr}\,a_1\,v_i + 8\,\Omega\,\dot{\phi}\,e_{mr}^2\,\theta_0\,C_{lmr} \\
- 8\,\Omega\,\dot{\theta}\,e_{mr}^2\,C_{lmr}\,a_0 + 32\,R_{mr}\,e_{mr}\,C_{lmr}\,\dot{a}_0\,\dot{b}_1 + 12\,R_{mr}\,\dot{x}\,\theta_0\,C_{lmr}\,\dot{a}_0 \\
+ 3\,R_{mr}\,\dot{x}\,A_{1,\mathrm{mr}}\,C_{lmr}\,\dot{a}_1 - 9\,R_{mr}\,\dot{x}\,B_{1,\mathrm{mr}}\,C_{lmr}\,\dot{b}_1 + 3\,R_{mr}\,\dot{x}\,C_{lmr}\,\dot{a}_1\,b_1 \\
+ 3\,R_{mr}\,\dot{x}\,C_{lmr}\,a_1\,\dot{b}_1 + 3\,R_{mr}\,\dot{y}\,A_{1,\mathrm{mr}}\,C_{lmr}\,\dot{b}_1 - 3\,R_{mr}\,\dot{y}\,B_{1,\mathrm{mr}}\,C_{lmr}\,\dot{a}_1 - 36\,R_{mr}\,\dot{y}\,C_{lmr}\,\dot{a}_0\,a_0 \\
- 15\,R_{mr}\,\dot{y}\,C_{lmr}\,\dot{a}_1\,a_1 - 21\,R_{mr}\,\dot{y}\,C_{lmr}\,\dot{b}_1\,b_1 + 12\,\Omega\,R_{mr}\,\dot{x}\,C_{lmr}\,{a_0}^2 + 12\,\Omega\,R_{mr}\,\dot{x}\,C_{lmr}\,{a_1}^2 \\
+ 8\,\Omega\,R_{mr}^2\,\theta_0\,C_{lmr}\,\dot{b}_1 - 8\,\Omega\,R_{mr}^2\,B_{1,\mathrm{mr}}\,C_{lmr}\,\dot{a}_0 - 24\,\Omega\,R_{mr}^2\,C_{lmr}\,\dot{a}_0\,a_1 \\
- 8\,\Omega\,R_{mr}^2\,C_{lmr}\,\dot{a}_1\,a_0 - 12\,e_{mr}\,\dot{x}\,\theta_0\,C_{lmr}\,\dot{a}_0 - 3\,e_{mr}\,\dot{x}\,A_{1,\mathrm{mr}}\,C_{lmr}\,\dot{a}_1 + 9\,e_{mr}\,\dot{x}\,B_{1,\mathrm{mr}}\,C_{lmr}\,\dot{b}_1 \\
- 3\,e_{mr}\,\dot{x}\,C_{lmr}\,\dot{a}_1\,b_1 - 3\,e_{mr}\,\dot{x}\,C_{lmr}\,a_1\,\dot{b}_1 - 3\,e_{mr}\,\dot{y}\,A_{1,\mathrm{mr}}\,C_{lmr}\,\dot{b}_1 + 3\,e_{mr}\,\dot{y}\,B_{1,\mathrm{mr}}\,C_{lmr}\,\dot{a}_1 \\
+ 36\,e_{mr}\,\dot{y}\,C_{lmr}\,\dot{a}_0\,a_0 + 15\,e_{mr}\,\dot{y}\,C_{lmr}\,\dot{a}_1\,a_1 + 21\,e_{mr}\,\dot{y}\,C_{lmr}\,\dot{b}_1\,b_1 + 12\,\Omega\,e_{mr}\,\dot{x}\,C_{lmr}\,{a_0}^2 \\
+ 6\,\Omega\,e_{mr}\,\dot{x}\,C_{lmr}\,{a_1}^2 + 6\,\Omega\,e_{mr}\,\dot{x}\,C_{lmr}\,{b_1}^2 - 4\,\Omega\,e_{mr}^2\,\theta_0\,C_{lmr}\,\dot{b}_1 + 4\,\Omega\,e_{mr}^2\,B_{1,\mathrm{mr}}\,C_{lmr}\,\dot{a}_0 \\
- 12\,\Omega\,e_{mr}^2\,C_{lmr}\,\dot{a}_0\,a_1 + 4\,\Omega\,e_{mr}^2\,C_{lmr}\,\dot{a}_1\,a_0 + 24\,\dot{x}\,\dot{y}\,\theta_0\,C_{lmr}\,b_1 - 24\,\dot{x}\,\dot{y}\,B_{1,\mathrm{mr}}\,C_{lmr}\,a_0 \\
+48\,\dot{x}\,\dot{y}\,C_{lmr}\,a_0\,a_1+4\,\Omega^2\,R_{mr}\,e_{mr}\,\theta_0\,C_{lmr}\,a_1+8\,\Omega^2\,R_{mr}\,e_{mr}\,A_{1,\mathrm{mr}}\,C_{lmr}\,a_0-4\,\Omega^2\,R_{mr}\,e_{mr}\,C_{lmr}\,a_0\,b_1 \\
+ 8\,\Omega\,\dot{\phi}\,R_{mr}\,e_{mr}\,\theta_0\,C_{lmr} - 8\,\Omega\,\dot{\theta}\,R_{mr}\,e_{mr}\,C_{lmr}\,a_0 - 4\,\Omega\,R_{mr}\,e_{mr}\,\theta_0\,C_{lmr}\,\dot{b}_1 \\
+ 4\,\Omega\,R_{mr}\,e_{mr}\,B_{1,\mathrm{mr}}\,C_{lmr}\,\dot{a}_0 + 36\,\Omega\,R_{mr}\,e_{mr}\,C_{lmr}\,\dot{a}_0\,a_1 + 4\,\Omega\,R_{mr}\,e_{mr}\,C_{lmr}\,\dot{a}_1\,a_0 \\
- 12\,\Omega\,R_{mr}\,\dot{x}\,B_{1,\mathrm{mr}}\,C_{lmr}\,a_1 + 36\,\Omega\,R_{mr}\,\dot{y}\,\theta_0\,C_{lmr}\,a_0 + 24\,\Omega\,R_{mr}\,\dot{y}\,A_{1,\mathrm{mr}}\,C_{lmr}\,a_1 \\
- 12\,\Omega\,R_{mr}\,\dot{y}\,B_{1,\mathrm{mr}}\,C_{lmr}\,b_1 - 12\,\Omega\,R_{mr}\,\dot{y}\,C_{lmr}\,a_1\,b_1 + 6\,\Omega\,e_{mr}\,\dot{x}\,A_{1,\mathrm{mr}}\,C_{lmr}\,b_1 \\
+ 6\,\Omega\,e_{mr}\,\dot{x}\,B_{1,\mathrm{mr}}\,C_{lmr}\,a_1 + 36\,\Omega\,e_{mr}\,\dot{y}\,\theta_0\,C_{lmr}\,a_0 + 18\,\Omega\,e_{mr}\,\dot{y}\,A_{1,\mathrm{mr}}\,C_{lmr}\,a_1 \\
- 18\,\Omega\,e_{mr}\,\dot{y}\,B_{1,\mathrm{mr}}\,C_{lmr}\,b_1) \qquad \text{(C.3.1)}
\end{gathered}
$$

$$
\begin{gathered}
F_y = -\frac{1}{96}\rho\,b\,c_{mr}\;(R_{mr} - e_{mr})\;(24\,R_{mr}\,\dot{z}\,C_{lmr}\,\dot{a}_1 - 24\,R_{mr}\,C_{lmr}\,\dot{a}_1\,v_i - 16\,\dot{\theta}\,R_{mr}^2\,C_{lmr}\,\dot{a}_0 \\
- 24\,e_{mr}\,\dot{z}\,C_{lmr}\,\dot{a}_1 + 24\,e_{mr}\,C_{lmr}\,\dot{a}_1\,v_i + 8\,\dot{\theta}\,e_{mr}^2\,C_{lmr}\,\dot{a}_0 - 72\,\dot{x}\,\dot{z}\,C_{lmr}\,a_0 - 24\,\dot{y}\,\dot{z}\,\theta_0\,C_{lmr} \\
+ 72\,\dot{x}\,C_{lmr}\,a_0\,v_i + 24\,\dot{y}\,\theta_0\,C_{lmr}\,v_i - 16\,R_{mr}^2\,C_{lmr}\,\dot{a}_0\,\dot{a}_1 - 16\,e_{mr}^2\,C_{lmr}\,\dot{a}_0\,\dot{a}_1 - 24\,\dot{x}^2\,\theta_0\,C_{lmr}\,b_1 \\
+ 24\,\dot{x}^2\,B_{1,\mathrm{mr}}\,C_{lmr}\,a_0 - 48\,\dot{x}^2\,C_{lmr}\,a_0\,a_1 + 24\,\Omega\,R_{mr}\,\dot{y}\,C_d + 24\,\dot{\theta}\,R_{mr}\,\dot{z}\,C_{lmr} - 24\,\dot{\theta}\,R_{mr}\,C_{lmr}\,v_i \\
+24\,\Omega\,e_{mr}\,\dot{y}\,C_d+24\,\dot{\theta}\,e_{mr}\,\dot{z}\,C_{lmr}-24\,\dot{\theta}\,e_{mr}\,C_{lmr}\,v_i-16\,\Omega^2\,R_{mr}^2\,\theta_0\,C_{lmr}\,b_1+8\,\Omega^2\,R_{mr}^2\,B_{1,\mathrm{mr}}\,C_{lmr}\,a_0 \\
+ 8\,\Omega^2\,R_{mr}^2\,C_{lmr}\,a_0\,a_1 - 4\,\Omega^2\,e_{mr}^2\,\theta_0\,C_{lmr}\,b_1 + 8\,\Omega^2\,e_{mr}^2\,B_{1,\mathrm{mr}}\,C_{lmr}\,a_0 - 4\,\Omega^2\,e_{mr}^2\,C_{lmr}\,a_0\,a_1 \\
+ 8\,\dot{\theta}\,R_{mr}\,e_{mr}\,C_{lmr}\,\dot{a}_0 + 3\,\dot{\phi}\,R_{mr}\,\dot{x}\,A_{1,\mathrm{mr}}\,C_{lmr} - 3\,\dot{\theta}\,R_{mr}\,\dot{x}\,B_{1,\mathrm{mr}}\,C_{lmr} + 15\,\dot{\phi}\,R_{mr}\,\dot{x}\,C_{lmr}\,b_1 \\
+ 21\,\dot{\theta}\,R_{mr}\,\dot{x}\,C_{lmr}\,a_1 - 3\,\dot{\phi}\,R_{mr}\,\dot{y}\,B_{1,\mathrm{mr}}\,C_{lmr} + 9\,\dot{\theta}\,R_{mr}\,\dot{y}\,A_{1,\mathrm{mr}}\,C_{lmr} - 3\,\dot{\phi}\,R_{mr}\,\dot{y}\,C_{lmr}\,a_1 \\
- 3\,\dot{\theta}\,R_{mr}\,\dot{y}\,C_{lmr}\,b_1 - 12\,\Omega\,R_{mr}\,\dot{z}\,A_{1,\mathrm{mr}}\,C_{lmr} - 36\,\Omega\,R_{mr}\,\dot{z}\,C_{lmr}\,b_1 + 12\,\Omega\,R_{mr}\,A_{1,\mathrm{mr}}\,C_{lmr}\,v_i \\
+ 36\,\Omega\,R_{mr}\,C_{lmr}\,b_1\,v_i + 8\,\Omega\,\dot{\theta}\,R_{mr}^2\,\theta_0\,C_{lmr} + 8\,\Omega\,\dot{\phi}\,R_{mr}^2\,C_{lmr}\,a_0 + 3\,\dot{\phi}\,e_{mr}\,\dot{x}\,A_{1,\mathrm{mr}}\,C_{lmr} \\
- 3\,\dot{\theta}\,e_{mr}\,\dot{x}\,B_{1,\mathrm{mr}}\,C_{lmr} + 15\,\dot{\phi}\,e_{mr}\,\dot{x}\,C_{lmr}\,b_1 + 21\,\dot{\theta}\,e_{mr}\,\dot{x}\,C_{lmr}\,a_1 - 3\,\dot{\phi}\,e_{mr}\,\dot{y}\,B_{1,\mathrm{mr}}\,C_{lmr} \\
+ 9\,\dot{\theta}\,e_{mr}\,\dot{y}\,A_{1,\mathrm{mr}}\,C_{lmr} - 3\,\dot{\phi}\,e_{mr}\,\dot{y}\,C_{lmr}\,a_1 - 3\,\dot{\theta}\,e_{mr}\,\dot{y}\,C_{lmr}\,b_1 - 12\,\Omega\,e_{mr}\,\dot{z}\,A_{1,\mathrm{mr}}\,C_{lmr}
\end{gathered}
$$

$$
\begin{aligned}
&+ 12\,\Omega\, e_{mr}\, \dot{z}\, C_{lmr}\, b_1 + 12\,\Omega\, e_{mr}\, A_{1,\mathrm{mr}}\, C_{lmr}\, v_i - 12\,\Omega\, e_{mr}\, C_{lmr}\, b_1\, v_i + 8\,\Omega\, \dot{\theta}\, e_{mr}^2\, \theta_0\, C_{lmr} \\
&+ 8\,\Omega\, \dot{\phi}\, e_{mr}^2\, C_{lmr}\, a_0 + 32\, R_{mr}\, e_{mr}\, C_{lmr}\, \dot{a}_0\, \dot{a}_1 + 3\, R_{mr}\, \dot{x}\, A_{1,\mathrm{mr}}\, C_{lmr}\, \dot{b}_1 - 3\, R_{mr}\, \dot{x}\, B_{1,\mathrm{mr}}\, C_{lmr}\, \dot{a}_1 \\
&+ 36\, R_{mr}\, \dot{x}\, C_{lmr}\, \dot{a}_0\, a_0 + 21\, R_{mr}\, \dot{x}\, C_{lmr}\, \dot{a}_1\, a_1 + 15\, R_{mr}\, \dot{x}\, C_{lmr}\, \dot{b}_1\, b_1 + 12\, R_{mr}\, \dot{y}\, \theta_0\, C_{lmr}\, \dot{a}_0 \\
&+ 9\, R_{mr}\, \dot{y}\, A_{1,\mathrm{mr}}\, C_{lmr}\, \dot{a}_1 - 3\, R_{mr}\, \dot{y}\, B_{1,\mathrm{mr}}\, C_{lmr}\, \dot{b}_1 - 3\, R_{mr}\, \dot{y}\, C_{lmr}\, \dot{a}_1\, b_1 - 3\, R_{mr}\, \dot{y}\, C_{lmr}\, a_1\, \dot{b}_1 \\
&+ 12\,\Omega\, R_{mr}\, \dot{y}\, C_{lmr}\, {a_0}^2 + 12\,\Omega\, R_{mr}\, \dot{y}\, C_{lmr}\, {b_1}^2 + 8\,\Omega\, R_{mr}^2\, \theta_0\, C_{lmr}\, \dot{a}_1 + 8\,\Omega\, R_{mr}^2\, A_{1,\mathrm{mr}}\, C_{lmr}\, \dot{a}_0 \\
&+ 24\,\Omega\, R_{mr}^2\, C_{lmr}\, \dot{a}_0\, b_1 + 8\,\Omega\, R_{mr}^2\, C_{lmr}\, a_0\, \dot{b}_1 - 3\, e_{mr}\, \dot{x}\, A_{1,\mathrm{mr}}\, C_{lmr}\, \dot{b}_1 + 3\, e_{mr}\, \dot{x}\, B_{1,\mathrm{mr}}\, C_{lmr}\, \dot{a}_1 \\
&- 36\, e_{mr}\, \dot{x}\, C_{lmr}\, \dot{a}_0\, a_0 - 21\, e_{mr}\, \dot{x}\, C_{lmr}\, \dot{a}_1\, a_1 - 15\, e_{mr}\, \dot{x}\, C_{lmr}\, \dot{b}_1\, b_1 - 12\, e_{mr}\, \dot{y}\, \theta_0\, C_{lmr}\, \dot{a}_0 \\
&- 9\, e_{mr}\, \dot{y}\, A_{1,\mathrm{mr}}\, C_{lmr}\, \dot{a}_1 + 3\, e_{mr}\, \dot{y}\, B_{1,\mathrm{mr}}\, C_{lmr}\, \dot{b}_1 + 3\, e_{mr}\, \dot{y}\, C_{lmr}\, \dot{a}_1\, b_1 + 3\, e_{mr}\, \dot{y}\, C_{lmr}\, a_1\, \dot{b}_1 \\
&+ 12\,\Omega\, e_{mr}\, \dot{y}\, C_{lmr}\, {a_0}^2 + 6\,\Omega\, e_{mr}\, \dot{y}\, C_{lmr}\, {a_1}^2 + 6\,\Omega\, e_{mr}\, \dot{y}\, C_{lmr}\, {b_1}^2 - 4\,\Omega\, e_{mr}^2\, \theta_0\, C_{lmr}\, \dot{a}_1 \\
&- 4\,\Omega\, e_{mr}^2\, A_{1,\mathrm{mr}}\, C_{lmr}\, \dot{a}_0 + 12\,\Omega\, e_{mr}^2\, C_{lmr}\, \dot{a}_0\, b_1 - 4\,\Omega\, e_{mr}^2\, C_{lmr}\, a_0\, \dot{b}_1 - 24\, \dot{x}\, \dot{y}\, \theta_0\, C_{lmr}\, a_1 \\
&- 24\, \dot{x}\, \dot{y}\, A_{1,\mathrm{mr}}\, C_{lmr}\, a_0 + 48\, \dot{x}\, \dot{y}\, C_{lmr}\, a_0\, b_1 - 4\,\Omega^2\, R_{mr}\, e_{mr}\, \theta_0\, C_{lmr}\, b_1 + 8\,\Omega^2\, R_{mr}\, e_{mr}\, B_{1,\mathrm{mr}}\, C_{lmr}\, a_0 \\
&-4\,\Omega^2\, R_{mr}\, e_{mr}\, C_{lmr}\, a_0\, a_1 + 8\,\Omega\, \dot{\theta}\, R_{mr}\, e_{mr}\, \theta_0\, C_{lmr} + 8\,\Omega\, \dot{\phi}\, R_{mr}\, e_{mr}\, C_{lmr}\, a_0 - 4\,\Omega\, R_{mr}\, e_{mr}\, \theta_0\, C_{lmr}\, \dot{a}_1 \\
&-4\,\Omega\, R_{mr}\, e_{mr}\, A_{1,\mathrm{mr}}\, C_{lmr}\, \dot{a}_0 - 36\,\Omega\, R_{mr}\, e_{mr}\, C_{lmr}\, \dot{a}_0\, b_1 - 4\,\Omega\, R_{mr}\, e_{mr}\, C_{lmr}\, a_0\, \dot{b}_1 - 36\,\Omega\, R_{mr}\, \dot{x}\, \theta_0\, C_{lmr}\, a_0 \\
&-12\,\Omega\, R_{mr}\, \dot{x}\, A_{1,\mathrm{mr}}\, C_{lmr}\, a_1 + 24\,\Omega\, R_{mr}\, \dot{x}\, B_{1,\mathrm{mr}}\, C_{lmr}\, b_1 - 12\,\Omega\, R_{mr}\, \dot{x}\, C_{lmr}\, a_1\, b_1 - 12\,\Omega\, R_{mr}\, \dot{y}\, A_{1,\mathrm{mr}}\, C_{lmr}\, b_1 \\
&-36\,\Omega\, e_{mr}\, \dot{x}\, \theta_0\, C_{lmr}\, a_0 - 18\,\Omega\, e_{mr}\, \dot{x}\, A_{1,\mathrm{mr}}\, C_{lmr}\, a_1 + 18\,\Omega\, e_{mr}\, \dot{x}\, B_{1,\mathrm{mr}}\, C_{lmr}\, b_1 + 6\,\Omega\, e_{mr}\, \dot{y}\, A_{1,\mathrm{mr}}\, C_{lmr}\, b_1 \\
&+ 6\,\Omega\, e_{mr}\, \dot{y}\, B_{1,\mathrm{mr}}\, C_{lmr}\, a_1) \qquad \text{(C.3.2)}
\end{aligned}
$$

$$
\begin{aligned}
F_z = &-\frac{1}{24}\rho\, b\, c_{mr}\, C_{lmr}\, \left(R_{mr} - e_{mr}\right) (6\, \dot{x}^2\, \theta_0 + 6\, \dot{y}^2\, \theta_0 + 4\,\Omega^2\, R_{mr}^2\, \theta_0 + 4\,\Omega^2\, e_{mr}^2\, \theta_0 \\
&- 3\, \dot{\phi}\, R_{mr}\, \dot{x} - 3\, \dot{\theta}\, R_{mr}\, \dot{y} + 6\,\Omega\, R_{mr}\, \dot{z} - 6\,\Omega\, R_{mr}\, v_i - 3\, \dot{\phi}\, e_{mr}\, \dot{x} - 3\, \dot{\theta}\, e_{mr}\, \dot{y} + 6\,\Omega\, e_{mr}\, \dot{z} \\
&- 6\,\Omega\, e_{mr}\, v_i - 3\, R_{mr}\, \dot{x}\, \dot{b}_1 - 3\, R_{mr}\, \dot{y}\, \dot{a}_1 - 4\,\Omega\, R_{mr}^2\, \dot{a}_0 + 3\, e_{mr}\, \dot{x}\, \dot{b}_1 + 3\, e_{mr}\, \dot{y}\, \dot{a}_1 + 2\,\Omega\, e_{mr}^2\, \dot{a}_0 \\
&+ 4\,\Omega^2\, R_{mr}\, e_{mr}\, \theta_0 + 2\,\Omega\, R_{mr}\, e_{mr}\, \dot{a}_0 - 6\,\Omega\, R_{mr}\, \dot{x}\, B_{1,\mathrm{mr}} + 6\,\Omega\, R_{mr}\, \dot{y}\, A_{1,\mathrm{mr}} - 6\,\Omega\, e_{mr}\, \dot{x}\, B_{1,\mathrm{mr}} \\
&+ 6\,\Omega\, e_{mr}\, \dot{x}\, a_1 + 6\,\Omega\, e_{mr}\, \dot{y}\, A_{1,\mathrm{mr}} - 6\,\Omega\, e_{mr}\, \dot{y}\, b_1) \qquad \text{(C.3.3)}
\end{aligned}
$$

C.4 Main Rotor Torques

$$
\begin{aligned}
T_x = &-\frac{1}{48} b\, (12\, \rho\, c_{mr}\, e_{mr}^2\, \dot{x}\, \dot{z}\, C_{lmr} - 24\, K_{smr}\, b_1 + 6\, \rho\, c_{mr}\, e_{mr}^3\, \dot{x}\, C_{lmr}\, \dot{a}_0 - 12\, \rho\, c_{mr}\, e_{mr}^2\, \dot{x}\, C_{lmr}\, v_i \\
&- 4\,\Omega^2\, \rho\, c_{mr}\, e_{mr}^4\, B_{1,\mathrm{mr}}\, C_{lmr} + 2\,\Omega^2\, \rho\, c_{mr}\, e_{mr}^4\, C_{lmr}\, a_1 - 4\,\Omega\, \dot{\phi}\, \rho\, c_{mr}\, e_{mr}^4\, C_{lmr} \\
&- 9\, \rho\, c_{mr}\, e_{mr}^2\, \dot{x}^2\, B_{1,\mathrm{mr}}\, C_{lmr} + 3\, \rho\, c_{mr}\, e_{mr}^2\, \dot{x}^2\, C_{lmr}\, a_1 - 3\, \rho\, c_{mr}\, e_{mr}^2\, \dot{y}^2\, B_{1,\mathrm{mr}}\, C_{lmr} \\
&-3\, \rho\, c_{mr}\, e_{mr}^2\, \dot{y}^2\, C_{lmr}\, a_1 + 2\,\Omega\, \rho\, c_{mr}\, e_{mr}^4\, C_{lmr}\, \dot{b}_1 - 12\, \rho\, R_{mr}\, c_{mr}\, e_{mr}\, \dot{x}\, \dot{z}\, C_{lmr} + 12\, \rho\, R_{mr}\, c_{mr}\, e_{mr}\, \dot{x}\, C_{lmr}\, v_i \\
&+ 4\,\Omega\, \rho\, R_{mr}^3\, c_{mr}\, e_{mr}\, C_{lmr}\, \dot{b}_1 + 12\,\Omega\, \rho\, c_{mr}\, e_{mr}^3\, \dot{x}\, \theta_0\, C_{lmr} - 6\,\Omega\, \rho\, c_{mr}\, e_{mr}^3\, \dot{y}\, C_{lmr}\, a_0 \\
&+ 9\, \rho\, R_{mr}\, c_{mr}\, e_{mr}\, \dot{x}^2\, B_{1,\mathrm{mr}}\, C_{lmr} - 12\, \rho\, R_{mr}\, c_{mr}\, e_{mr}^2\, \dot{x}\, C_{lmr}\, \dot{a}_0 + 6\, \rho\, R_{mr}^2\, c_{mr}\, e_{mr}\, \dot{x}\, C_{lmr}\, \dot{a}_0 \\
&- 3\, \rho\, R_{mr}\, c_{mr}\, e_{mr}\, \dot{x}^2\, C_{lmr}\, a_1 + 3\, \rho\, R_{mr}\, c_{mr}\, e_{mr}\, \dot{y}^2\, B_{1,\mathrm{mr}}\, C_{lmr} + 3\, \rho\, R_{mr}\, c_{mr}\, e_{mr}\, \dot{y}^2\, C_{lmr}\, a_1 \\
&+ 4\,\Omega^2\, \rho\, R_{mr}^3\, c_{mr}\, e_{mr}\, B_{1,\mathrm{mr}}\, C_{lmr} + 4\,\Omega^2\, \rho\, R_{mr}^3\, c_{mr}\, e_{mr}\, C_{lmr}\, a_1 - 6\,\Omega\, \rho\, R_{mr}^2\, c_{mr}\, e_{mr}^2\, C_{lmr}\, \dot{b}_1
\end{aligned}
$$

$$\begin{gathered}
+ 6\,\rho\,c_{mr}\,e_{mr}^2\,\dot{x}\,\dot{y}\,A_{1,\mathrm{mr}}\,C_{lmr} - 6\,\rho\,c_{mr}\,e_{mr}^2\,\dot{x}\,\dot{y}\,C_{lmr}\,b_1 + 4\,\Omega\,\dot{\phi}\,\rho\,R_{mr}^3\,c_{mr}\,e_{mr}\,C_{lmr} \\
- 6\,\Omega^2\,\rho\,R_{mr}^2\,c_{mr}\,e_{mr}^2\,C_{lmr}\,a_1 - 6\,\rho\,R_{mr}\,c_{mr}\,e_{mr}\,\dot{x}\,\dot{y}\,A_{1,\mathrm{mr}}\,C_{lmr} + 6\,\rho\,R_{mr}\,c_{mr}\,e_{mr}\,\dot{x}\,\dot{y}\,C_{lmr}\,b_1 \\
- 12\,\Omega\,\rho\,R_{mr}^2\,c_{mr}\,e_{mr}\,\dot{x}\,\theta_0\,C_{lmr} + 6\,\Omega\,\rho\,R_{mr}^2\,c_{mr}\,e_{mr}\,\dot{y}\,C_{lmr}\,a_0)
\end{gathered} \tag{C.4.1}$$

$$\begin{gathered}
T_y = \frac{1}{48} b\,(24\,K_{smr}\,a_1 - 12\,\rho\,c_{mr}\,e_{mr}^2\,\dot{y}\,\dot{z}\,C_{lmr} - 6\,\rho\,c_{mr}\,e_{mr}^3\,\dot{y}\,C_{lmr}\,\dot{a}_0 + 12\,\rho\,c_{mr}\,e_{mr}^2\,\dot{y}\,C_{lmr}\,v_i \\
-4\,\Omega^2\,\rho\,c_{mr}\,e_{mr}^4\,A_{1,\mathrm{mr}}\,C_{lmr} + 2\,\Omega^2\,\rho\,c_{mr}\,e_{mr}^4\,C_{lmr}\,b_1 + 4\,\Omega\,\rho\,\dot{\theta}\,c_{mr}\,e_{mr}^4\,C_{lmr} - 3\,\rho\,c_{mr}\,e_{mr}^2\,\dot{x}^2\,A_{1,\mathrm{mr}}\,C_{lmr} \\
-3\,\rho\,c_{mr}\,e_{mr}^2\,\dot{x}^2\,C_{lmr}\,b_1 - 9\,\rho\,c_{mr}\,e_{mr}^2\,\dot{y}^2\,A_{1,\mathrm{mr}}\,C_{lmr} + 3\,\rho\,c_{mr}\,e_{mr}^2\,\dot{y}^2\,C_{lmr}\,b_1 - 2\,\Omega\,\rho\,c_{mr}\,e_{mr}^4\,C_{lmr}\,\dot{a}_1 \\
+12\,\rho\,R_{mr}\,c_{mr}\,e_{mr}\,\dot{y}\,\dot{z}\,C_{lmr} - 12\,\rho\,R_{mr}\,c_{mr}\,e_{mr}\,\dot{y}\,C_{lmr}\,v_i - 4\,\Omega\,\rho\,R_{mr}^3\,c_{mr}\,e_{mr}\,C_{lmr}\,\dot{a}_1 - 6\,\Omega\,\rho\,c_{mr}\,e_{mr}^3 \\
\dot{x}\,C_{lmr}\,a_0 - 12\,\Omega\,\rho\,c_{mr}\,e_{mr}^3\,\dot{y}\,\theta_0\,C_{lmr} + 3\,\rho\,R_{mr}\,c_{mr}\,e_{mr}\,\dot{x}^2\,A_{1,\mathrm{mr}}\,C_{lmr} + 3\,\rho\,R_{mr}\,c_{mr}\,e_{mr}\,\dot{x}^2\,C_{lmr}\,b_1 \\
+ 9\,\rho\,R_{mr}\,c_{mr}\,e_{mr}\,\dot{y}^2\,A_{1,\mathrm{mr}}\,C_{lmr} + 12\,\rho\,R_{mr}\,c_{mr}\,e_{mr}^2\,\dot{y}\,C_{lmr}\,\dot{a}_0 - 6\,\rho\,R_{mr}^2\,c_{mr}\,e_{mr}\,\dot{y}\,C_{lmr}\,\dot{a}_0 \\
- 3\,\rho\,R_{mr}\,c_{mr}\,e_{mr}\,\dot{y}^2\,C_{lmr}\,b_1 + 4\,\Omega^2\,\rho\,R_{mr}^3\,c_{mr}\,e_{mr}\,A_{1,\mathrm{mr}}\,C_{lmr} + 6\,\Omega\,\rho\,R_{mr}^2\,c_{mr}\,e_{mr}^2\,C_{lmr}\,\dot{a}_1 \\
+ 4\,\Omega^2\,\rho\,R_{mr}^3\,c_{mr}\,e_{mr}\,C_{lmr}\,b_1 + 6\,\rho\,c_{mr}\,e_{mr}^2\,\dot{x}\,\dot{y}\,B_{1,\mathrm{mr}}\,C_{lmr} - 6\,\rho\,c_{mr}\,e_{mr}^2\,\dot{x}\,\dot{y}\,C_{lmr}\,a_1 \\
- 4\,\Omega\,\rho\,\dot{\theta}\,R_{mr}^3\,c_{mr}\,e_{mr}\,C_{lmr} - 6\,\Omega^2\,\rho\,R_{mr}^2\,c_{mr}\,e_{mr}^2\,C_{lmr}\,b_1 - 6\,\rho\,R_{mr}\,c_{mr}\,e_{mr}\,\dot{x}\,\dot{y}\,B_{1,\mathrm{mr}}\,C_{lmr} \\
+ 6\,\rho\,R_{mr}\,c_{mr}\,e_{mr}\,\dot{x}\,\dot{y}\,C_{lmr}\,a_1 + 6\,\Omega\,\rho\,R_{mr}^2\,c_{mr}\,e_{mr}\,\dot{x}\,C_{lmr}\,a_0 + 12\,\Omega\,\rho\,R_{mr}^2\,c_{mr}\,e_{mr}\,\dot{y}\,\theta_0\,C_{lmr})
\end{gathered} \tag{C.4.2}$$

$$\begin{gathered}
T_z = \frac{1}{96}\rho\,b\,c_{mr}\,\left(R_{mr} - e_{mr}\right)\,(C_{lmr}\,\Omega^2\,R_{mr}^3\,{a_1}^2\,6 + B_{1,\mathrm{mr}}\,C_{lmr}\,\Omega^2\,R_{mr}^3\,a_1\,6 + C_{lmr}\,\Omega^2\,R_{mr}^3\,{b_1}^2\,6 \\
+ A_{1,\mathrm{mr}}\,C_{lmr}\,\Omega^2\,R_{mr}^3\,b_1\,6 - C_d\,\Omega^2\,R_{mr}^3\,12 - C_{lmr}\,\Omega^2\,R_{mr}^2\,e_{mr}\,{a_1}^2\,10 - B_{1,\mathrm{mr}}\,C_{lmr}\,\Omega^2\,R_{mr}^2\,e_{mr}\,a_1\,2 \\
-C_{lmr}\,\Omega^2\,R_{mr}^2\,e_{mr}\,{b_1}^2\,10 - A_{1,\mathrm{mr}}\,C_{lmr}\,\Omega^2\,R_{mr}^2\,e_{mr}\,b_1\,2 - C_d\,\Omega^2\,R_{mr}^2\,e_{mr}\,12 + C_{lmr}\,\Omega^2\,R_{mr}\,e_{mr}^2\,{a_1}^2\,2 \\
-B_{1,\mathrm{mr}}\,C_{lmr}\,\Omega^2\,R_{mr}\,e_{mr}^2\,a_1\,2 + C_{lmr}\,\Omega^2\,R_{mr}\,e_{mr}^2\,{b_1}^2\,2 - A_{1,\mathrm{mr}}\,C_{lmr}\,\Omega^2\,R_{mr}\,e_{mr}^2\,b_1\,2 - C_d\,\Omega^2\,R_{mr}\,e_{mr}^2\,12 \\
+ C_{lmr}\,\Omega^2\,e_{mr}^3\,{a_1}^2\,2 - B_{1,\mathrm{mr}}\,C_{lmr}\,\Omega^2\,e_{mr}^3\,a_1\,2 + C_{lmr}\,\Omega^2\,e_{mr}^3\,{b_1}^2\,2 - A_{1,\mathrm{mr}}\,C_{lmr}\,\Omega^2\,e_{mr}^3\,b_1\,2 \\
- C_d\,\Omega^2\,e_{mr}^3\,12 + C_{lmr}\,\Omega\,\dot{\phi}\,R_{mr}^3\,a_1\,12 + B_{1,\mathrm{mr}}\,C_{lmr}\,\Omega\,\dot{\phi}\,R_{mr}^3\,6 - C_{lmr}\,\Omega\,\dot{\phi}\,R_{mr}^2\,e_{mr}\,a_1\,4 \\
+ B_{1,\mathrm{mr}}\,C_{lmr}\,\Omega\,\dot{\phi}\,R_{mr}^2\,e_{mr}\,6 - C_{lmr}\,\Omega\,\dot{\phi}\,R_{mr}\,e_{mr}^2\,a_1\,4 + B_{1,\mathrm{mr}}\,C_{lmr}\,\Omega\,\dot{\phi}\,R_{mr}\,e_{mr}^2\,6 \\
- C_{lmr}\,\Omega\,\dot{\phi}\,e_{mr}^3\,a_1\,4 + B_{1,\mathrm{mr}}\,C_{lmr}\,\Omega\,\dot{\phi}\,e_{mr}^3\,6 - C_{lmr}\,\Omega\,\dot{\theta}\,R_{mr}^3\,b_1\,12 - A_{1,\mathrm{mr}}\,C_{lmr}\,\Omega\,\dot{\theta}\,R_{mr}^3\,6 \\
+C_{lmr}\,\Omega\,\dot{\theta}\,R_{mr}^2\,e_{mr}\,b_1\,4 - A_{1,\mathrm{mr}}\,C_{lmr}\,\Omega\,\dot{\theta}\,R_{mr}^2\,e_{mr}\,6 + C_{lmr}\,\Omega\,\dot{\theta}\,R_{mr}\,e^2\,b_1\,4 - A_{1,\mathrm{mr}}\,C_{lmr}\,\Omega\,\dot{\theta}\,R_{mr}\,e_{mr}^2\,6 \\
+ C_{lmr}\,\Omega\,\dot{\theta}\,e_{mr}^3\,b_1\,4 - A_{1,\mathrm{mr}}\,C_{lmr}\,\Omega\,\dot{\theta}\,e_{mr}^3\,6 - \theta_0\,C_{lmr}\,\Omega\,R_{mr}^3\,\dot{a}_0\,12 - C_{lmr}\,\Omega\,R_{mr}^3\,\dot{a}_1\,b_1\,12 \\
- A_{1,\mathrm{mr}}\,C_{lmr}\,\Omega\,R_{mr}^3\,\dot{a}_1\,6 + C_{lmr}\,\Omega\,R_{mr}^3\,a_1\,\dot{b}_1\,12 + B_{1,\mathrm{mr}}\,C_{lmr}\,\Omega\,R_{mr}^3\,\dot{b}_1\,6 + \theta_0\,C_{lmr}\,\Omega\,R_{mr}^2\,e_{mr}\,\dot{a}_0\,4 \\
+ C_{lmr}\,\Omega\,R_{mr}^2\,e_{mr}\,\dot{a}_1\,b_1\,20 + A_{1,\mathrm{mr}}\,C_{lmr}\,\Omega\,R_{mr}^2\,e_{mr}\,\dot{a}_1\,2 - C_{lmr}\,\Omega\,R_{mr}^2\,e_{mr}\,a_1\,\dot{b}_1\,20 \\
- B_{1,\mathrm{mr}}\,C_{lmr}\,\Omega\,R_{mr}^2\,e_{mr}\,\dot{b}_1\,2 + C_{lmr}\,\Omega\,R_{mr}^2\,\dot{x}\,a_0\,b_1\,16 + A_{1,\mathrm{mr}}\,C_{lmr}\,\Omega\,R_{mr}^2\,\dot{x}\,a_0\,8 \\
+ C_{lmr}\,\Omega\,R_{mr}^2\,\dot{y}\,a_0\,a_1\,16 + B_{1,\mathrm{mr}}\,C_{lmr}\,\Omega\,R_{mr}^2\,\dot{y}\,a_0\,8 + \theta_0\,C_{lmr}\,\Omega\,R_{mr}^2\,\dot{z}\,16 - \theta_0\,C_{lmr}\,\Omega\,R_{mr}^2\,v_i\,16 \\
+ \theta_0\,C_{lmr}\,\Omega\,R_{mr}\,e_{mr}^2\,\dot{a}_0\,4 - C_{lmr}\,\Omega\,R_{mr}\,e_{mr}^2\,\dot{a}_1\,b_1\,4 + A_{1,\mathrm{mr}}\,C_{lmr}\,\Omega\,R_{mr}\,e_{mr}^2\,\dot{a}_1\,2 \\
+C_{lmr}\,\Omega\,R_{mr}\,e_{mr}^2\,a_1\,\dot{b}_1\,4 - B_{1,\mathrm{mr}}\,C_{lmr}\,\Omega\,R_{mr}\,e_{mr}^2\,\dot{b}_1\,2 - C_{lmr}\,\Omega\,R_{mr}\,e_{mr}\,\dot{x}\,a_0\,b_1\,8 + A_{1,\mathrm{mr}}\,C_{lmr}\,\Omega\,R_{mr} \\
e_{mr}\,\dot{x}\,a_0\,8 + \theta_0\,C_{lmr}\,\Omega\,R_{mr}\,e_{mr}\,\dot{x}\,a_1\,12 - C_{lmr}\,\Omega\,R_{mr}\,e_{mr}\,\dot{y}\,a_0\,a_1\,8 + B_{1,\mathrm{mr}}\,C_{lmr}\,\Omega\,R_{mr}\,e_{mr}\,\dot{y}\,a_0\,8 \\
-\theta_0\,C_{lmr}\,\Omega\,R_{mr}\,e_{mr}\,\dot{y}\,b_1\,12 + \theta_0\,C_{lmr}\,\Omega\,R_{mr}\,e_{mr}\,\dot{z}\,16 - \theta_0\,C_{lmr}\,\Omega\,R_{mr}\,e_{mr}\,v_i\,16 + \theta_0\,C_{lmr}\,\Omega\,e_{mr}^3\,\dot{a}_0\,4
\end{gathered}$$

$$
\begin{gathered}
- C_{lmr}\,\Omega\,e_{mr}^3\,\dot{a}_1\,b_1\,4 + A_{1,\mathrm{mr}}\,C_{lmr}\,\Omega\,e_{mr}^3\,\dot{a}_1\,2 + C_{lmr}\,\Omega\,e_{mr}^3\,a_1\,\dot{b}_1\,4 - B_{1,\mathrm{mr}}\,C_{lmr}\,\Omega\,e_{mr}^3\,\dot{b}_1\,2 \\
- C_{lmr}\,\Omega\,e_{mr}^2\,\dot{x}\,a_0\,b_1\,8 + A_{1,\mathrm{mr}}\,C_{lmr}\,\Omega\,e_{mr}^2\,\dot{x}\,a_0\,8 + \theta_0\,C_{lmr}\,\Omega\,e_{mr}^2\,\dot{x}\,a_1\,12 \\
- C_{lmr}\,\Omega\,e_{mr}^2\,\dot{y}\,a_0\,a_1\,8 + B_{1,\mathrm{mr}}\,C_{lmr}\,\Omega\,e_{mr}^2\,\dot{y}\,a_0\,8 - \theta_0\,C_{lmr}\,\Omega\,e_{mr}^2\,\dot{y}\,b_1\,12 \\
+\theta_0\,C_{lmr}\,\Omega\,e_{mr}^2\,\dot{z}\,16-\theta_0\,C_{lmr}\,\Omega\,e_{mr}^2\,v_i\,16+C_{lmr}\,\dot{\phi}^2\,R_{mr}^3\,6+C_{lmr}\,\dot{\phi}^2\,R_{mr}^2\,e_{mr}\,6+C_{lmr}\,\dot{\phi}^2\,R_{mr}\,e_{mr}^2\,6 \\
+ C_{lmr}\,\dot{\phi}^2\,e_{mr}^3\,6 + C_{lmr}\,\dot{\phi}\,R_{mr}^3\,\dot{b}_1\,12 - C_{lmr}\,\dot{\phi}\,R_{mr}^2\,e_{mr}\,\dot{b}_1\,4 - \theta_0\,C_{lmr}\,\dot{\phi}\,R_{mr}^2\,\dot{x}\,8 \\
+ C_{lmr}\,\dot{\phi}\,R_{mr}^2\,\dot{y}\,a_0\,16 - C_{lmr}\,\dot{\phi}\,R_{mr}\,e^2\,\dot{b}_1\,4 - \theta_0\,C_{lmr}\,\dot{\phi}\,R_{mr}\,e_{mr}\,\dot{x}\,8 + C_{lmr}\,\dot{\phi}\,R_{mr}\,e_{mr}\,\dot{y}\,a_0\,16 \\
- C_{lmr}\,\dot{\phi}\,e_{mr}^3\,\dot{b}_1\,4 - \theta_0\,C_{lmr}\,\dot{\phi}\,e_{mr}^2\,\dot{x}\,8 + C_{lmr}\,\dot{\phi}\,e_{mr}^2\,\dot{y}\,a_0\,16 + C_{lmr}\,\dot{\theta}^2\,R_{mr}^3\,6 + C_{lmr}\,\dot{\theta}^2\,R_{mr}^2\,e_{mr}\,6 \\
+ C_{lmr}\,\dot{\theta}^2\,R_{mr}\,e_{mr}^2\,6 + C_{lmr}\,\dot{\theta}^2\,e_{mr}^3\,6 + C_{lmr}\,\dot{\theta}\,R_{mr}^3\,\dot{a}_1\,12 - C_{lmr}\,\dot{\theta}\,R_{mr}^2\,e_{mr}\,\dot{a}_1\,4 \\
- C_{lmr}\,\dot{\theta}\,R_{mr}^2\,\dot{x}\,a_0\,16 - \theta_0\,C_{lmr}\,\dot{\theta}\,R_{mr}^2\,\dot{y}\,8 - C_{lmr}\,\dot{\theta}\,R_{mr}\,e_{mr}^2\,\dot{a}_1\,4 - C_{lmr}\,\dot{\theta}\,R_{mr}\,e_{mr}\,\dot{x}\,a_0\,16 \\
- \theta_0\,C_{lmr}\,\dot{\theta}\,R_{mr}\,e_{mr}\,\dot{y}\,8 - C_{lmr}\,\dot{\theta}\,e_{mr}^3\,\dot{a}_1\,4 - C_{lmr}\,\dot{\theta}\,e_{mr}^2\,\dot{x}\,a_0\,16 - \theta_0\,C_{lmr}\,\dot{\theta}\,e_{mr}^2\,\dot{y}\,8 \\
+ C_{lmr}\,R_{mr}^3\,\dot{a}_0^2\,12 + C_{lmr}\,R_{mr}^3\,\dot{a}_1^2\,6 + C_{lmr}\,R_{mr}^3\,\dot{b}_1^2\,6 - C_{lmr}\,R_{mr}^2\,e_{mr}\,\dot{a}_0^2\,20 - C_{lmr}\,R_{mr}^2\,e_{mr}\,\dot{a}_1^2\,10 \\
- C_{lmr}\,R_{mr}^2\,e_{mr}\,\dot{b}_1^2\,10 - C_{lmr}\,R_{mr}^2\,\dot{x}\,\dot{a}_0\,a_1\,16 + B_{1,\mathrm{mr}}\,C_{lmr}\,R_{mr}^2\,\dot{x}\,\dot{a}_0\,8 - C_{lmr}\,R_{mr}^2\,\dot{x}\,\dot{a}_1\,a_0\,16 \\
- \theta_0\,C_{lmr}\,R_{mr}^2\,\dot{x}\,\dot{b}_1\,8 + C_{lmr}\,R_{mr}^2\,\dot{y}\,\dot{a}_0\,b_1\,16 - A_{1,\mathrm{mr}}\,C_{lmr}\,R_{mr}^2\,\dot{y}\,\dot{a}_0\,8 - \theta_0\,C_{lmr}\,R_{mr}^2\,\dot{y}\,\dot{a}_1\,8 \\
+C_{lmr}\,R_{mr}^2\,\dot{y}\,a_0\,\dot{b}_1\,16-C_{lmr}\,R_{mr}^2\,\dot{z}\,\dot{a}_0\,32+C_{lmr}\,R_{mr}^2\,\dot{a}_0\,v_i\,32+C_{lmr}\,R_{mr}\,e_{mr}^2\,\dot{a}_0^2\,4+C_{lmr}\,R_{mr}\,e_{mr}^2\,\dot{a}_1^2\,2 \\
+C_{lmr}\,R_{mr}\,e_{mr}^2\,\dot{b}_1^2\,2+C_{lmr}\,R_{mr}\,e_{mr}\,\dot{x}\,\dot{a}_0\,a_1\,8-B_{1,\mathrm{mr}}\,C_{lmr}\,R_{mr}\,e_{mr}\,\dot{x}\,\dot{a}_0\,4+C_{lmr}\,R_{mr}\,e_{mr}\,\dot{x}\,\dot{a}_1\,a_0\,8 \\
+\theta_0\,C_{lmr}\,R_{mr}\,e_{mr}\,\dot{x}\,\dot{b}_1\,4-C_{lmr}\,R_{mr}\,e_{mr}\,\dot{y}\,\dot{a}_0\,b_1\,8+A_{1,\mathrm{mr}}\,C_{lmr}\,R_{mr}\,e_{mr}\,\dot{y}\,\dot{a}_0\,4+\theta_0\,C_{lmr}\,R_{mr}\,e_{mr}\,\dot{y}\,\dot{a}_1\,4 \\
-C_{lmr}\,R_{mr}\,e_{mr}\,\dot{y}\,a_0\,\dot{b}_1\,8+C_{lmr}\,R_{mr}\,e_{mr}\,\dot{z}\,\dot{a}_0\,16-C_{lmr}\,R_{mr}\,e_{mr}\,\dot{a}_0\,v_i\,16+C_{lmr}\,R_{mr}\,\dot{x}^2\,{a_0}^2\,12+C_{lmr}\,R_{mr} \\
\dot{x}^2\,{a_1}^2\,9-B_{1,\mathrm{mr}}\,C_{lmr}\,R_{mr}\,\dot{x}^2\,a_1\,3+C_{lmr}\,R_{mr}\,\dot{x}^2\,{b_1}^2\,3+A_{1,\mathrm{mr}}\,C_{lmr}\,R_{mr}\,\dot{x}^2\,b_1\,3-C_d\,R_{mr}\,\dot{x}^2\,12-C_{lmr}\,R_{mr}\,\dot{x} \\
\dot{y}\,a_1\,b_1\,12+A_{1,\mathrm{mr}}\,C_{lmr}\,R_{mr}\,\dot{x}\,\dot{y}\,a_1\,6+B_{1,\mathrm{mr}}\,C_{lmr}\,R_{mr}\,\dot{x}\,\dot{y}\,b_1\,6+C_{lmr}\,R_{mr}\,\dot{x}\,\dot{z}\,a_1\,24-B_{1,\mathrm{mr}}\,C_{lmr}\,R_{mr}\,\dot{x}\,\dot{z}\,12 \\
-C_{lmr}\,R_{mr}\,\dot{x}\,a_1\,v_i\,24+B_{1,\mathrm{mr}}\,C_{lmr}\,R_{mr}\,\dot{x}\,v_i\,12+C_{lmr}\,R_{mr}\,\dot{y}^2\,{a_0}^2\,12+C_{lmr}\,R_{mr}\,\dot{y}^2\,{a_1}^2\,3+B_{1,\mathrm{mr}}\,C_{lmr} \\
R_{mr}\,\dot{y}^2\,a_1\,3+C_{lmr}\,R_{mr}\,\dot{y}^2\,{b_1}^2\,9-A_{1,\mathrm{mr}}\,C_{lmr}\,R_{mr}\,\dot{y}^2\,b_1\,3-C_d\,R_{mr}\,\dot{y}^2\,12-C_{lmr}\,R_{mr}\,\dot{y}\,\dot{z}\,b_1\,24+A_{1,\mathrm{mr}}\,C_{lmr} \\
R_{mr}\,\dot{y}\,\dot{z}\,12+C_{lmr}\,R_{mr}\,\dot{y}\,b_1\,v_i\,24-A_{1,\mathrm{mr}}\,C_{lmr}\,R_{mr}\,\dot{y}\,v_i\,12+C_{lmr}\,R_{mr}\,\dot{z}^2\,24-C_{lmr}\,R_{mr}\,\dot{z}\,v_i\,48+C_{lmr}\,R_{mr} \\
{v_i}^2\,24+C_{lmr}\,e_{mr}^3\,\dot{a}_0^2\,4+C_{lmr}\,e_{mr}^3\,\dot{a}_1^2\,2+C_{lmr}\,e_{mr}^3\,\dot{b}_1^2\,2+C_{lmr}\,e_{mr}^2\,\dot{x}\,\dot{a}_0\,a_1\,8-B_{1,\mathrm{mr}}\,C_{lmr}\,e_{mr}^2\,\dot{x}\,\dot{a}_0\,4 \\
+ C_{lmr}\,e_{mr}^2\,\dot{x}\,\dot{a}_1\,a_0\,8 + \theta_0\,C_{lmr}\,e_{mr}^2\,\dot{x}\,\dot{b}_1\,4 - C_{lmr}\,e_{mr}^2\,\dot{y}\,\dot{a}_0\,b_1\,8 + A_{1,\mathrm{mr}}\,C_{lmr}\,e_{mr}^2\,\dot{y}\,\dot{a}_0\,4 \\
+\theta_0\,C_{lmr}\,e_{mr}^2\,\dot{y}\,\dot{a}_1\,4-C_{lmr}\,e_{mr}^2\,\dot{y}\,a_0\,\dot{b}_1\,8+C_{lmr}\,e_{mr}^2\,\dot{z}\,\dot{a}_0\,16-C_{lmr}\,e_{mr}^2\,\dot{a}_0\,v_i\,16+C_{lmr}\,e_{mr}\,\dot{x}^2\,{a_0}^2\,12 \\
+C_{lmr}\,e_{mr}\,\dot{x}^2\,{a_1}^2\,9-B_{1,\mathrm{mr}}\,C_{lmr}\,e_{mr}\,\dot{x}^2\,a_1\,3+C_{lmr}\,e_{mr}\,\dot{x}^2\,{b_1}^2\,3+A_{1,\mathrm{mr}}\,C_{lmr}\,e_{mr}\,\dot{x}^2\,b_1\,3-C_d\,e_{mr}\,\dot{x}^2\,12 \\
- C_{lmr}\,e_{mr}\,\dot{x}\,\dot{y}\,a_1\,b_1\,12 + A_{1,\mathrm{mr}}\,C_{lmr}\,e_{mr}\,\dot{x}\,\dot{y}\,a_1\,6 + B_{1,\mathrm{mr}}\,C_{lmr}\,e_{mr}\,\dot{x}\,\dot{y}\,b_1\,6 + C_{lmr}\,e_{mr}\,\dot{x}\,\dot{z}\,a_1\,24 \\
- B_{1,\mathrm{mr}}\,C_{lmr}\,e_{mr}\,\dot{x}\,\dot{z}\,12 - C_{lmr}\,e_{mr}\,\dot{x}\,a_1\,v_i\,24 + B_{1,\mathrm{mr}}\,C_{lmr}\,e_{mr}\,\dot{x}\,v_i\,12 + C_{lmr}\,e_{mr}\,\dot{y}^2\,{a_0}^2\,12 \\
+C_{lmr}\,e_{mr}\,\dot{y}^2\,{a_1}^2\,3+B_{1,\mathrm{mr}}\,C_{lmr}\,e_{mr}\,\dot{y}^2\,a_1\,3+C_{lmr}\,e_{mr}\,\dot{y}^2\,{b_1}^2\,9-A_{1,\mathrm{mr}}\,C_{lmr}\,e_{mr}\,\dot{y}^2\,b_1\,3-C_d\,e_{mr}\,\dot{y}^2\,12 \\
-C_{lmr}\,e_{mr}\,\dot{y}\,\dot{z}\,b_1\,24+A_{1,\mathrm{mr}}\,C_{lmr}\,e_{mr}\,\dot{y}\,\dot{z}\,12+C_{lmr}\,e_{mr}\,\dot{y}\,b_1\,v_i\,24-A_{1,\mathrm{mr}}\,C_{lmr}\,e_{mr}\,\dot{y}\,v_i\,12+C_{lmr}\,e_{mr}\,\dot{z}^2\,24 \\
- C_{lmr}\,e_{mr}\,\dot{z}\,v_i\,48 + C_{lmr}\,e_{mr}\,{v_i}^2\,24)
\end{gathered}
\tag{C.4.3}
$$

Appendix D

Pose Estimation

D.1 State-error covariance propagation

In order to propagate the state-error covariance, the partial derivative of the state-difference equation with respect to the state variables and noise terms are given below,

$$\mathbf{A}_k = \left[\frac{\partial \vec{\mathbf{p}}_{k+1}}{\partial \vec{\mathbf{x}}_k}, \frac{\partial \vec{\mathbf{v}}_{k+1}}{\partial \vec{\mathbf{x}}_k}, \frac{\partial \vec{\mathbf{q}}_{k+1}}{\partial \vec{\mathbf{x}}_k}, \frac{\partial \vec{\boldsymbol{\omega}}_{b,k+1}}{\partial \vec{\mathbf{x}}_k}, \frac{\partial \vec{\mathbf{a}}_{b,k+1}}{\partial \vec{\mathbf{x}}_k}\right]^T \tag{D.1.1}$$

$$\frac{\partial \vec{\mathbf{p}}_{k+1}}{\partial \vec{\mathbf{x}}_k} = \left[\mathbf{I}^{3\times3}, \Delta t \cdot \mathbf{I}^{3\times3}, \mathbf{0}^{3\times4}, \mathbf{0}^{3\times3}, \mathbf{0}^{3\times3}\right] \tag{D.1.2}$$

$$\frac{\partial \vec{\mathbf{v}}_{k+1}}{\partial \vec{\mathbf{x}}_k} = \left[\mathbf{0}^{3\times3}, \mathbf{I}^{3\times3}, \Delta t \frac{\partial \vec{\mathbf{a}}_k}{\partial \vec{\mathbf{q}}_k}, \mathbf{0}^{3\times3}, \Delta t \frac{\partial \vec{\mathbf{a}}_k}{\partial \vec{\mathbf{a}}_{b,k}}\right] \tag{D.1.3}$$

$$\frac{\partial \vec{\mathbf{a}}_k}{\partial \vec{\mathbf{q}}_k} = \left[\begin{array}{cccc} \frac{\partial R_{eb}(\vec{\mathbf{q}}_k)}{\partial q_1}\tilde{\mathbf{a}}_k & \frac{\partial R_{eb}(\vec{\mathbf{q}}_k)}{\partial q_2}\tilde{\mathbf{a}}_k & \frac{\partial R_{eb}(\vec{\mathbf{q}}_k)}{\partial q_3}\tilde{\mathbf{a}}_k & \frac{\partial R_{eb}(\vec{\mathbf{q}}_k)}{\partial q_4}\tilde{\mathbf{a}}_k \end{array}\right]$$

$$\frac{\partial R_{eb}(\vec{\mathbf{q}}_k)}{\partial q_1} = 2\begin{bmatrix} q_{1,k} & -q_{4,k} & q_{3,k} \\ q_{4,k} & q_{1,k} & -q_{2,k} \\ -q_{3,k} & q_{2,k} & q_{1,k} \end{bmatrix}$$

$$\frac{\partial R_{eb}(\vec{\mathbf{q}}_k)}{\partial q_2} = 2\begin{bmatrix} q_{2,k} & q_{3,k} & q_{4,k} \\ q_{3,k} & -q_{2,k} & -q_{1,k} \\ q_{4,k} & q_{1,k} & -q_{2,k} \end{bmatrix}$$

$$\frac{\partial R_{eb}(\vec{\mathbf{q}}_k)}{\partial q_3} = 2\begin{bmatrix} -q_{3,k} & q_{2,k} & q_{1,k} \\ q_{2,k} & q_{3,k} & q_{4,k} \\ -q_{1,k} & q_{4,k} & -q_{3,k} \end{bmatrix}$$

$$\frac{\partial R_{eb}(\vec{\mathbf{q}}_k)}{\partial q_4} = 2\begin{bmatrix} -q_{4,k} & -q_{1,k} & q_{2,k} \\ q_{1,k} & -q_{4,k} & q_{3,k} \\ q_{2,k} & q_{3,k} & q_{4,k} \end{bmatrix}$$

$$\frac{\partial \vec{\mathbf{a}}_k}{\partial \vec{\mathbf{a}}_{b,k}} = -R_{eb}(\vec{\mathbf{q}}_k)$$

$$\frac{\partial \vec{\mathbf{q}}_{k+1}}{\partial \vec{\mathbf{x}}_k} = \left[\mathbf{0}^{4\times 3}, \mathbf{0}^{4\times 3}, \frac{\partial \vec{\mathbf{q}}_{k+1}}{\partial \vec{\mathbf{q}}_k}, \frac{\partial \vec{\mathbf{q}}_{k+1}}{\partial \vec{\boldsymbol{\omega}}_{b,k}}, \mathbf{0}^{4\times 3}\right] \tag{D.1.4}$$

$$\frac{\partial \vec{\mathbf{q}}_{k+1}}{\partial \vec{\mathbf{q}}_k} = \frac{\Delta t}{2}\begin{bmatrix} \frac{2}{\Delta t} & -\tilde{\omega}_x & -\tilde{\omega}_y & -\tilde{\omega}_z \\ \tilde{\omega}_x & \frac{2}{\Delta t} & \tilde{\omega}_z & -\tilde{\omega}_y \\ \tilde{\omega}_y & -\tilde{\omega}_z & \frac{2}{\Delta t} & \tilde{\omega}_x \\ \tilde{\omega}_z & \tilde{\omega}_y & -\tilde{\omega}_x & \frac{2}{\Delta t} \end{bmatrix}$$

$$\frac{\partial \vec{\mathbf{q}}_{k+1}}{\partial \vec{\boldsymbol{\omega}}_{b,k}} = -\frac{\Delta t}{2}\begin{bmatrix} -q_{2,k} & -q_{3,k} & -q_{4,k} \\ q_{1,k} & -q_{4,k} & q_{3,k} \\ q_{4,k} & q_{1,k} & -q_{2,k} \\ -q_{3,k} & q_{2,k} & q_{1,k} \end{bmatrix}$$

$$\frac{\partial \vec{\boldsymbol{\omega}}_{b,k+1}}{\partial \vec{\mathbf{x}}_k} = \left[\mathbf{0}^{3\times 3}, \mathbf{0}^{3\times 3}, \mathbf{0}^{3\times 4}, \mathbf{I}^{3\times 3}, \mathbf{0}^{3\times 3}\right] \tag{D.1.5}$$

$$\frac{\partial \vec{\mathbf{a}}_{b,k+1}}{\partial \vec{\mathbf{x}}_k} = \left[\mathbf{0}^{3\times 3}, \mathbf{0}^{3\times 3}, \mathbf{0}^{3\times 4}, \mathbf{0}^{3\times 3}, \mathbf{I}^{3\times 3}\right] \tag{D.1.6}$$

To propagate the nonadditive process noise:

$$\mathbf{W}_k = \left[\frac{\partial \vec{\mathbf{p}}_{k+1}}{\partial \vec{\boldsymbol{\eta}}_k}; \frac{\partial \vec{\mathbf{v}}_{k+1}}{\partial \vec{\boldsymbol{\eta}}_k}; \frac{\partial \vec{\mathbf{q}}_{k+1}}{\partial \vec{\boldsymbol{\eta}}_k}; \frac{\partial \vec{\boldsymbol{\omega}}_{b,k+1}}{\partial \vec{\boldsymbol{\eta}}_k}; \frac{\partial \vec{\mathbf{a}}_{b,k+1}}{\partial \vec{\boldsymbol{\eta}}_k}\right] \tag{D.1.7}$$

$$\frac{\partial \vec{\mathbf{p}}_{k+1}}{\partial \vec{\boldsymbol{\eta}}_k} = \left[\Delta t \cdot \mathbf{I}^{3\times 3}, \mathbf{0}^{3\times 3}, \mathbf{0}^{3\times 3}, \mathbf{0}^{3\times 3}, \mathbf{0}^{3\times 3}, \mathbf{0}^{3\times 3}\right] \tag{D.1.8}$$

$$\frac{\partial \vec{\mathbf{v}}_{k+1}}{\partial \vec{\boldsymbol{\eta}}_k} = \left[\mathbf{0}^{3\times 3}, \Delta t \cdot \mathbf{I}^{3\times 3}, \Delta t \cdot R_{eb}(\vec{\mathbf{q}}_k), \mathbf{0}^{3\times 3}, \mathbf{0}^{3\times 3}, -\Delta t \cdot R_{eb}(\vec{\mathbf{q}}_k)\right] \tag{D.1.9}$$

$$\frac{\partial \vec{\mathbf{q}}_{k+1}}{\partial \vec{\boldsymbol{\eta}}_k} = \left[\mathbf{0}^{3\times 3}, \mathbf{0}^{3\times 3}, \mathbf{0}^{3\times 3}, \frac{\partial \vec{\mathbf{q}}_{k+1}}{\partial \vec{\boldsymbol{\eta}}_{\omega_k}}, \frac{\partial \vec{\mathbf{q}}_{k+1}}{\partial \vec{\boldsymbol{\eta}}_{\omega_{b,k}}}, \mathbf{0}^{3\times 3}\right] \tag{D.1.10}$$

$$\frac{\partial \vec{\mathbf{q}}_{k+1}}{\partial \vec{\boldsymbol{\eta}}_{\omega_k}} = \frac{\Delta t}{2}\begin{bmatrix} -q_{2,k} & -q_{3,k} & -q_{4,k} \\ q_{1,k} & -q_{4,k} & q_{3,k} \\ q_{4,k} & q_{1,k} & -q_{2,k} \\ -q_{3,k} & q_{2,k} & q_{1,k} \end{bmatrix}$$

$$\frac{\partial \vec{\mathbf{q}}_{k+1}}{\partial \vec{\boldsymbol{\eta}}_{\omega_{b,k}}} = -\frac{\Delta t}{2}\begin{bmatrix} -q_{2,k} & -q_{3,k} & -q_{4,k} \\ q_{1,k} & -q_{4,k} & q_{3,k} \\ q_{4,k} & q_{1,k} & -q_{2,k} \\ -q_{3,k} & q_{2,k} & q_{1,k} \end{bmatrix}$$

$$\frac{\partial \vec{\boldsymbol{\omega}}_{k+1}}{\partial \vec{\boldsymbol{\eta}}_k} = \left[\mathbf{0}^{3\times 3}, \mathbf{0}^{3\times 3}, \mathbf{0}^{3\times 3}, \mathbf{0}^{3\times 3}, \Delta t \cdot \mathbf{I}^{3\times 3}, \mathbf{0}^{3\times 3}\right] \tag{D.1.11}$$

$$\frac{\partial \vec{\mathbf{a}}_{k+1}}{\partial \vec{\boldsymbol{\eta}}_k} = \left[\mathbf{0}^{3\times 3}, \mathbf{0}^{3\times 3}, \mathbf{0}^{3\times 3}, \mathbf{0}^{3\times 3}, \mathbf{0}^{3\times 3}, \Delta t \cdot \mathbf{I}^{3\times 3}\right] \tag{D.1.12}$$

D.2 Error-covariance Correction

The derivative of the measurement vector with respect to the state is given by,

$$\mathbf{C}_{k,i} = \frac{\partial \vec{\mathbf{h}}_i}{\partial \vec{\mathbf{x}}} = \begin{bmatrix} \frac{\partial u_i(\vec{\mathbf{x}})}{\partial \vec{\mathbf{x}}} \\ \frac{\partial v_i(\vec{\mathbf{x}})}{\partial \vec{\mathbf{x}}} \end{bmatrix} \tag{D.2.1}$$

Recall,

$$\frac{\partial}{\partial x}\left[\frac{f(x)}{g(x)}\right] = \frac{\partial}{\partial x}\left[f(x)g^{-1}(x)\right] \tag{D.2.2}$$

$$= f'(x)g^{-1}(x) + f(x)(-1)g^{-2}(x)g'(x) \tag{D.2.3}$$

$$= \frac{f'(x)g(x) - f(x)g'(x)}{g^2(x)} \tag{D.2.4}$$

With the elements of $\vec{\mathbf{B}}_i$ defined in Eq. 4.4.6 - 4.4.8, define 4.4.3 and 4.4.4 as follows, for simplicity,

$$u_i(\vec{\mathbf{x}}) = \frac{au_i(\vec{\mathbf{x}})}{bu_i(\vec{\mathbf{x}})} \tag{D.2.5}$$

$$v_i(\vec{\mathbf{x}}) = \frac{av_i(\vec{\mathbf{x}})}{bv_i(\vec{\mathbf{x}})} \tag{D.2.6}$$

$$au_i'(x) = K_{11,i}\frac{\partial B_{1,i}}{\partial \vec{\mathbf{x}}} + K_{12,i}\frac{\partial B_{2,i}}{\partial \vec{\mathbf{x}}} + K_{13,i}\frac{\partial B_{3,i}}{\partial \vec{\mathbf{x}}} \tag{D.2.7}$$

$$av_i'(x) = K_{21,i}\frac{\partial B_{1,i}}{\partial \vec{\mathbf{x}}} + K_{22,i}\frac{\partial B_{2,i}}{\partial \vec{\mathbf{x}}} + K_{23,i}\frac{\partial B_{3,i}}{\partial \vec{\mathbf{x}}} \tag{D.2.8}$$

$$bu_i'(x) = bv_i'(x) = K_{31,i}\frac{\partial B_{1,i}}{\partial \vec{\mathbf{x}}} + K_{32,i}\frac{\partial B_{2,i}}{\partial \vec{\mathbf{x}}} + K_{33,i}\frac{\partial B_{3,i}}{\partial \vec{\mathbf{x}}} \tag{D.2.9}$$

$$\frac{\partial B_{1,i}}{\partial \vec{\mathbf{x}}} = \left[1\ 0\ 0 \vdots 0\ 0\ 0 \vdots \frac{\partial B_{1,i}}{\partial \vec{\mathbf{q}}_k} \vdots 0\ 0\ 0 \vdots 0\ 0\ 0\right] \tag{D.2.10}$$

$$\frac{\partial B_{2,i}}{\partial \vec{\mathbf{x}}} = \left[0\ 1\ 0 \vdots 0\ 0\ 0 \vdots \frac{\partial B_{2,i}}{\partial \vec{\mathbf{q}}_k} \vdots 0\ 0\ 0 \vdots 0\ 0\ 0\right] \tag{D.2.11}$$

$$\frac{\partial B_{3,i}}{\partial \vec{\mathbf{x}}} = \left[0\ 0\ 1 \vdots 0\ 0\ 0 \vdots \frac{\partial B_{3,i}}{\partial \vec{\mathbf{q}}_k} \vdots 0\ 0\ 0 \vdots 0\ 0\ 0\right] \tag{D.2.12}$$

$$\frac{\partial B_{1,i}}{\partial \vec{\mathbf{q}}_k} = 2\begin{bmatrix} q_1X - q_4Y + q_3Z \\ q_2X + q_3Y + q_4Z \\ -q_3X + q_2Y + q_1Z \\ -q_4X - q_1Y + q_2Z \end{bmatrix}^T \tag{D.2.13}$$

$$\frac{\partial B_{2,i}}{\partial \vec{\mathbf{q}}_k} = 2 \begin{bmatrix} q_4X + q_1Y - q_2Z \\ q_3X - q_2Y - q_1Z \\ q_2X + q_3Y + q_4Z \\ q_1X - q_4Y + q_3Z \end{bmatrix}^T \tag{D.2.14}$$

$$\frac{\partial B_{3,i}}{\partial \vec{\mathbf{q}}_k} = 2 \begin{bmatrix} -q_3X + q_2Y + q_1Z \\ q_4X + q_1Y - q_2Z \\ -q_1X + q_4Y - q_3Z \\ q_2X + q_3Y + q_4Z \end{bmatrix}^T \tag{D.2.15}$$

Appendix E

Control Design

E.1 Rotor Drive Control

A robust PI controller was design to control the speed of the rotor. The controller that gives the nominal plant a peak sensitivity of 3 dB is,

$$G_m(w) = \frac{w/2.5 + 1}{w} \tag{E.1.1}$$

The rotor speed during an active flight test with collective excitation is shown in Fig. E.1.

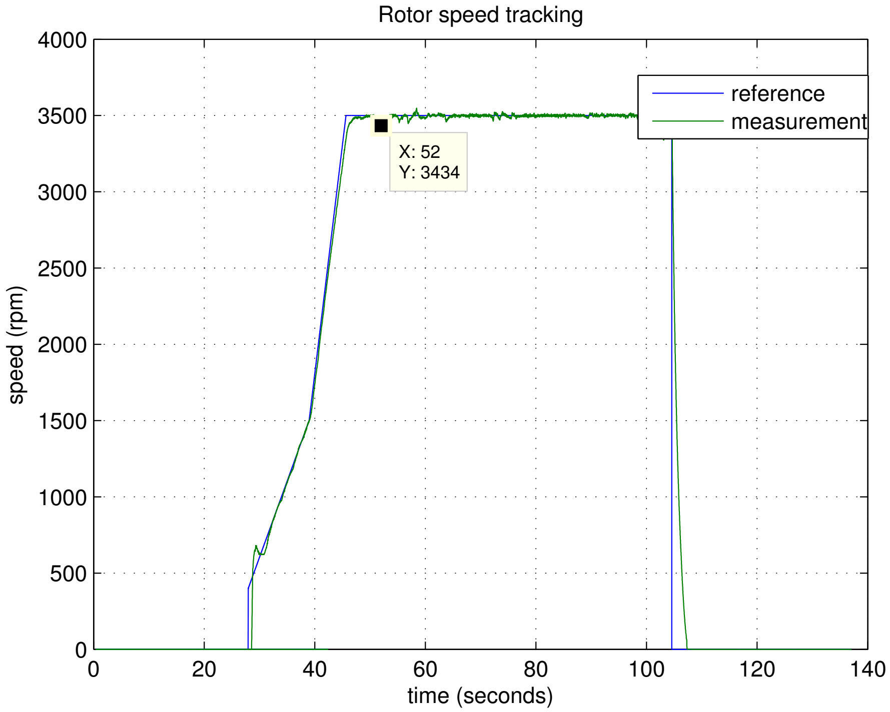

Figure E.1.1: Tracking response of rotor drive system

E.2 Independent Helicopter Control

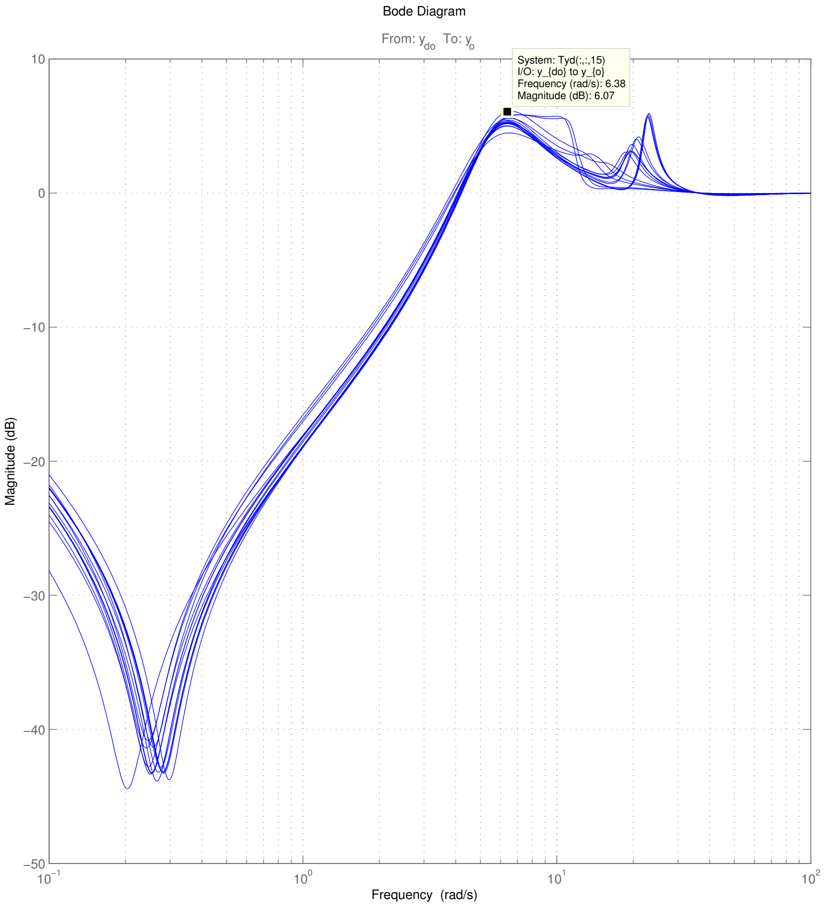

Figure E.2.1: Sensitivity magnitude plot for the roll loop

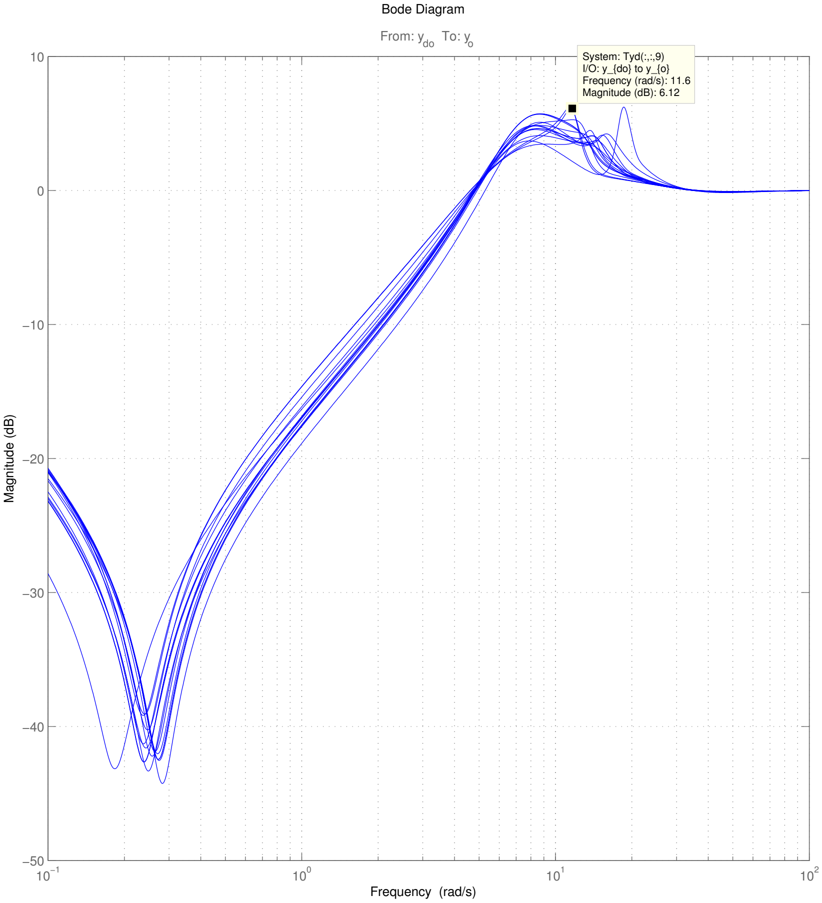

Figure E.2.2: Sensitivity magnitude plot for the pitch loop

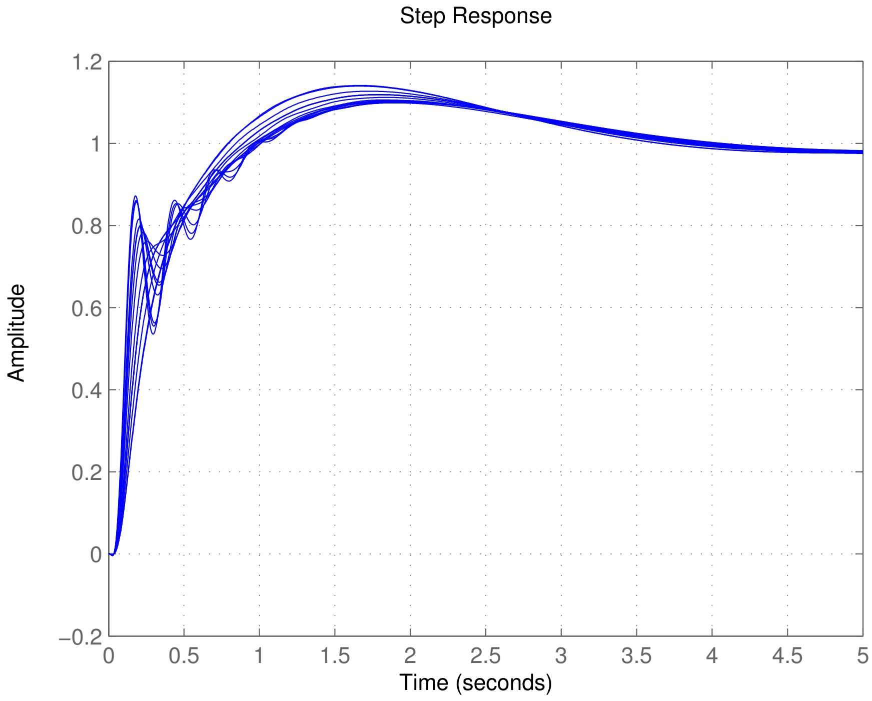

Figure E.2.3: Step response of yaw loop from reference to output

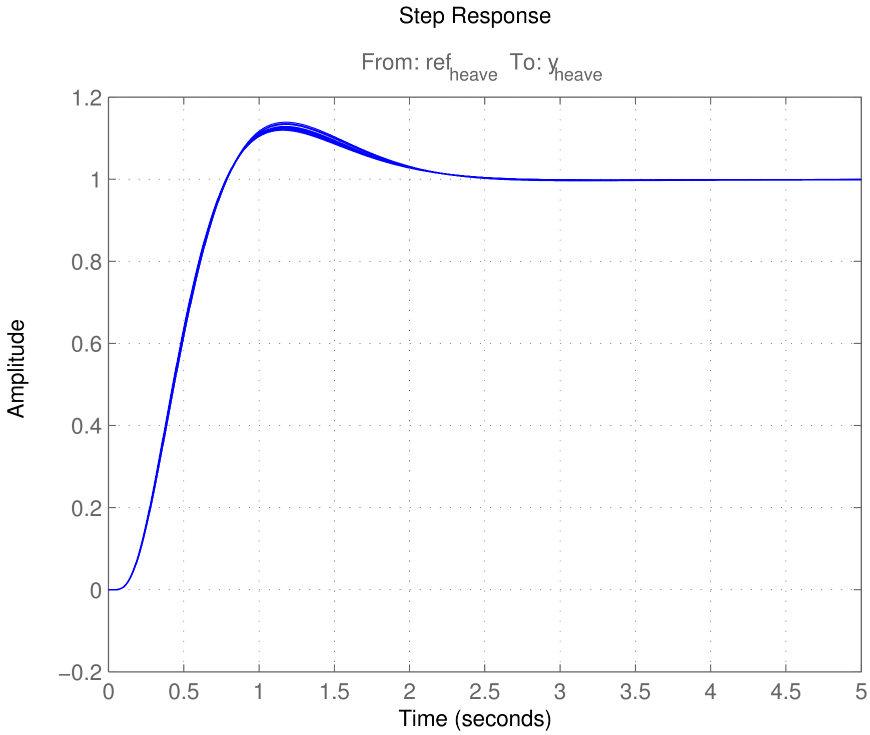

Figure E.2.4: Step response of heave loop from reference to output

E.3 Coordinated Helicopter Control

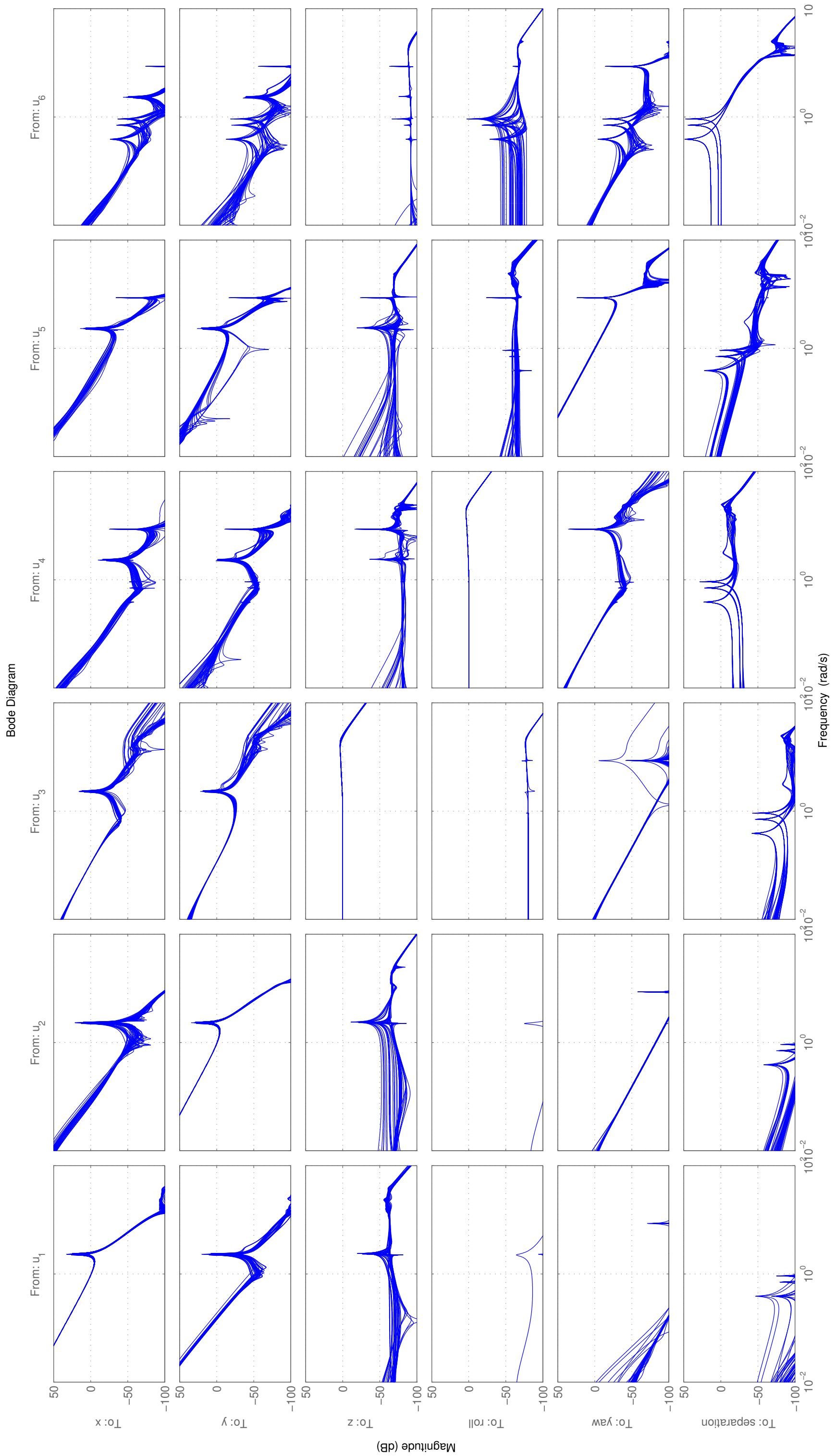

Figure E.3.1: Magnitude plot of the twin-helicopter system plant set

Output Disturbance Rejection Specifications

Column 1:

$$|a_{11}(j\omega)| = \left| \frac{41(j\omega)^2}{\left(\frac{j\omega}{0.22}\right)^2 + 2 \cdot 0.6 \left(\frac{j\omega}{0.22}\right) + 1} \right| \tag{E.3.1}$$

$$|a_{21}(j\omega)| = \left| \frac{8.3(j\omega)^2}{\left(\left(\frac{j\omega}{0.11}\right)^2 + 2 \cdot 0.707 \left(\frac{j\omega}{0.11}\right) + 1\right) \cdot \left(\left(\frac{j\omega}{3}\right)^2 + 2 \cdot 0.707 \left(\frac{j\omega}{3}\right) + 1\right)} \right| \tag{E.3.2}$$

$$|a_{31}(j\omega)| = \left| \frac{0.003(j\omega)^2}{\left(\left(\frac{j\omega}{1}\right)^2 + 2 \cdot 0.707 \left(\frac{j\omega}{1}\right) + 1\right) \cdot \left(\left(\frac{j\omega}{2}\right)^2 + 2 \cdot 0.707 \left(\frac{j\omega}{2}\right) + 1\right)} \right| \tag{E.3.3}$$

$$|a_{41}(j\omega)| = \left| \frac{0.000165(j\omega)^2}{\left(\left(\frac{j\omega}{1}\right)^2 + 2 \cdot 0.707 \left(\frac{j\omega}{1}\right) + 1\right) \cdot \left(\left(\frac{j\omega}{2}\right)^2 + 2 \cdot 0.707 \left(\frac{j\omega}{2}\right) + 1\right)} \right| \tag{E.3.4}$$

$$|a_{51}(j\omega)| = \left| \frac{0.0003(j\omega)^2}{\left(\left(\frac{j\omega}{1}\right)^2 + 2 \cdot 0.707 \left(\frac{j\omega}{1}\right) + 1\right) \cdot \left(\left(\frac{j\omega}{2}\right)^2 + 2 \cdot 0.707 \left(\frac{j\omega}{2}\right) + 1\right)} \right| \tag{E.3.5}$$

$$|a_{61}(j\omega)| = \left| \frac{0.0003(j\omega)^2}{\left(\left(\frac{j\omega}{1}\right)^2 + 2 \cdot 0.707 \left(\frac{j\omega}{1}\right) + 1\right) \cdot \left(\left(\frac{j\omega}{2}\right)^2 + 2 \cdot 0.707 \left(\frac{j\omega}{2}\right) + 1\right)} \right| \tag{E.3.6}$$

Column 2:

$$|a_{12}(j\omega)| = \left| \frac{8.3(j\omega)^2}{\left(\left(\frac{j\omega}{0.11}\right)^2 + 2 \cdot 0.707 \left(\frac{j\omega}{0.11}\right) + 1\right) \cdot \left(\left(\frac{j\omega}{3}\right)^2 + 2 \cdot 0.707 \left(\frac{j\omega}{3}\right) + 1\right)} \right| \tag{E.3.7}$$

$$|a_{22}(j\omega)| = \left| \frac{41(j\omega)^2}{\left(\frac{j\omega}{0.22}\right)^2 + 2 \cdot 0.6 \left(\frac{j\omega}{0.22}\right) + 1} \right| \tag{E.3.8}$$

$$|a_{32}(j\omega)| = \left| \frac{0.006(j\omega)^2}{\left(\left(\frac{j\omega}{1}\right)^2 + 2 \cdot 0.707 \left(\frac{j\omega}{1}\right) + 1\right) \cdot \left(\left(\frac{j\omega}{3}\right)^2 + 2 \cdot 0.707 \left(\frac{j\omega}{3}\right) + 1\right)} \right| \tag{E.3.9}$$

$$|a_{42}(j\omega)| = \left| \frac{0.00003(j\omega)^2}{\left(\left(\frac{j\omega}{1}\right)^2 + 2 \cdot 0.707 \left(\frac{j\omega}{1}\right) + 1\right) \cdot \left(\left(\frac{j\omega}{3}\right)^2 + 2 \cdot 0.707 \left(\frac{j\omega}{3}\right) + 1\right)} \right| \tag{E.3.10}$$

$$|a_{52}(j\omega)| = \left| \frac{0.0165(j\omega)^2}{\left(\left(\frac{j\omega}{0.11}\right)^2 + 2 \cdot 0.707\left(\frac{j\omega}{0.11}\right) + 1\right) \cdot \left(\left(\frac{j\omega}{3}\right)^2 + 2 \cdot 0.707\left(\frac{j\omega}{3}\right) + 1\right)} \right| \tag{E.3.11}$$

$$|a_{62}(j\omega)| = \left| \frac{0.00003(j\omega)^2}{\left(\left(\frac{j\omega}{1}\right)^2 + 2 \cdot 0.707\left(\frac{j\omega}{1}\right) + 1\right) \cdot \left(\left(\frac{j\omega}{3}\right)^2 + 2 \cdot 0.707\left(\frac{j\omega}{3}\right) + 1\right)} \right| \tag{E.3.12}$$

Column 3:

$$|a_{13}(j\omega)| = \left| \frac{4(j\omega)}{\left(\frac{j\omega}{0.11} + 1\right) \cdot \left(\left(\frac{j\omega}{3}\right)^2 + 2 \cdot 0.707\left(\frac{j\omega}{3}\right) + 1\right)} \right| \tag{E.3.13}$$

$$|a_{23}(j\omega)| = \left| \frac{10(j\omega)}{\left(\left(\frac{j\omega}{0.5}\right)^2 + 2 \cdot 0.707\left(\frac{j\omega}{0.5}\right) + 1\right) \cdot \left(\left(\frac{j\omega}{3}\right)^2 + 2 \cdot 0.707\left(\frac{j\omega}{3}\right) + 1\right)} \right| \tag{E.3.14}$$

$$|a_{33}(j\omega)| = \left| \frac{0.5(j\omega)}{(j\omega)/4 + 1} \right| \tag{E.3.15}$$

$$|a_{43}(j\omega)| = \left| \frac{0.0005(j\omega)}{((j\omega)/1 + 1)\,((j\omega)/10 + 1)} \right| \tag{E.3.16}$$

$$|a_{53}(j\omega)| = \left| \frac{0.05(j\omega)}{((j\omega)/9 + 1)^2} \right| \tag{E.3.17}$$

$$|a_{63}(j\omega)| = \left| \frac{0.005(j\omega)}{((j\omega)/0.1 + 1)\,((j\omega)/20 + 1)} \right| \tag{E.3.18}$$

Column 4:

$$|a_{14}(j\omega)| = \left| \frac{20(j\omega)^2}{\left(\left(\frac{j\omega}{0.11}\right)^2 + 2 \cdot 0.707\left(\frac{j\omega}{0.11}\right) + 1\right) \cdot \left(\left(\frac{j\omega}{1}\right)^2 + 2 \cdot 0.707\left(\frac{j\omega}{1}\right) + 1\right)} \right| \tag{E.3.19}$$

$$|a_{24}(j\omega)| = \left| \frac{100(j\omega)^2}{\left(\left(\frac{j\omega}{0.11}\right)^2 + 2 \cdot 0.707\left(\frac{j\omega}{0.11}\right) + 1\right) \cdot \left(\left(\frac{j\omega}{1}\right)^2 + 2 \cdot 0.707\left(\frac{j\omega}{1}\right) + 1\right)} \right| \tag{E.3.20}$$

$$|a_{34}(j\omega)| = \left| \frac{0.0003(j\omega)^2}{\left(\left(\frac{j\omega}{2}\right)^2 + 2 \cdot 0.707\left(\frac{j\omega}{2}\right) + 1\right) \cdot \left(\left(\frac{j\omega}{5}\right)^2 + 2 \cdot 0.707\left(\frac{j\omega}{5}\right) + 1\right)} \right| \tag{E.3.21}$$

$$|a_{44}(j\omega)| = \left|\frac{j\omega}{(j\omega)/2+1}\right| \tag{E.3.22}$$

$$|a_{54}(j\omega)| = \left|\frac{16.5(j\omega)^2}{\left(\left(\frac{j\omega}{0.11}\right)^2 + 2\cdot 0.707\left(\frac{j\omega}{0.11}\right)+1\right)\cdot\left(\left(\frac{j\omega}{7}\right)^2 + 2\cdot 0.707\left(\frac{j\omega}{7}\right)+1\right)}\right| \tag{E.3.23}$$

$$|a_{64}(j\omega)| = \left|\frac{16.5(j\omega)^2}{\left(\left(\frac{j\omega}{0.3}\right)^2 + 2\cdot 0.707\left(\frac{j\omega}{0.3}\right)+1\right)\cdot\left(\left(\frac{j\omega}{2}\right)^2 + 2\cdot 0.707\left(\frac{j\omega}{2}\right)+1\right)}\right| \tag{E.3.24}$$

Column 5:

$$|a_{15}(j\omega)| = \left|\frac{16(j\omega)^2}{\left(\left(\frac{j\omega}{0.2}\right)^2 + 2\cdot 1\left(\frac{j\omega}{0.2}\right)+1\right)\cdot\left(\left(\frac{j\omega}{2}\right)^2 + 2\cdot 0.6\left(\frac{j\omega}{2}\right)+1\right)}\right| \tag{E.3.25}$$

$$|a_{25}(j\omega)| = \left|\frac{8(j\omega)^2}{\left(\left(\frac{j\omega}{0.3}\right)^2 + 2\cdot 0.707\left(\frac{j\omega}{0.3}\right)+1\right)\cdot\left(\left(\frac{j\omega}{2}\right)^2 + 2\cdot 0.707\left(\frac{j\omega}{2}\right)+1\right)}\right| \tag{E.3.26}$$

$$|a_{35}(j\omega)| = \left|\frac{0.001(j\omega)^2}{\left(\left(\frac{j\omega}{4}\right)^2 + 2\cdot 0.6\left(\frac{j\omega}{4}\right)+1\right)\cdot\left(\left(\frac{j\omega}{4}\right)^2 + 2\cdot 0.6\left(\frac{j\omega}{4}\right)+1\right)}\right| \tag{E.3.27}$$

$$|a_{45}(j\omega)| = \left|\frac{0.001(j\omega)^2}{\left(\left(\frac{j\omega}{4}\right)^2 + 2\cdot 0.6\left(\frac{j\omega}{4}\right)+1\right)\cdot\left(\left(\frac{j\omega}{4}\right)^2 + 2\cdot 0.6\left(\frac{j\omega}{4}\right)+1\right)}\right| \tag{E.3.28}$$

$$|a_{55}(j\omega)| = \left|\frac{5.6(j\omega)^2}{\left(\frac{j\omega}{0.6}\right)^2 + 2\cdot 0.7\left(\frac{j\omega}{0.6}\right)+1}\right| \tag{E.3.29}$$

$$|a_{65}(j\omega)| = \left|\frac{0.8(j\omega)^2}{\left(\left(\frac{j\omega}{0.5}\right)^2 + 2\cdot 1\cdot\left(\frac{j\omega}{0.5}\right)+1\right)\cdot\left(\left(\frac{j\omega}{7}\right)^2 + 2\cdot 1\cdot\left(\frac{j\omega}{7}\right)+1\right)}\right| \tag{E.3.30}$$

Column 6:

$$|a_{16}(j\omega)| = \left|\frac{0.02(j\omega)}{\left(\frac{j\omega}{0.11}+1\right)\cdot\left(\left(\frac{j\omega}{3}\right)^2 + 2\cdot 0.707\left(\frac{j\omega}{3}\right)+1\right)}\right| \tag{E.3.31}$$

$$|a_{26}(j\omega)| = \left|\frac{0.3(j\omega)^2}{\left(\left(\frac{j\omega}{0.11}\right)^2 + 2\cdot 0.707\left(\frac{j\omega}{0.11}\right)+1\right)\cdot\left(\left(\frac{j\omega}{3}\right)^2 + 2\cdot 0.707\left(\frac{j\omega}{3}\right)+1\right)}\right| \tag{E.3.32}$$

$$|a_{36}(j\omega)| = \left| \frac{0.0001(j\omega)^2}{\left(\left(\frac{j\omega}{6}\right)^2 + 2\cdot 1\left(\frac{j\omega}{6}\right) + 1\right)^2} \right| \tag{E.3.33}$$

$$|a_{46}(j\omega)| = \left| \frac{0.01(j\omega)}{\left(\left(\frac{j\omega}{8}\right)^2 + 2\cdot 1\cdot\left(\frac{j\omega}{8}\right) + 1\right)\cdot\left(\left(\frac{j\omega}{15}\right)^2 + 2\cdot 1\cdot\left(\frac{j\omega}{15}\right) + 1\right)} \right| \tag{E.3.34}$$

$$|a_{56}(j\omega)| = \left| \frac{0.02(j\omega)}{((j\omega)/2 + 1)\left(\left(\frac{j\omega}{15}\right)^2 + 2\cdot 0.707\cdot\left(\frac{j\omega}{15}\right) + 1\right)} \right| \tag{E.3.35}$$

$$|a_{66}(j\omega)| = \left| \frac{3.08(j\omega)}{(j\omega)/0.65 + 1} \right| \tag{E.3.36}$$

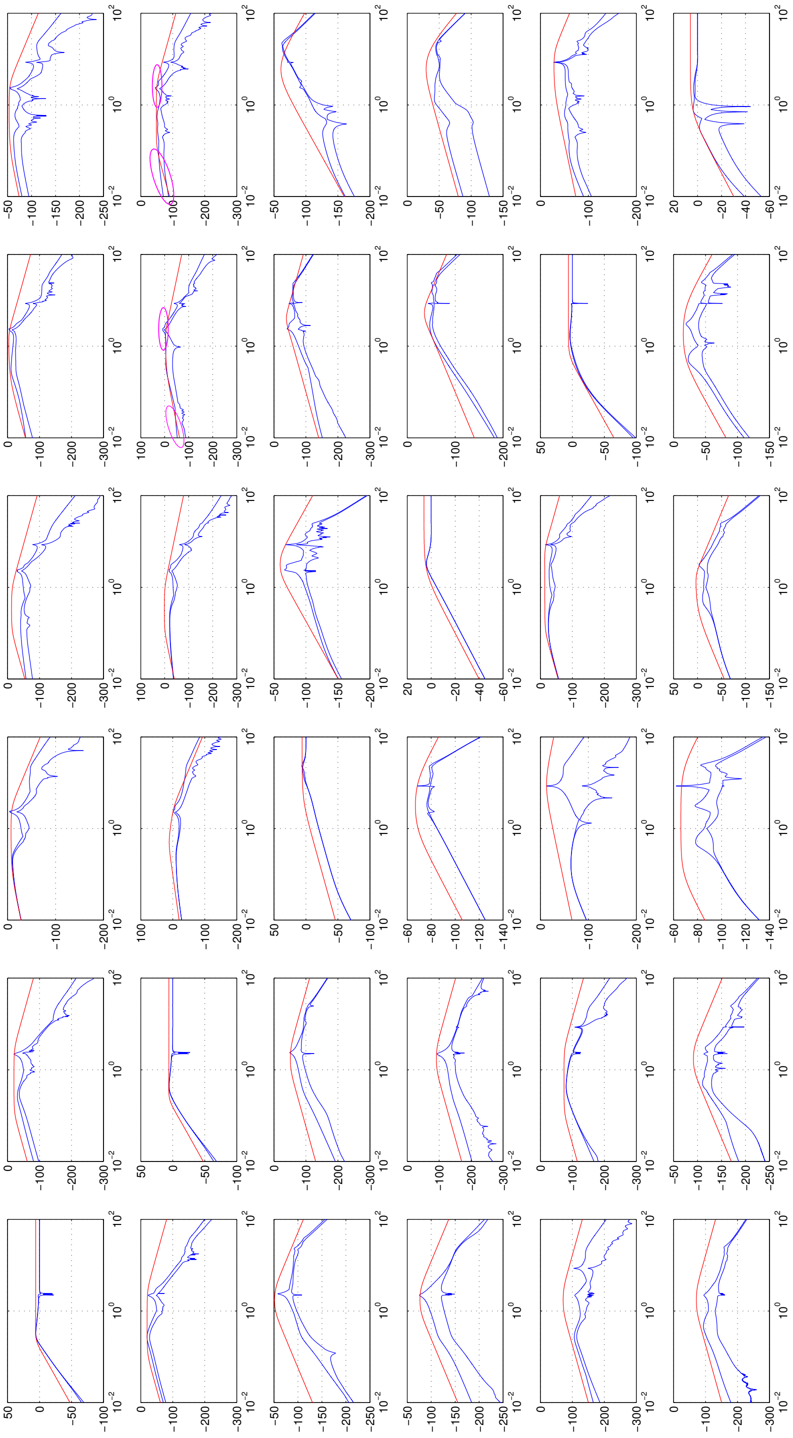

Figure E.3.2: Bode magnitude plot of the minimum and maximum sensitivity envelope of the closed-loop system (blue) *after* tuning g_{33} controller; sensitivity specifications (red); highlighting sensitivity violation (magenta) for next loop design stage; x-axis: frequency in rad/s; y-axis: magnitude in dB

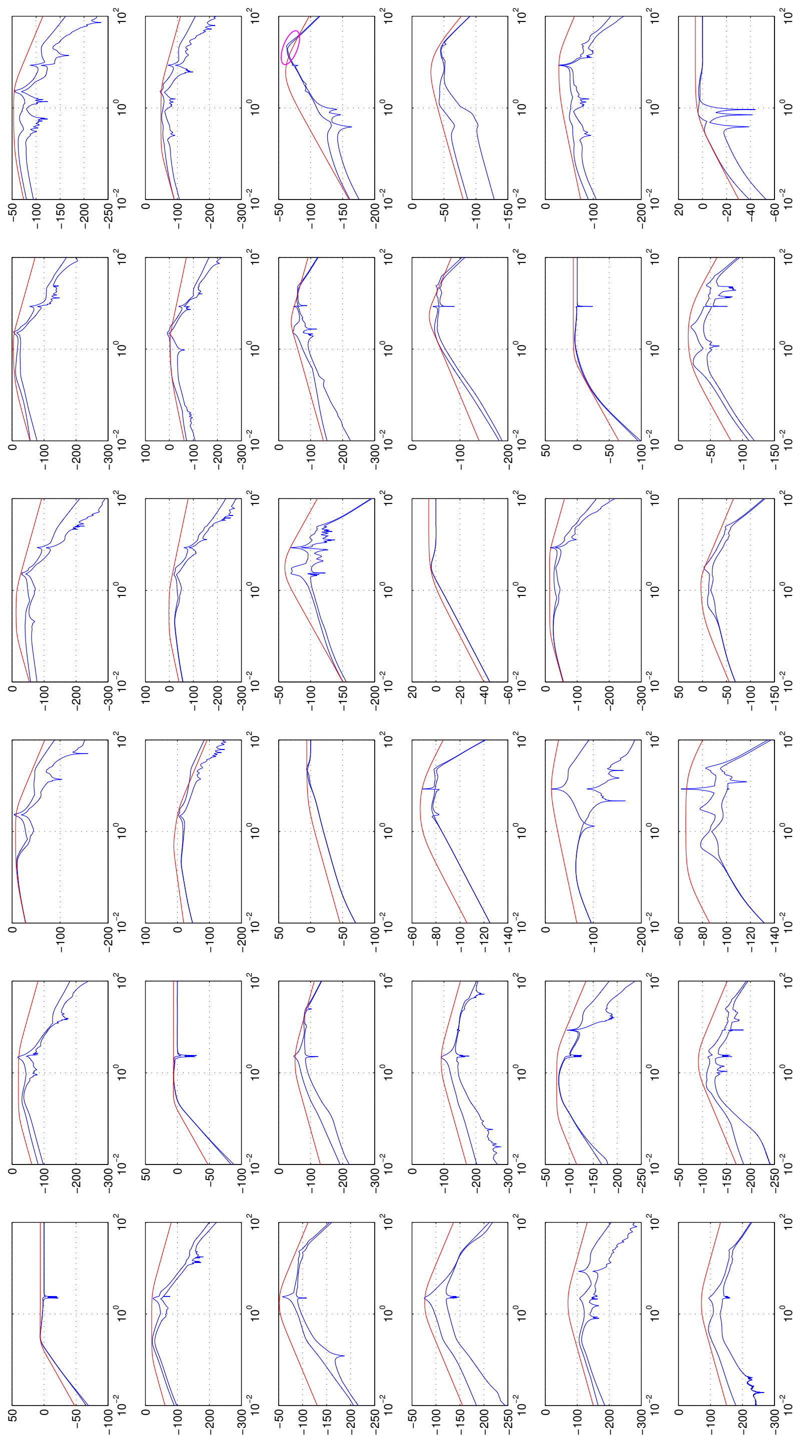

Figure E.3.3: Bode magnitude plot of the minimum and maximum sensitivity envelope of the closed-loop system (blue) *after* tuning g_{33} and g_{22} controllers; sensitivity specifications (red); highlighting sensitivity violation (magenta) for next loop design stage; x-axis: frequency in rad/s; y-axis: magnitude in dB

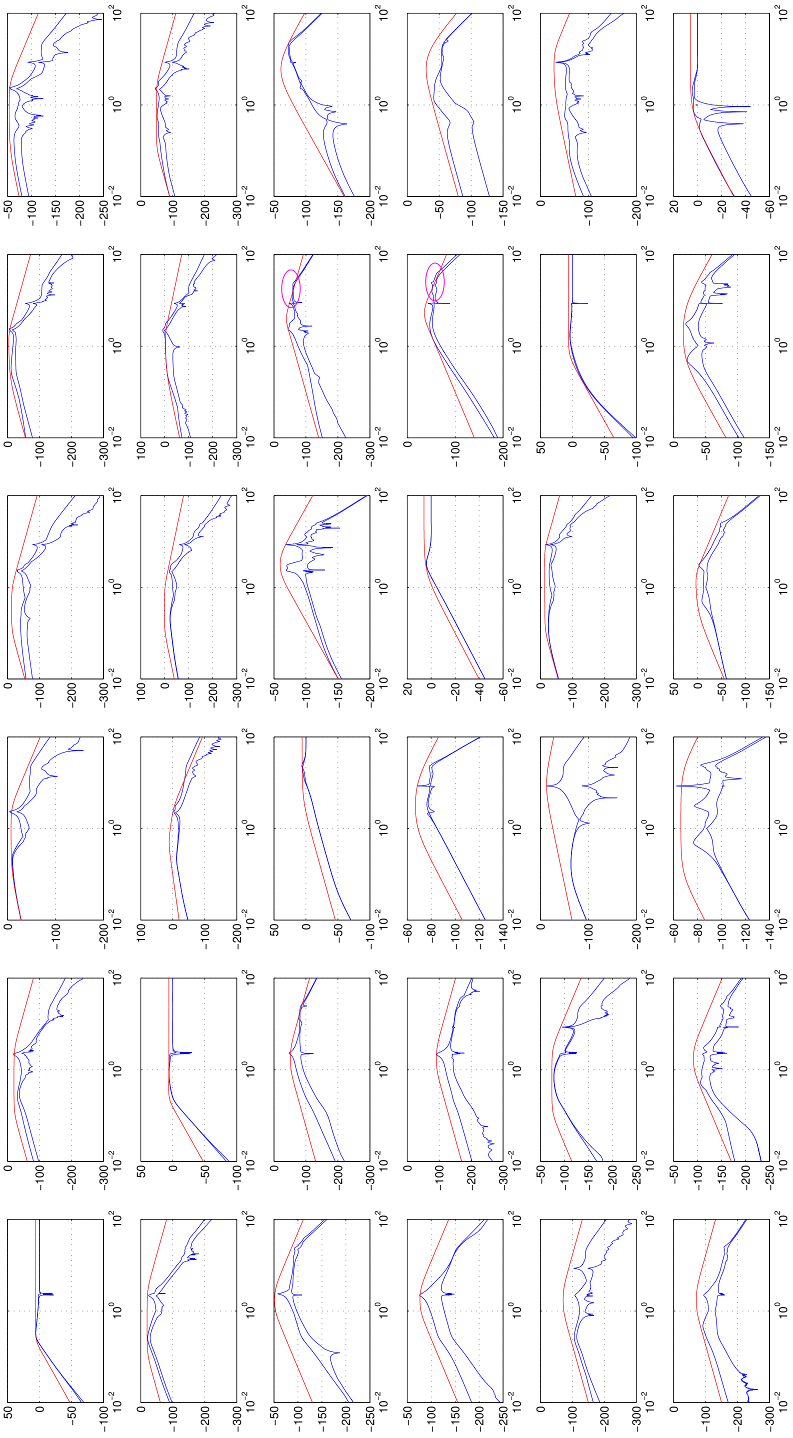

Figure E.3.4: Bode magnitude plot of the minimum and maximum sensitivity envelope of the closed-loop system (blue) *after* tuning g_{33}, g_{22} and g_{66} controllers; sensitivity specifications (red); highlighting sensitivity violation (magenta) for next loop design stage; x-axis: frequency in rad/s; y-axis: magnitude in dB

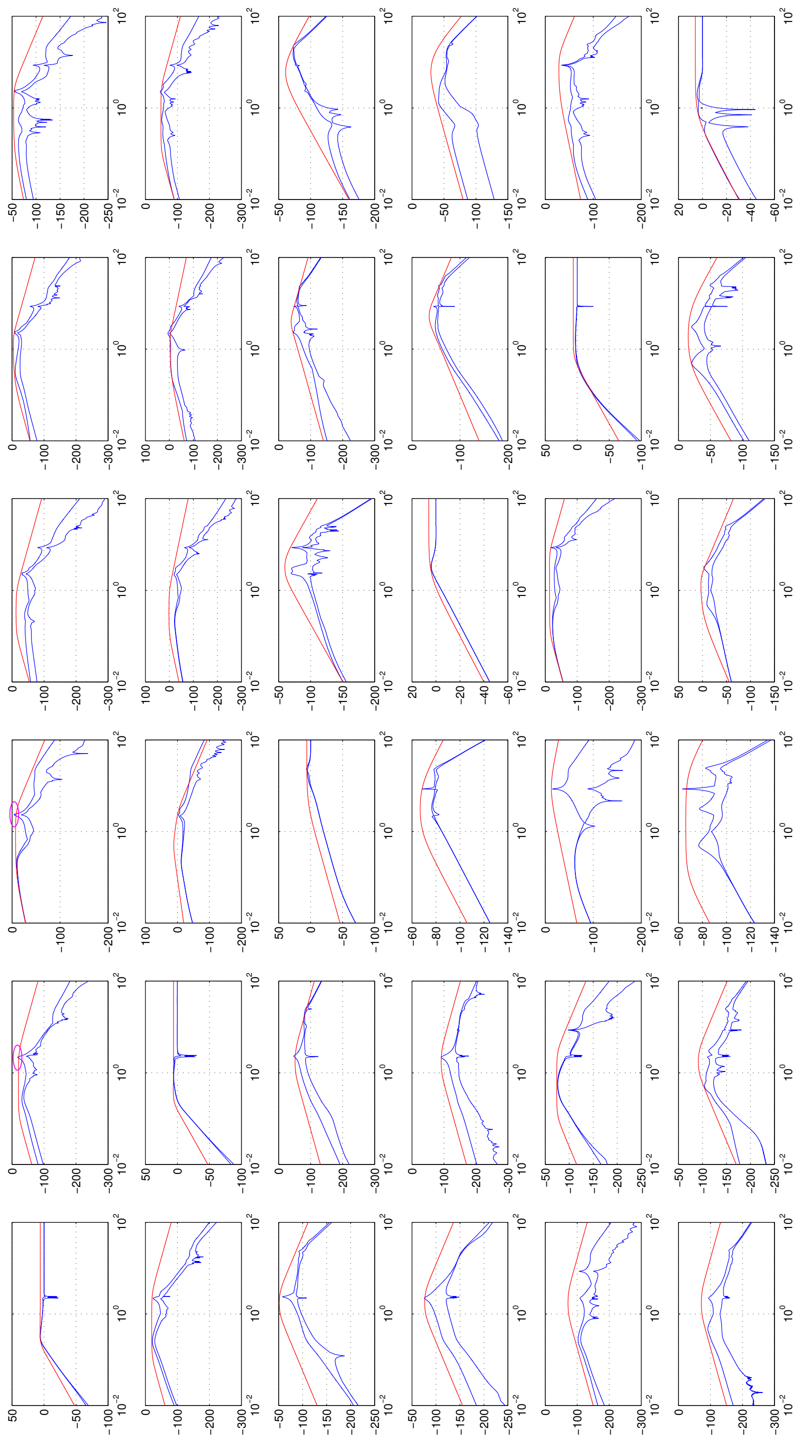

Figure E.3.5: Bode magnitude plot of the minimum and maximum sensitivity envelope of the closed-loop system (blue) *after* tuning g_{33}, g_{22}, g_{66} and g_{55} controllers; sensitivity specifications (red); highlighting sensitivity violation (magenta) for next loop design stage; x-axis: frequency in rad/s; y-axis: magnitude in dB

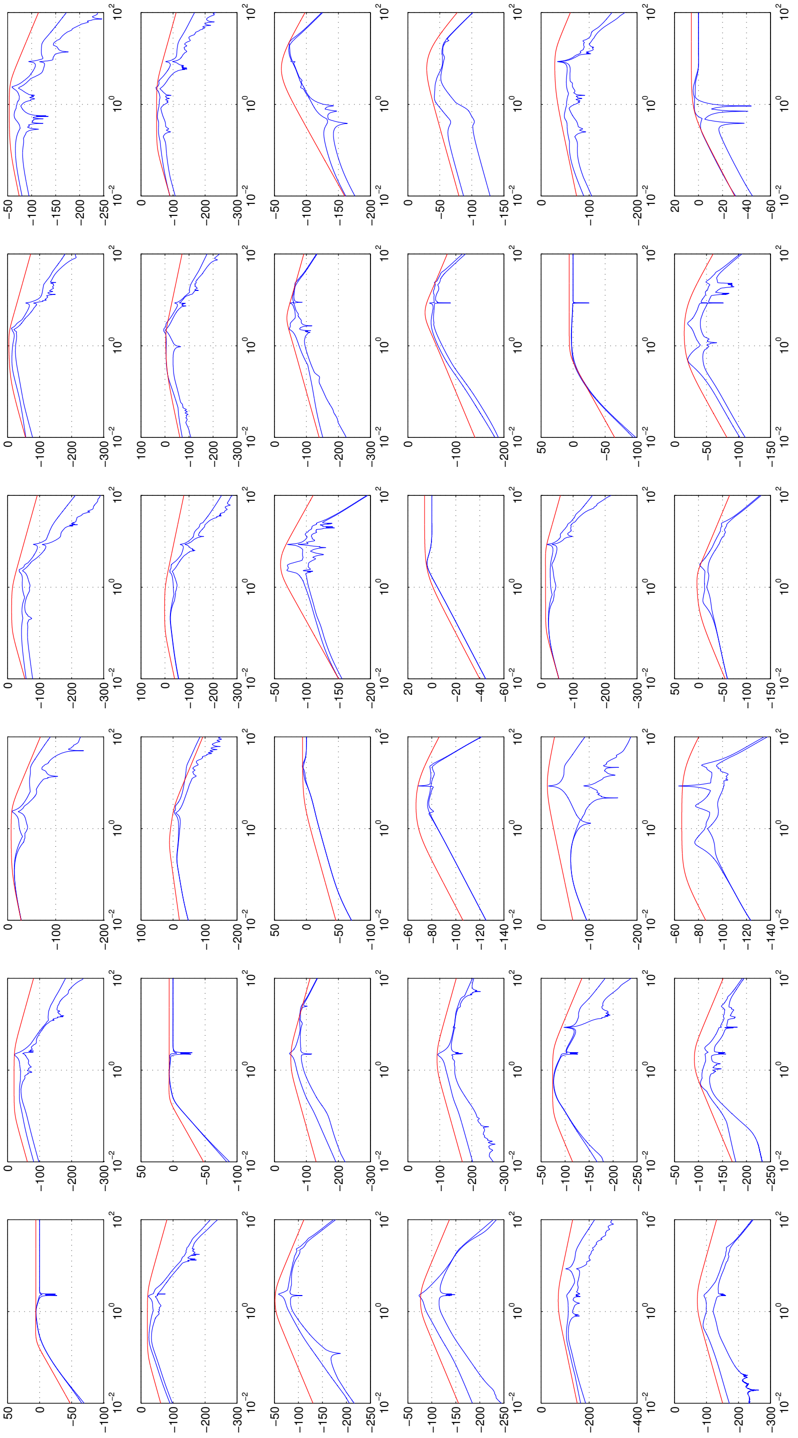

Figure E.3.6: Bode magnitude plot of the minimum and maximum sensitivity envelope of the closed-loop system (blue) *after* tuning g_{33}, g_{22}, g_{66}, g_{55} and g_{11} controllers; sensitivity specifications (red); x-axis: frequency in rad/s; y-axis: magnitude in dB

References

Baskett, B. J. (2000), Aeronautical design standard performance specification handling qualities requirements for military rotorcraft, Technical report, DTIC Document.

Bernard, M. & Kondak, K. (2009), Generic slung load transportation system using small size helicopters, *in* 'Robotics and Automation, 2009. ICRA'09. IEEE International Conference on', IEEE, pp. 3258–3264.

Bisgaard, M., Bendtsen, J. D. & Cour-Harbo, A. L. (2009), 'Modeling of generic slung load system', *Journal of guidance, control, and dynamics* **32**(2), 573–585.

Boje, E. (2002), 'Non-diagonal controllers in MIMO quantitative feedback design', *International Journal of Robust and Nonlinear Control* **12**(4), 303–320.

Boje, E. & Nwokah, O. D. (1999), 'Quantitative multivariable feedback design for a turbofan engine with forward path decoupling', *International Journal of robust and nonlinear control* **9**(12), 857–882.

Borghesani, C., Chait, Y. & Yaniv, O. (1994), 'The qft toolbox for matlab', *The MathWorks* .

Bouguet, J. (2008), 'Camera calibration toolbox for matlab. caltech'.

Bristol, E. (1966), 'On a new measure of interaction for multivariable process control', *IEEE transactions on automatic control* **11**(1), 133–134.

Brown, R. G. & Hwang, P. Y. (1997), 'Introduction to random signals and applied kalman filtering. 1997', *NY John Wiley and Sons* .

Cicolani, L. S. & Kanning, G. (1992), *Equations of motion of slung-load systems, including multilift systems*, Vol. 3280, National Aeronautics and Space Administration, Office of Management, Scientific and Technical Information Program.

Delaney, B. (1998), 'On the trail of the shadow woman: The mystery of motion capture', *Computer Graphics and Applications, IEEE* **18**(5), 14–19.

Diebel, J. (2006), 'Representing attitude: Euler angles, unit quaternions, and rotation vectors', *Matrix* **58**, 15–16.

Eitelberg, E. (1988), 'Sampling rate design based on (1- st/2)', *International Journal of Control* **48**(4), 1423–1432.

Eitelberg, E. (1999), *Load sharing control*, NOYB Press.

Eitelberg, E. (2000), *Ed. Eitelberg's Control Engineering: Course Notes*, NOYB Press.
URL: *https://books.google.co.za/books?id=IVGTygAACAAJ*

Eitelberg, E. (2003), On multivariable tracking, *in* '6th International Symposium on Quantitative Feedback Theory in conjunction with the First African Control Conference, University of Cape Town, South Africa', Vol. 2, pp. 514–519.

Eitelberg, E. (2006), 'On multiloop interaction and relative and bristol gains', *Journal of dynamic systems, measurement, and control* **128**(4), 929–937.

ETH Zürich (2013), 'University of eth', `http://www.idsc.ethz.ch/Research_DAndrea/Flying_Machine_Arena/infrastructure`. Accessed June 5, 2013.

FAS, M. N. A. (2000), 'Uh-60 black hawk', `https://fas.org/man/dod-101/sys/ac/uh-60.htm`. Accessed February 20, 2017.

Garcia-Sanz, M. (2008-2017), 'The qft toolbox for matlab', `http://codypower.com`.

Garcia-Sanz, M., Eguinoa, I., Barreras, M. & Bennani, S. (2008), 'Nondiagonal mimo qft controller design for darwin-type spacecraft with large flimsy appendages', *Journal of Dynamic Systems, Measurement, and Control* **130**(1), 011006.

Garofalo, F., Iannelli, L. & Vasca, F. (2002), Participation factors and their connections to residues and relative gain array, *in* 'Proc. of the 15th Triennal World Congress, Barcelona, Spain', pp. 125–130.

Goldstein, H. (1965), *Classical mechanics*, Pearson Education India.

Gonzalez, R. C. & Woods, R. E. (2002), 'Digital image processing'.

Gupte, S., Mohandas, P. I. T. & Conrad, J. M. (2012), A survey of quadrotor unmanned aerial vehicles, *in* 'Southeastcon, 2012 Proceedings of IEEE', IEEE, pp. 1–6.

Hald, U. B., Hesselbæk, M. V. & Siegumfeldt, M. (2006), *Nonlinear modeling and optimal control of a miniature autonomous helicopter*, Aalborg University.

Hartley, R. & Zisserman, A. (2003), *Multiple view geometry in computer vision*, Cambridge university press.

Hess, R. & Gorder, P. (1993), 'Quantitative feedback theory applied to the design of a rotorcraft flight control system', *Journal of guidance, control, and dynamics* **16**(4), 748–753.

Horowitz, I. (1982), 'Improved design technique for uncertain multiple-input-multiple-output feedback systems', *International Journal of Control* **36**(6), 977–988.

Horowitz, I. (2001), 'Survey of quantitative feedback theory (qft)', *International journal of robust and nonlinear control* **11**(10), 887–921.

Horowitz, I. M. (1993), *Quantitative feedback design*, QFT publications Boulder, CO.

Houpis, C. H. & Garcia-Sanz, M. (2012), *Wind energy systems: control engineering design*, CRC press.

Houpis, C. H., Rasmussen, S. J. & Garcia-Sanz, M. (2006), *Quantitative feedback theory: fundamentals and applications*, Vol. 20, CRC Press.

How, J. P., BEHIHKE, B., Frank, A., Dale, D. & Vian, J. (2008), 'Real-time indoor autonomous vehicle test environment', *IEEE control systems* **28**(2), 51–64.

Incorporated, E. A.-C. (2013), 'Erickson air-crane photo gallery', `http://www.ericksonaircrane.com/photogallery.php`. Accessed June 10, 2013.

Karaoglu, B. & Heinzelman, W. (2010), Multicasting vs. broadcasting: What are the tradeoffs?, *in* 'Global Telecommunications Conference (GLOBECOM 2010), 2010 IEEE', IEEE, pp. 1–5.

Kundur, P., Balu, N. J. & Lauby, M. G. (1994), *Power system stability and control*, Vol. 7, McGraw-hill New York.

La Civita, M., Papageorgiou, G., Messner, W. & Kanade, T. (2002), Design and flight testing of a high-bandwidth h-infinity loop shaping controller for a robotic helicopter, *in* 'AIAA Guidance, Navigation, and Control Conference and Exhibit', p. 4836.

Li, Z., Horn, J. F. & Langelaan, J. W. (2014), Coordinated transport of a slung load by a team of autonomous rotorcraft, *in* 'AIAA Guidance, Navigation, and Control Conference', p. 0968.

Limebeer, D. J. (1982), 'The application of generalized diagonal dominance to linear system stability theory', *International Journal of Control* **36**(2), 185–212.

Ljung, L. (1998), *System identification: Theory for the user*, Springer.

Lupashin, S., Hehn, M., Mueller, M. W., Schoellig, A. P., Sherback, M. & DAndrea, R. (2014), 'A platform for aerial robotics research and demonstration: The flying machine arena', *Mechatronics* **24**(1), 41–54.

Maciejowski, J. M. (1989), *Multivariable feedback design*, Vol. 72, Addison-Wesley UK.

Mansor, H., Zaeri, A. H., Noor, S. M., Ahmad, R. R., Taip, F. S. & Ali, H. I. (2010), 'Design of qft controller for a bench-top helicopter system model', *International Journal of Simulation System, Science & Technology* **11**(5), 8–16.

Marins, J. L., Yun, X., Bachmann, E. R., McGhee, R. B. & Zyda, M. J. (2001), An extended kalman filter for quaternion-based orientation estimation using marg sensors, *in* 'Intelligent Robots and Systems, 2001. Proceedings. 2001 IEEE/RSJ International Conference on', Vol. 4, IEEE, pp. 2003–2011.

Mettler, B., Tischler, M. B. & Kanade, T. (1999), System identification of small-size unmanned helicopter dynamics, *in* 'Annual Forum Proceedings- American Helicopter Society', Vol. 2, pp. 1706–1717.

Michael, N., Mellinger, D., Lindsey, Q. & Kumar, V. (2010), 'The grasp multiple micro-uav testbed', *IEEE Robotics & Automation Magazine* **17**(3), 56–65.

MIPS Technologies Inc. (2010), 'Beyond the Hype: MIPS - the Processor for MCUs', `http://www.techbriefs.com/dl/insider072110.php?i=8575&d=1`. Accessed June, 2012.

Mittal, M., Prasad, J. & Schrage, D. P. (1991), 'Nonlinear adaptive control of a twin lift helicopter system', *Control Systems, IEEE* **11**(3), 39–45.

Muir, A. (2013), 'What do you want from motion capture?', `http://diydrones.com/profiles/blogs/what-do-you-want-from-motion-capture`. Accessed June 5, 2013.

NWW (2016), 'National wind watch, faq', `https://www.wind-watch.org/faq-size.php`. Accessed February 20, 2017.

Padfield, G. D. (2008), *Helicopter flight dynamics*, John Wiley & Sons.

Raptis, I. A. & Valavanis, K. P. (2010), *Linear and Nonlinear Control of Small-scale unmanned Helicopters*, Vol. 45, Springer Science & Business Media.

Real-Time Linux (2010), 'Real-time linux wiki', `https://rt.wiki.kernel.org/`. Accessed September 13, 2015.

Reddi, Y. (2011), Robust multivariable control design : an application to a bank-to-turn missile, Master's thesis, University of KwaZulu Natal, Durban, South Africa.

Reddi, Y. & Boje, E. (2012), Disturbance rejection design for a bank-to-turn missile using decoupling quantitative feedback theory, *in* 'Robust Control Design', Vol. 7, pp. 139–144.

Reddi, Y. & Boje, E. (2014), System identification for low-cost small-scale helicopters, *in* 'World Congress', Vol. 19, pp. 8831–8836.

Seddon, J. M. & Newman, S. (2011), *Basic helicopter aerodynamics*, Vol. 40, John Wiley & Sons.

Sgt. Susan Wilt, 2nd BCT, n. A. D. P. (2008), 'Hanging there', `https://www.army.mil/e2/-images/2008/11/24/26110/`. Accessed February 20, 2017.

Sidi, M. J. (2001), *Design of Robust Control Systems: From classical to modern practical approaches*, Krieger Publishing Company Malbar, FL.

Skogestad, S. & Postlethwaite, I. (2007), *Multivariable feedback control: analysis and design*, Vol. 2, Wiley New York.

Smart, R. (2013), 'ALIGN T-REX 250SE Super Combo', `http://www.rcsmart.com.my/webshaper/store/viewProd.asp?pkProductItem=3216`. Accessed June 10, 2013.

Smerlas, A., Postlethwaite, I., Walker, D., Strange, M., Howitt, J., Horton, R., Gubbels, A. & Baillie, S. (1998), Design and flight testing of an h-infinity controller for the nrc bell 205 experimental fly-by-wire helicopter, *in* 'AIAA Guidance, Navigation, and Control Conference and Exhibit, Boston, MA', pp. 1023–1033.

Srinivasulu, P. & Vaidyanathan, C. (1976), *Handbook of machine foundations*, Tata McGraw-Hill Education.

Trawny, N. & Roumeliotis, S. I. (2005), 'Indirect kalman filter for 3d attitude estimation', *University of Minnesota, Dept. of Comp. Sci. & Eng., Tech. Rep* **2**.

Van Der Merwe, R. & Wan, E. A. (2004), Sigma-point kalman filters for integrated navigation, *in* 'Proceedings of the 60th Annual Meeting of the Institute of Navigation (ION)', pp. 641–654.

Vicon (2004), 'Vicon MX Hardware System Reference', `http://bdml.stanford.edu/twiki/pub/Haptics/MotionDisplayKAUST/ViconHardwareReference.pdf`. Accessed April, 2013.

Vicon (2013), 'University of pennsylvania grasp lab', `http://www.vicon.com/company/documents/UPENNGraspLab.pdf`. Accessed June 5, 2013.

Walker, D., Turner, M. & Gubbels, A. (2001), Practical aspects of implementing h-infinity controllers on a fbw research helicopter, Technical report, LEICESTER UNIV (UNITED KINGDOM) DEPT OF ENGINEERING.

Wendel, J., Meister, O., Schlaile, C. & Trommer, G. F. (2006), 'An integrated gps/mems-imu navigation system for an autonomous helicopter', *Aerospace Science and Technology* **10**(6), 527–533.

Yaniv, O. (2013), *Quantitative feedback design of linear and nonlinear control systems*, Vol. 509, Springer Science & Business Media.

Ypma, T. J. (1995), 'Historical development of the newton-raphson method', *SIAM review* **37**(4), 531–551.

Index